FINITE ELEMENT ANALYSIS OF INDUSTRIAL CIRCULAR SAWBLADE WITH RESPECT TO TENSIONING, ROTATING, CUTTING, AND EXPANSION SLOTS

by

Charles B. Ponton

Thesis submitted to the Faculty of the

Virginia Polytechnic Institute and State University

in partial fulfillment of the requirements for the degree of

MASTER OF SCIENCE

in

Mechanical Engineering

APPROVED:

_____

Dr. R.L. West, Chairman

_____ _____

Dr. S. M. Duma Dr. C. Reinholtz

February 05, 2007
Blacksburg, Virginia

Key Words: Circular Saw, Saw Tensioning, Saw Doctoring, Residual Stress, Centrifugal Force, Plastic Deformation

Finite Element Analysis of Industrial Circular Sawblade with Respect to Tensioning, Rotating, Cutting, and Expansion Slots

Charles B. Ponton

(Abstract)

Little research has been done to determine the stress states developed in an industrial sawblade for various operating conditions. The stresses are developed from the forces generated during the cutting of materials, and also from the vibration of the sawblade. The difficulty of analyzing these stresses and vibrations results from the sawblade's high speed of rotation, which make it difficult to instrument the sawblade for analysis. Stress and vibration can ruin the sawblade from loss of material properties due to heat build-up and fatigue failure. The sawblade industry raised natural frequencies away from the operating frequencies to overcome the vibrations.

To raise the natural frequencies of the sawblades away from the operating frequencies, residual stresses have been intentionally induced in the sawbody. The residual stresses come from plastically deforming the sawbody with one or more concentric rings. Experts who determine the location, depth, and number of residual stress rings are called "saw doctors". This thesis quantifies the residual stresses induced by saw doctors.

Developing and evaluating finite element models of an industrial sawblade while undergoing the effects from rotating and cutting are also included in the thesis. In addition, the effects on the sawblades performance due to various numbers and lengths of expansion slots and sawblade tensioning are explored. Models of the sawblade are plastically deformed leaving residual stresses which are analyzed to determine the natural frequencies of the sawblade. The thesis quantifies the above mechanisms for a sawblade under the loads developed from rotation and a load case representing the cutting process. The work developed in this thesis is a first step toward characterizing the effects of specific mechanisms which can be used to design better, longer lasting sawblades.

Acknowledgements

The author is grateful to Dr. Dillard (Professor/Director, Ctr. for Adhesive & Sealant Science) whose experience was fundamental for the writing of this thesis. The author sends special thanks to R.S. Ponton (thanks Dad), President of *ICE* (International Carbide & Engineering, Inc.) for providing key information used in this research paper. Thanks go to John Hodges and Herb Wright of Reed's Carbide Saw and Tool for their tour and explanation of tensioning sawblades. Thanks go to Glenn Rebholz for his encouragement from his reading the thesis and for pointing out grammatical errors. Thanks go to Travis Bash for his help with the sawblade free-vibration frequency analysis. Much thanks goes to Dr. West for his time, knowledge, attention, and patience through this research and writing process. Thanks to my wife for her encouragement and patience throughout this study and life.

Outline

List of Figures

List of Tables

Commonly Used Variables

a = Inner Radius
A_o = Initial Area
A = Area
b = Outer Radius
bpt = Bite Per Tooth
C_1 = Constant
C_2 = Constant
E = Modulus of Elasticity
ε = True Strain
ε_{el} = Elastic Strain
ε_{nom} = Nominal Strain
ε_{pl} = Plastic Strain
ε_{tot} = Total Strain
F = Force
F' = Force per second
F_r = Feed Rate (board feet per minute)
l_o = Initial Length
M_1 = Constant
M_2 = Constant
P' = Pressure per second
PPT = Pressure per Tooth
ρ = Mass Density [N-s^2/mm^4 or lbf-s^2/inches^4]
r = Arbitrary Radial Position
σ = True Engineering Stress
σ_{nom} = Nominal Stress
σ_{rr} = Radial Stress
A_l = Arclength
S11 = Radial Stress
$\sigma_{\theta\theta}$ = Tangential Stress
= Circumferential Stress
S22 = Tangential Stress
= Circumferential Stress
S' = von Mises Stress
σ_{ult} = Ultimate Stress
T' = Teeth per second
u = Radial Displacement
U1 = Radial Displacement
U2 = Tangential Displacement
U3 = Axial Displacement
υ = Poisson's Ratio
W = Power
ω = Angular Velocity (rad/s)

Chapter 1

Introduction

1.1 *Problem or Needs Statement*

This research paper presents a systematic approach to analyzing the stresses and natural frequencies found in circular sawblades. Because sawblades are spinning when in use, the problem of finding the actual stresses and natural frequencies in the blades when in use has been difficult to measure in the past. Therefore, it is necessary to analyze these stresses and natural frequencies using analytical tools available today such as finite element analysis (FEA). This thesis will determine the stresses in the sawblade under a load condition representative of the cutting process. Using finite element analysis, the stresses can be estimated anywhere in the body of the sawblade. More importantly, FEA allows these resultant stresses to be seen beneath the surface of the sawblade. The resultant stresses seen beneath the surface of the sawblade are difficult and often impossible to know unless specialty tools like finite element analysis are used for investigation.

This thesis also determines the natural frequencies and the resulting effects on the natural frequencies induced in the sawblades from the spinning and cutting processes. Therefore, the use of saw tensioning (which intentionally induces residual stresses into the sawblade) will be analyzed, quantified, and discussed as a means of making sawblades last longer and at the same time help realize solutions to problems with noise, natural frequency and longevity of the sawblades. Knowing the value of the natural frequencies of the sawblade, as well as the value of the residual stresses and their locations, will help solve the need to quantify the stress effects and help the saw manufacturers incorporate these modifications into their future designs for better sawblades.

1.2 *Concept for solution*

To resolve the issues of finding stresses and natural frequencies in the sawblades several methods were used. First, the material properties chosen from those of actual

sawblades are used to represent the sawblade in all finite element models in this study. The material properties will be used in all calculations, illustrating the stresses seen by the sawblade, and the interpretation of results will be explained. Then, a small amount of experimental data was collected using an actual sawblade to verify the fundamental natural frequencies seen in the sawblade during a non-rotating analysis. Several computer models have been built from the baseline model to complex models representing real world effects on a sawblade. These methods are compared and validate each other throughout both the research and the thesis.

Material properties are found from material properties tables found in material handbooks, Brockenbrough, Merritt [10]. Then, these properties are placed in the form needed for solving our stresses in sawblades addressed in this thesis. The exact material properties of sawblades in the plastic zone, as well as the material properties of the hardened steel rollers were not available and therefore, the closest material properties (A514 Steel) were substituted to most closely represent the "real world" process and results of the analyzed topics of this research.

Hand calculations were used to provide baseline results later used as a reference solution for comparison of model results. The hand calculations began with simple axisymmetric models, and then increased in complexity. The hand calculations are used to obtain needed results from stress strain/curves (including the plastic stress zone information) in the form needed for the analysis. In addition, many hand calculations are used to find the pressures seen by the sawblade's tips during the wood cutting process.

These calculations were then followed by an experimental study using an actual sawblade, modal hammer, accelerometer, and data acquisition computer to verify and investigate the natural frequencies of a typical sawblade. This type of analysis was used as a way to verify the natural frequencies seen in the computer analysis results.

In this thesis, computer models start from a simple axisymmetric disc case. The models are built step-by-step increasing their complexity until three-dimensional models of actual sawblades in use are analyzed. By increasing the model's complexity, the computer models in this research have been able to be used in a boot-strap process. The complex models' results were checked against the previously simpler models' results to see if the new results "make sense" and were in agreement with prior results or if the results deviate from what is expected by observing the previously simpler case's results.

Thus, the building of the models in this way has provided a basis to compare the results to match and enable the engineer to see if the results found are credible. This self-check of building the models from simpler models has driven the analysis closer to modeling an actual sawblade in use and closer to correctly representing the sawblade's stresses in the real world. Furthermore, the finite element analysis allows the engineer to see firsthand what the stresses are anywhere in the sawblade. The finite element analysis quantifies these stress effects and the natural frequencies seen by the sawblade both before and during the rotation of the sawblade.

Furthermore, the computer model also analyzes the effects of expansion slots, the number of expansion slots, and the length these expansion slots have on stresses and natural frequencies seen in a sawblade. Expansion slots are 1-in to 2 ½-in long by 0.010-in to 0.060-in wide slots cut into the sawblade from the outer rim towards the center.

Finite element analysis is used to represent the effects of plastically deforming the sawblade to leave residual stresses in the body of the sawblade. These residual stresses result in higher natural frequencies in the sawblade, with fewer tendencies for a sawblade to be noisy; the sawblade will cut truer, enabling a longer-running, safer sawblade.

1.3 *Objectives*

There are many facets of what happens with a sawblade when rotating and cutting. For example, the different types of wood, dirt or gravel embedded in wood, type of material being cut, knots in the wood, binding of the saw in the wood, and atmospheric conditions as well as other conditions can affect the cutting and performance of a sawblade. In addition, affects come from the sawing machine itself with regard to its power, trueness, and stability to hold and turn the sawblade on a true axis.

There are heating effects from the cutting that will cause the sawblade to operate less than desirable. For example, heating during the brazing of the saw tips may change the state of the metal by weakening the material or leaving thermal residual stresses in the sawbody material. Or perhaps, the carbide saw teeth are not properly brazed onto the sawblade. Other examples are the rubbing of the sawbody on the material being cut which can rapidly overheat the sawbody's material and cause the sawblade to no longer

run true in the cut. This may result in a wobbly saw, and could even cause the sawblade to rupture.

Some of the affects on the cutting performance of a sawblade are directly controllable. For instance, the torque used to tighten the sawblade onto the sawing machine can have an effect on the wobble and trueness of the cut and sawblade performance. Choosing the correct sawblade for the type of material and cutting speed and material feed is essential for optimum performance. Running sharp sawblades has an enormous impact on the cutting performance and the longevity of the sawblades and the fatigue on the sawing machine.

1.4 *Scope of the Work – Which of the Objectives This Thesis is Going to Discuss*

As fore-mentioned, the problem of finding the actual stresses and natural frequencies in the saw blades when in motion until recently has been difficult to measure. The points dealt with in this thesis are

1) Stress analysis
    a) Stress from the effects of centrifugal forces
    b) Stress from the effects of the saw collar
    c) Stress from effects of differing densities from saw teeth and the steel sawbody
    d) Stress from the cutting forces
    e) Stress from expansion slots and varying number and expansion slot length
    f) Stress from contact between the roller and the sawbody
    g) Residual stress left in sawbody (steel placed in plastic zone)
    h) Varying the number and location of residual stress rings in the sawbody
2) Modal analysis
    a) Natural frequency of a non-rotating and rotating disc
    b) Natural frequency of a non-rotating and rotating annulus
    c) Natural frequency of a non-rotating and rotating sawblade with and without a saw collar
    d) Natural frequency of a non-rotating and rotating sawblade with no residual stresses

e) Natural frequency of a non-rotating and rotating sawblade with varying number of expansion slots
f) Natural frequency of a non-rotating and rotating annulus with varying residual stresses

1.5 *Outline of Thesis*

This thesis begins by establishing a background on sawblades with regard to the tensioning, excitation frequencies, the use of expansion slots, and the spin speeds of the sawblade. Next, the materials used and the dimensions and geometry of the sawblade are discussed. Assumptions made and values used in the following computational design of our experiments are discussed.

The background on sawblades discussion is followed by extensive building of the models for the purpose of verifying the analysis of the rotating sawblade. The stresses in the sawblade as well as the natural frequencies explored with various geometries of expansion slots and varying residual stresses within the sawblade are discussed. Several calculations are performed and discussed to support the computer models. The thesis ends with a conclusion of the results found and recommendations for further work.

Chapter 2

Background of a Sawblade

Although there has been much study of thin clamped rotating discs and the tensioning of sawblades, a detailed literature search in this area has not yet been conducted. In addition, there is not much written material on the tensioning of a sawblade to be found. Much of the knowledge of saw tensioning is passed on through the "saw doctors" themselves to future "saw doctors" at the hammering benches in saw shops. Y. M. Stakiev, who has been conducting research on the thin clamped disc problem for 35 years in Russia, says "There are problems which have not even been designated and described in the technical literature on the subject", Stakhiev [4]

2.1 *Saw Tensioning and Tensioning Theory*

Lunstrum's book titled "*Circular Sawmills and Their Efficient Operation*" [3] describes the operations of a sawmill. It gives detail regarding saw tensioning, collars, arbors, saw speeds and saw blades used in sawmill operations. Further, it gives many troubleshooting techniques for saw millers to use to check their sawblades, arbors, collars, mill foundations, saw-feed conditions and many other problems encountered with a sawmill operation.

In regards to saw tensioning, Lunstrum defines saw tensioning as "the prestretching of the inner area of the plate. This prestretching of the inner area produces a state of tension in the rim area. To work best, a saw must be tensioned properly for the speed at which it turns while in the cut." The rotational stresses and the heating of the tooth zone caused by friction between the carbide and steel contacting the wood fibers during normal saw operation cause the outer rim to be stretched more than the inner area. As seen in Figure 2.1, the central area, inner area and rim of a sawbody are shown. This stretching, which causes higher tangential stress at the rim, is held back by the cooler metal that is closer, radially, to the inner area of the sawbody. Because the cooler metal does not stretch as much as the outer rim, it tends to hold back the outer rim from stretching, causing the outer rim to be in a state of compression. When the two areas of

the sawbody (inner area and rim area) are at very different stress-states at operating speeds, buckling and weaving of the saw is likely to occur. This buckling and weaving causes the sawblade to deviate from a straight line cut resulting in poorly cut lumber.

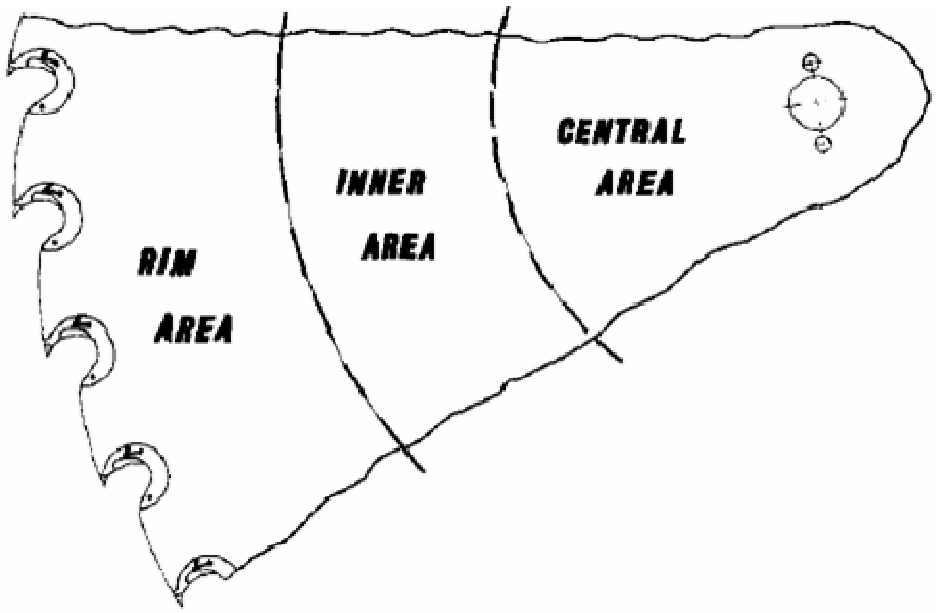

Figure 2.1 The three areas of a saw plate involved in tensioning a saw, Lunstrum [3].

When the tension forces are in stable equilibrium, the saw stands up straight when spinning at the correct speed while it is cutting the lumber. If the tension forces are not in stable equilibrium, the saw may look like one of several drawings seen in Figure 2.2.

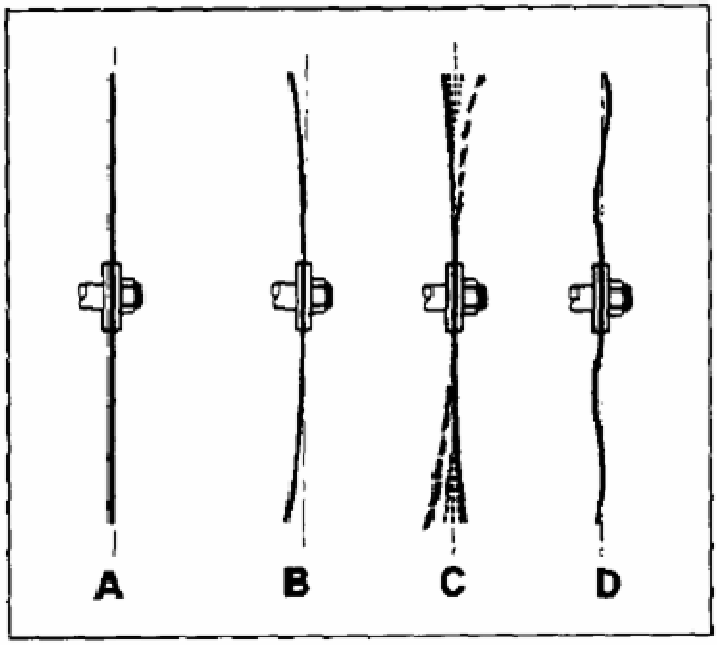

Figure 2.2 Sawblades in and out of tension, Lunstrum [3].

Figure 2.2-A represents a sawblade that is tensioned properly running at the speed the blade was tensioned. The stresses are in stable equilibrium. However, in Figure 2.2-B, the blade is tensioned "loose" or "open." It appears like a dish because it has excessive tension in its central area, and the central area is too large, causing the rim to be in tension. Also, a large central area contributes to the rim being too short. Heating in the center is a common problem of a blade that is over tensioned. In other words, the sawblade behaves like a Bellville washer – it can pop back and forth, it is unstable. During this popping back and forth, the sawblade is undergoing reverse flexure.

Figure 2.2-C represents a blade that is tensioned improperly due to the rim being too large and the central area too small. The rim is also in compression causing the bowed look. This saw is also known as a fast saw and heating at the rim is common.

Figure 2.2-D is a saw having irregular tension. This saw contains areas that are tight and loose.

Saw tensioning is performed to be sure that the sawblade does not contain areas that are not "level". A level sawblade will not contain knots, twists or high or low spots. A "saw doctor" utilizes a hammering process to properly tension the saw. This trained specialist must concentrate his efforts to both tension the saw and level the saw at the same time. To keep good tensioning in a sawblade, the saw must not become hot. Excess heat will inevitably remove the tensioning from a saw and cause the effects of Figure 2.2 B, C and D to be evident. When tensioning a sawblade, the amount of tension to be hammered into the saws is dependent upon numerous factors. Such factors include: diameter, gauge, saw speed, number of teeth, kind of wood sawn, horsepower available and carriage speed. Sawblades of larger diameter, smaller thickness, higher rpm and more heavily force fed lumber require more tension than a saw having the reverse of these characteristics, Lunstrum [3].

Williston in his book "Saws Design Selection Operation Maintenance," [6] gives a great description as to how to tension sawblades. He gives good detail for leveling and good general guidelines of how much tension a particular sawblade needs.

Another source of information on saw tensioning is found from the analysis work done by Y. M. Stakiev in "Research on circular saw disc problems." His research says that saw tensioning can be done by one of several methods: hammering, rolling, rotation tensioning, diamond burnishing, thermal tensioning. Stakiev did research on the natural

frequency effects from tensioning a sawblade that has fixity of a single tooth representing the brief moment when the tooth is in the cut of the wood. Furthermore, this paper describes the differences in the forced vibrations from a sawblade in air versus the sawblade in a vacuum where the self-induced vibrations do not exist. Thereby, he proves that the self-induced vibrations of a sawblade are caused by the ambient air. Much of Y. M. Stakiev's work is focused on guided sawblades, which use guide pins on the outer radius of the sawbody to keep the sawblade running true. The guide pins reduce the vibrations because of the extra boundary conditions. Stakiev also used the saw collars clamped at 25 percent of the sawblade on his sawblades for the natural frequency analyses.

Stakiev does prove through experimental efforts that the natural frequencies are increased with increasing tension along the same radial line. Increasing tension is done by roll tensioning and increasing the pressures on the sawblade. He is able to raise the non-rotating natural frequency of a particular sawblade from 112 Hz to 154 Hz. He also does experiments on the bending stiffness of the same sawblade where the stiffness of the outer area of the sawblade is increased with increased tension. He used the self-weight sag test, a straight edge, and measured the light gap that was produced by supporting the sawblade at certain fulcrum points, Stakiev [4].

2.2 *The Excitation Frequencies of the Sawblade*

In the analysis of our 18-in sawblades analyzed, the nominal speed is 10,000 surface feet per minute (sfpm), which is 2122 rpm or 35 Hz. The sawblade is very lightly damped system that is hard mounted and has no isolation to inhibit excitation of the resonant frequencies. Because it is impossible to perfectly balance a sawblade, this 35 Hz frequency from the rotation of the sawblade is one of the excitation frequencies that are input to the sawblade. It is this frequency that excites any and all natural frequencies in the sawblade. This is characteristic of a nonlinear system. Therefore, the further away the natural frequency is from excitation frequency the less likely we are to induce large displacements from the blade being driven at frequencies below the first and second natural frequency. Because tensioning the sawblade raises the first, second and all following natural frequencies, the better we can tension the sawblade, the better we can make the blades perform. "Better" in this case does not necessarily mean more and more

tension, but the correct amount of tension. A sawblade with too much tension will behave similar to a sawblade with no tension, except that a sawblade with too much tension has to be scrapped because there is no reasonable means to remove the extra tension.

Another excitation frequency input to the sawblade is the teeth striking the wood during the cutting process. For example, our 18-in sawblade has 24 teeth and spins at 2122 rpm. Therefore, the teeth strike the wood at a frequency of 849 Hz. To know how to tension the sawblade to keep these operating conditions away from the natural frequency of the sawblade is a difficult task.

2.3 *Expansion Slots*

Sawblades need expansion slots because the expansion slots help to relieve stress and strain in the rim of the sawblade. An example of a typical expansion slot is shown in Figure 2.3. The von Mises equivalent stresses shown in Figure 2.3 are due to the rotational forces inducing circumferential stresses at the rim of the sawblade. Also, expansion slots relieve the stresses due to the thermal expansion from the sawblade tips' cutting action of the wood. The saw heats up from the cutting action beginning at the outer most point of the saw tips, Plank and Stephenson [1]. The expansion slots are generally wide enough to not allow any closing of the slot which would cause one side of the slot to come into contact with the other when the saw is heated with a torch to braze the tips onto the sawblade. Without expansion slots, these stresses and strains could cause "lumps" to occur in the body of the saw, and the lumps would cause the sawblade to wobble and not run true. Another word synonymous with expansion slot is strain relief because of the action performed by expansion slots.

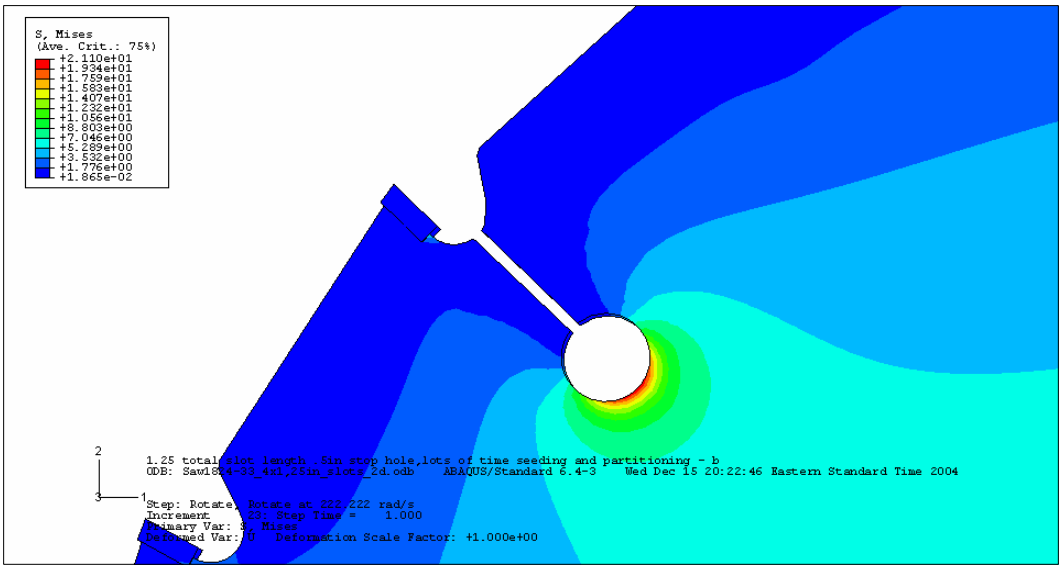

Figure 2.3 Typical expansion slot**.**

Another Theory for the Necessity of Expansion Slots. Expansion slots break up the wave that propagates around the sawblade during the cutting action. When each tooth initially strikes the wood to be cut, the impact creates an elastic wave that is sent around the rim of the sawblade. This wave is reinforced by the next tooth's impact and resulting elastic wave being sent. Soon, the waves build upon each other creating a wave of significantly more amplitude than any single wave, thus propagating a wave of increasing amplitude, which could in turn cause the sawblade to vibrate at such amplitudes that the sawblade could result in fatigue fracture. The expansion slots are believed to break up the propagating waves when the waves come into contact with them. Therefore, the waves only have a low number of tooth impacts to increase amplitude before they are interrupted by the expansion slots. At this time, the waves are small enough to not contribute to excess vibration amplitudes, thus prolonging the sawblade's run life, Ponton [2].

Expansion Slots and Noise. Adding to the propagating wave theory, the expansion slots also reduce the noise generated by the sawblade by breaking up the pressure waves from the teeth. For example, a spinning disc creates virtually no noise; however, a spinning sawblade makes a lot of noise. The teeth in the sawblade generate pressure waves as they rotate in a circle. The noise is affected by the gullet shape and number of teeth – the higher the number of teeth, the higher the pitch of sound. Successive waves of nearly

equal pressure and equal spacing produce sound. However, any geometrical feature which breaks up this repetitive pattern tends to lower the sound levels. The expansion slots do their job as a geometric feature which breaks up this wave, Plank and Stephenson [1].

Adverse Stress Effects. When considering the sawblade's run life, the expansion slots do have their drawbacks. The most likely point of failure of the sawblade is in the hole at the bottom of the expansion slot. This failure is due to a number of factors including: stress concentration, a lever "arm" effect, and fatigue that result from the aforementioned effects.

The expansion slot is an area of stress concentration because it is a highly localized stress effect. The expansion slot is similar to a crack in the steel because the sawblade is discontinuous at the expansion slot. A large radius "stop hole" is used to prevent the "crack" (expansion slot) from growing beyond its designated designed geometry. This large radius "stop hole" acts like a termination point for a crack that has developed.

The expansion slot has an opening and closing effect because of the high forces acting near perpendicular to the saw tips before and after the expansion slot. For instance, if the expansion slot is 1.25 inches long from the bottom of a 0.5 inch deep gullet, then the force exerted on the saw tip before or after the expansion slot is exerted over a 1.75 inch lever arm, with the moment acting at the bottom of the gullet. This produces higher than average stresses at the bottom of the expansion slot as compared to the rest of the sawbody. And, the expansion slot tends to open or spread apart as if there is a hinge at the bottom of the stop hole.

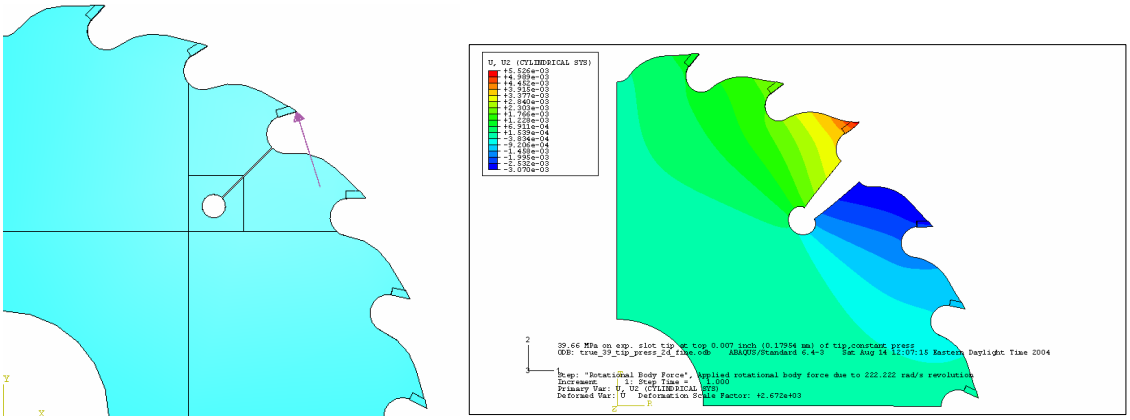

a b

Figure 2.4 (a) shows pressure from cutting action on tip after expansion slot**,** (b) shows lever arm acton at bottom of expansion slot due to the pressure and displacement of sawbody (exagerated displacement).

Due to the repetitive on/off cutting force on the saw teeth, these stresses on the bottom of the expansion slot contribute to fatigue failure of the sawblade. In fact, the highest failure of the sawbody comes from cracks propagating from the bottom of the expansion slot. The expansion slots are very helpful in prolonging the life of the sawblade, but because of their increase in stress (when compared to the rest of the sawblade) are still not without fault. We can improve sawblades simply by shortening the expansion slot length and making the stop holes large. These issues will be dealt with later in the thesis when the value of the stresses at the expansion slots is addressed.

2.4 *Rotational Speeds (desired and safety factor)*

During the analysis, the spin speeds used for the models and hand calculations were all 10,000 surface feet per minute (sfpm). The rim speed in linear feet is 10,000 sfpm. This is the speed recommended by the manufacturer for the sawblades and the speed we simulated, Ponton [2]. Therefore, for an 18-in sawblade, the spin speed of the blade is 2122 rpm, or in other words the rotational frequency is 35 Hz. This rotational speed is a nominal value for this and many other sawblades. Because 10,000 sfpm is a nominal value for many sawblades, it was recommended to use this target value, we used this speed during all calculations and analyses, Ponton [2]. However, sawblade spin speeds can range from about 6000 sfpm for sawing frozen wood to as high as 28,000

sfpm (extreme cases) for smooth end trimming, Quelch [5], and Williston [6]. Many manufacturers stamp a maximum safe speed on their sawblade.

Chapter 3

Material Properties and Dimensions of Typical Cut-Off Sawblade, and those Used in the Design of Our Experiment

This section gives details of the geometry of typical circular sawblades and the dimensions we used in the design of our experiments. It gives rise to the adaptation of the sawblade onto a machine for it use. Attention is given to details of the carbide tips that are used on a typical circular sawblade as well.

3.1 *Nominal Dimensions and Parameters of a Typical Cut-Off Sawblade*

These nominal dimensions were obtained from R.S. Ponton. There are many more dimensions and parameters of a typical sawblade than meets the eye upon initial inspection. All these parameters have importance for the sawblade to operate properly and cut cleanly through a piece of material, whether the material is wood, plastic, aluminum, masonry, or any other material that is able to cut with a circular sawblade. In our analysis, we have concentrated on a typical sawblade that is made to cross-cut through a board of lumber. In other words, we are analyzing a trim saw (also called a cut-off saw). That is to say that these blades are used to cut perpendicular to the grain of the lumber – one board at a time. Therefore, much of the explanation of the typical sawblade and its parameters will concentrate on a typical cut-off sawblade. More detail showing the trim saw in action is given in Section 8.1.

Nominal Dimensions and Sawblade Features Explained. The many dimensions and parameters of a typical cut-off sawblade can be seen in Figure 3.1 and Figure 3.2. Because the dimensions and parameters can be broken into two areas, the parameters are given as:

1) dimensions of the sawblade as a whole.
2) dimensions of the sawblade's rim or outer area.

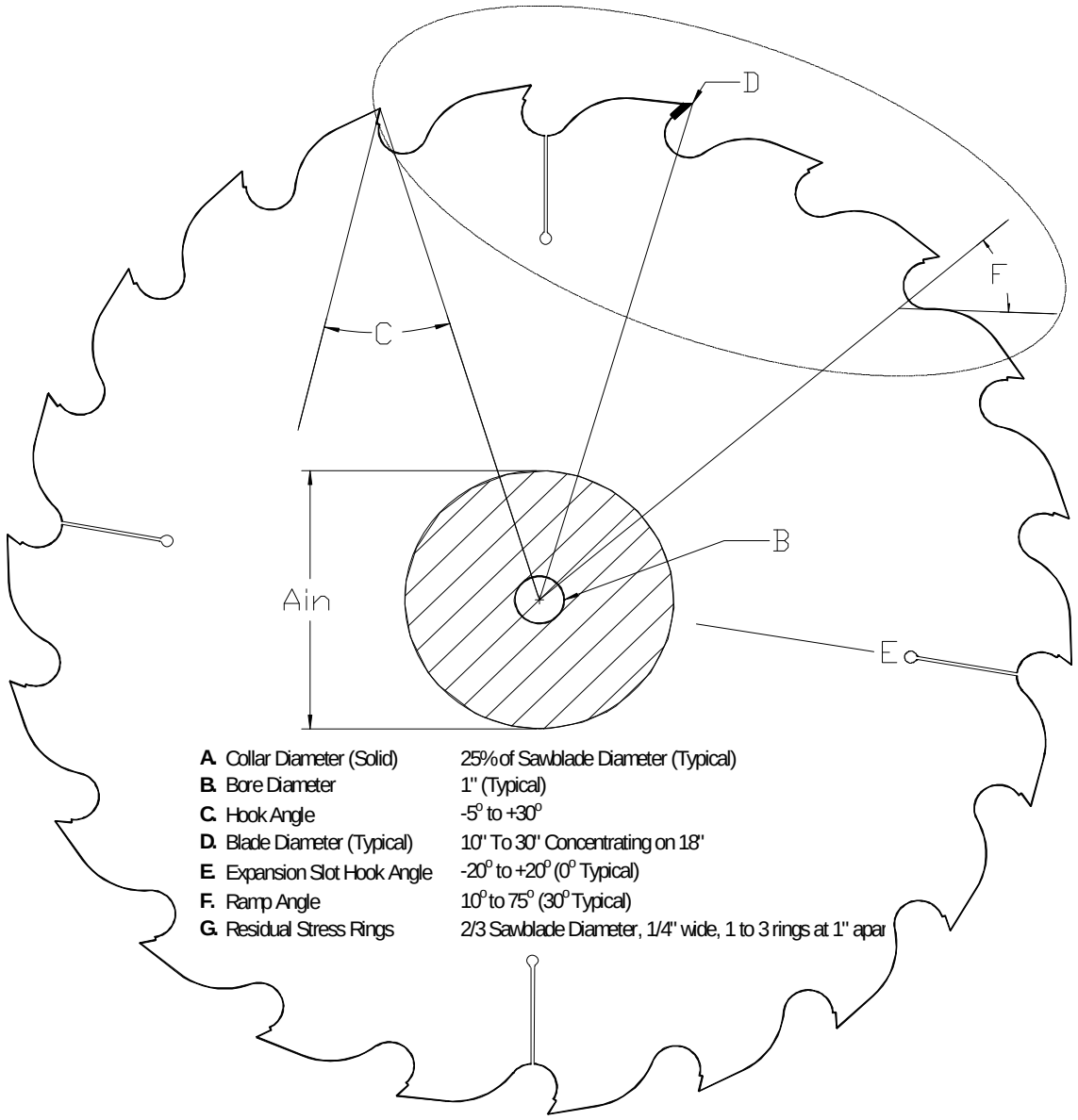

Figure 3.1 Typical nominal parameters of a typical circular cut-off sawblade as a whole. The circled region is the zoomed-area seen in Figure 3.2.

Sawblade as a Whole. Considering the sawblade as a whole using Figure 3.1, dimension "A" is the collar diameter. This is the region used to fix the sawblade to the saw arbor (or shaft) on the sawing machine. The saw arbor is a short, finely machined, threaded shaft that is nearly perfectly balanced. Because there needs to be a solid way to transfer the torque from the sawing machine to the sawblade, the sawblade is sandwiched securely between two round, dish shaped, heavy collars. These are called "saw collars" and are connected to the threaded saw arbor by large nuts that are torqued forcefully to clamp the saw collars onto the blade. These saw collars are very stiff and are much thicker than the

sawblade itself. Furthermore, the saw collars are designed in such a way that they only contact the blade at the outer most diameter of the saw collar, and if used properly they prevent any slippage between the saw collar and the sawblade. For smaller industrial cut-off saws, which are considered to be 10 to 30 inches in diameter, the typical collar diameter is generally about 25 percent of the sawblade diameter. The sawblade diameter is the diameter of the circle of outermost tips of the saw teeth, also dimension "D" in Figure 3.1.

Dimension "B" in Figure 3.1 is the bore diameter. The bore diameter is a precisely machined hole located at the center of the sawblade. Being located as close to the exact center of the sawblade as possible, the bore aligns the sawblade and geometrically centers the sawblade onto the saw arbor.

Dimension "C" seen in Figure 3.1 is the hook angle, which is the angle between two lines which intersect at the point of a tooth. One of these lines is drawn along the face of the carbide tip and the second line is drawn radially from the center of the sawblade. The hook angle's design will have consideration of the type of material being cut and the horsepower of the saw machine. In general, for every positive 10 degrees of the hook angle, the saw machine is required to produce 30 percent less horsepower to make the same cut. Thus it saves energy using a more positive hook angle. However, the tip of the carbide tooth of a more positive hook angle has a sharper edge and is able to withstand less blunt impact because the tip has less material at its cutting point. The hook angles of typical carbide tipped sawblade range from -5^{o} to $+30^{o}$.

The expansion slot hook angle is dimension "E" as shown in Figure 3.1. This is the angle formed between a line drawn through the center of the expansion slot and a line drawn radially from the center of the sawblade.

The shoulder ramp angle, dimension "F" in Figure 3.1, is the angle formed between a line drawn radially through the bottom center of the gullet and a line drawn tangential to the gullet arc at its forward end. The gullet is the large empty area preceding each saw tooth used to catch the sawdust from the tooth.

Finally from Figure 3.1, we have the residual stress rings (not shown). These rings were explained earlier in Section 2.1; however, their typical dimensions were not mentioned. The typical location of the residual stress rings is said to be two-thirds of the sawblade diameter. Moreover, these rings are drawn onto the sawblade as concentric

circles about one to 1 and 1/2 inches apart. The average sawblade has around one to three residual stress rings placed into the sawbody. The rings leave a slight indention in the steel sawbody that is between 1/8 and 1/4 inch wide.

Sawblade Outer Area. Figure 3.2 is a zoomed-in picture of the oval drawn on Figure 3.1. This is the outer rim area and it shows the dimensions of the carbide teeth, gullets, shoulders, saw teeth pockets, with more detail dimensions of the expansion slots and stop hole radii. Dimension “A” in Figure 3.2 is the carbide teeth length, which is measured from a tooth’s bottom side to the outermost point on the sawblade. Dimension “B”, the gullet radius, is the radius of the area designed to catch the sawdust during the cutting action of the saw tooth and release the sawdust when the saw tooth exits the material. Dimension “C” is the shoulder relief angle. The shoulder is the steel material behind the saw tooth that gives the saw tooth enough support to withstand the punishment required to cut material. The shoulder relief angle is the angle that keeps the shoulder from rubbing on the cut material as the material is pushed into the spinning blade. Also, the shoulder relief angle gives rise to the shoulder radius, dimension “D”, which is the radius of the fast dropping off-slope behind the shoulder that leads to the preceding gullet.

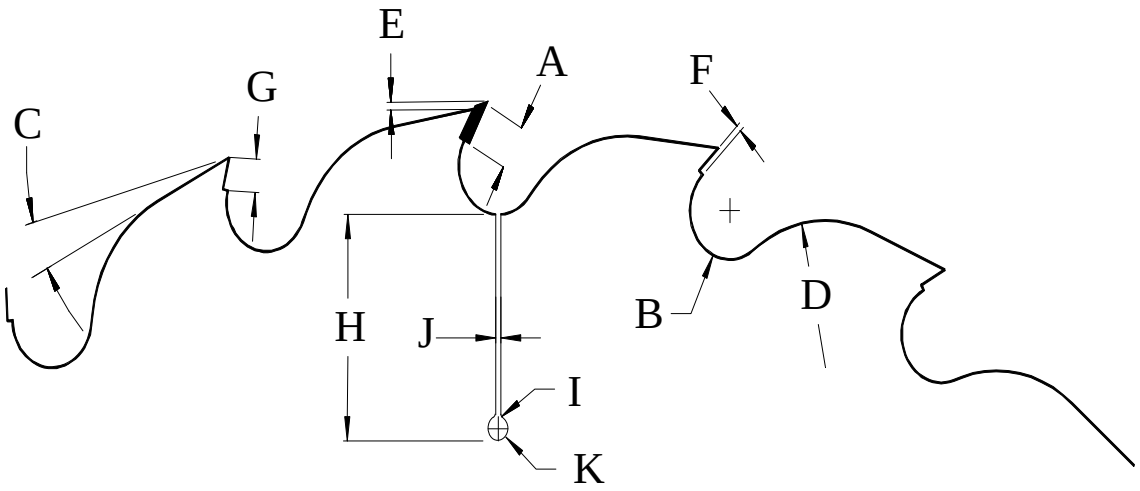

A. Carbide Tip Length	0.250" to 0.500"
B. Gullet Radius	Application Specified
C. Shoulder Relief Angle	10^{0} or Greater (for Smaller Diameter Blades)
D. Shoulder Radius	Application Specified
E. Top Clearance	0.000" to 0.030"
F. Pocket Width	1/2 Thickness of Carbide (Typical)
G. Pocket Depth	Derived From Carbide Back Length
H. Expansion Slot Length	Variable
I. Beginning of Stop Hole	0.039"
J. Expansion Slot Width	0.010" to 0.060"
K. Stop Hole Radius	1/4" (or 1/2" Stop Hole)

Figure 3.2 Zoomed-in picture of the oval in Figure 3.1 showing the typical parameters of a circular cut-off sawblade's outer rim area.

In Figure 3.2, the top clearance, dimension "E", is the distance from the top of the saw tooth pocket to the top of the tooth. Dimension "F" is the pocket width. This width is typically half the thickness of the carbide. Pocket depth, dimension "G", is the depth of the saw tooth pocket. This dimension is also derived from the carbide being used on the sawblade. The expansion slot length, seen as dimension "H" in Figure 3.2, is the length of the expansion slot from the beginning (at the bottom of its gullet) to the bottom of its stop hole. Dimension "I" is the beginning of the stop hole radius. This radius provides a smooth transition from the straight expansion slot to the stop hole. This beginning stop hole radius is generally quite small compared to the stop hole radius. The expansion slot width, dimension "J", is the actual width of the expansion slot. The expansion slot was discussed in detail in section 2.3. The stop hole, dimension "K", is larger than the expansion slot in order to give an end to the crack-like dimensions of the expansion slot. Because the stop hole and the expansion slot lead to being places of stress concentration, the expansion slot is ended with this large hole relative to the expansion slot. The stop hole is generally about 1/2" in diameter.

Carbide Tip Dimensions Explained. Because of the need to only model the carbide as a three-dimensional approximate shape, the writer has decided to omit the detailed nominal geometry of the carbide tip on a typical cut-off sawblade. The typical carbide is closely represented in the computer models in the later chapters. The difference between the carbide on a real sawblade and the carbide on the computer models is the tapering of the sides of the carbide. This tapering is due to the removal of the material by a side grinder that grinds both sides of the carbide using a diamond wheel. This grinding is done in such a way that the carbide is tapered both front to back and top to bottom on the carbide tip's sides. In other words, the top and face of the carbide are the widest parts of the carbide tip. Any direction away from the top and face is progressively narrower. This geometry of the carbide tooth arises because of the need to have the face of the carbide teeth strike the wood with no rubbing of the sides of the carbide tip after the face has made the initial cut into the wood - the tapering of the sides of the carbide tip is a must on a real sawblade.

3.2 *Dimensions Used in the Sawblades used in the Thesis*

In the thesis, we have chosen to concentrate our diameter only on 457.2 mm (18-in). Also, the thickness of all models analyzed in this thesis is 3.4036 mm (0.134 inches). The bore of our models is 1-in. Because the nominal dimension of the collars used to fix the blades to the saw arbor is 25 percent of the diameter, all collars in this research are 25 percent of the outer diameter. Therefore, all collars modeled are 114.3 mm (4.5 inches) in diameter. There were two types of 18-in cut-off sawblades analyzed in this research. Both consist of 24 carbide teeth. The first sawblade is a typical lumber cut-off sawblade with a positive hook angle of 31.03^{o} made by International Carbide and Engineering, Inc. (***ICE***^{TM}) with part number 130-1824-248; see Figure 3.3 for shape of geometry. The second sawblade analyzed is a nail cutting sawblade also made by ***ICE***^{TM} with part number 105-1824-233. This sawblade is designed to cut through nails embedded in lumber and has a 0^{o} hook angle. On the latter sawblade, the gullets are as shallow as possible for the sawbody to better handle the larger stresses associated with a carbide tooth sawblade cutting straight through a hardened steel screw nail that has been embedded in the lumber in any direction including parallel to the body of the sawblade.

However, the analysis in this thesis does not consider the impacts or the cutting of the nails or the added stresses associated with nail cutting.

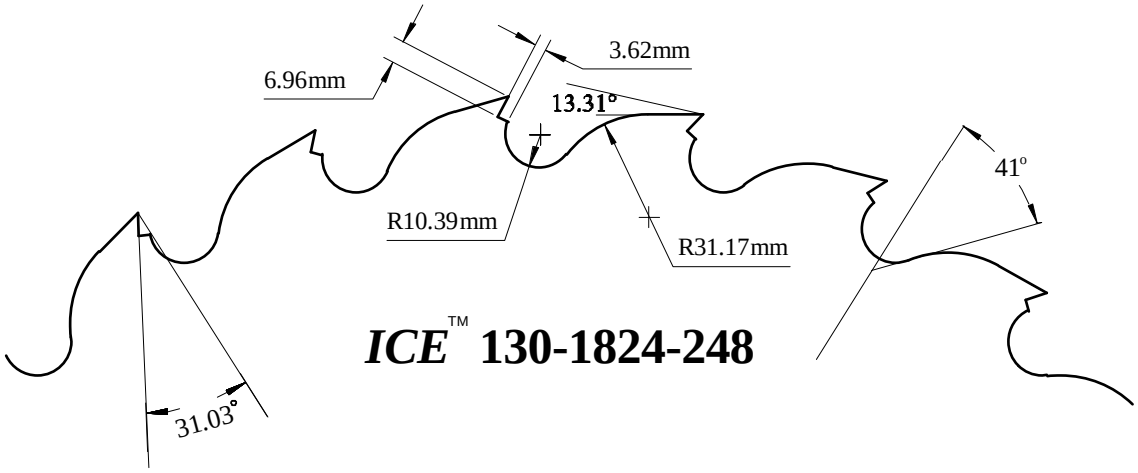

Figure 3.3. Dimensions used for standard 18-in with 24 teeth cut-off sawblade.

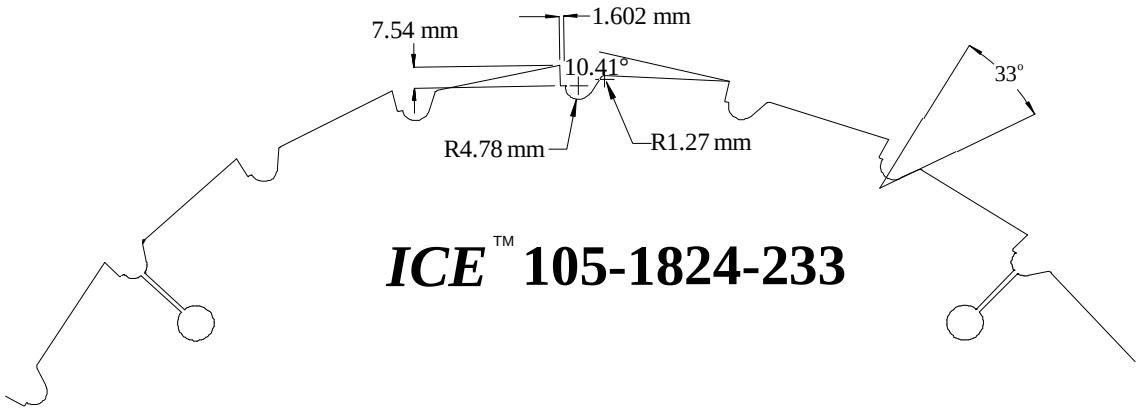

Figure 3.4. Dimensions used for 18-in with 24 teeth, nail cutting sawblade.

Expansion Slots Modeled in Thesis. For rotating discs with expansion slots, the total length of the four expansion slots varied from 1.5-in, 2-in, and 2.5-in long with 0^o hook angle. For the nail cutting sawblade with the four expansion slots, the slots on the nail cutting sawblade ranged from one inch to 2 and 1/2 inches in ¼ inch increments. One sawblade model was run with a negative 10^o expansion slot hook angle. All other models with expansion slots had a 0^o hook angle.

Standard Cut-off Sawblade Dimensions. The standard cut-off sawblade used in the thesis is discussed here. The angles leading back to the preceding gullet from the top of

the saw pocket are called the shoulder relief (or clearance) angles and the shoulder ramp angles. For the standard cut-off sawblade, the shoulder relief angle is 13.31^{o}. Furthermore, the ramp angle is 41^{o}. The radius of the shoulder is 1.227-in (31.2 mm). The gullet radius is 10.39 mm (0.409-in). For the carbide tooth pocket, the width of the saw pocket is 3.62 mm (0.143-in). Furthermore, the pocket depth is 6.96 mm (0.274-in).

Nail Cutting Sawblade Dimensions. The nail cutting sawblade (***ICE***^{TM} 105-1824-233), which is used in the thesis, parameters are discussed here. For the nail cutting sawblade, the shoulder relief angle is 10.41^{o}. Furthermore, the ramp angles are 35^{o}. The shoulder radius is 0.05-in (1.27 mm). The gullet radius is 4.78 mm (0.188-in) For the carbide tooth pocket is 1.602 mm (0.063-in). Furthermore, the pocket depth is 7.54 mm (0.297-in).

Steel Roller Dimensions. The dimensions of the roller used in the thesis are seen in Figure 3.5. Table 3-1 shows the dimensions used to describe the roller. For computational savings, in most analyses, only the bottom ¼ of the roller is modeled.

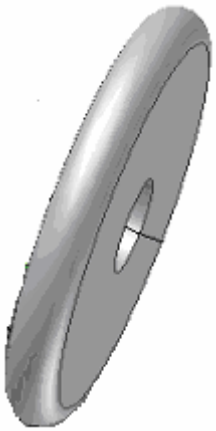

Figure 3.5 Roller used in thesis.

Table 3-1 Dimensions of roller used in design of experiment.

Geometry Parameters: Steel Roller Top is Same as Bottom Roller	**(inches)**	**(mm)**
Diameter of roller	4	101.6
Crown Radius	4	101.6
Actual Height at center to top (shortened to approximately ½ of total Outer Radius of roller)	1.071	27.2125
Width	0.75	19.05

3.3 *Material Properties of Steel Sawbody (including the plastic zone), Carbide Tips, and Steel Rollers; Including all Assumptions Made to get these Properties*

This section defines all the properties input into ABAQUS (the finite element analysis computer program used in the thesis) and used for the hand calculations for the steel sawbody, carbide tips, and steel roller. These properties include the modulus of elasticity, mass density, and Poisson's ratio and can be seen in Table 3-2. This section also gives details on obtaining the plastic strain from a typical stress/strain curve of steel and the plastic strain used as input for the steel sawbody. The yield stress of the steel used in the sawbody is also discussed later in this section.

Table 3-2 Material properties of steel and carbide.

Material Properties: Steel Sawbody and Roller		
	Metric	*English*
Elastic Modulus	205,000 MPa	2.97e7 psi
Poisson's Ratio	$\nu = 0.3$	$\nu = 0.3$
Mass Density	7.85 e-9 $N\text{-}s^2/mm^4$	7.345 e-4 $lbf\text{-}s^2/in^4$
Yield strength Sawbody / Roller	Sawbody = 690 MPa / Roller = 1170 MPa	Sawbody = 100,000 psi / Roller = 169,000 psi
Material Properties: Carbide		
	Metric	*English*
Elastic Modulus	6.05e5 MPa	8.774e10 psi
Poisson's Ratio	$\nu = 0.3$	$\nu = 0.3$
Mass Density	1.42 e-8 $\frac{N\text{-}s^2}{mm^4}$	1.33 e-3 $\frac{lbf\text{-}s^2}{in^4}$
Tensile Strength, Ultimate	344 MPa	49,900 psi
Compressive Yield Strength	2683 MPa	389,000 psi

The modulus of elasticity of steel is almost always the same. No matter if the steel has undergone heat treating, alloying, or which manufacturing process is used in making the steel, Beer and Johnson, Jr. [11]. Therefore, the value of the modulus of elasticity (or Young's modulus) used for both the steel sawbody and the steel roller is the same and the modulus can be found in many materials handbooks giving the material properties for most any steel.

Plasticity. When defining the nonlinear effects of plasticity in ABAQUS, true stress and true plastic strain is used instead of engineering (also called nominal) stress and engineering (also called nominal) strain. Unfortunately, the data given on most stress/strain curves is given in terms of nominal stress/strain. For this reason, conversion from nominal stress/strain to true stress/strain must be used for ABAQUS to correctly represent the material. In addition, the true strain must be converted to plastic strain for plasticity models to be correctly represented in ABAQUS, Hibbit, Karlsson and Sorensen [7].

To convert from nominal stress/strain to true stress/strain, one must consider the incompressible nature of plastic deformation. The incompressibility can be stated mathematically as a constant volume constraint according to:

$$l_o A_o = lA \qquad [3.3\text{-}1]$$

where l_o and A_o are the initial length and initial area, respectively. Furthermore, l and A are the final (or current) length and final (or current) area of the deformed object, respectively. Solving for the final area in terms of the original area, and original and final lengths, we get

$$A = A_o \frac{l_o}{l} \qquad [3.3\text{-}2]$$

True Engineering Stress from Nominal Stress. The true engineering stress, σ, can be obtained using the normal stress formula and substituting in the original area for A, which results in

$$\sigma = \frac{F}{A} = \frac{F}{A_o}\frac{l}{l_o} = \sigma_{nom}\left(\frac{l}{l_o}\right) \qquad [3.3\text{-}3]$$

where F is the force applied to the object, and σ_{nom} is the nominal stress found on most stress/strain curves in engineering textbooks and data reference books. Equation 3.3-3 can be written in terms that directly relates the nominal stress to engineering stress, making one more substitution using the fact that

$$\frac{l}{l_o} = \frac{\Delta l}{l} + \frac{l_o}{l_o} = \varepsilon_{nom} + 1 \qquad [3.3\text{-}4]$$

where ε_{nom} is the nominal strain taken from most stress/strain curves. Thus, Equations 3.3-1 through 3.3-4 yield the following final equation for true stress as a function of nominal stress and strain:

$$\sigma = \sigma_{nom}(\varepsilon_{nom} + 1) \qquad [3.3\text{-}5]$$

True Strain. Solving for true strain, ε, is simpler. First consider the origin of true strain, derived from

$$d\varepsilon = \frac{dl}{l} \qquad [3.3\text{-}6]$$

and yields:

$$\varepsilon = \int_{l_o}^{l} \frac{dl}{l} = \ln\left(\frac{l}{l_o}\right) \qquad [3.3\text{-}7]$$

Now, express the nominal strain as

$$\varepsilon_{nom} = \frac{l - l_o}{l_o} = \frac{l}{l_o} - \frac{l_o}{l_o} = \frac{l}{l_o} - 1 \qquad [3.3\text{-}8]$$

Adding one to both sides of this expression and taking the natural log of both sides of the equation, the definition for true strain is obtained in terms of the nominal strain found on most stress/strain curves. The final equation used to convert the nominal strain to true strain is

$$\varepsilon = \ln(1 + \varepsilon_{nom}) = \varepsilon_{TOT} \qquad [3.3\text{-}9]$$

Next, convert the true strain to the plastic strain, ε_{pl}, for the required input into ABAQUS. Usually, the total strains are displayed on stress/strain curves. This data must be converted to plastic strain. The plastic strain is found by subtracting the total strain from the elastic strain where the elastic strain is the stress divided by the modulus of elasticity. Because an object first has to experience elastic strain before undergoing plastic strain, we must account for the elastic strain when trying to find the amount of plastic strain. Therefore, plastic strain is found using:

$$\varepsilon_{pl} = \varepsilon_{tot} - \varepsilon_{el} = \varepsilon_{tot} - \sigma / E \qquad [3.3\text{-}10]$$

where ε_{tot} is the total strain, ε_{el} is the elastic strain, σ is the true stress, and E is the modulus of elasticity. σ / E is equal to the elastic strain. This is better illustrated in a general case of total strain being decomposed into elastic and plastic strains in Figure 3.6.

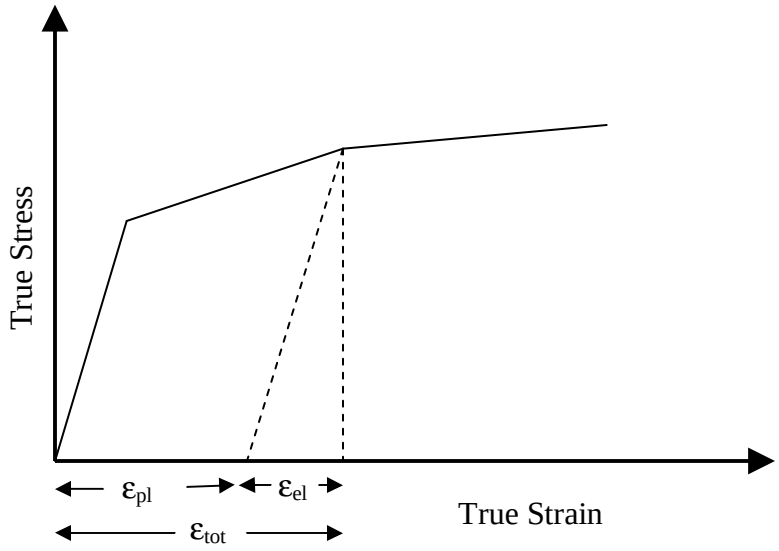

Figure 3.6 Illustrates how plastic strain is obtained from the total strain and elastic strain. The slope of the dashed line is the same as the beginning slope on curve, Hibbit, Karlsson & Sorensen [7].

Steels used in research. For the purpose of this research the properties of A514 heat-treated alloy construction steel is used because of the availability of the plastic stress zone data for this material. Therefore, Figure 3.7 through Figure 3.9 show the properties (after the yield point) for the steel used in the analysis of all the steel sawbodies throughout this research.

Figure 3.7 is the nominal stress/strain curve for A514 steel. These values were used in the calculations to obtain the true stress and true strain using Equation 3.3-5 and Equation 3.3-9, respectively.

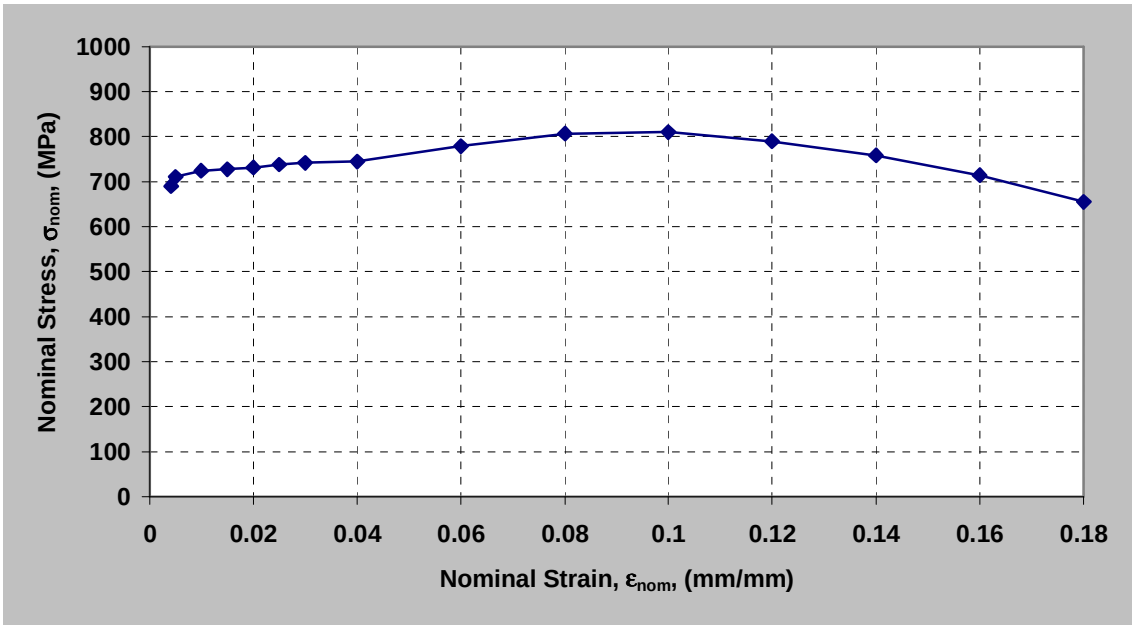

Figure 3.7 Nominal stress/strain curve found in Brockenbrough's Structural Steel Designer's Handbook. Curve begins at the yield stress of A514 heat-treated construction steel which is 690 MPa or 100 kpsi, after Brockenbrough and Merritt [10].

Figure 3.7 is used to obtain the true stress and true strain curve seen in Figure 3.8. Compared to the nominal stress/strain values, the true stress/strain values are slightly higher and have moved to the left on the graph. These values were used to find the true stress and plastic strain.

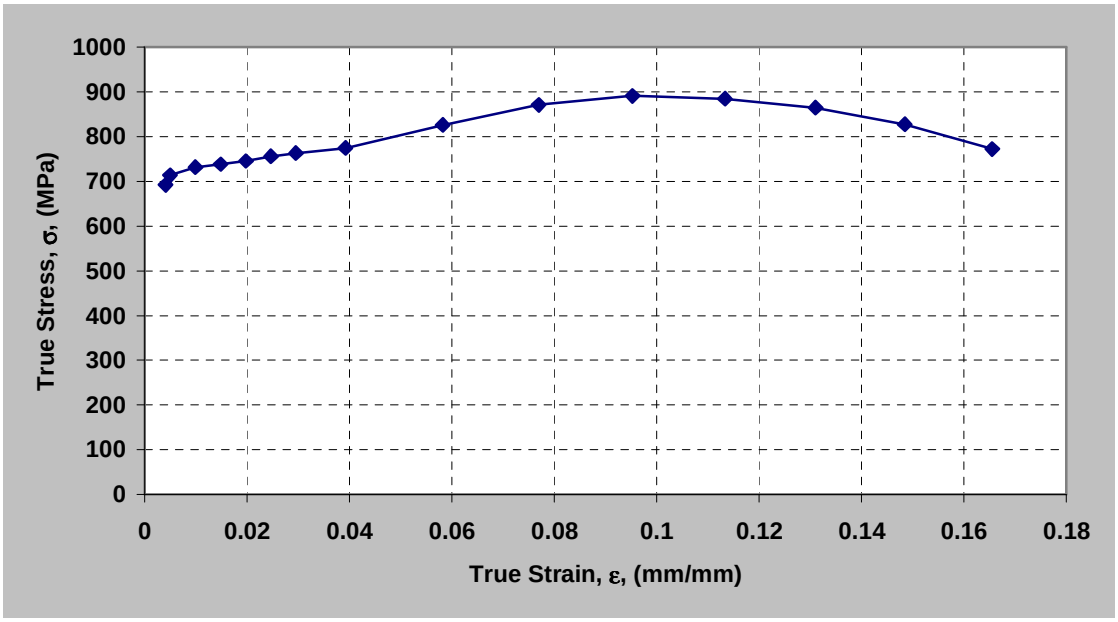

Figure 3.8 True stress, true strain curve for A514 heat-treated construction steel. Curve begins at the yield true stress which is 690 MPa or 100 kpsi, after Brockenbrough and Merritt [10].

For the analysis to be used in the plastic zone of the steel sawbody, the actual property values used in the analysis can be found in Figure 3.9. This graph represents the plastic strain, which is the total strain minus the elastic strain the material experiences.

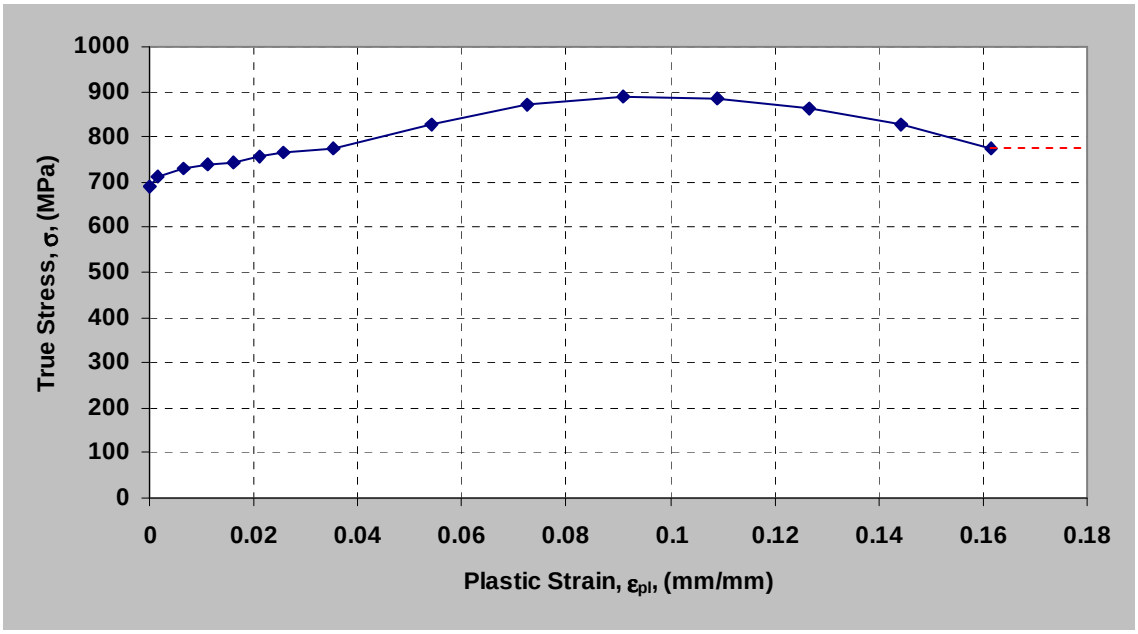

Figure 3.9 Actual values input into ABAQUS for the plastic strains and yield stresses. Curve begins at the yield stress, which is 690 MPa or 100 kpsi and located at zero plastic strain. The dashed red line extending from the far right of the curve indicates the slope ABAQUS uses to extrapolate strain beyond the data points, after Brockenbrough and Merritt [10].

ABAQUS can take any number of data points to represent the plastic strain. ABAQUS interpolates between each data point with a line. Furthermore, when the stress in the material reaches the end of the data points given to ABAQUS, ABAQUS continues on from the last point and treats the material as perfectly plastic. As seen in Figure 3.9, the dashed red line extending from the far right of the curve indicates how the material property is handled in ABAQUS after the last input data point. In other words, the material will continue to deform continuously until the stress is reduced below the last input data point, Hibbit, Karlsson & Sorensen [7].

It is the difference in yield stresses between the steel in the sawbody and the steel comprising the rollers that allows the rollers to leave a permanent plastic deformation in the sawbody. The material found in the steel rollers was not exactly known to the author after attempts to attain the information from the manufacturer. However, the steel in the rollers was chosen to be a steel of high yield strength. The rollers used on a saw stretcher

roller machine are used for several years and will deform hundreds of sawblades throughout the saw rollers' lifetime according to Mr. John Hodges of Reeds Carbide Saw and Tool in Lynchburg, VA [14]. Therefore, during the analysis, a check was made to ensure the yield stress seen by the rollers does not exceed the yield strength of a high yield strength quality steel – AISI 4140H. AISI 4140H is a low alloy steel with medium carbon, the yield strength is 1170 MPa.

Chapter 4

Assumptions Made During the Thesis Study

Saw Collar. It is very important that there is no slippage between the sawblade and the saw collar to prevent heating of the blade due to friction. Because the saw collar provides extra stiffness to the sawblade and also transfers all the torque to the sawblade from the saw arbor, the saw collars are made heavy and they are torqued very tightly to the saw blade. During the thesis study, effects have been taken into account between the clamping of the saw collar and the sawblade in order to transfer the power from the saw arbor to the sawblade. There are two extremes of the clamping force between the saw collars to the sawblade that could take place:

1) the clamping force is zero
2) the clamping force is infinite

The latter infinite clamping force is equivalent to saying that the saw collar is infinitely stiff, there is no slippage between the sawblade and the collar, and the saw collar will not allow the sawblade to deviate in any direction away from the end of the clamp. Thus, an infinitely stiff boundary condition exists at the outer diameter of the saw collar.

The "real world" is best represented by an infinitely stiff saw collar because experience shows that if any slippage occurs between the saw collar and the sawbody, heating of the sawbody will occur rapidly and the sawblade will lose its tension and will be of no use to the saw miller, Ponton [2]. However, the saw collar in the real world is not infinitely stiff, but the best representation of the real world lies quite close to the infinitely stiff range between the saw collar and the sawblade. Because of the relative stiffness of the saw collar used compared to the stiffness in the axial direction of the sawblade, we assumed the saw collar infinitely stiff. Therefore, the analysis used throughout most of this research considers the boundary condition representing the contact between the sawblade and the saw collar to be infinitely stiff in all directions. Chapter 5 takes these two extremes into account and quantifies them using both hand calculations and the computer models.

Carbide Tips. Because modeling the exact geometry of the carbide tips would make the modeling of the geometry very difficult using finite elements, the assumption was made

during the analysis to approximate the shape of the teeth. However, the shape used to approximate the true shape is quite close to the actual shape – less the tapering of the sides of the tooth. That is to say, the amount of material removed from the sides of the teeth is considered negligible in our analysis. Furthermore, the tapering of the carbide tip in actual carbide-tipped sawblade is subtle. In fact, the amount of tapering from the top to the bottom of the tooth (also called the radial angle) is 1-1/2°. And, the tapering from the front of the tooth to its back (also called the tangential angle) is 3^{o}. Thus, the amount of carbide removed from the saw tooth's sides is quite small. Therefore, it was decided to create a model of the saw teeth with a more square shape at the sides of the carbide tip than to represent the real world "approximation".

Since in a perfect world the edges of the saw tooth are tapered so the sides of the tooth do not come into contact with the wood, we have assumed no lateral force on the cutting tips of the sawblades analyzed. Thus, it is valid to assume that the only part of the tip which touches the wood is the top edge of the face of the carbide tip. All other edges are tapered such that they do not touch the wood (in a perfect world).

Chapter 5

Verifying the Finite Element Analysis – Building the Model

To verify the computer model used in the research, we based the analysis on known and/or derived hand calculations from trusted advanced mechanics of materials book by Boresi and Schmidt [8]. The various simple computer models matched the answers obtained from the hand calculations almost exactly, proving validity for our models. Also, the signal-to-noise ratio for each tested case was extremely high, showing an almost exact correlation between the hand calculations and the computer models that the research is based upon.

These simple models, used to base the research on, were of a rotating solid disc and an annulus. Having the same dimensions as the sawblade to be analyzed, the solid disc and the annulus made a solid foundation to confirm the results of the sawblade model. The solid disc and annulus were modeled as both an axisymmetric model and a three-dimensional eighth-model.

For the annulus cases we changed the boundary condition to represent the two extremes of the clamping forces of the collar on the sawblade. The next sections quantify and prove the validity of the simpler models the sawblade models are based upon. These sections also show the boundary conditions and models used in the finite element models.

5.1 *Rotating Solid Disc Hand Calculations versus the Finite Element Analysis*

This section will open up by illustrating the hand calculations used for validating the finite element analysis results, and then the computer model and its parameters are shown and discussed. Finally in this section, the axisymmetric model results are compared to the hand calculations. For the solid rotating disc, exact hand calculations are given in Boresi and Schmidt [8]. These hand calculations represent the stresses and displacements of a solid disc that is rotating about its center. Then, these hand calculation results are compared with the computer model results for a solid disc rotating about its center and modeled as an axisymmetric model.

Solid Disc Hand Calculations. The radial stress, σ_{rr}, along any arbitrary radial position, r, in a solid disc rotating about its center is found using the following equation:

$$\sigma_{rr} = \frac{(3+\upsilon)}{8}\left[1-\frac{r^2}{b^2}\right]\rho b^2\omega^2 \qquad [5.1\text{-}1]$$

where υ is Poisons ratio for the saw steel, b is the outer radius of the disc, ρ is the mass density ($\frac{\text{N-s}^2}{\text{mm}^4}$ or $\frac{\text{lbf-s}^2}{\text{in}^4}$), and ω is the angular velocity (rad/s).

Also, the circumferential (or tangential) stress, $\sigma_{\theta\theta}$ in a solid disc rotating about its center is found using:

$$\sigma_{\theta\theta} = \frac{(3+\upsilon)}{8}\left[1-\frac{(1+3\upsilon)}{(3+\upsilon)}\frac{r^2}{b^2}\right]\rho b^2\omega^2 \qquad [5.1\text{-}2]$$

and the radial displacement of an arbitrary radial position is found using:

$$u = \frac{(1-\upsilon^2)}{8E}\rho r^3\omega^2 + C_1 r + \frac{1}{r}C_2 \qquad [5.1\text{-}3]$$

where C_1 and C_2 are constants of integration. These constants are defined by the following equations:

$$C_1 = \frac{(3+\upsilon)(1-\upsilon)}{8E}\rho b^2\omega^2 \qquad [5.1\text{-}4]$$

and

$$C_2 = 0 \qquad [5.1\text{-}4]$$

for a solid disc.

Axisymmetric Model of Solid Disc. The computer axisymmetric-model results for the radial stress are shown in Figure 5.1. Here, the radial stress is displayed in the form of colors that are defined by the legend at the upper left of the picture. This figure represents an axisymmetric model of a solid disc rotating about its center. The axisymmetric model represents only a cross-section of the actual disc. To define the complete geometry of the solid disc, this cross-section would have to be rotated about its axis of revolution (in Figure 5.1) 360^{o}. Because all stresses and displacements are symmetric about the center axis of the solid disc, this axisymmetric model makes an excellent representation of the solid disc. For clarity, Figure 5.1 through Figure 5.4 defines the x-axis (or 1-axis) oriented left and right, the y-axis (or 2-axis) oriented up and down, and the z-axis (or 3-axis) oriented into the paper. Furthermore, these axis coordinates can also be thought as the 1-axis represents the radial direction on the solid disc, the 2-axis represents the direction through the thickness of the disc, and the 3-axis represents the tangential direction of the solid disc. (These coordinates will stay the same throughout the paper for the axisymmetric model, however; the coordinate numbers for 3-dimensional models will not be the same as the axisymmetric models.)

The axisymmetric models shown in Figure 5.1 through Figure 5.4 are only half the thickness of the solid disc the models represent. Using half thickness is an excellent representation of a solid disc rotating about its center because the loading and geometry are symmetric about a radial centerline located along half the thickness of the solid disc. In other words, the displacements along the centerline of the solid disc in this model are only radial or tangential and at no time does any point on the centerline deviate in the y-direction. Any stress on any particular element above the centerline could be thought of as being mirrored about the centerline for any element in the same location below the centerline. Therefore, the true thickness represented by this model is 3.4036 mm (0.134-in), but the model is only half as thick measuring 1.7018 mm (0.067-in) thick. Using axisymmetric and half thickness in this model greatly reduce the elements required and the computational time required to solve this model.

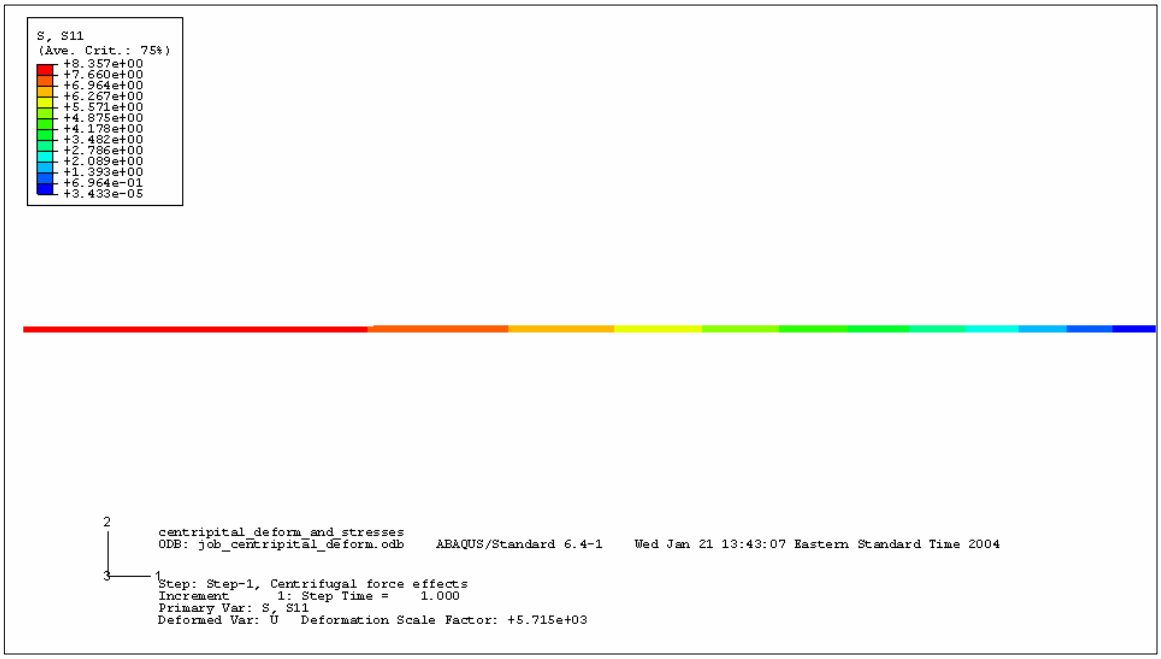

Figure 5.1 Axisymmetric model showing radial stress (S11) in solid disc. The radius is 228.6 mm (9-in). Due to symmetric conditions about the 1-axis (x-axis), which is along the center of the solid disc, the thickness used in the model is half the thickness of actual solid disc represented. Rotating at 222.222 rad/s (10,000 sfpm).

Boundary Condition of Solid Disc. For the axisymmetric models, using only the half thickness requires a boundary condition to be applied to the entire bottom line of the model shown in Figure 5.1. On this line, a y-symmetric boundary condition is used. Y-symmetric boundary condition in an axisymmetric model means that U2=UR1=UR3=0 (or the displacement in the 2 direction and the rotation about the 1-axis and the rotation about the 3-axis is 0). The loading of the axisymmetric model is done by using a rotational body force. This force is applied to the whole model by using the mass density of the solid disc and calculating its force from rotation on the spinning disc. The innermost modeled region of the disc has the most mass pulling force outwards versus a point radially further away from the center of the disc. This centrifugal force develops into stresses in the rotating body from its normal acceleration.

Results of Rotating Solid Disc. Figure 5.2 shows the tangential stress of the solid disc. This result is similar to the result found in Figure 5.1 because the radial stress and tangential stress are nearly the same in a solid disc. Typically for results displayed for the computer models in this thesis, red represents the maximum value and dark blue represents the minimum value on the plot. Colors in between red and dark blue are

between the ranges of values from the red to dark blue. The legend for the range of the variable plotted is located on the plot at the left in all computer-analysis pictures in this thesis. Particular attention must be paid to the sign of the values of the stress and displacements and the exponent of those values. Typically in the analysis, a negative sign for stresses indicates that the element is in compression. Likewise, a positive sign indicates that the stresses in the area are in tension. For displacement plots, a negative sign means the displacement is in the negative direction of the coordinate system. Likewise for displacement plots, a positive sign means the displacement is in the positive direction. For stresses with a very small value relative to the other values in the model, the value is likely approaching zero. For example, the minimum value in Figure 5.1 is 3.433E-05 MPa and the maximum value is 8.357 MPa. The minimum value is actually approaching zero, and should be considered zero in practice for the radial stress at the outer edge of the disc. Experience and engineering intuition help to decide which values represent zero in the analysis results.

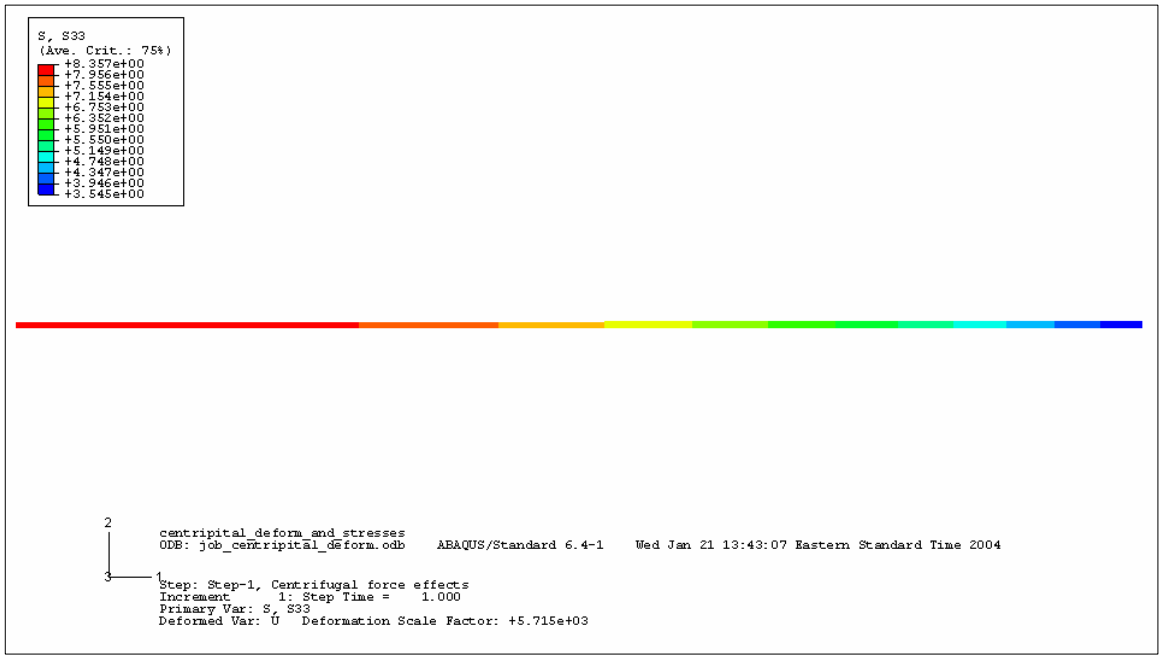

Figure 5.2 Aaxisymmetric model showing tangential stress (S33) in solid disc.

Convergence of the results in the analysis of the axisymmetric model were good. For example, the radial stress, tangential stress and displacement converged to below 0.001 percent difference from 1374 elements with 6 elements through the thickness to

1603 elements with 7 elements through the thickness. Quadratic 8-node axisymmetric elements (ABAQUS element designation CAX8R) were used. A zoomed-in picture of the mesh used in this axisymmetric model can be seen in Figure 5.3. The elements used in this mesh have nearly an aspect ratio of 4.11:1, thus ensuring excellent results.

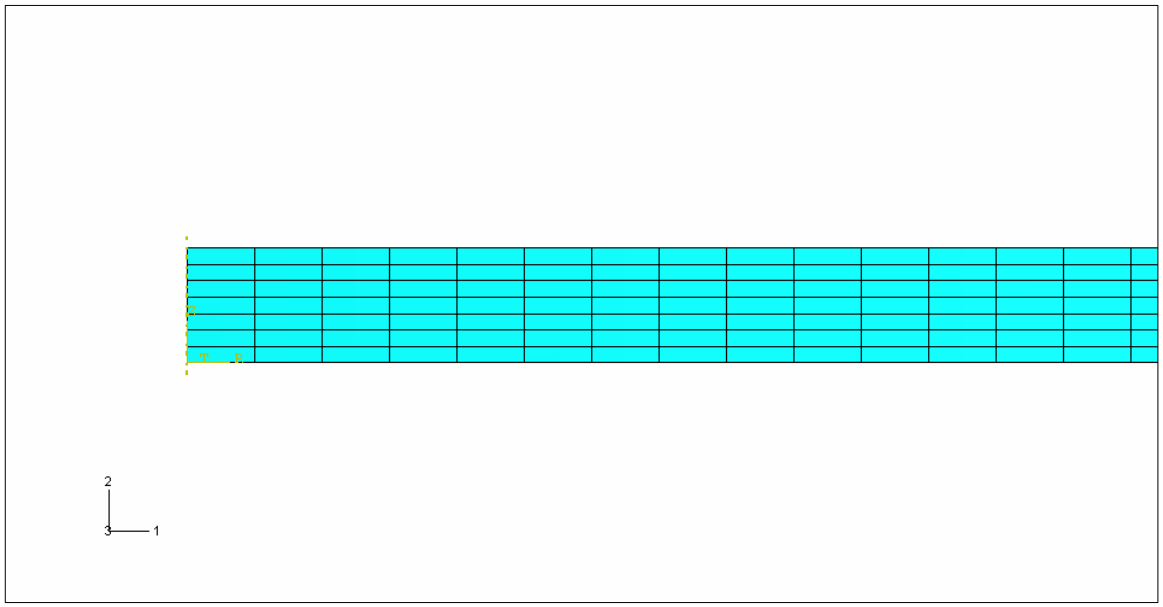

Figure 5.3 Zoomed-in picture of the meshing scheme used for the axisymmetric models. Modeling only half the thickness of the actual solid disc allows us to represent the whole thickness with half the number of elements.

The radial displacement shown in Figure 5.4 is radially outward (directed to the right in the figure). Because this model represents only a cross-section of a solid disc, the center of the solid disc is located at the left side of the figure. At the left side (center of disc), the resulting displacement from rotating is approximately zero (-1.029E-10).

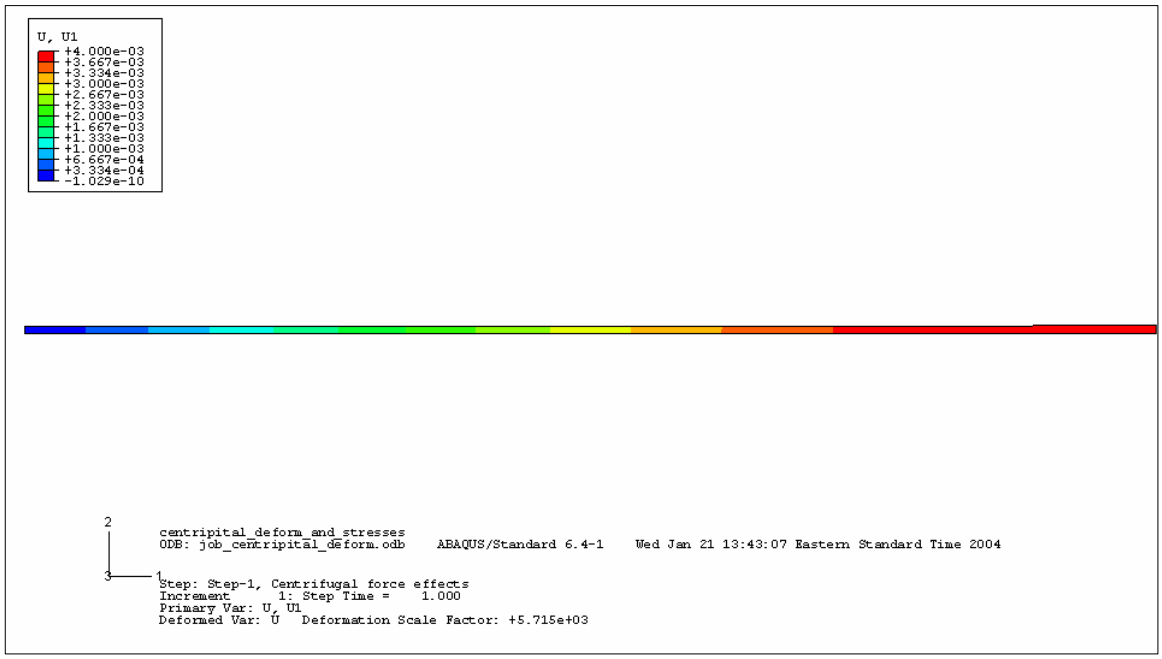

Figure 5.4 Axisymmetric model showing radial displacement (U1) in a solid disc.

Signal-to-Noise Ratio Defined. Signal-to-noise is typically used in describing the accuracy of instruments. However, this principal can also be used to describe the validity of finite element modeling results compared to the classical hand calculations. To illustrate the signal-to-noise used in this research, the method used needs to be explained.

Many values and calculations are used to obtain the signal-to-noise. To begin, the radius is divided into 100 radial locations of equal lengths apart. The errors between the finite element analysis and the computed hand calculations are found by subtracting the variable of interest (for example, the radial stress) of the hand calculation from the FE results at each radial location. Then the mean of these errors is found.

Next, the estimated error variance is found by taking the average of the squared difference between the mean of the errors and the error at each radial location. The estimated error standard deviation is simply the square root of the estimated error variance. Dividing maximum of the variable of interest by the estimated error standard deviation gives the signal-to-noise ratio used throughout this thesis.

Comparing Radial Stress. When comparing the hand calculated results for the radial stress (5.1-1) to the computer results, the two match extremely well. For example, the signal-to-noise ratio between the hand calculations of the radial stress and the

axisymmetric model results is 52700. Furthermore, the maximum error is very low at 9.18E-05 MPa and the estimated error standard deviation is 0.0001585 with a maximum stress of 8.357 MPa. These statistical analysis values obtained from comparing the hand calculations and the computer results prove that the computer results are very accurate and represent a rotating solid disc extremely well. The plots of the results of finite element analysis and the hand calculation results are seen in Figure 5.5, where the difference between the hand calculations and the computer model results are so close they are indistinguishable on the plot.

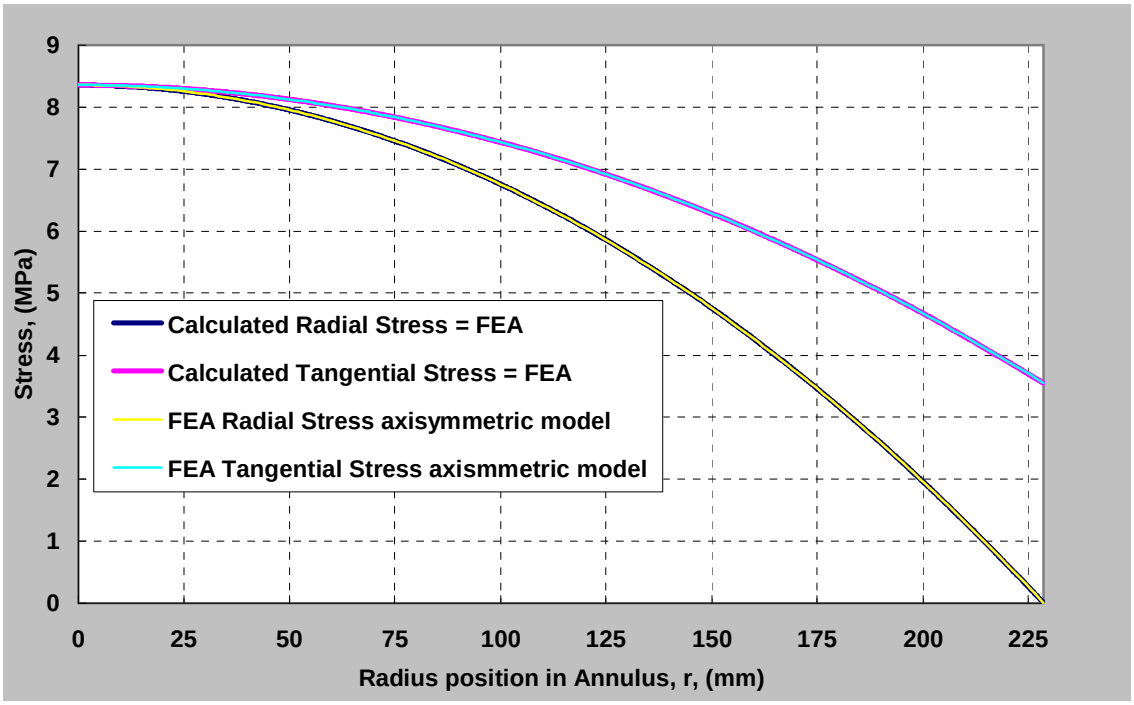

Figure 5.5 Shows the radial and tangential stress in a 9-in (228.6 mm) radius solid disc rotating about its center at an angular velocity of 222.222 rad/s (10,000 sfpm). The tangential stress is higher throughout the disc. Furthermore, both tangential and radial stresses are at a maximum at the center of the disc. At the outer radius, both radial and tangential stresses are at a minimum. Due to no material pulling outward from centrifugal force, the radial stress is zero at the outer radius.

Surface Traction. For both the radial stress and the tangential stress, the maximum stress is located at the solid disc's center. Furthermore, both radial and tangential stresses are at a minimum at the outer edge. However, the radial stress at the outer edge approaches zero because of the natural boundary condition. There is no force in the radial direction at the outside radius. This edge effect is due to each differential element within the solid disc receiving an outward pull, which transforms to a radial stress, due to the centrifugal force

on the adjacent element that is radially outward from it. Because the outer edge differential element does not have an adjacent element radially outward from it, the outer edge experiences no radial stress. In other words, the surface traction in the radial direction at the outer edge is zero.

This edge effect has been used in these models to check for convergence. If the outer edge was near zero, the model – at least at the outer edge was a good representation of a solid disc (or later a sawblade).

Comparing Tangential Stress. Now, the hand calculated results for the tangential stress is compared to the FE axisymmetric model results. As in the radial stress comparison, the tangential stress hand calculation results (Equation 5.1-2) compare favorably with the computer results. The signal-to-noise ratio between the hand calculations and the finite element analysis results is very high at 63700 with a maximum error of 0.000943 MPa and an estimated standard deviation error of 0.0001312. Furthermore, the maximum tangential stress is 8.357 MPa. Like the radial stress, the tangential stress plots of the hand calculations and the finite element analysis results are indistinguishable on Figure 5.5.

Comparing Radial Displacement. The radial displacement results between the hand calculations and the axisymmetric model results are compared. The radial displacement signal-to-noise ratio is 117,500 with a maximum error between the two cases of 3.30E-08 mm and a maximum displacement of 0.004 mm. The estimated error standard deviation is 3.40E-08. As seen in Figure 5.6, the radial displacement of a solid disc of eighteen inches diameter tapers off at its outer edge. The difference between the hand calculation and the axisymmetric results for radial displacement is negligible on the plot.

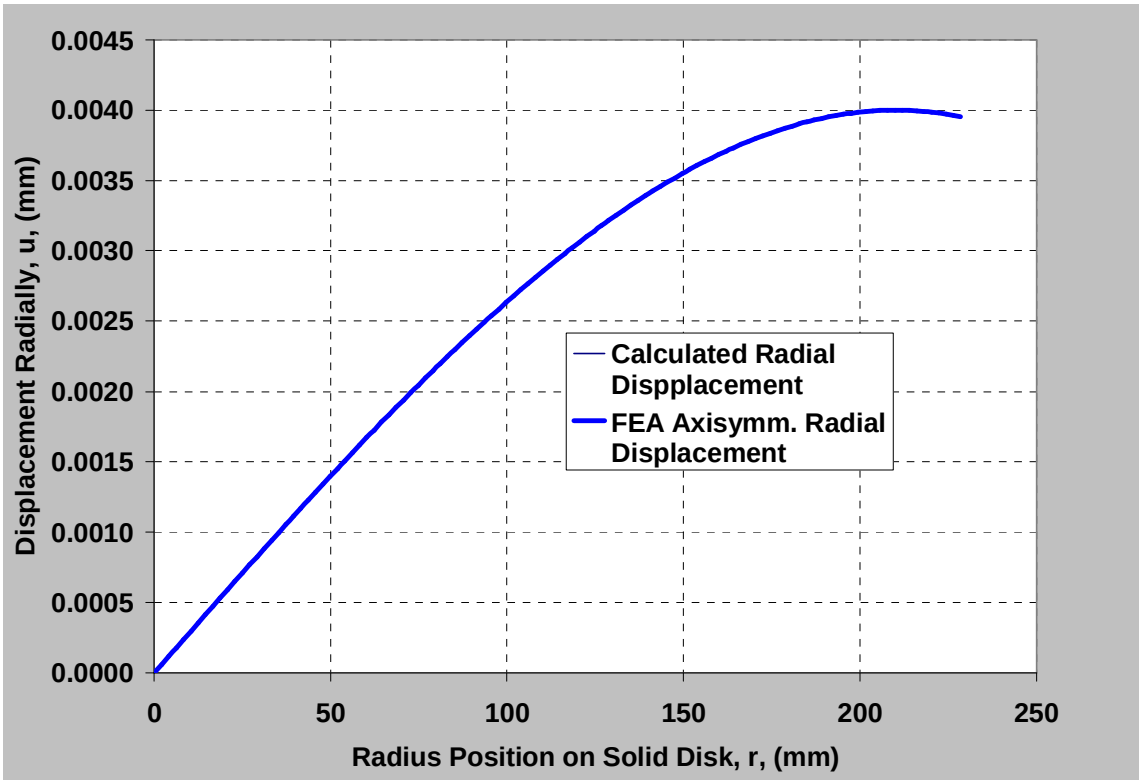

Figure 5.6 Hand calculation and finite element axisymmetric model of the radial displacement of an arbitrary radius position in a solid disc with a 9-in (228.6 mm) radius and an angular velocity of 222.222 rad/s (10,000 sfpm). The two graphs are so close they are indistinguishable.

Because we know that the center of the solid disc stays at the center, this is one good check for the correct representation of the solid disc model. For proof, the plot shows that the displacement at the center of the disc is zero. Furthermore, the fact that the computer model is nearly identical to the generally accepted hand calculations, we know that the computer model results represent accurately the true displacements in the model. These earlier models are the basis for the later research where a sawblade is analyzed. During the research, we used the experience gained from the solid disc and the annulus models to check for consistency in the sawblade models.

5.2 *Annulus without Inner Boundary Condition Hand Calculations versus Finite Element Analysis (axisymmetric and three-dimensional eight-model)*

When developing the model of the research to more closely resemble the dimensions of an 18-in sawblade with a hole in the center, an axisymmetric FE model

was compared to the generally known accepted equations. This was performed to check and validate the computer models against these generally accepted equations. These equations were for a rotating annulus with no inner boundary condition. The annulus is spinning about its center. Furthermore, using no inner boundary condition was also useful to obtain information and quantify the results of using no inner boundary condition and to compare to the results of using an infinite boundary condition representing the collar with infinite stiffness in section 5.4. Because the sawblade to be analyzed is mounted on the saw machine with stiff collars measuring 4.5-in (114.3 mm) diameter, we modeled the annulus as if the inner radius stops at the collars' mounting diameter. Also, this inner radius and all other parameters are included in the hand calculations.

Hand Calculations. The equations for the hand calculations for a spinning annulus with no inner boundary condition were obtained from Boresi and Schmidt [8], and then these equations were simplified for easier use. The radial stress, σ_{rr} in an annulus is found using:

$$\sigma_{rr} = \frac{E}{1-\upsilon^2}\left[-\frac{(3+\upsilon)(1-\upsilon^2)}{8E}\rho r^2\omega^2 + (1+\upsilon)M_1 - \frac{(1-\upsilon)}{r^2}M_2\right] \qquad [5.2\text{-}1]$$

where the ρ is the mass density in units ($\frac{\text{N-s}^2}{\text{mm}^4}$ or $\frac{\text{lbf-s}^2}{\text{in}^4}$), r is an arbitrary radial location where the stressed is to be determined, M_1 and M_2 are constants. These constants are obtained using:

$$M_1 = \frac{(3+\upsilon)(1-\upsilon^2)}{8(1+\upsilon)E}(a^2+b^2)\rho\omega^2 \qquad [5.2\text{-}2]$$

and

$$M_2 = \frac{(3+\upsilon)(1-\upsilon^2)}{8(1-\upsilon)E}a^2b^2\rho\omega^2 \qquad [5.2\text{-}3]$$

where *a* is the inner radius of the annulus and b is the outer radius of the annulus.

Substituting for the constants M_1 and M_2 from Equations 5.2-2 and 5.2-3 into Equation 5.2-1 and reducing yields the final equation:

$$\sigma_{rr} = \frac{3+\upsilon}{8}\rho b^2\omega^2\left[1+\frac{a^2-r^2}{b^2}-\frac{a^2}{r^2}\right] \qquad [5.2\text{-}4]$$

Next, the tangential stress is expressed as

$$\sigma_{\theta\theta} = \frac{E}{1-\upsilon^2}\left[-\frac{(1+3\upsilon)(1-\upsilon^2)}{8E}\rho r^2\omega^2+(1+\upsilon)M_1+\frac{(1-\upsilon)}{r^2}M_2\right] \qquad [5.2\text{-}5]$$

Substituting for the constants M_1 and M_2 from Equations 5.2-2 and 5.2-3 into Equation 5.2-4 and reducing yields the final equation:

$$\sigma_{\theta\theta} = \frac{3+\upsilon}{8}\rho b^2\omega^2\left[1+\frac{(3+\upsilon)a^2-(1+3\upsilon)r^2}{(3+\upsilon)b^2}+\frac{a^2}{r^2}\right] \qquad [5.2\text{-}6]$$

Lastly, the displacement was found using the equation:

$$u = \frac{(1-\upsilon^2)}{8E}\rho r^3\omega^2+\mathrm{M_1 r}+\frac{1}{\mathrm{r}}M_2 \qquad [5.2\text{-}7]$$

The displacement, *u*, in this formula tells how far an arbitrary radial position, *r*, has moved radially outward on the annulus.

Other useful equations used for finding the stresses in a rotating annulus are

$$\sigma_{rr}(\max) = \frac{3+\upsilon}{8}\rho b^2\omega^2\left(1-\frac{a}{b}\right)^2 \qquad [5.2\text{-}8]$$

which tells the maximum stress in the radial direction. This maximum radial stress location is on a radial circle with radial position, *r(@* σ_{rr} max*)*, located at

$$r(@\sigma_{rr}\ \max) = \sqrt{ab} \qquad [5.2\text{-}8]$$

For our model with inner radius of 57.15 mm (2.25-in) and outer radius of 228.6 mm (9-in), the radial location of the maximum radial stress occurs at 114.3 mm (4.5-in). The maximum tangential stress is found according to

$$\sigma_{\theta\theta}(\max) = \frac{3+\upsilon}{4}\rho b^2\omega^2\left[1+\frac{(1-\upsilon)}{(3+\upsilon)}\frac{a^2}{b^2}\right] \qquad [5.2\text{-}9]$$

This maximum tangential stress in a spinning annulus is located at the inner radius ($r = a$).

5.2.1 *Axisymmetric Model of Annulus with Inner Natural Boundary Condition*

Radial Stress. The axisymmetric model of the spinning annulus results for the radial stress is shown in Figure 5.7. This figure represents an axisymmetric model of an annulus rotating about its geometrical center or axis of rotation. This is the same annulus the hand calculations represent.

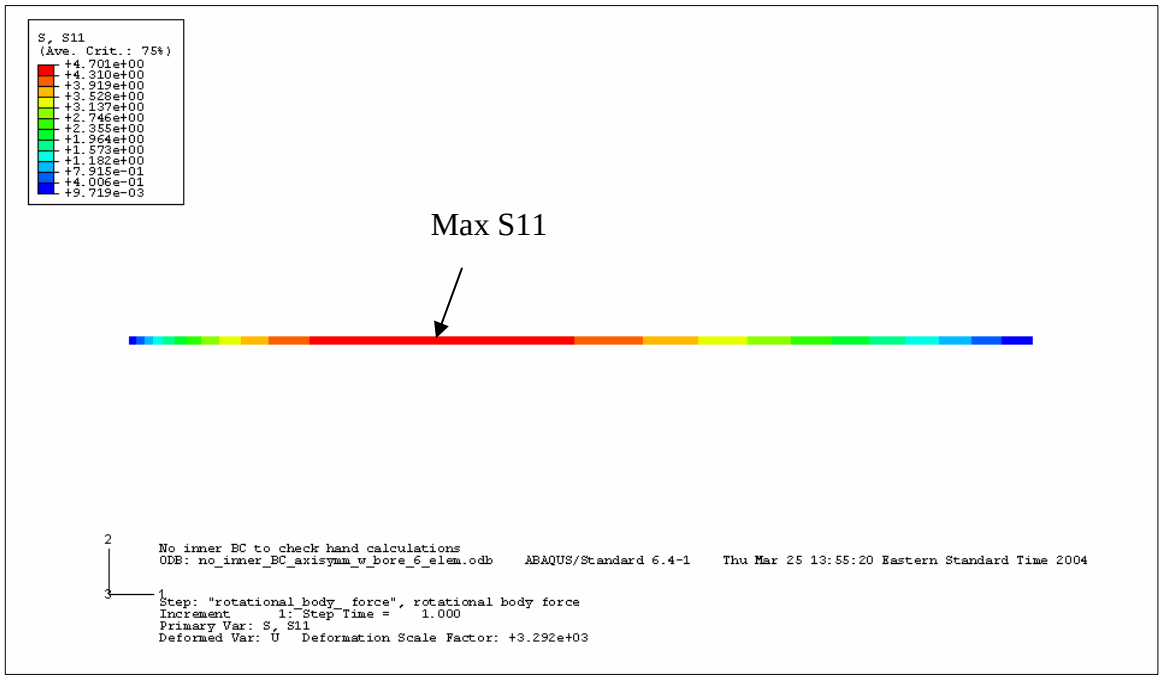

Figure 5.7 Axisymmetric model showing radial stress (S11) in an annulus. The inner radius is 57.15 mm (4.5-in) and the outer radius is 228.6 mm (9-in). Due to symmetric loading conditions and geometry about the 1-axis (x axis), which is along the center of the solid disc, the thickness used in the model is half the thickness of actual annulus represented. This annulus is rotating at 222.222 rad/s (10,000 sfpm). The maximum radial stress is located at 114.3 mm (4.508-in).

The axisymmetric model represents only a cross-section of the actual annulus. To make the whole model of the solid disc, this cross-section would have to be rotated about a line located 57.15 mm (4.5-in) from the left vertical line of the annulus by 360^{o}. Because all stresses and displacements are symmetric about the center axis of the annulus, this axisymmetric model makes an excellent representation of the whole annulus. For clarity in Figure 5.7 through Figure 5.9, the x-axis (or 1-axis) is left and right, the y-axis (or 2-axis) is up and down, and the z-axis (or 3-axis) is into the paper. Furthermore, the 1-axis represents the radial direction on the annulus, the 2-axis represents the direction through the thickness of the annulus disc, and the 3-axis represents the tangential direction of the annulus.

As in the solid-disc axisymmetric model, the half thickness was again used to make the axisymmetric model representing the annulus. Similar to the solid disc axisymmetric model, we again used a y-symmetric boundary condition along the whole bottom line. Explicitly this means that the boundary condition along the whole bottom line is U1=UR1=UR3=0 (or y-symmetric). Because the annulus is symmetric about the bottom line and the loading is also symmetric about the bottom line, this “half-modeling”

is an excellent way to keep the number of elements and computational time to a minimum. The meshing scheme is shown in Figure 5.8, where the aspect ratio is excellent at nearly one to one. Again, the 8-node quadratic, quadrilateral axisymmetric element (ABAQUS designation CAXR8) is used for the analysis.

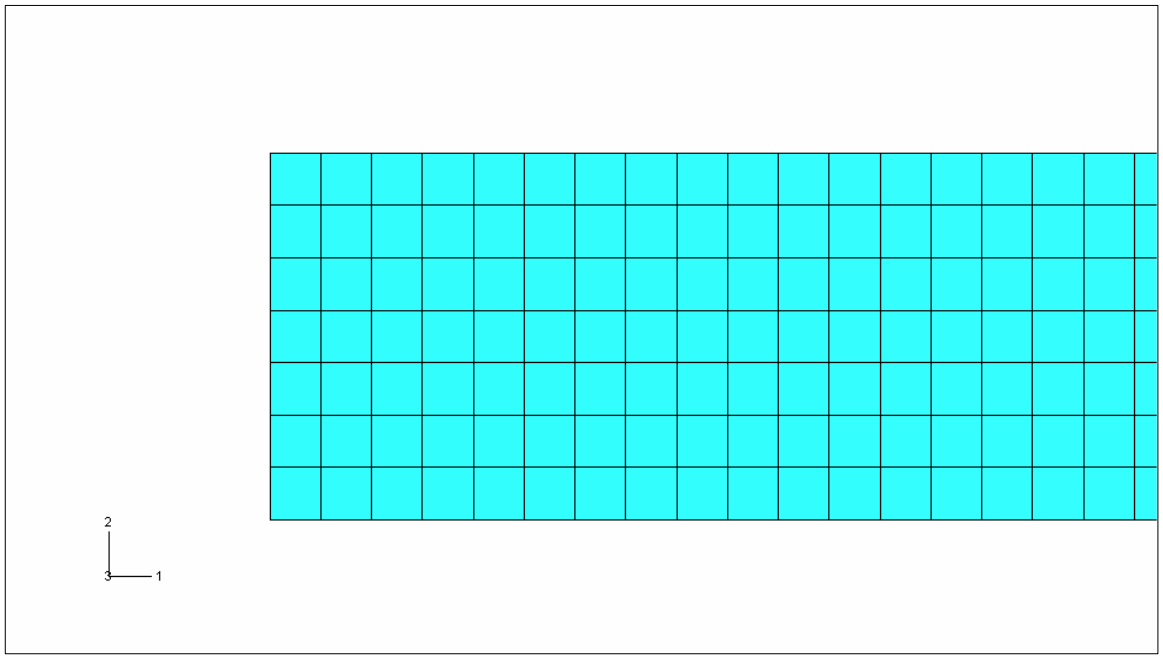

Figure 5.8 Meshing scheme used for annulus (zoomed-in on left side).

When converging the results of this axisymmetric model, it is found that the displacement, radial stress and the tangential stress all showed less than a 0.001 percent difference between 3624 and 4935 elements. Because an annulus with no inner boundary conditions will have a radial stress of 0 at the inside radius, this value was attempted to be reached for the minimum radial stress. Furthermore, the attempt to make the radial stress results equal to zero at the inner radius serves as a check for the model. The final converged result gave a minimum radial stress of 0.008329 MPa at the left side. This result being higher than zero is due to the force that the inner radius element places on itself because of its mass density and centrifugal acceleration. If this element could be made infinitely small, the resulting radial stress would be exactly zero. However, infinitely small elements are not possible with current technology. But, for practical purposes, the results for the radial stress, tangential stress and radial displacement are quite accurate.

Radial Displacement. The result for radial displacement is seen in Figure 5.9. The left vertical line of this axisymmetric model is located a distance of 57.15 mm (4.5-in) from the geometrical center of the annulus. Furthermore, this line represents the inner radius, while the right red line is the outer radius of the annulus. All displacements are positive and to the right. More discussion of the reasons of the distribution of the displacement will be discussed a next few paragraphs.

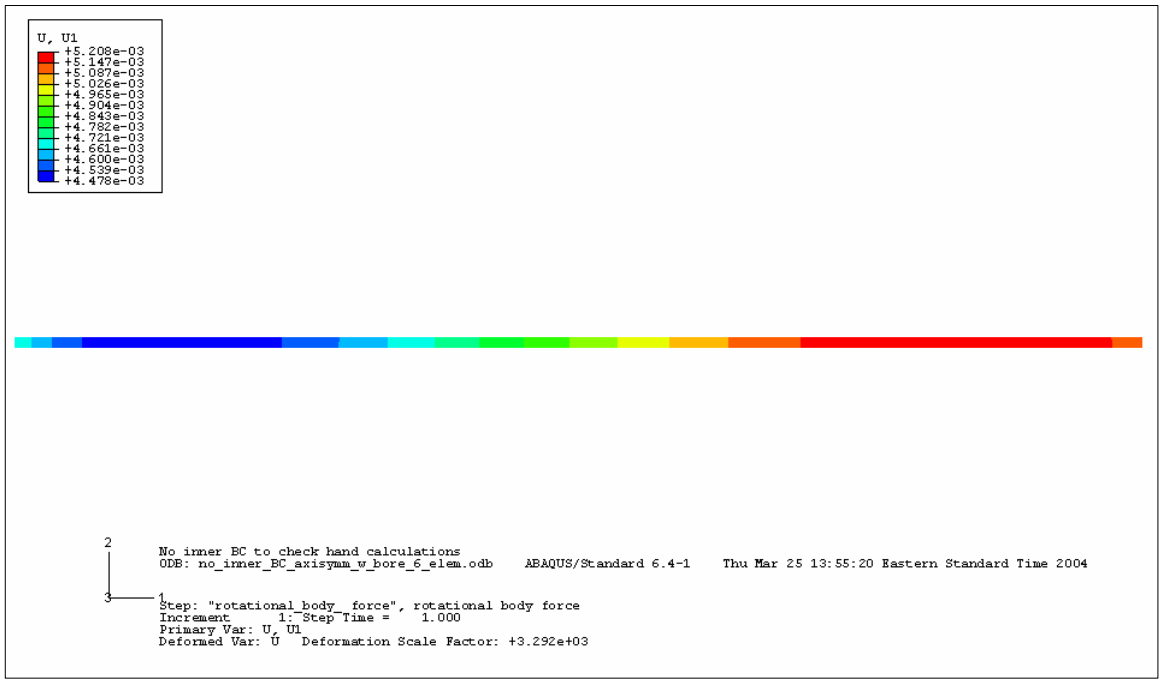

Figure 5.9 Axisymmetric model showing radial displacement (U1) in an annulus.

Comparing Axisymmetric Model with Hand Calculations. When comparing the axisymmetric model results with the hand calculations from Equations 5.2-4 and 5.2-6, the results are nearly identical, see Figure 5.10. For example, the signal-to-noise ratio between the hand calculations of the radial stress and the axisymmetric model results of a rotating annulus is 1460. Furthermore, the maximum error is very low at 0.0001732 MPa and the estimated standard deviation error is 0.00322 with a maximum stress of 4.70 MPa. These statistical analysis values obtained from comparing the hand calculations and the finite element analysis results prove that the computer model results are very accurate and represent a rotating annulus very well. The plots of the results of computer model and the hand calculation results are seen in Figure 5.10, where the difference between the

hand calculations and the computer model results is so close that it is impossible to tell apart on the plots.

Signal-to-noise is used to quantify the difference between the hand calculations of the tangential stress and those values obtained from the axisymmetric model. The signal-to-noise ratio of 4815 is computed with a maximum error of 0.0366 MPa across the radius of the disc. The estimated standard deviation error was 0.00352 and the maximum stress was 16.9 MPa. This proves the strong correlation between the generally accepted hand calculations and the axisymmetric model results for the tangential stress. These results can be seen in Figure 5.10.

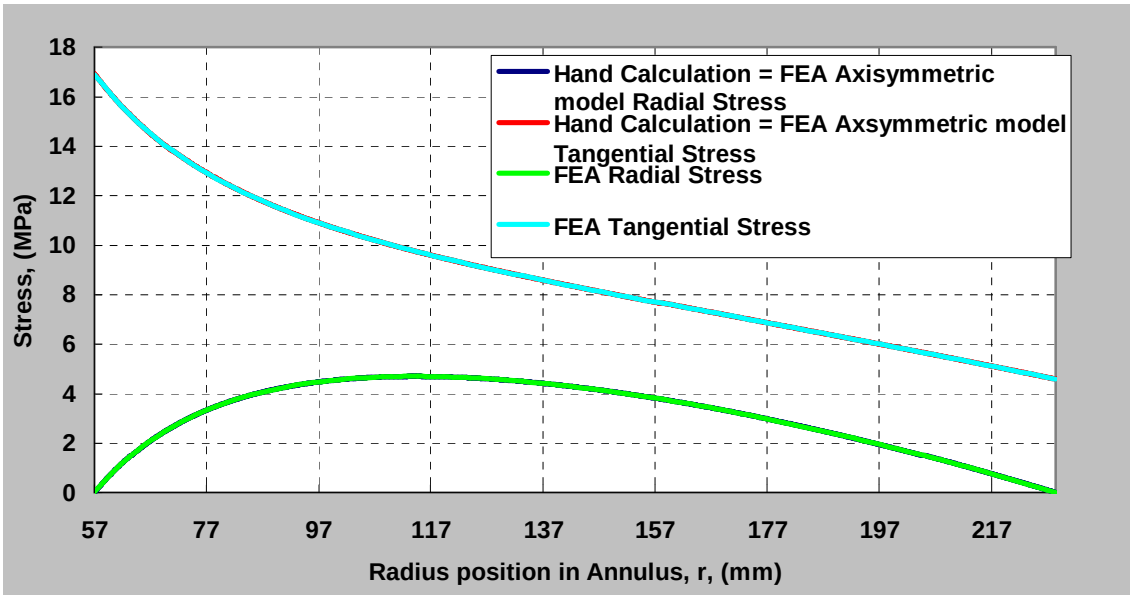

Figure 5.10 Shows the radial and tangential stress in a 9-in (228.6 mm) radius annulus with inner radius of 2.25 inches (57.15 mm) and having no inner boundary condition. For both the radial stress and the tangential stress, the axisymmetric model matches exactly to the hand calculations. The tangential stress is higher than the radial stress at any position within the annulus. Further, the radial stress is a parabola with end points equal to zero at the inner and outer radius of the annulus.

Radial Stress. Because the rotating annulus in this analysis does not have an inner boundary condition, the radial stress is zero at the inside radius, r = a. This is the natural boundary condition of the inner radius. This boundary condition must be met because each infinitesimal element at the inner radius has no material radially inward. Having no material radially inward to resist the centrifugal force, and that the inner radius has zero radial stress at the inner edge because there is no force applied there. This zero boundary

condition gave a good check to the convergence of the computer model throughout the analysis of the axisymmetric model.

As the arbitrary radial position on the rotating annulus goes away from the inner radius, the stress is acting in the radial outward direction. This result is because the annulus is being stretched radially outward from the centrifugal force. The maximum radial stress, occurs at σ_r max@ $r = \sqrt{ab}$ position because outward to this radial position the annulus is stretching farther than inward to this position. In our case, the maximum radial stress occurs at 114.3 mm (4.5-in), which gives 4.700 MPa from the hand calculations. This hand calculation of the maximum radial stress is compared to the maximum stress predicted by the computer model at 114.5 mm (4.508-in), which also gives 4.700 MPa.

At the outer edge of the annulus, the radial stress again experiences the natural boundary condition. Because there is no radially outward material to an infinitesimal element located at the outer edge, there is no rotational force effect pulling radially outward on any elements located at the outer edge. Therefore, the radial stress from centrifugal force at this outer free boundary condition is zero.

This is illustrated using the fundamental equations governing the physics of the rotating disc. The radial stress is a direct result of the strains experienced by each particle of the disc. Radial stress, σ_r is

$$\sigma_r = E\left[\varepsilon_r - \upsilon(\varepsilon_\theta + \varepsilon_l)\right] \qquad [5.2\text{-}10]$$

where the radial strain, ε_r is

$$\varepsilon_r = \frac{\partial u}{\partial r} \qquad [5.2\text{-}11]$$

Because strain in the axial direction, $\varepsilon_l << \varepsilon_r$ & ε_θ, Equation 5.2-10 becomes

$$\sigma_r \cong E\left[\varepsilon_r - \upsilon\varepsilon_\theta\right] \qquad [5.2\text{-}12]$$

Because the inner and outer radii have natural boundary conditions, the surface tractions in the normal direction are zero. Low radial strain at the outer radius results in low radial stress at the outer radius.

Tangential Stress. For the tangential stress in the rotating annulus with natural boundary condition, the tangential stress is highest at the inner radius and the minimum tangential stress is located at the outer radius. The distribution of the tangential stresses is seen in Figure 5.11.

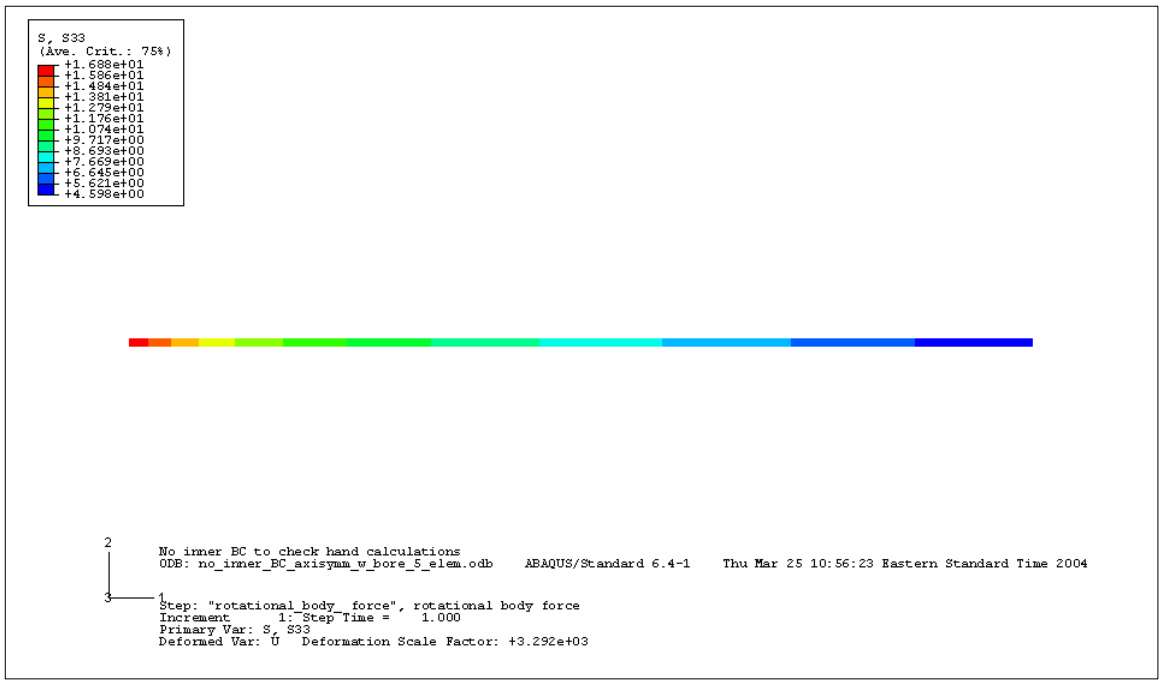

Figure 5.11 Axisymmetric model showing tangential stress (S33) in an annulus.

The tangential stress at the inner radius is higher than any position radially outward from the inner radius because there is less material to stretch at the inner radius. This higher stress can be illustrated by comparing a short rod and a long rod, as seen in Figure 5.12. Each has stiffness, $k = AE/L$ in the axial direction. If the short rod is pulled, it will elongate less than if a long rod (having the same spring rate) is pulled with the same force. In other words, a short rod is more resistant to elongation than a long one. Likewise, when it comes to tangential displacement deltas, the inner radius is more resistant to elongate than the outer radius because at the inner radius, the arc around the

inner circle, is shorter than the arc of the outer radius circle. Therefore, there will be higher stresses at the inner radius because the inner radius will more strongly oppose the stretching. Moreover, the outer radius will more readily stretch and more easily become larger than the inner radius.

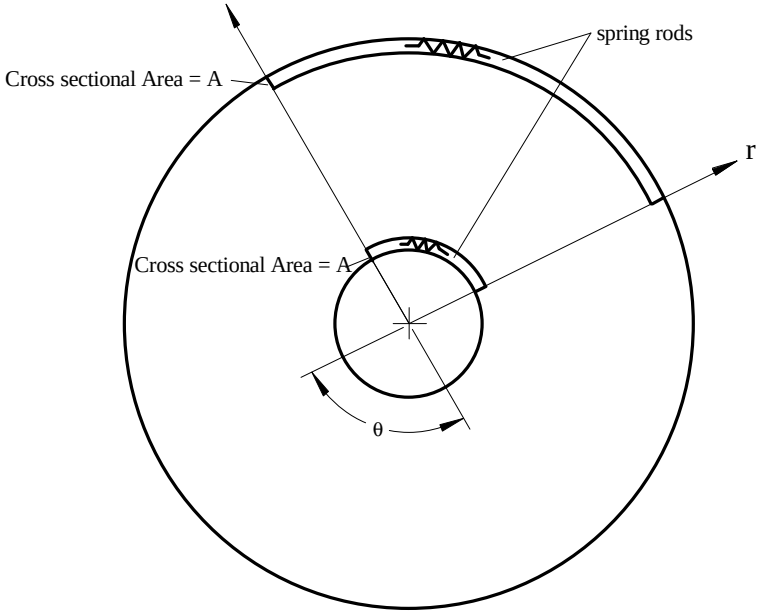

Figure 5.12 Spring Rod elements on inside and outside radius.

This can be further illustrated by tangential stress, σ_θ, is found according to

$$\sigma_\theta = E\left[\varepsilon_\theta - \upsilon(\varepsilon_r + \varepsilon_l)\right] \qquad [5.2\text{-}13]$$

where ε_θ is the strain in the tangential direction, ε_r is the strain in the radial direction, and ε_l is the strain in the axial direction.

Strain, is typically seen as

$$\varepsilon = \frac{\triangle l}{l} \qquad [5.3\text{-}14]$$

but, in our case in the strain in the tangential direction is the change in the arc length. The change in arch length, Δl is

$$\Delta l = (r+u)\theta - r\theta = u\theta \qquad [5.3\text{-}15]$$

where u is again the change in radial displacement. The original arc length is

$$l = r\theta \qquad [5.3\text{-}16]$$

Because the displacement in the tangential direction, u_θ, is independent of the angular location, θ, ε_θ is also independent of θ. Therefore, the tangential strain is

$$\varepsilon_\theta = \frac{u}{r}$$

[5.3-17]

And because the strain in the axial direction, $\varepsilon_l << \varepsilon_r$ & ε_θ Equation 5.2-9 becomes

$$\sigma_\theta \cong E(\varepsilon_\theta - \upsilon\varepsilon_r) \qquad [5.2\text{-}18]$$

Therefore, even though the displacements in the radial and tangential directions at the outer radius are larger than those displacements at the inner radius, the tangential strains at the inner radius are higher because the amount of change per original arc length is greater. In other words, the denominator of equation 5.3-13 is smaller for the inner radius resulting in larger tangential strains, and thereby resulting in larger tangential stresses at the inner radius.

5.2.2 *Three-Dimensional Model of Annulus with Inner Natural Boundary Condition*

Next, the three-dimensional models of a rotating annulus with natural boundary conditions are shown and discussed because of various sawblade models being represented by a 3-D model. Moreover, the only way to capture the effects the geometry is to use a three-dimensional model. For example, the features only represent able by a 3-D model are the gullets and expansion slots and the carbide tips, which have nearly three times the density of steel. The best way to validate the future FE sawblade models results is to prove the validity of 3-D FE models as compared to known hand calculations.

Boundary Conditions. The three-dimensional annulus' boundary conditions are many. The inner radius face and the outer radius face are unconstrained allowing the whole annulus to grow outwards with the only resistance being the annulus itself. This three-dimensional eighth-model is only half the thickness of the annulus. A boundary condition ties all elements and nodes to stay on the symmetry plane located on the bottom face. This face is located on the large arch's face on the bottom of the annulus, as seen in Figure 5.13 (c). For any point on a spinning annulus located along a radial line, all loading and geometry is symmetric. In other words, all elements will stay on the same radial line and move only in a radial direction. Furthermore, all stresses are the same at any point on the disc located the same distance from the center and having the same axial position. This phenomenon allows us to only a portion of the annulus, however the model used is a quarter of the circle of the annulus for the ease of using the coordinate axes as planes of symmetry. However, this simplification process requires the boundary conditions of the straight edges to keep the edges straight and keep the elements on the edges. These boundary condition locations are seen in Figure 5.13 (a) and (b) as a red face. The straight edge (actually a face) at the bottom in Figure 5.13 (a), the boundary condition is y-symmetric (U2 = UR1 = UR3 = 0). The straight edge (actually a face) at the left in Figure 5.13 (b), the boundary condition is x-symmetric (U1 = UR2 = UR3 = 0).

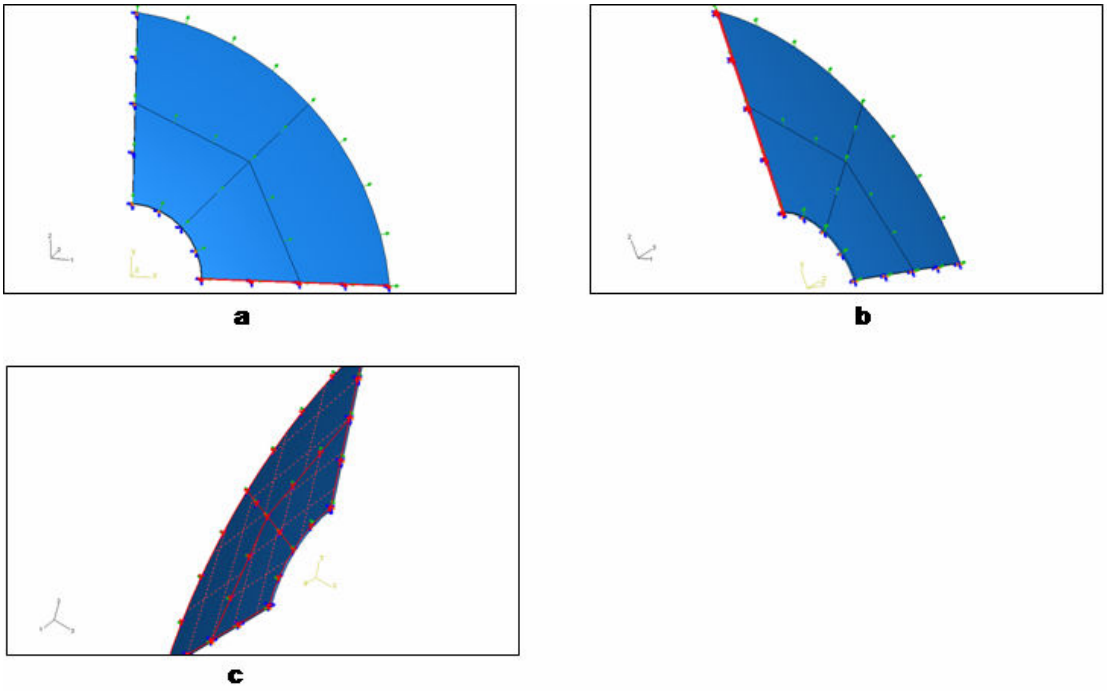

Figure 5.13 Boundary conditions for the three-dimensional eighth-model. (a) shows the placement of the lower face (red) with a boundary condition of y-symmetric (b) shows the placement of the left face (red) with a boundary condition of x-symmetric. (c) shows an upside down view of the annuls with a boudary condition of z-symmetric on the bottom face (red). The partitioning scheme is also shown as lines on the face. These lines go all the way through the part.

The partitioning scheme for the eighth-model is shown Figure 5.13 (a). These lines on the face break the geometry into 4-sided partitions by going all the way through the thickness of the part. Four-sided partitioning allows for better meshing when using a brick element. For example, without making 4-sided partitioning for a brick element, the mesh may not pass the statistical analysis or the aspect ratio may be too high for good results to be obtained. For the mesh in this three-dimensional model, a 20-node brick quadrilateral element (ABAQUS designation C3D20R) with reduced integration was used. The mesh can be seen in Figure 5.14.

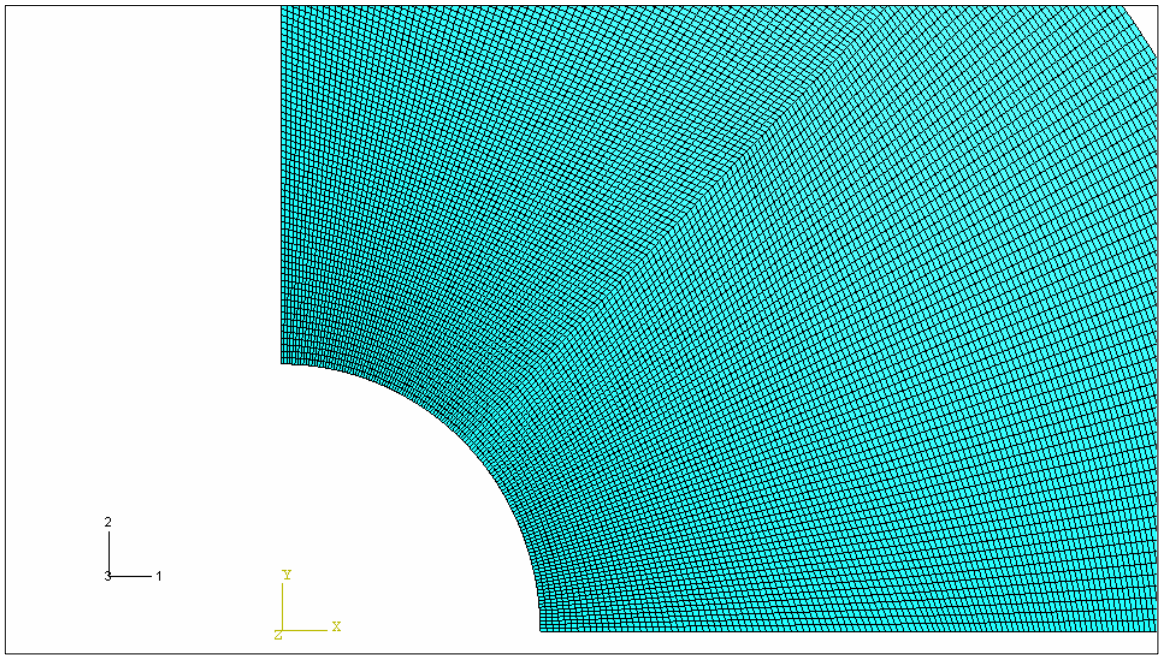

Figure 5.14 Meshing scheme used for three-dimensional annulus. There are 2 elements through the thickness.

Results. A cylindrical coordinate system is used for all three-dimensional models. For example, the 1-axis is the radial direction, the 2-axis is the tangential axis (or θ direction), and the 3-axis is the thickness axis (or z-axis). The radial stress distribution is shown in Figure 5.15. This distribution is the same as used to compare the signal-to-noise ratio for radial stress seen later in the plots comparing the three-dimensional model results to the hand calculations for the radial stress in the annulus rotating at 10,000 sfpm (222.222 rad/s). The loading used is a rotational body force that is acted upon the whole three-dimensional annulus. Also, the convergence of the stresses is shown in Figure 5.31 where the all the stresses converged well within 0.01 percent difference between the meshes.

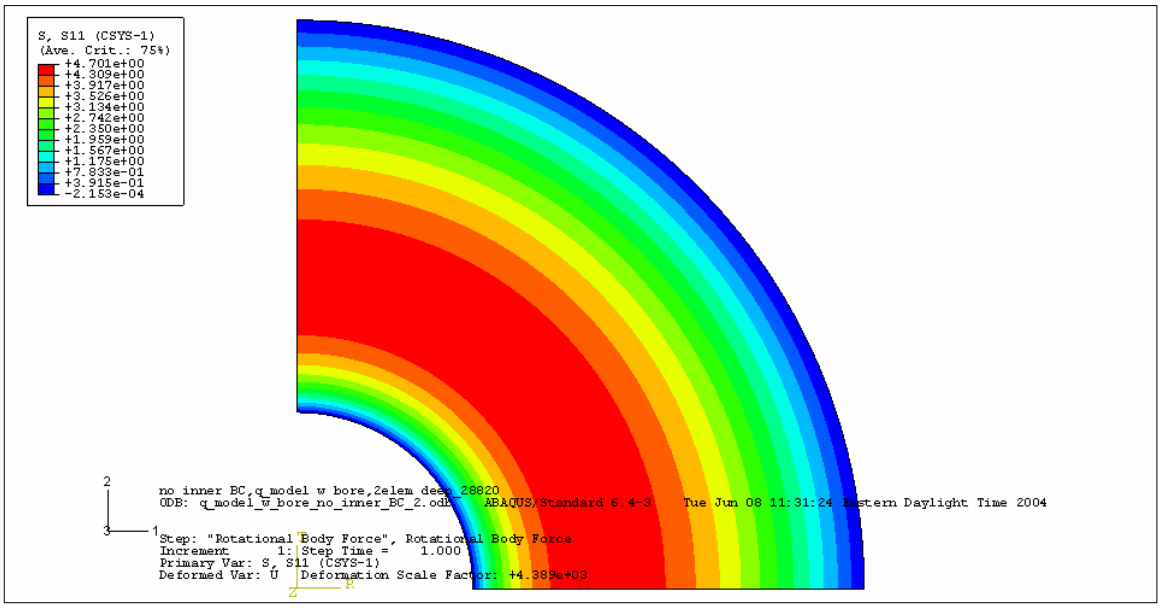

Figure 5.15 Three-dimensional model of annulus showing radial stress (S11) distribution.

The next stress shown for the three-dimensional annulus is the tangential stress, seen in Figure 5.16. This stress is along the 2-axis (or θ-axis). The resulting picture is symmetric about the center of the annulus, proving that our boundary conditions have worked to keep the eighth-model's stress distribution accurate. This model represents correctly the stress distribution in the rotating annulus as will be shown when comparing the hand calculations to the three-dimensional model.

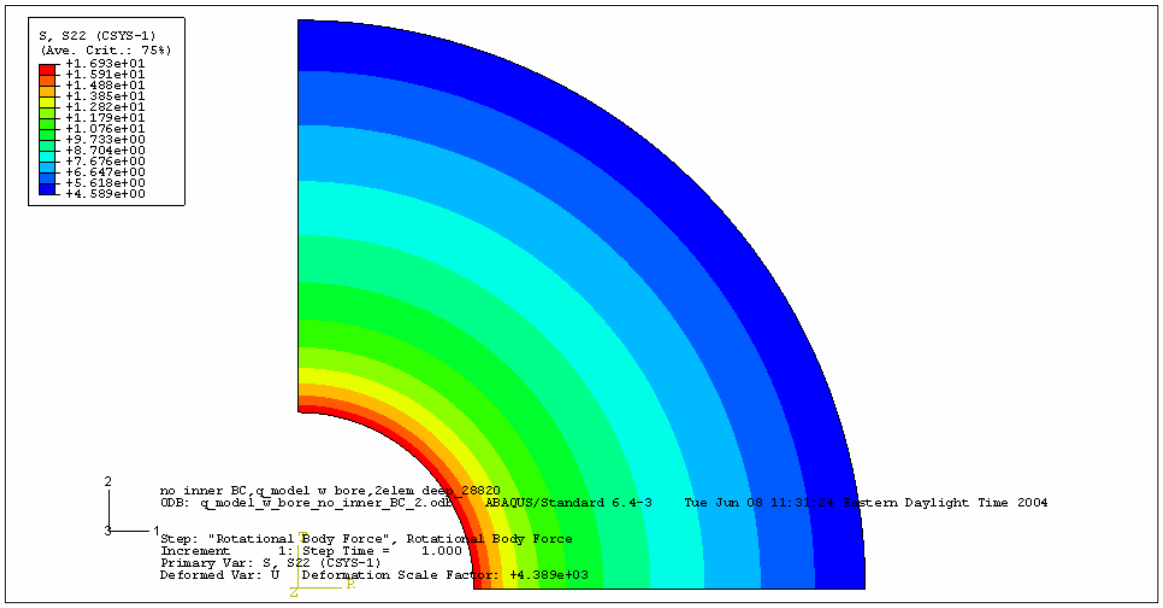

Figure 5.16 Three-dimensional model of annulus showing tangential stress (S22) distribution.

When the annulus rotates, it tends to grow in the radial direction that is symmetric about the center of the annulus, as seen in Figure 5.17. Here, the minima and maxima are within the annulus and shown in dark blue and red, respectively. This is better illustrated in Figure 5.18. The analyses shown in pictures in Figure 5.15 through Figure 5.17 are used in the comparison between the three-dimensional model results and the hand calculations and axisymmetric model.

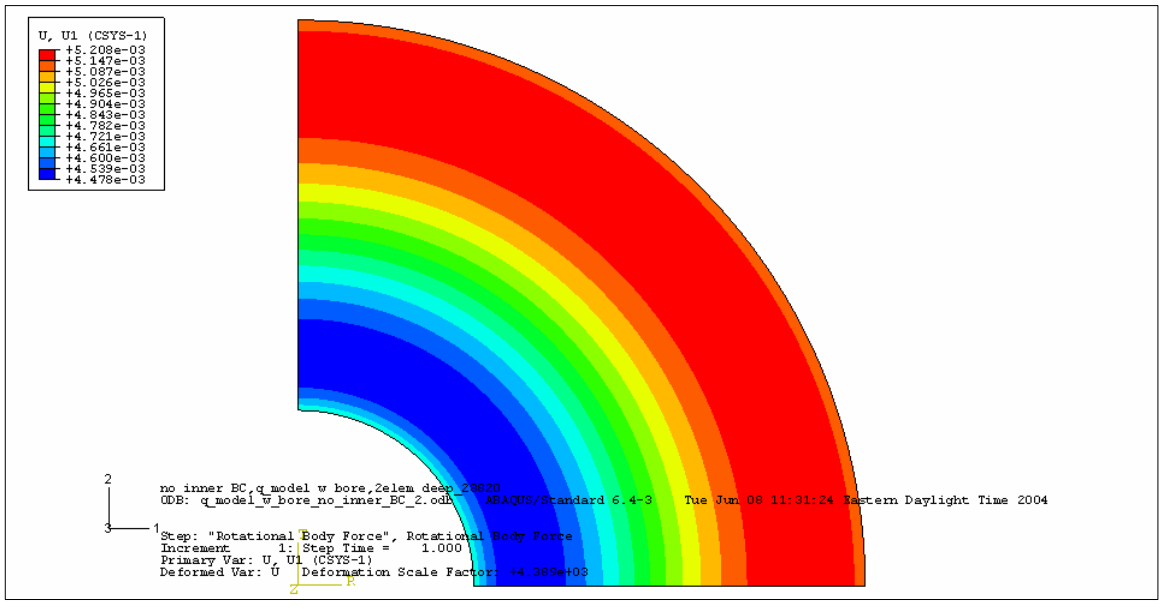

Figure 5.17 Radial displacement (U1) of three-dimensional annulus.

Comparison of 3-D Model to Hand Calculations. Much like the statistical comparisons between the hand calculations and the axisymmetric model, statistical comparisons between the hand calculations and the three-dimensional model of a rotating annulus were performed. These statistics quantify the accuracy, validity, and correct representation of the three-dimensional computer models used in this research, as seen in Table 5-1 the distributions are plotted in Figure 5.18 and Figure 5.19.

Table 5-1 Statistical comparison of annulus with natural inner boundary condition.

		Maximum Error, (mm or MPa)	Standard Deviation	Maximum Value of Variable, (mm or MPa)	Signal-to-Noise Ratio
Axisymmetric	u_r	8.02E-09	1.64E-08	0.00521	303,000
	σ_{rr}	0.00146	0.000481	4.70	9760
	$\sigma_{\theta\theta}$	0.00314	0.000465	16.9	36,490
3-D Model	u_r	8.02E-09	1.72E-08	0.00521	303,000
	σ_{rr}	1.46E-03	4.81E-04	4.70	9760
	$\sigma_{\theta\theta}$	3.14E-03	4.65E-04	16.9	36,500

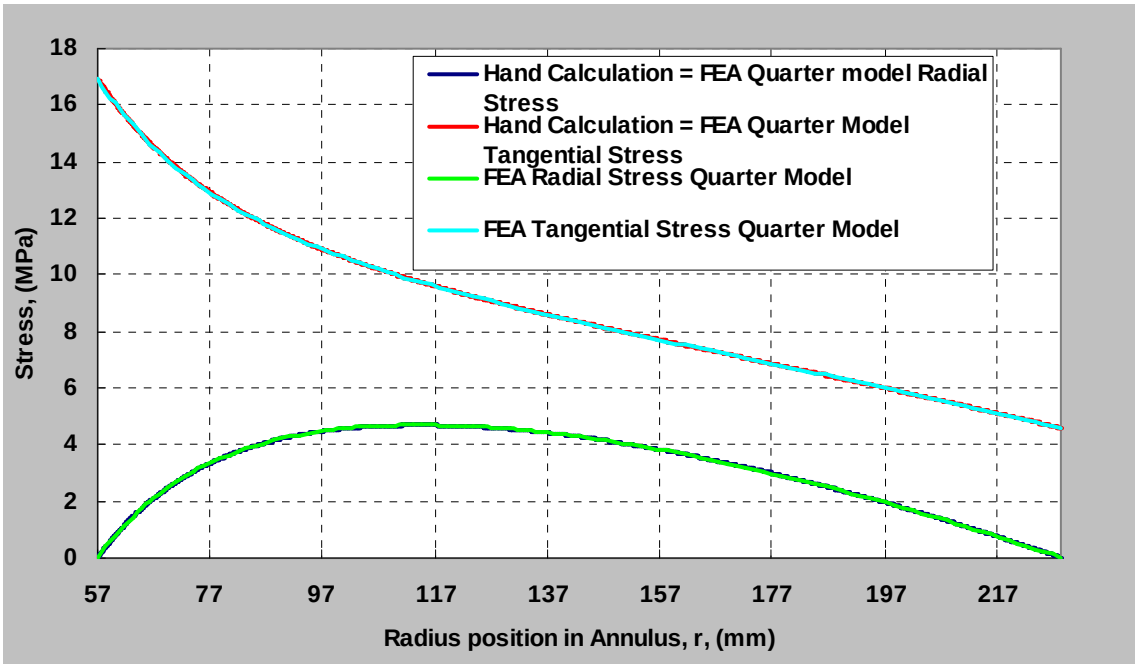

Figure 5.18 Shows the radial and tangential stress in a 9-in (228.6 mm) radius annulus with inner radius of 2.25 inches (57.15 mm) and having no inner boundary condition. Here an eighth-model is used to represent the analytical results. For both the radial stress and the tangential stress, the eighth-model matches exactly to the hand calculations. The tangential stress is higher than the radial stress at any position within the annulus. Further, the radial stress is a parabola with end points equal to zero at the inner and outer radius of the annulus.

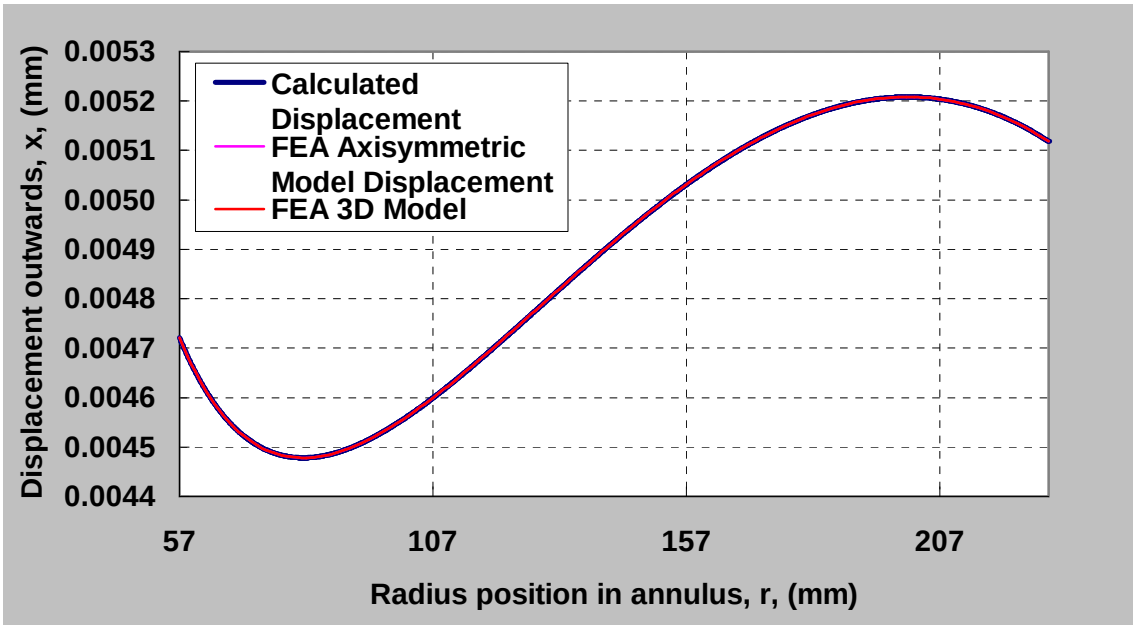

Figure 5.19 Shows the radial outward displacement in a 228.6 mm (9-in) radius annulus with inner radius of 57.15 mm (2.25 inches) and having no inner boundary condition. The displacement acts as a second order curve, with maximum near the outer edge.

5.3 *Annulus with Fixed Inner BC Simulating the Saw Collar Hand Calculations versus Finite Element Analysis*

The 457.2 mm (18-in) annulus using an infinite boundary condition at the inner radius was modeled next. Throughout this thesis, this infinite stiff boundary condition on the inner radius will be referred to as the saw collar boundary condition and is located at 2.25-in from the geometric center.

For this section, first, I derived the equations from the known boundary conditions, and then the axisymmetric model is discussed and compared to the hand calculations. Next, the 3-D model is discussed and compared to the hand calculations.

Hand Calculations. The disc shown in Figure 5.20 is constrained from moving outward at the inner radius. The inner radius, *a* [mm], in our case is the point of contact of the saw collar on the annulus, the outer radius of the disc or sawblade is *b* [mm]. The angular velocity in the hand calculations is represented by ω [rad/s]. Figure 5.20 is used in solving Equations 5.3-1 through 5.3-6.

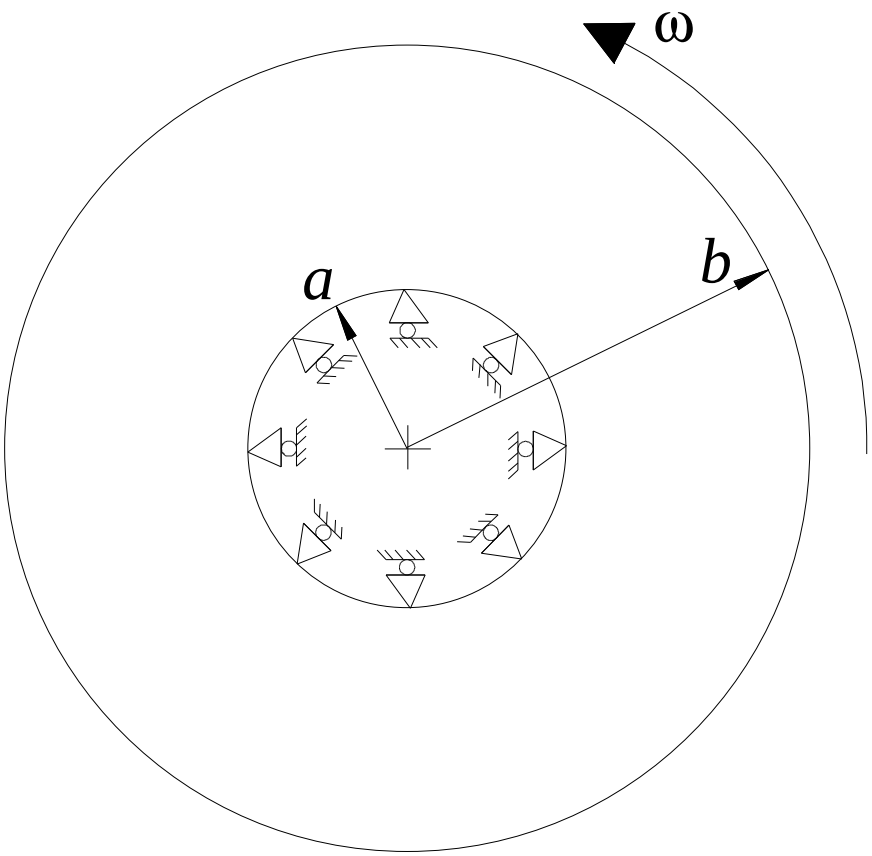

Figure 5.20 Spinning annulus constrained at inner radius, *a*.

According to Boresi and Schmidt [8], the general solution of a rotating disc is

$$u = -\frac{(1-\upsilon^2)}{8E}\rho r^3\omega^2 + N_1 r + \frac{1}{r}N_2 \qquad [5.3\text{-}1]$$

where u [mm] is the radial displacement in the radial direction at an arbitrary radius, r [mm], where $a \le r \le b$. Also, ρ is the density [$\frac{\text{N-s}^2}{\text{mm}^4}$ or $\frac{\text{lbf-s}^2}{\text{in}^4}$], ω is the angular velocity [rad/s], N_1 and N_2 are constants.

When solving for the boundary conditions, the inner radius of the sawblade is considered to be fixed. Furthermore, due to the fixed inner radius in Figure 5.20, Equation 5.3-1 equals 0 mm displacement at $r = a$. Using these boundary conditions in Equation 5.3-1, we can solve for constant N_1 in terms of N_2, which yields

$$N_1 = \frac{(1-\upsilon^2)}{8E}\rho a^2\omega^2 - \frac{1}{a^2}N_2 \qquad [5.3\text{-}2]$$

Because we need two equations to solve for the two unknown constants N_1 and N_2, we use the outer radius natural boundary condition in Figure 5.20 at radius *b*. Due to *r* = *b* being a free edge, there is no material to pull outwardly from the centrifugal force effect on the outer edge, therefore at *r* = *b* the radial stress, $\sigma_{rr} = 0$. Hence, there is no radial force on the edge, so the fibers are not stretched in the radial direction. Therefore, the radial stress $\sigma_{rr} = 0$ at *r* = *b* in Figure 5.20. Now, we can solve for the radial stress, σ_{rr} using these conditions in the equation:

$$\sigma_{rr} = \frac{E}{1-\upsilon^2}\left[-\frac{(3+\upsilon)(1+\upsilon^2)}{8E}\rho r^2\omega^2 + (1+\upsilon)N_1 - \frac{(1-\upsilon)}{r^2}N_2\right] \qquad [5.3\text{-}3]$$

Next, by setting $\sigma_{rr} = 0$, dividing Equation 5.3-3 by $E/(1-\nu^2)$ and solving for N_2, we obtain

$$N_2 = \frac{\frac{-\rho b^2\omega^2}{8E}\left[(3+\upsilon)(1-\upsilon^2)\right] + \frac{\rho a^2\omega^2}{8E}\left[(1+\upsilon)(1-\upsilon^2)\right]}{\frac{(1+\upsilon)}{a^2} + \frac{(1-\upsilon)}{b^2}} \qquad [5.3\text{-}4]$$

Substituting Equation 5.3-4 into Equation 5.3-2, we obtain an expression for the constant N_1, which yields

$$N_1 = \frac{(1-\upsilon^2)}{8E}\rho a^2\omega^2 - \frac{1}{a^2}\left[\frac{\frac{\rho b^2\omega^2}{8E}\left[-(3+\upsilon)(1-\upsilon^2)\right] + \frac{\rho a^2\omega^2}{8E}\left[(1+\upsilon)(1-\upsilon^2)\right]}{\frac{(1+\upsilon)}{a^2} + \frac{(1-\upsilon)}{b^2}}\right] \qquad [5.3\text{-}5]$$

Using the criteria of $\sigma_{rr} = 0$ at $r = b$ and $u = 0$ at $r = a$, we have solved for N_1 and N_2 using Equations 5.3-1 and 5.3-3. Using N_1 and N_2 we can solve for the tangential stress, $\sigma_{\theta\theta}$,

$$\sigma_{\theta\theta} = \frac{E}{1-\upsilon^2}\left[-\frac{(1+3\upsilon)(1-\upsilon^2)}{8E}\rho r^2\omega^2 + (1+\upsilon)N_1 + \frac{(1-\upsilon)}{r^2}N_2\right] \qquad [5.3\text{-}6]$$

5.3.1 *Axisymmetric Model of Annulus with Fixed Inner BC Simulating the Saw Collar*

Boundary Conditions and Rotational Body Forces. For the axisymmetric model of the annulus with an infinitely stiff inner boundary condition, the results were obtained using the following boundary conditions and parameters. The boundary conditions are seen in Table 5-2 for the annulus in Figure 5.21. The boundary conditions used for the annulus with an inner radius were much the same as the boundary conditions used for the annulus with no inner radius in section 5.2. For example, the model was only half the thickness (1.7018 mm) of the annulus represented (3.4036 mm). The annulus had inner radius and outer radius dimensions of 57.15 mm (4.5-in) and 228.6 mm (9-in), respectively. All loading and geometry was symmetric about the center line through the thickness of the annulus.

Therefore, to keep all elements on this center line, a y-symmetric boundary condition was used along the entire bottom line. An extra boundary condition was applied to the left line of the axisymmetric model, which represented the stiff saw machine collar's attachment point to the annulus. This left line represents the inner radius of the annulus. For instance, the boundary condition on this left line was x-symmetric meaning that the left line (or inner radius) could not move off its original position before or after rotational forces are applied. Again, the rotational body forces were applied to the whole model at a rotation of 222.222 rad/s (10,000 sfpm).

Table 5-2 Boundary conditions of annulus with saw collar boundary condition.

Region	Boundary Condition
Left Line	xsymm U1 = UR2 = UR3 = 0
Whole Bottom line	ysymm U2 = UR1 = UR3 = 0

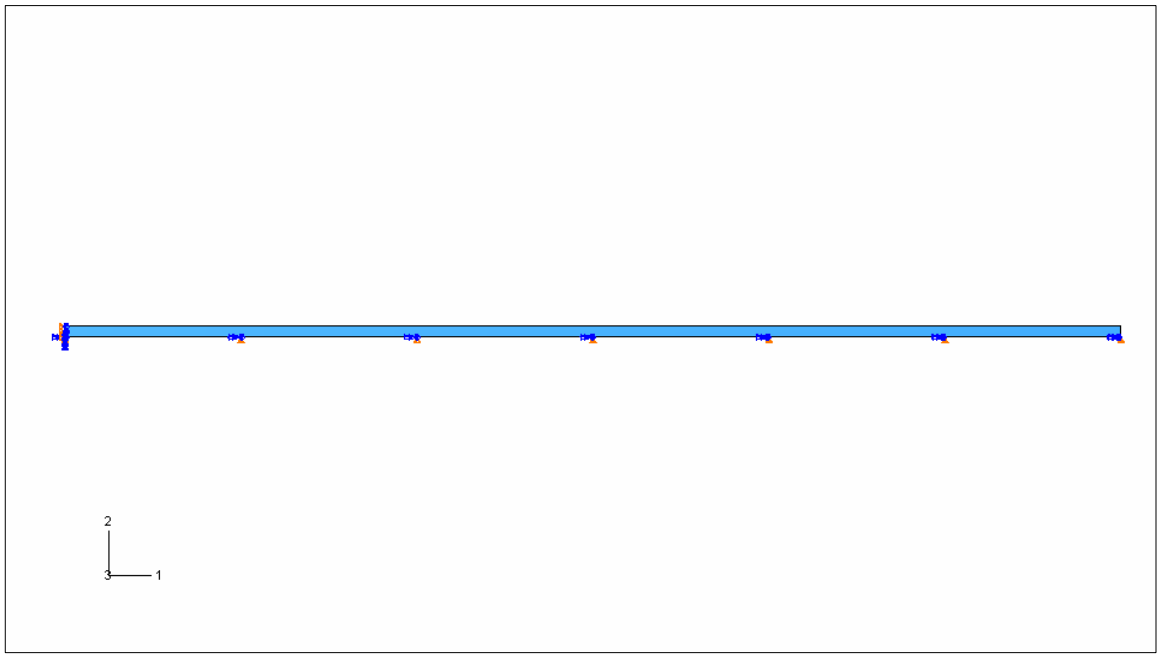

Figure 5.21 Boundary conditions of annulus with saw collar boundary condition representing the saw collar.

Radial Displacement. The radial displacement results are shown in Figure 5.22. Here it can be seen that the annulus displaces radially outward (to the right in picture) from the rotational forces. The inner radius displaces zero because the inner radius has a fixed boundary condition. The elements used to analyze this axisymmetric model are 8-node quadratic, quadrilateral axisymmetric elements (ABAQUS designation CAXR8). Because the axisymmetric model is a rectangle and gives rise to an easy square mesh, the meshing scheme used produced an aspect ratio near one to one. The maximum radial displacement converged to less than 0.001 percent from a model with 3624 elements to a model with 4935 elements. The maximum radial displacement is 0.003393 mm (1.336E-4-in) and is located at the outer radius.

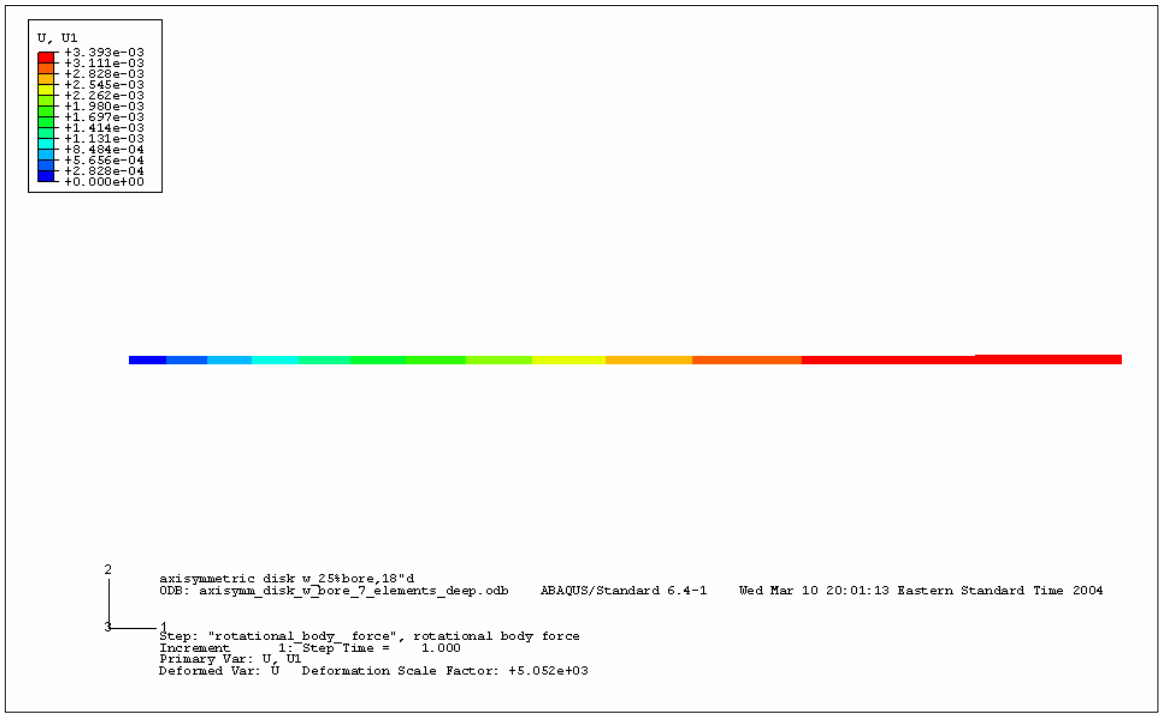

Figure 5.22 Radial displacement, U1, of annulus with infinite stiffness inner radius boundary condition (inner radius is at left line). Annulus dimensions for the inner radius and outer radius are 57.15 mm (4.5-in) and 228.6 mm (9-in), respectively.

Radial Stress. The radial displacement is accompanied by a radial stress. The maximum radial stress area is shown in Figure 5.23. The distribution is shown in a few paragraphs where the computer model results are compared to the known hand calculations for an annulus with fixed inner radius. The maximum radial stress of 11.80 MPa converged to less than 0.001 percent between 4935 elements and 3624 elements. The maximum radial stress is located at the inner radius. Because of the fixed displacement boundary condition at the inner radius, the rotational body force from the annulus pulls strongest at the inner radius. This inner radius carries all the centrifugal force from the whole annulus and the inner radius has to hold the annulus from stretching outward.

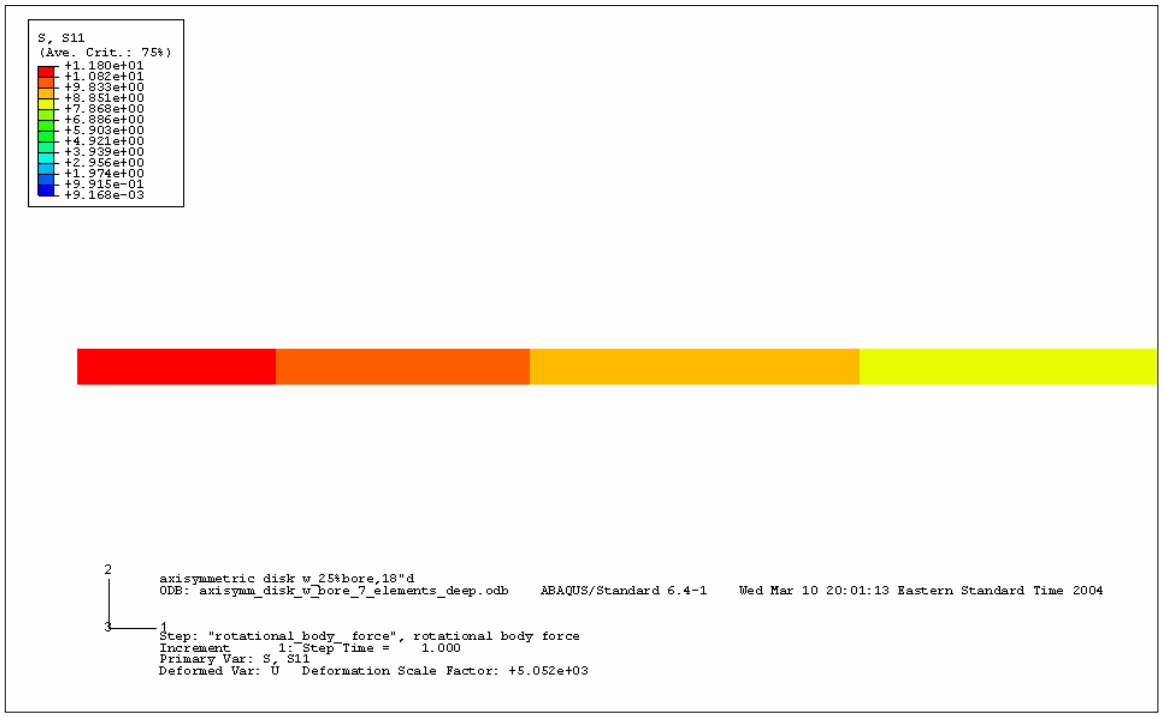

Figure 5.23 Radial stress (S11) of an annulus with inner infinite radius boundary condition. Maximum radial stress is at inner radius (shown here).

Tangential Stress. Because the inner radius is fixed and cannot stretch in the radial direction, the tangential stress at the inner radius is not the location of the maximum tangential stress as in the case with no inner radial boundary condition. Because the tangential strain, $\varepsilon_\theta = u/r$ at the inner radius where the displacement in the radial direction, $u_r = 0$ (because the arc length does not change), results in low tangential stress.

Since the saw collar stiffness is much higher than the blade stiffness in the radial and tangential directions, the blade is not allowed to deform. Therefore, no deformation results as no stress at the inner radius of the sawblade.

The maximum tangential stress is located near the inner radius at a location 110.9 mm from the geometric center of the annulus (or 53.75 mm from the inner radius). This location is the point of highest displacement of an element in the radial direction. Therefore, this is also where the highest tangential stress is located.

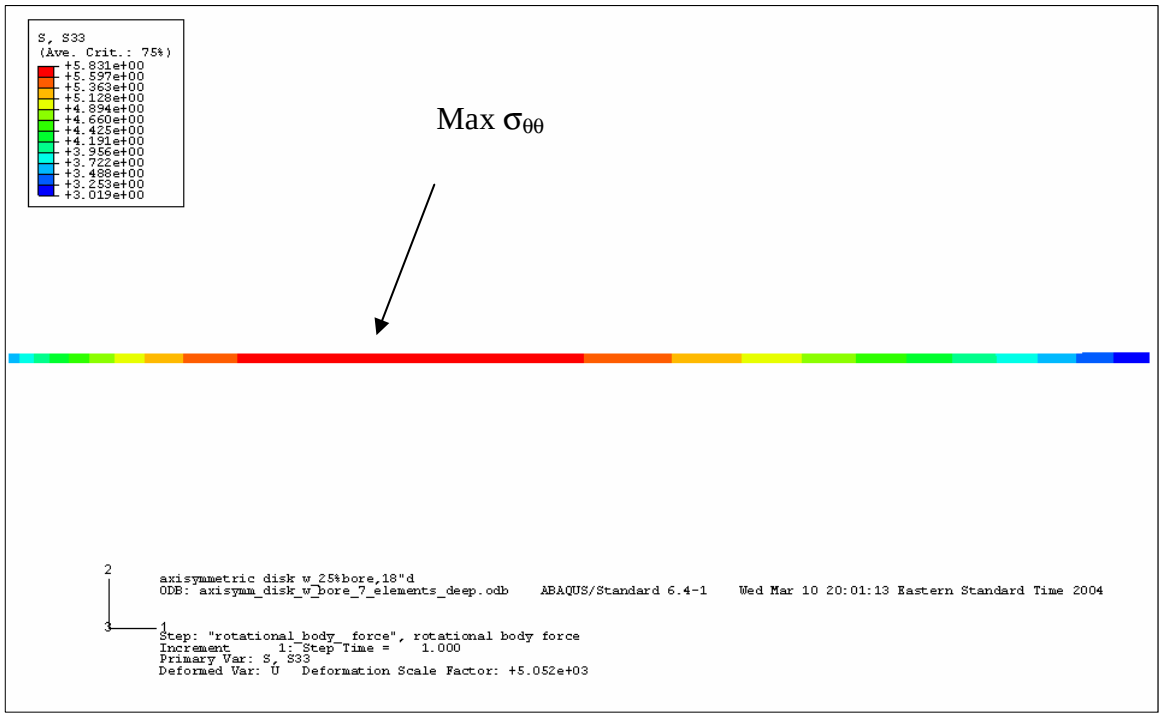

Figure 5.24 Tangential stress (S33 for axisymmetric models) of an annulus with an inner infinite radius boundary condition. Maximum tangential stress is located at 110.9 mm (4.37-in) radially from geometric center.

Comparison of Axisymmetric Model with Hand Calculations. These axisymmetric model results were quite accurate with a high signal-to-noise ratio. This is seen in Table 5-3. When comparing the results of the axisymmetric model with an infinite stiffness inner radius boundary condition to the hand calculations, the results are nearly the same. These values show the closeness of the axisymmetric model to the hand calculations using equations 5.3-1, 5.3-3, and 5.3-6. As seen in Figure 5.25 and Figure 5.26, the graphs are unable to distinguish the difference between the hand calculations and the finite element analysis results.

Table 5-3 Statistical comparison of axisymmetric computer model versus hand calculations.

		Maximum Error, (mm or MPa)	Standard Deviation, (mm or MPa)	Signal-to-Noise Ratio
Axisymmetric	u_r	-7.55E-08	1.63E-08	208,000
	σ_{rr}	1.06E-04	3.06E-04	38,700
	$\sigma_{\theta\theta}$	8.55E-05	2.65E-04	22,000

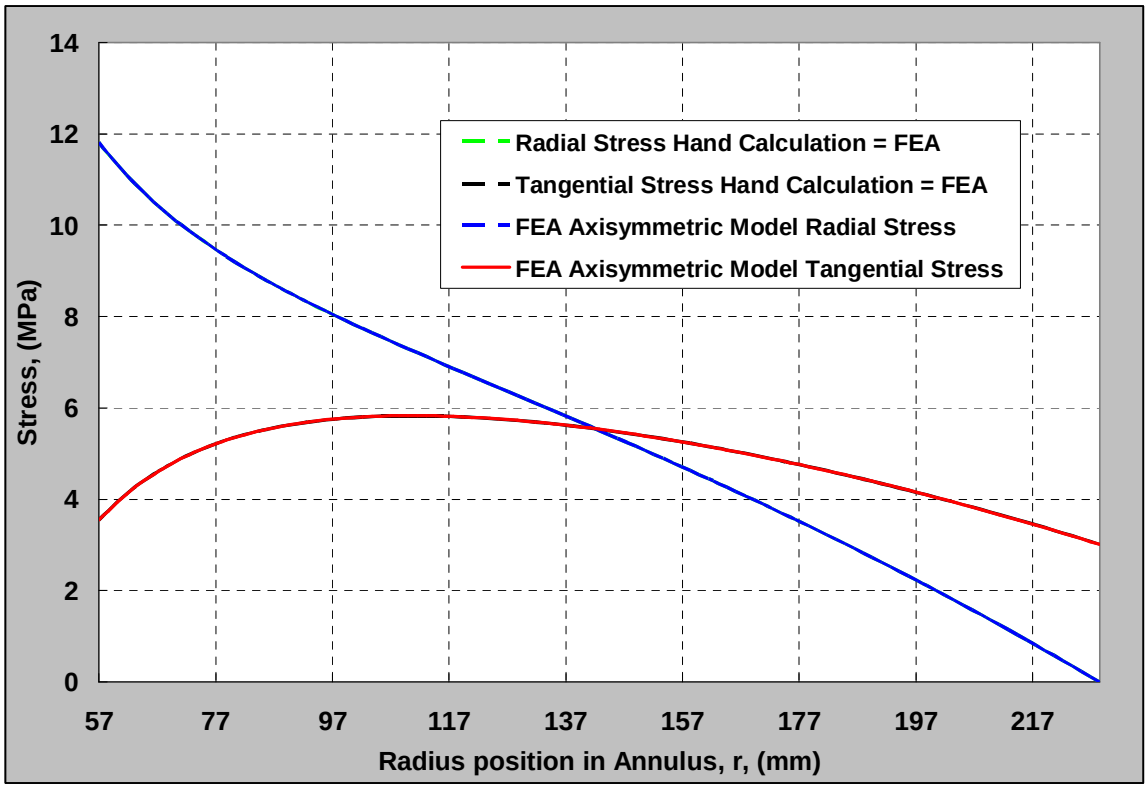

Figure 5.25 Shows the radial and tangential stress in a 9-in (228.6 mm) radius axisymmetric model annulus with inner radius of 2.25 inches (57.15 mm). The inner radius boundary condition is fixed (infinite stiffness). Both computer model and hand calculation results are shown. Further, the angular velocity is 222.222 rad/s (10,000 sfpm). The computer model results follow closely to the calculated results. In fact, the two agree almost exactly for the tangential stress. The tangential stress and radial stress are equal at 142.9 mm.

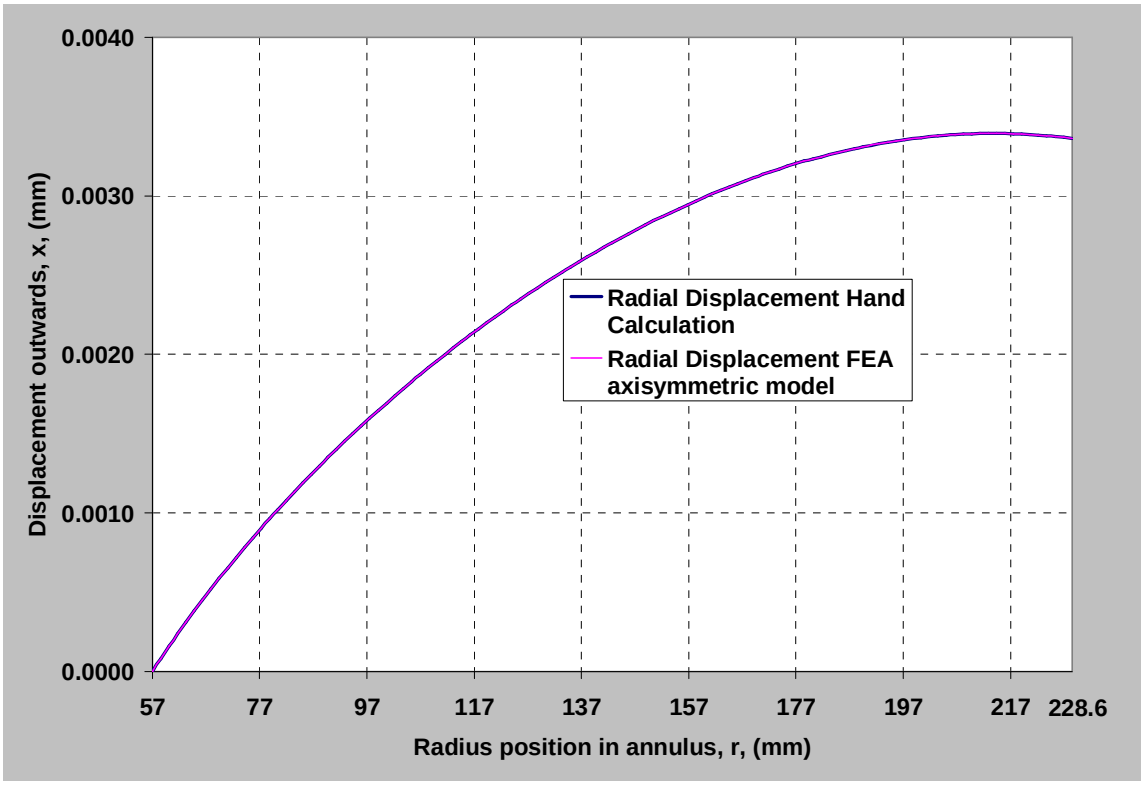

Figure 5.26 Hand calculations compared to the axisymmetric model results for radial displacement. The radial displacement of a 9-in (228.6 mm) radius annulus with an inner radius of 2.25 inches (57.15 mm) and having a saw collar boundary condition. Further, the angular velocity is 222.222 rad/s (10,000 sfpm).

When analyzing the results of the annulus with a prescribed displacement of zero due to a practically infinite saw collar stiffness at the inner radius, the radial stress is highest at the inner radius. At the inner radius of this annulus, the entire effect of the rotational body force is reacted by the inner radius displacement boundary condition. The radial stress is highest at this point. At the outer radius, the radial stress is zero because of the natural boundary condition having surface tractions of zero in the normal direction. In other words, the outermost element is not affected by the centrifugal force from an element radially outward because it is the last element radially on the annulus. Therefore, there is no force – thereby producing no radial stress on the outermost elements around the circumference.

The radial displacement is also affected by the radial force natural boundary condition. This is seen in Figure 5.26 as the curve seems to plateau near the outer radius. Because there is less radial load near the outer edge due to less mass, the radial displacement begins to decrease in value near the outer edge.

5.3.2 *Three-Dimensional Model of Annulus with Fixed Inner BC Simulating the Saw Collar*

Boundary Conditions. The boundary conditions are shown in Figure 5.27, the extra boundary condition is shown in part (d) of this figure. The saw collar boundary condition is fixed in the U1=U2=0, and is applied to the entire inner face of the annulus, seen in (d).

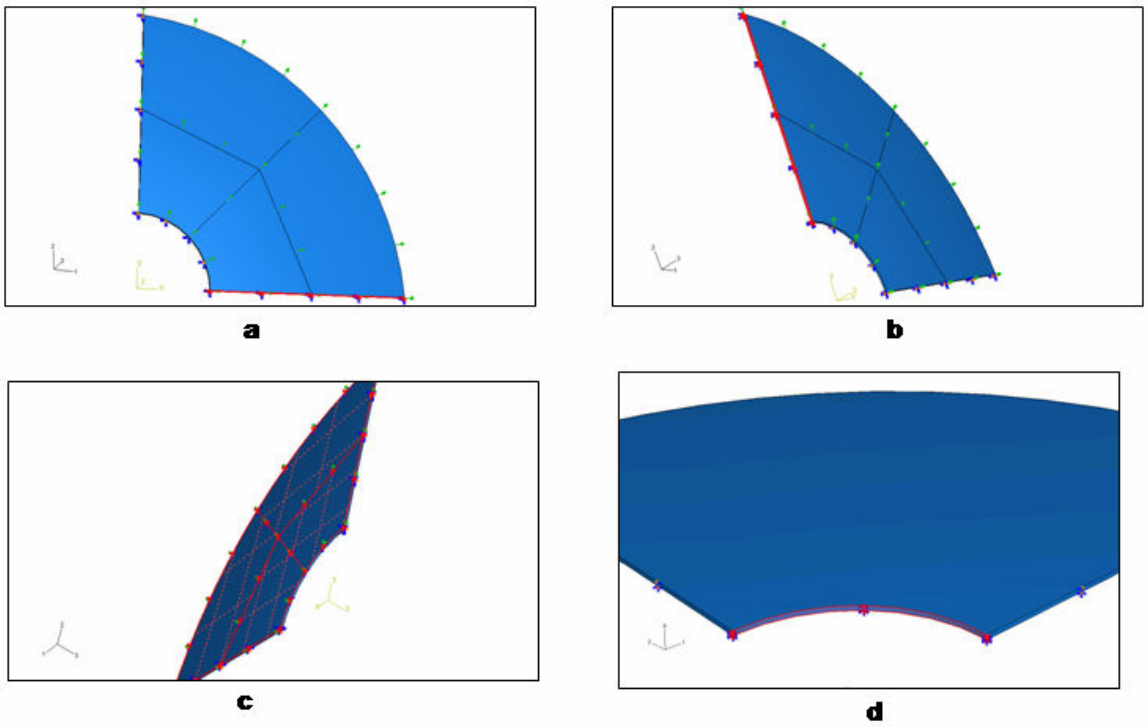

Figure 5.27 Boundary conditions for the three-dimensional eighth-model half thickness. (a) shows the placement of the lower face (red) with a boundary condition of y-symmetric. (b) shows the placement of the left face (red) with a boundary condition of x-symmetric. (c) shows an upside down view of the annuls with a boudary condition of z-symmetric on the bottom face (red). (d) shows the inner radius face boundary condition where U1=U2=0=UR1=UR2=UR3=0 (red). The partitioning scheme is also shown as lines on the face in (a). These lines go all the way through the part.

The boundary condition due to the saw collar gives the sawblade some added stiffness in the axial, radial and tangential direction relative to a sawblade with no clamp. The axial stiffness increase can be thought of as the saw collar holding the blade in one place axially on the saw arbor. Also, the increased stiffness in the radial direction is due to the collar keeping the sawblade centered on the saw arbor and not allowing the sawblade to be pushed off center by the force of the wood that passes around the sawblade during cutting. Furthermore, the tangential stiffness increase is due to the fact that the saw collar must hold the sawblade in the tangential direction to impart a torque

causing the sawblade to spin. The stiffness of the collar also holds the sawblade from expanding radially outward at the interface of the collar and the sawblade. Thus, with no slippage allowed between the saw collar and the sawblade (due to the fast onset of excess heat from friction that ruins a sawblade), the saw collar is best represented as a fixed boundary condition where the saw collars' outer radius meets the sawblade. This has similar effects as "cantilevered" boundary condition.

The results for radial displacement of the three-dimensional annulus with saw collar boundary condition on the face can be seen in Figure 5.28. The maximum displacement of the three-dimensional model is 0.003393 mm (1.336E-04-in) located at the outer rim of the annulus. Also, to see if the applied boundary conditions are applied correctly, the inner face displacement is 0 mm.

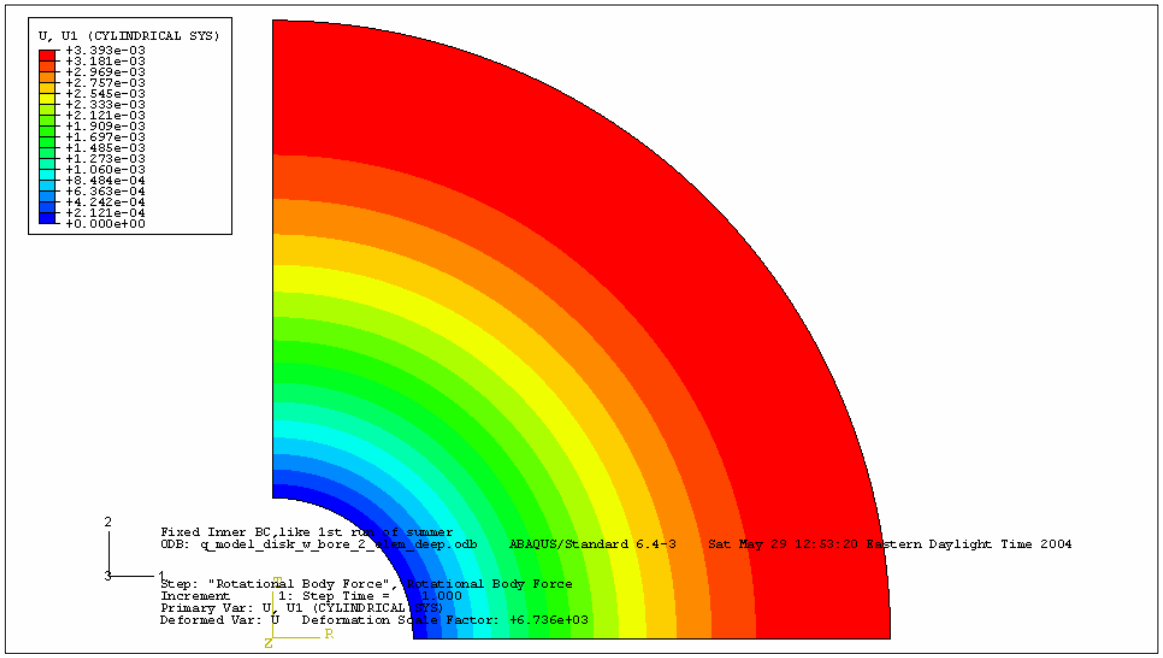

Figure 5.28 Radial displacement of annulus with saw collar boundary condition. The displacement is radially outward.

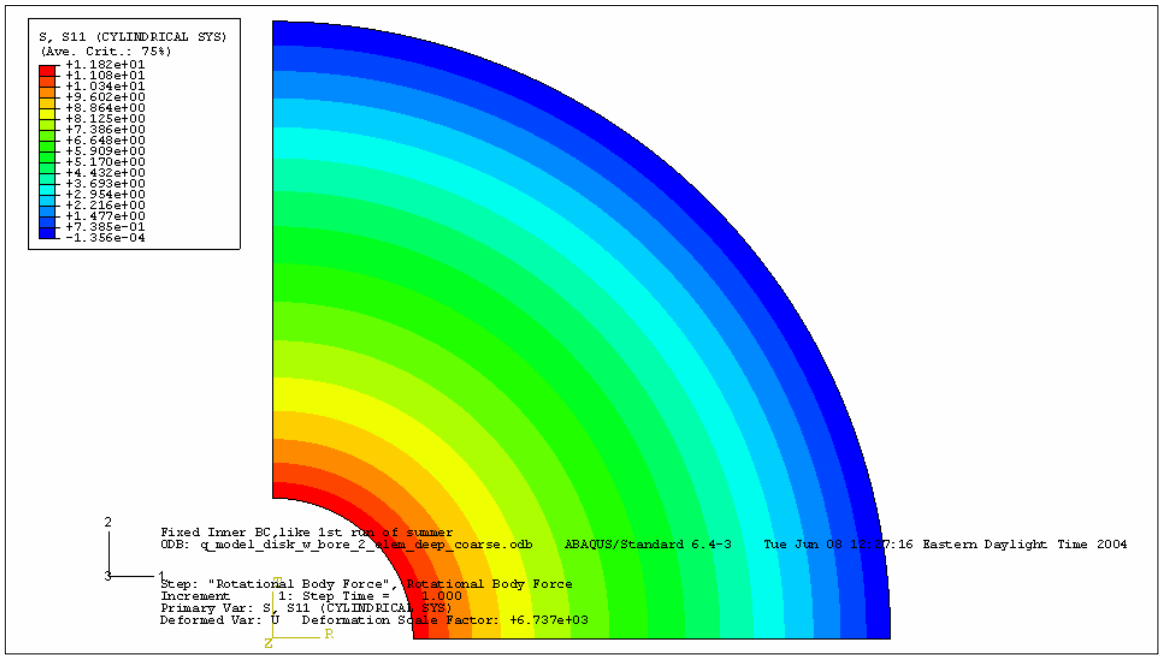

Figure 5.29 Radial stress (S11) of annulus with saw collar boundary condition. The maximum is at the inner radius.

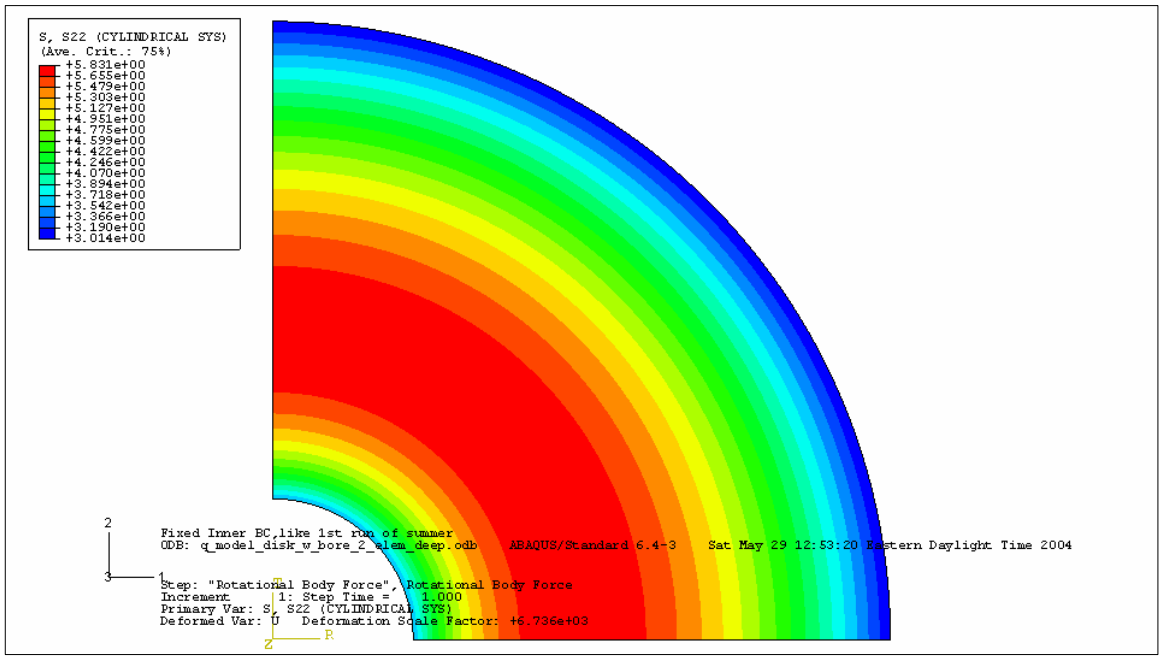

Figure 5.30 Tangential stress (S22 for three-dimensional models) of annulus with saw collar boundary condition. The maximum is located at 110.8 mm radially from the geometric center of the annulus.

The convergence of the three-dimensional one-eighth model with saw collar boundary condition is seen in Figure 5.31. The model showed excellent convergence with less than 0.01 percent difference between the last meshes.

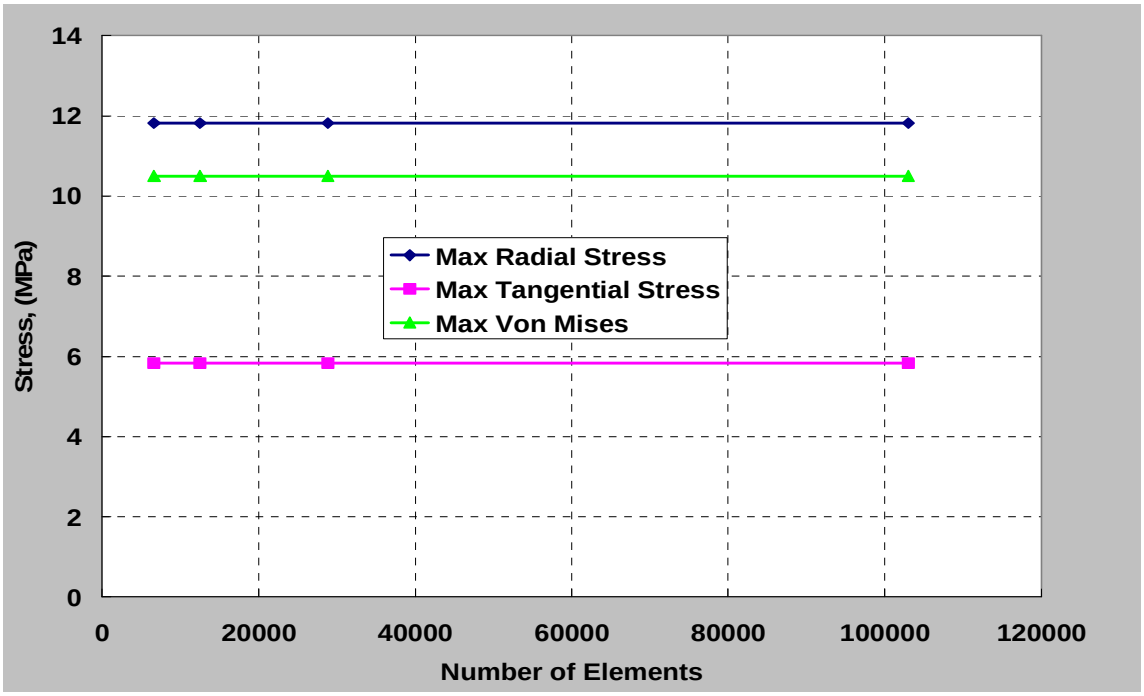

Figure 5.31 Convergence of 18-in annulus with 25 percent bore and saw collar boundary condition.

Comparison of Three-Dimensional Model to Hand Calculations. These final equations for u, σ_{rr}, and $\sigma_{\theta\theta}$, Equations 5.3-1, 5.3-3, and 5.3-6, respectively, are compared to the results obtained from the model are seen in Figure 5.32 and Figure 5.33. The difference between the hand calculations and the thee-dimensional model results are so close they are imperceptible on the graph. Table 5-4 shows the strong agreement of the models to the accepted hand calculations.

Table 5-4 Statistical comparison of three-dimensional model to hand calculations.

		Maximum Error, (mm or Mpa)	Standard Deviation	Signal-to-Noise Ratio
3-D Model	u_r	-7.57E-08	0.0002554	209500
	σ_{rr}	6.9 E-05	0.0003064	38600
	$\sigma_{\theta\theta}$	1.36E-04	1.62E-08	22800

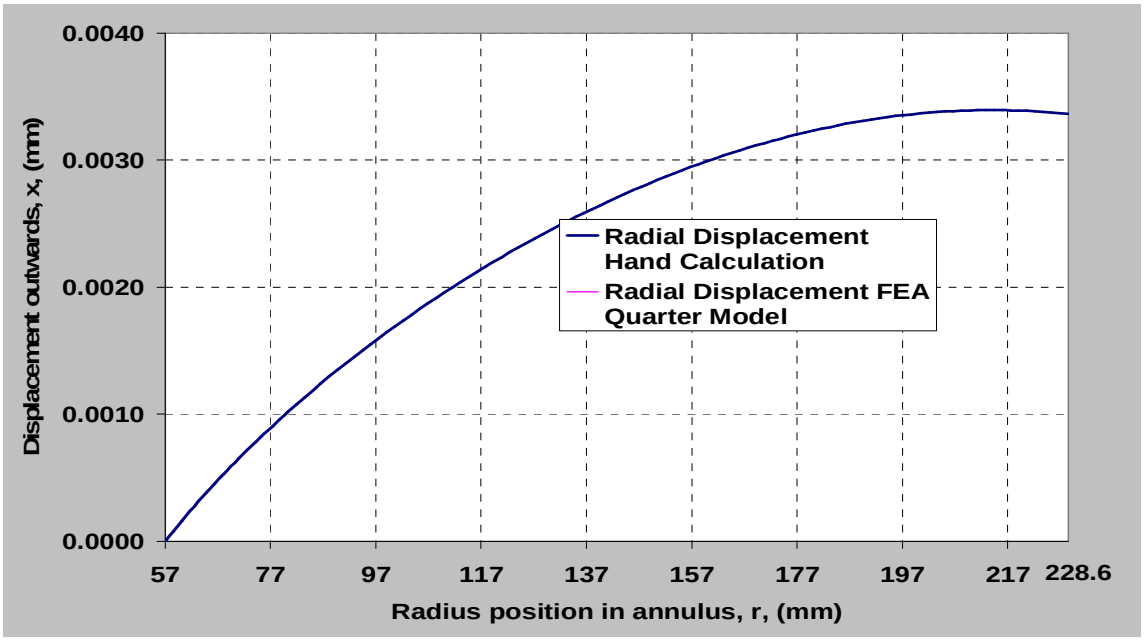

Figure 5.32 Hand calculations compared to eighth-model results for radial displacement. Shows the displacement of a 9-in (228.6 mm) radius annulus with an inner radius of 2.25 inches (57.15 mm) and having a saw collar boundary condition. The angular velocity is 222.222 rad/s (10,000 sfpm).

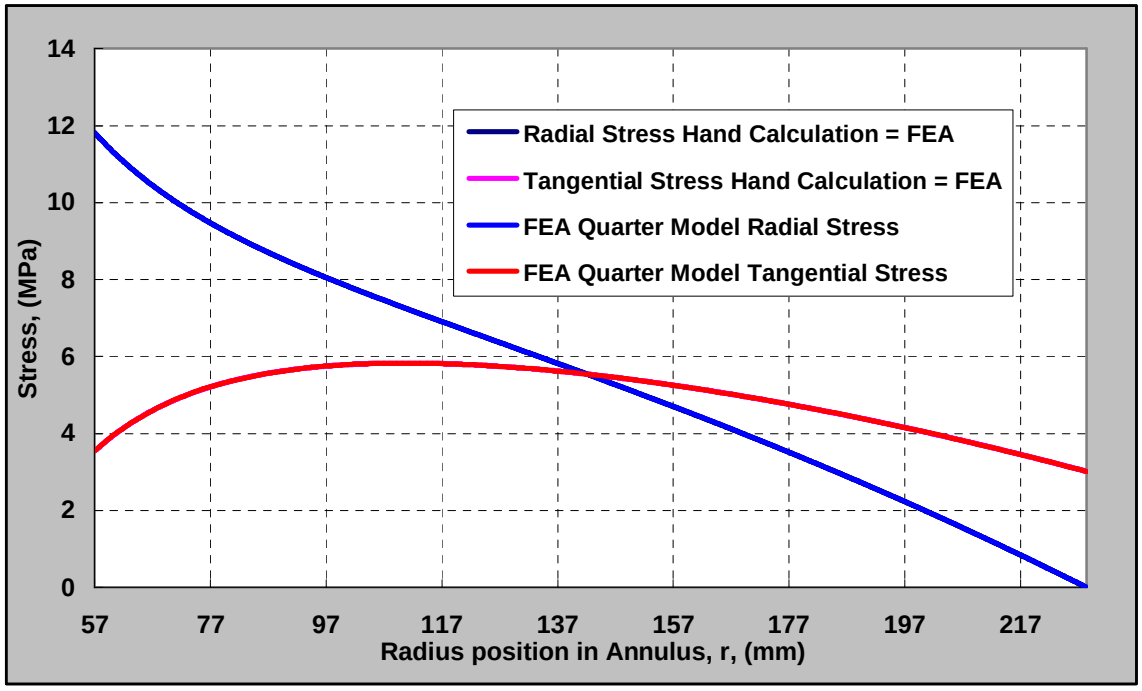

Figure 5.33 Shows the radial and tangential stress in a 9-in (228.6 mm) radius eighth-model annulus with inner radius of 2.25 inches (57.15 mm) and having a saw collar boundary condition. The angular velocity is 222.222 rad/s (10,000 sfpm). The computer model results follow closely to the calculated results. In fact, the two agree almost exactly for the tangential stress. The tangential stress and radial stress are equal at 142.9 mm.

5.4 *Annulus with Infinite Inner BC Compared to Annulus with no Inner BC*

As stated earlier, the finite element models are approaching a representative mounting of the sawblade on the saw machine. The real sawblade mounting boundary conditions lie somewhere in the range between the two curves seen in Figure 5.34 and Figure 5.35. The upper and lower limits are set by the two curves on each of these two graphs and the area between the two curves represents all the possibilities of the real world boundary condition on the modeled spinning annulus. The fact that the sawblade is being driven by the torque imparted by the collar and the sawblade cannot slip within the stiff collar gives rise for us to assume that the sawblade's inner boundary condition behaves more closely to the spinning disc with a fixed boundary condition.

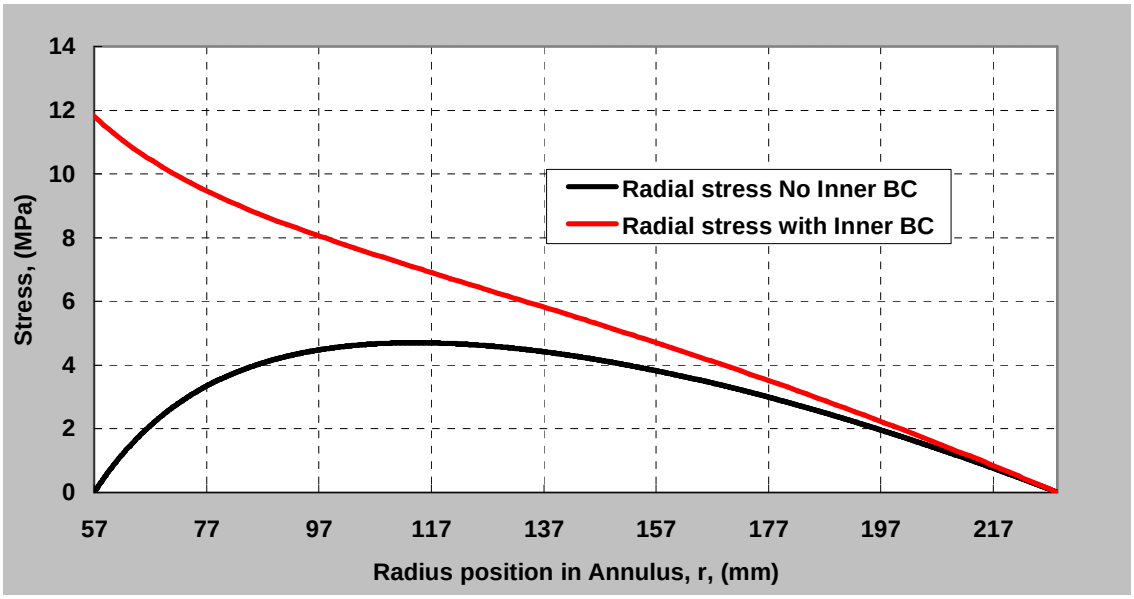

Figure 5.34 Compares the radial stress of a spinning disc with 25 percent bore and 228 mm (9-in) radius with and without an inner boundary condition. One disc has a saw collar boundary condition and the other has a free boundary condition at the inner radius of 57.15 mm (2.25-in).

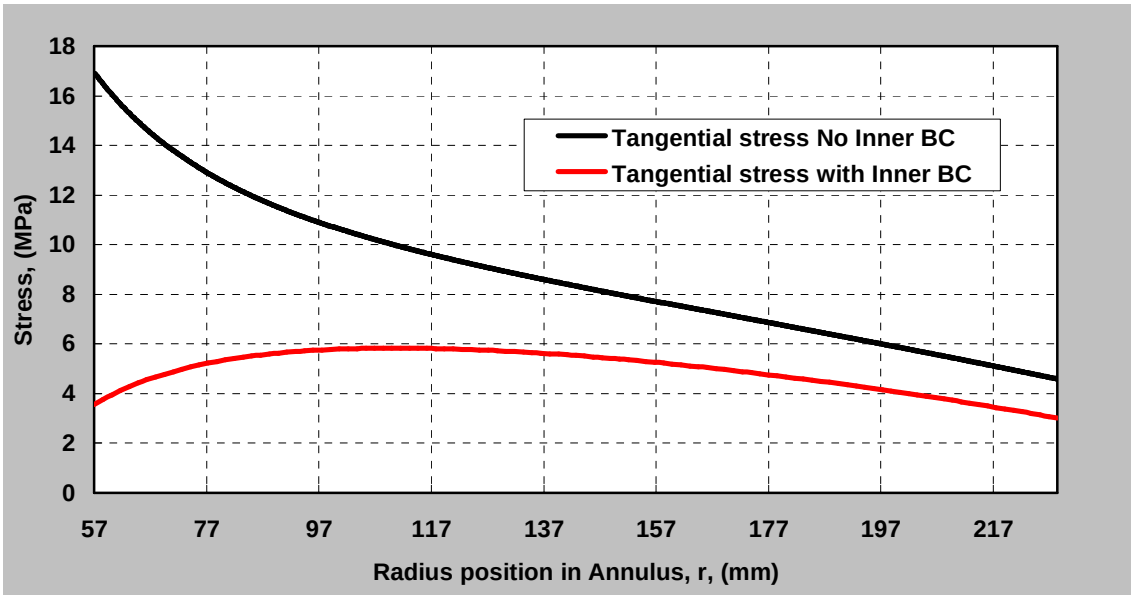

Figure 5.35 Compares the tangential stress of a spinning disc with 25 percent bore and 228 mm (9-in) radius with and without an inner boundary condition. One disc has a saw collar boundary condition and the other has a free boundary condition at the inner radius of 57.15 mm (2.25-in).

Chapter 6

Stress Due to Rotational Forces Only in Standard Sawblade without Expansion Slots

6.1 *Standard Sawblade without Carbide Tips*

Following the spinning annulus, the next step in building the sawblade in our analysis is to create a model that has the exact dimensions of the sawblade we intend to analyze. Like the last annulus case, the inner boundary condition of the standard sawblade is fixed – representing the clamping of the saw collar.

Cases of the spinning standard sawbody without carbide saw tips and no expansion slots were analyzed and compared to the spinning annulus case. Then, the carbide saw tips were added to the standard sawbody and compared to the case without carbide saw tips. These boundary conditions for the sawbody can be seen in Figure 6.1.

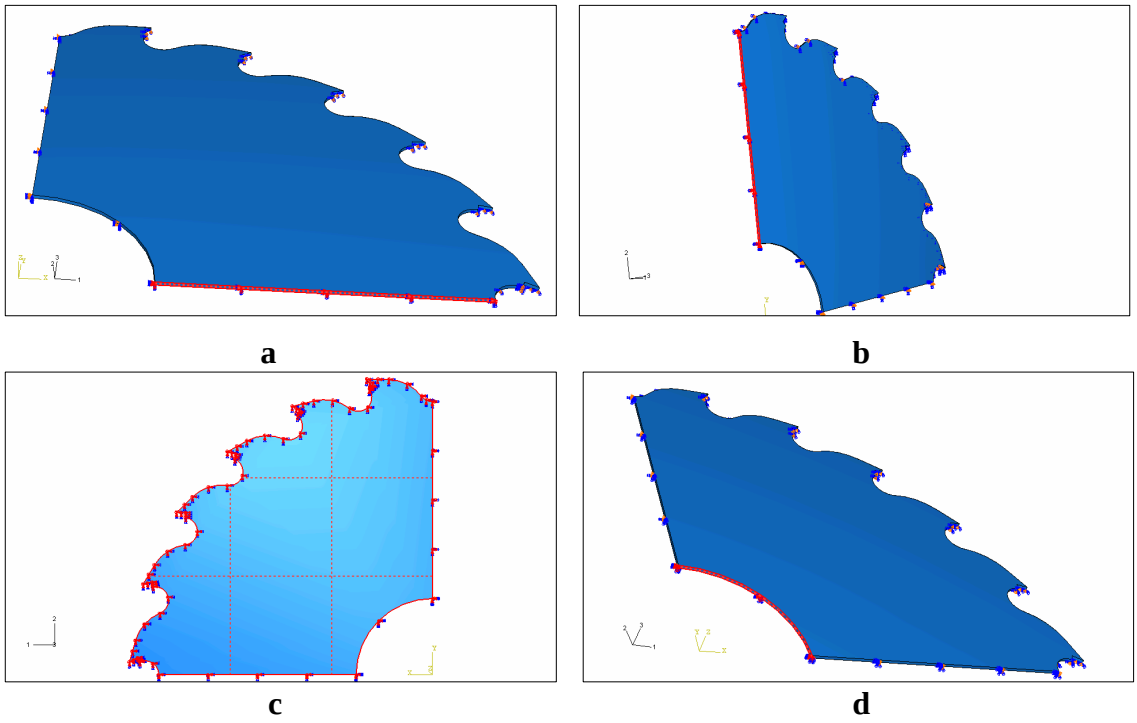

Figure 6.1 Boundary conditions for the three-dimensional eighth-model standard sawblade without tips (half thickness). (a) shows the placement of the lower face (red) with a boundary condition of y-symmetric. (b) shows the placement of the left face (red) with a boundary condition of x-symmetric. (c) shows an upside down view of the annuls with a boudary condition of z-symmetric on the bottom face (red). (d) shows the inner radius face boundary condition where U1=U2=0=UR1=UR2=UR3=0 (red).

Results of Spinning Standard Sawblade. Comparing the spinning standard sawbody to the spinning annulus was done to see if the results of the sawbody were consistent with the results seen in the spinning annulus case. Looking for large deviations between the two cases and finding none that were unjustifiable gave good reasoning to believe the sawblade was analyzed correctly. Table 6-1 shows the comparison between these two cases. The large percent difference between the tangential displacements of these two cases is due the gullets allowing for much larger tangential displacements at the outer rim. Because the gullets have no material they cannot carry any loads, and therefore cannot keep the material that is left on the outer rim from growing more in the tangential direction. The added tangential stress seen in the sawbody case is due to this same phenomenon – there is less material to carry the load, and therefore higher stresses are developed.

Table 6-1 Comparison of maximum results of annulus and standard sawblade without carbide saw tips.

Maximum (converged values)	Annulus (saw collar BC)	Standard Sawblade (No Tips)	%Difference
Radial Displacement, U1, (mm)	0.00339	0.00307	-9.3
Tangential Displacement, U2, (mm)	0.0000382	0.000356	-1032
Axial Displacement, U3, (mm)	-0.0000764	-0.0000694	-9.2
Radial Stress, S11, (MPa)	11.82	10.72	-9.3
Tangential Stress, S22, (MPa)	5.83	7.13	22.4
von Mises, S', (MPa)	10.5	9.53	-9.3

Also seen in Table 6-1, the axial displacement is actually showing half of the amount of the maximum contraction of the thickness of the sawbody. This is because only half of the sawbody was modeled due to the symmetry of the geometry. In other words, the maximum axial displacement shown in the table only accounts for the displacement a point on the inside surface of the sawblade moves toward the center of the sawbody. This contraction of the thickness is due to the to the Poisson's effects. As the sawbody expands outward, the thickness of the sawbody contracts due to radial and tangential loading that occurs. Therefore, the amount of contraction of the sawbody's whole thickness without tips is 0.0001388 mm (amount shown in Table 6-1). This

maximum contraction is located at the inner radius because the inner radius has the highest stress (both radial and von Mises).

Figure 6.2 shows the convergence of the maximum values of the radial, tangential and von Mises stresses found in our standard sawblade without tips. The percent difference for all stresses was less than 0.58 percent change from the last two meshes. These low percentages show proper convergence of the stresses in the model.

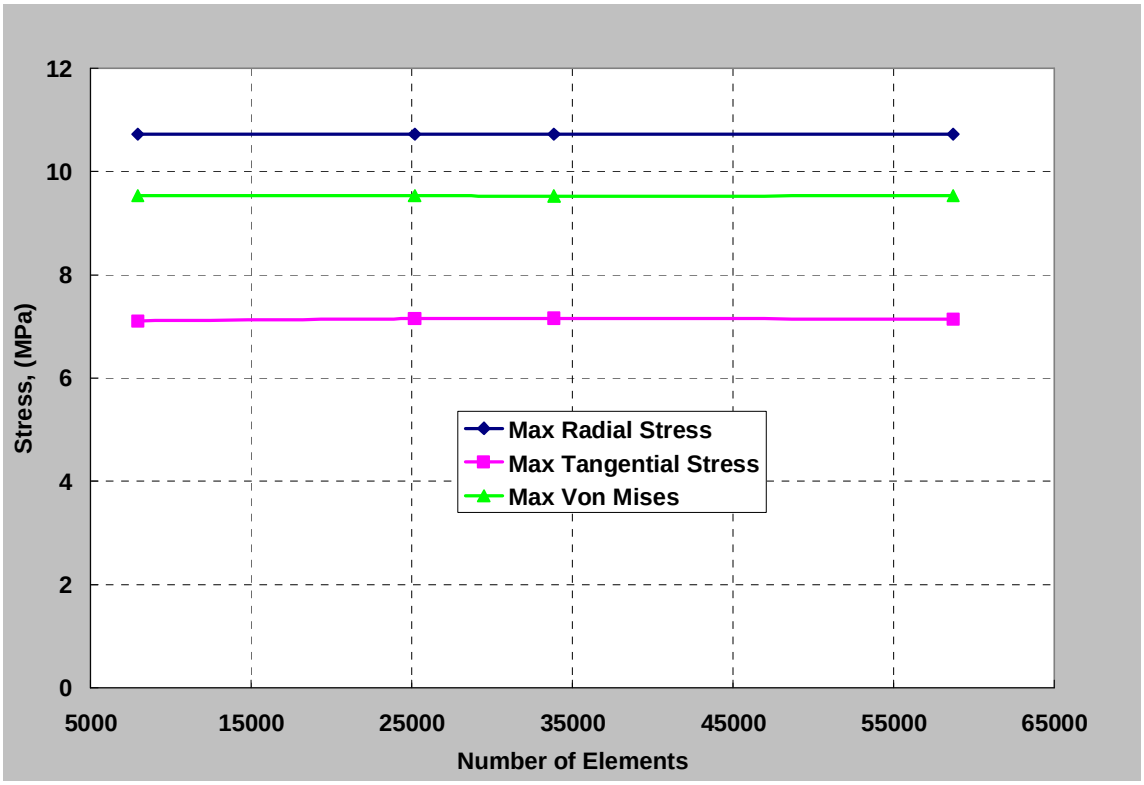

Figure 6.2 Converged values of maximum stresses of standard sawblade without tips.

Figure 6.3 shows the displacements radially and tangentially. As expected, the radial displacement gets higher the further away from the inner radius. The distribution of the radial displacement seen in a standard sawbody is much the same as that found in the spinning annulus with the same boundary conditions. In fact, using the spinning annulus to describe the radial stresses seen in a standard sawblade is a good first approximation.

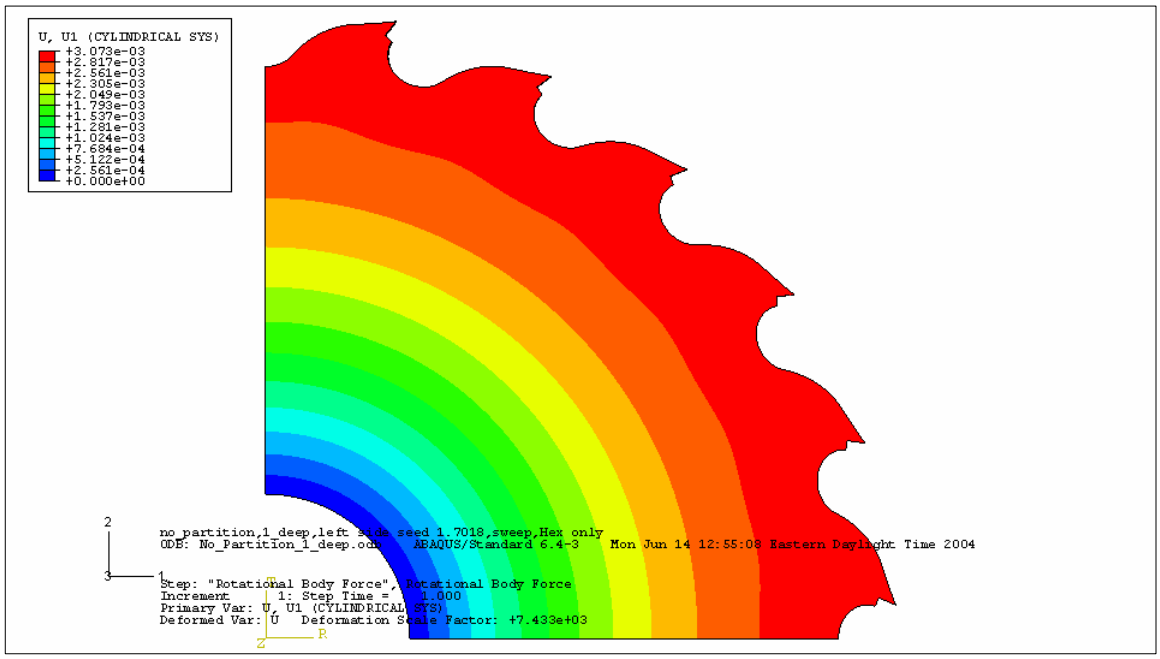

Figure 6.3 Radial displacement in a standard cut-off 18-in sawblade without carbide saw tips from centrifugal force effects. Maximum radial displacement of 0.00307 mm at outer radius (red). Minimum radial displacement of 0 mm at constrained, inner radius.

In Figure 6.4, we see the effects the gullets have on the tangential displacement. If one gullet, shoulder and tooth section is analyzed, an interesting phenomenon will occur. It will be seen that at the outer tip of the pocket (red), the tip of the sawbody displaces tangentially to the left (opposite the direction of rotation). Likewise, the back of the shoulder (blue) near the gullet will displace tangentially to the right (direction of rotation) as the sawblade is expanded radially due to the centrifugal force. In other words, the gullet, shoulder and tooth section will contract while the rest of the sawbody expands tangentially. Therefore, anytime the radius increases the circumference must also increase, which gives rise to tangential displacement within the sawbody.

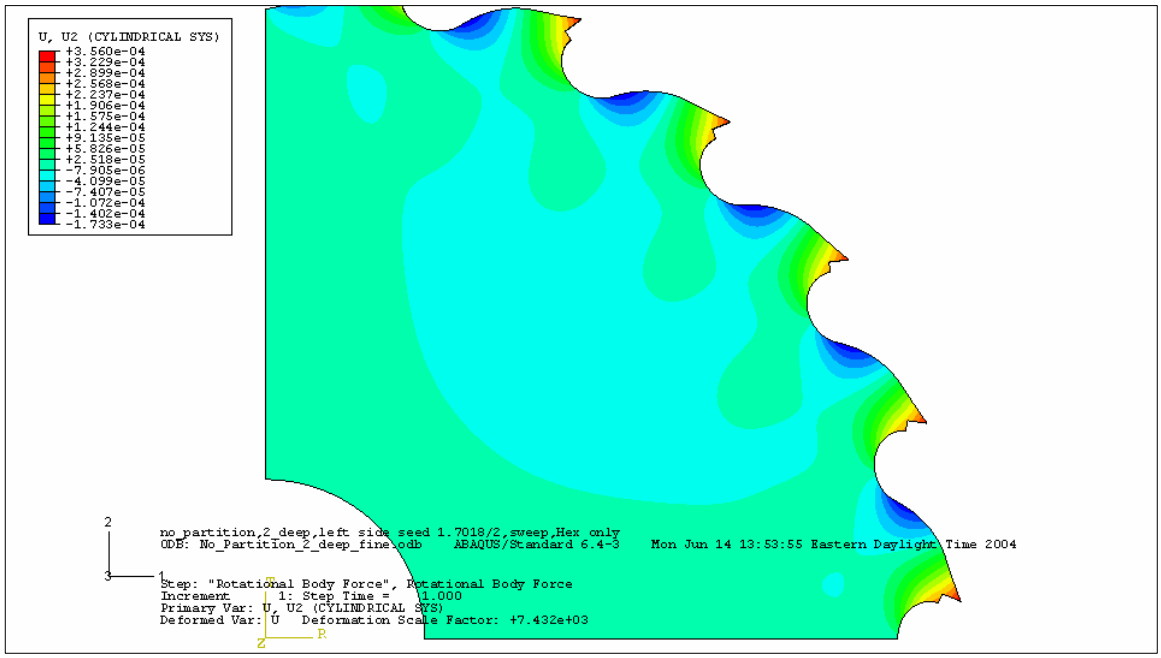

Figure 6.4 Tangential displacement in a standard cut-off 18-in 24 teeth sawblade from centrifugal force effects. Maximum of tangential displacement of 0.000356 mm (counterclockwise) is at tips. Minimum tangential displacement of -.0001733 mm (clockwise) is at back of shoulder.

The maximum radial stress, seen in Figure 6.5, is found at the inner radius because the material at the inner radius is constrained by the saw collar and has to hold back all the sawbody material's centrifugal force. As an arbitrary point moves from the inner radius to the outer radius of the sawbody, the radial stress gets lower.

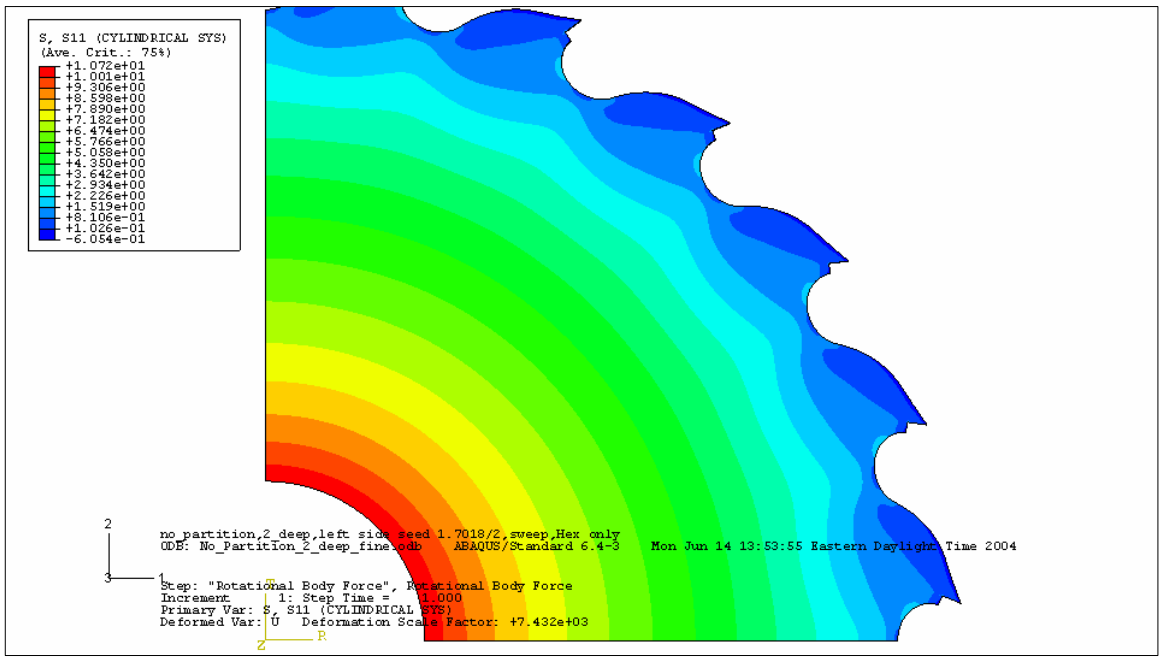

Figure 6.5 Distribution of radial stress from centrifugal force effects in sawbody without carbide saw tips. Maximum radial stress of 10.72 MPa is at inner radius.

The highest tangential stress is seen at the bottom of the gullets, as seen in Figure 6.6 and blown up in Figure 6.7. Thus, higher stresses are carried by the material at the bottom of the gullets. The shoulder and tooth area have plenty of material to withstand the stretching of the outer portion of the sawbody and therefore have lower tangential stresses.

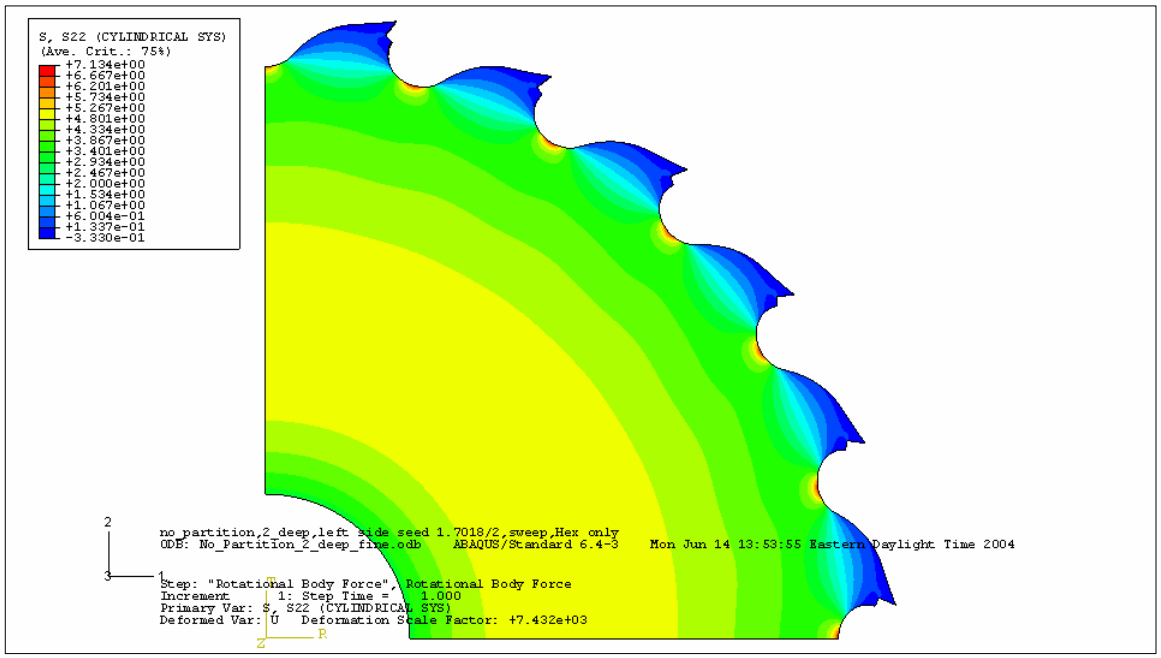

Figure 6.6 Distribution of tangential stress from centrifugal force effects in sawbody without carbide saw tips. Maximum tangential stress is 7.134 MPa (tensile) and at bottom of gullets (red). Minimum tangential stress is -.3330 MPa (compressive).

The tangential stress distribution at the maximum stress location is shown enlarged in Figure 6.7, where the smoothness of the distribution can be seen. We are concerned with the distribution of areas of abrupt changes in the stress patterns because they may lead us to believe that the finite element analysis has given incorrect information. However, this is not the case in Figure 6.7. Smooth transitions from the maximum to the minimum are seen and this level of change is acceptable for good results. For example, bad results would look like maximum and minimum stress very near each other with no reason for such an abrupt change.

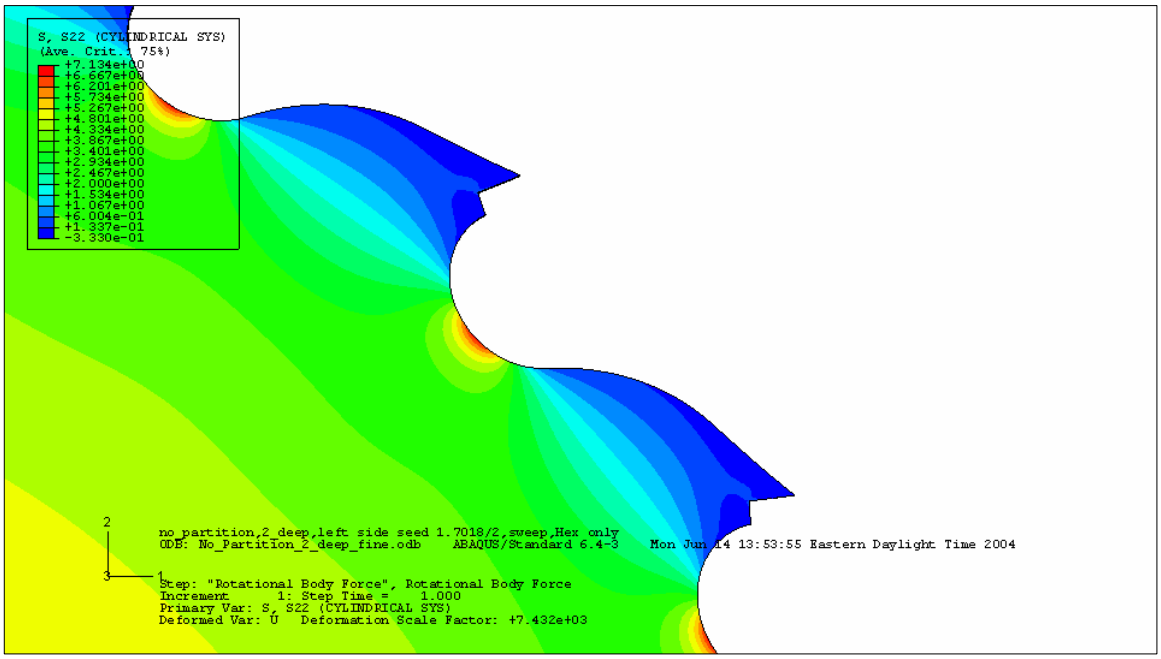

Figure 6.7 Zoomed in view of tangential stress at gullets and tips of sawbody without carbide saw tips.

The von Mises Stress. When analyzing stresses in ductile materials, we are concerned with one particular type of stress called the von Mises. The von Mises stress can be used to predict the onset of yielding for a ductile material, such as steel used to make the sawbody. The von Mises stress takes into account the stress in the x, y, and z directions as well as the shear in the xy, xz, and yz planes. The von Mises stress is an equivalent 1-D stress that is not dependent of the hydrostatic or average stress. Furthermore, when viewing the von Mises stress, the values are always positive. The von Mises, σ', is found using:

$$\sigma' = \frac{1}{\sqrt{2}}\left[\left(\sigma_x - \sigma_y\right)^2 + \left(\sigma_y - \sigma_z\right)^2 + \left(\sigma_z - \sigma_x\right)^2 + 6\left(\tau_{xy}{}^2 + \tau_{yz}{}^2 + \tau_{xz}{}^2\right)\right]^{\frac{1}{2}} \qquad [6.1\text{-}1]$$

where σ_x, σ_y, and σ_z are the normal stresses in the x, y and z directions, respectively. Also, τ_{xy}, τ_{yz}, and τ_{xz} are the shear stresses in the xy, yz and xz planes, respectively. The von Mises stress in the sawbody is seen in Figure 6.8.

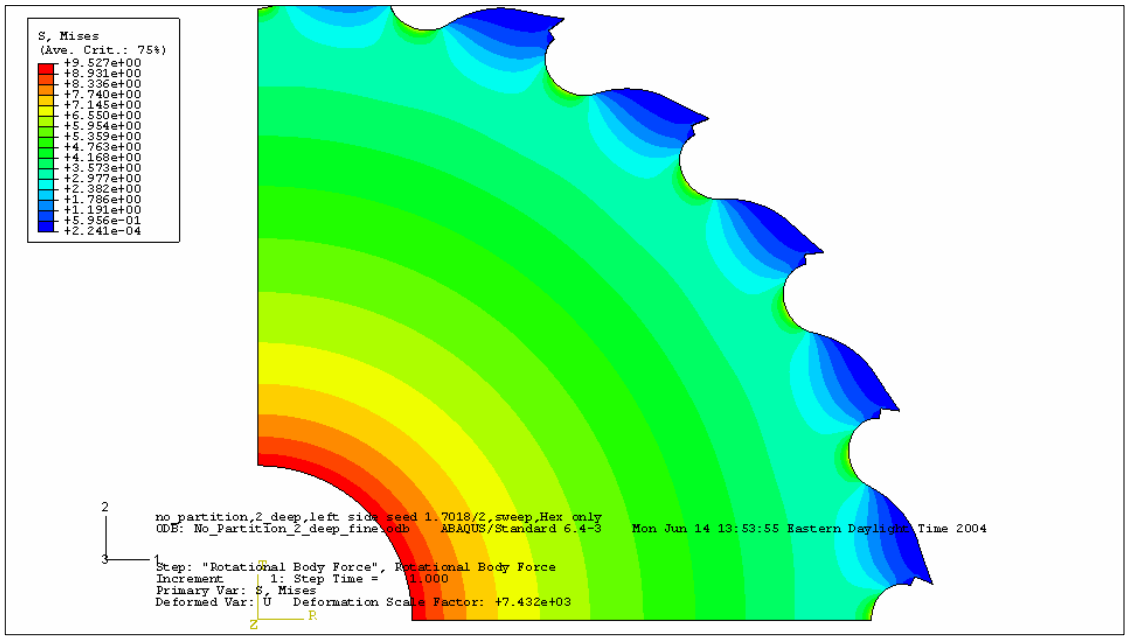

Figure 6.8 Distribution of von Misses stress from centrifugal force effects in sawbody without carbide saw tips.

6.2 *Standard Sawblade with Carbide Tips*

Next, we compared the stresses between a sawbody and a sawblade with carbide saw tips. These comparisons were done for two reasons: (1) to quantify the difference the added mass of the carbide had on the stresses of a spinning sawblade and (2) to have a check to be sure the added mass, differing densities and the tying of the carbide saw tips to the pockets of the sawblade were done correctly. The addition of the carbide saw tips should not change the stresses in the sawbody drastically. However, the stresses in the sawbody should be higher do to the extra mass of the carbide saw tips. The density of the carbide is nearly two times the density of the steel in the sawbody. The difference between the cases of a spinning sawblade with and without carbide saw tips can be seen in Table 6-2, where the maximum stresses for each case is shown.

Table 6-2 Comparison of maximum stresses of standard sawblade without tips and standard sawblade with tips.

Maximums (converged values)	Standard Sawblade (No Tips)	Standard Sawblade (With Tips)	%Difference
Radial Displacement, U1, (mm)	0.003074	0.00345	12.2
Tangential Displacement, U2, (mm)	0.000356	0.000652	83
Axial Displacement, U3, (mm)	-0.0000347	-0.0000354	2
Radial Stress, S11, (MPa)	10.72	10.94	2.1
Tangential Stress, S22, (MPa)	7.13	7.36	3.2
von Mises, S', (MPa)	9.53	9.73	2.1

The difference that stands out is the difference in the tangential displacement. The maximum tangential displacement is at the tip of the carbide saw tooth versus the case with no teeth the maximum tangential displacement is at the tip of the saw tooth pocket. It is found that the major portion of the tangential displacement is due to the tip moving along a curved path with its radius centered at the bottom of the gullet. The addition of length plus the addition of the extra mass of the carbide saw tooth compound to give higher tangential displacement for the case with saw teeth. The tangential displacement is seen in Figure 6.9. The distribution of tangential stress of the sawblade with tips is very near that of the sawblade without carbide saw tips. In other words, the gradient of the displacement from minimum displacement behind the shoulder to the maximum displacement at the end of the tips is nearly the same from one to the next.

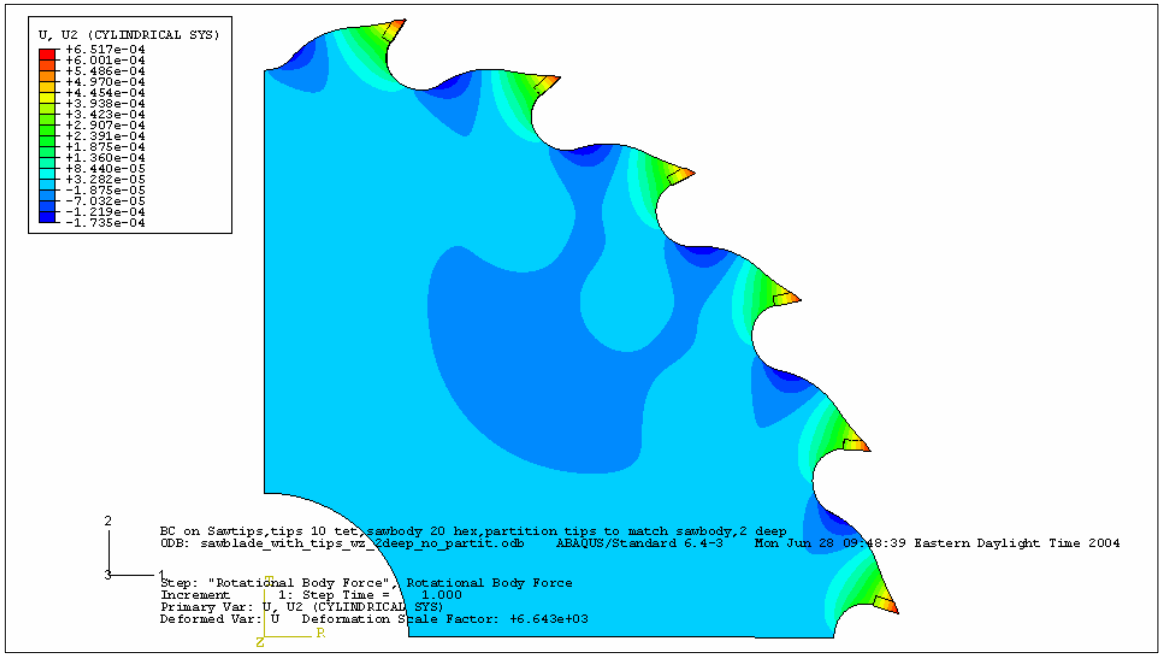

Figure 6.9 Tangential displacement for rotating 18-in standard cut-off sawblade with carbide saw tips.

For the convergence of the sawblade with carbide saw tips, the radial, tangential, and von Mises stresses all converged to within 0.73 percent between the last two meshes. This is illustrated in Figure 6.10. The distribution of stresses was also compared in our study and was found to be close from the no saw tips case to the case with saw tips.

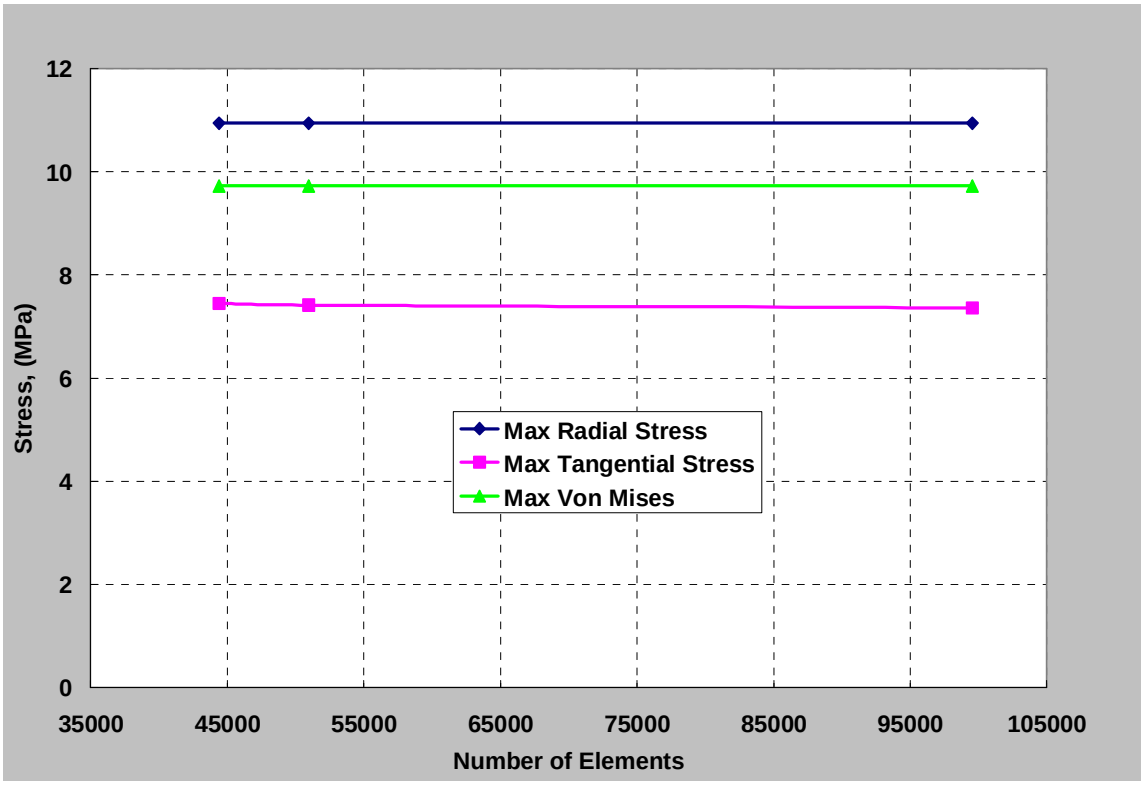

Figure 6.10 Convergence of stresses of sawblade with carbide saw tips.

Interface between the Carbide Tips and the Sawbody. It was found from the experience of analyzing the models with saw tips that a better partitioning of the saw body and saw tips was needed for more accurate analysis results. Furthermore, the *TIE command in ABAQUS was used to define constraint equations for displacement degrees of freedom between contacting surfaces at intersecting nodes at the sawbody and the saw tooth to be transition points where the extra mass of the carbide and the mass of the steel of the sawbody are carried over and allowed to talk to each other to correctly distribute each ones contribution to the added mass and stiffness for the analysis. Also, settings in

the program allow you to merge the elements that are within a certain distance to be connected together and share common nodes if partitioned correctly.

Partitioning the Mesh. Partitioning the sawblade and saw tooth at their interface helped the analysis to transition the nodes from one part to the next. Partitioning the saw body exactly the same as the back of the carbide saw teeth was found to be the best practice. This guaranteed that the nodes and elements had coincident points and edges from the sawbody to the carbide saw tips. The partitioning of the saw teeth and saw pocket can be seen in Figure 6.11 part (a) and (b). The partitioning of the saw pocket exactly matches the carbide tooth on the bottom and the back of the tooth. Again, half thickness is used to represent the whole sawblade to save computational power and time required to solve the results. This is the reason that it appears that the carbide tip would be off to one side, when in fact the saw tooth is actually centered on the saw body. The meshing of the carbide tooth can be seen in Figure 6.11 (c) and (d). Part c shows the back of the tooth where the partitioning has dictated the mesh to have elements along the partitions seen in part b. In part d, the elements of the tooth are shown through the sawbody to show that the partitioning of the saw tooth and sawbody are exact matches. The number of elements used through the thickness for the final meshing is seeded at two. Therefore, because half modeling is used due to symmetry, it is as if four elements through the thickness were used to model the sawblade.

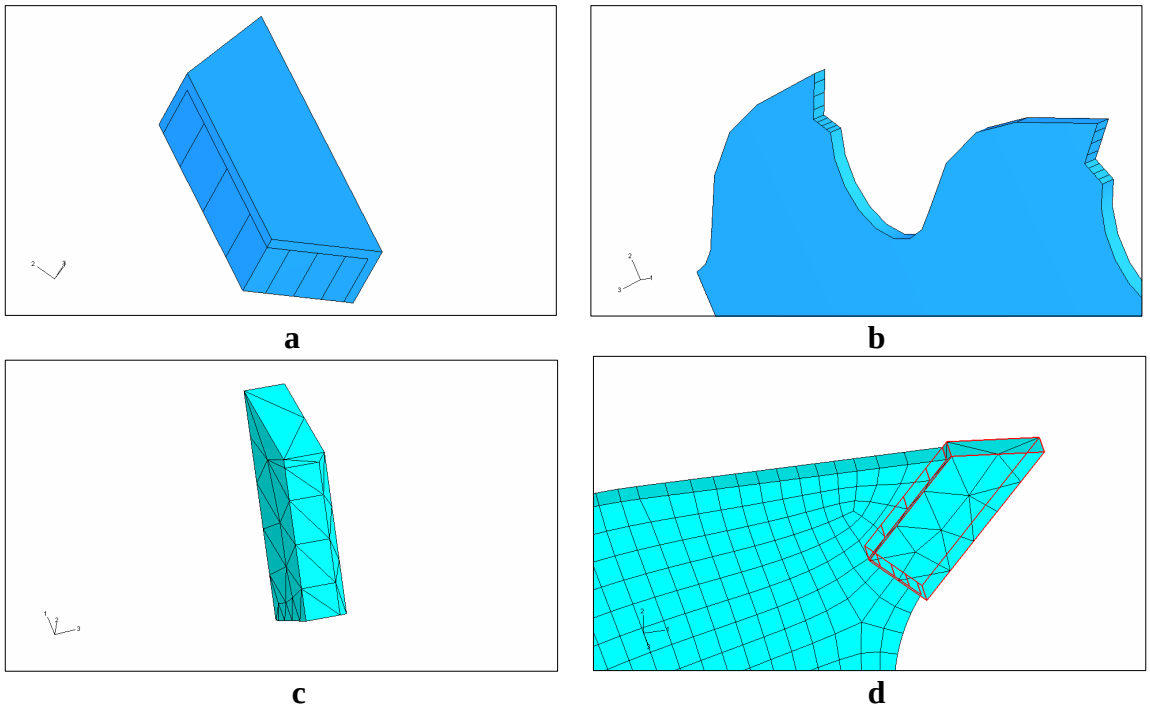

Figure 6.11 Partitioning and meshing of the carbide saw teeth and saw tooth pocket on the saw body.

Results. For the radial displacement of the standard cut-off sawblade, nearly the same distribution is seen as in the case without carbide saw tips. The radial displacement is still zero at the inner radius due to the saw collar displacement boundary condition, and the maximum is still at the outer-most portion of the sawblade (at the end of the carbide saw tips). Between these maximum and minimum locations, the sawblade stress has an increasing displacement gradient from inner to outer radius just as the case without carbide saw tips. Except in this case, the stress reaches a peak closer to the carbide saw tips due to the added mass.

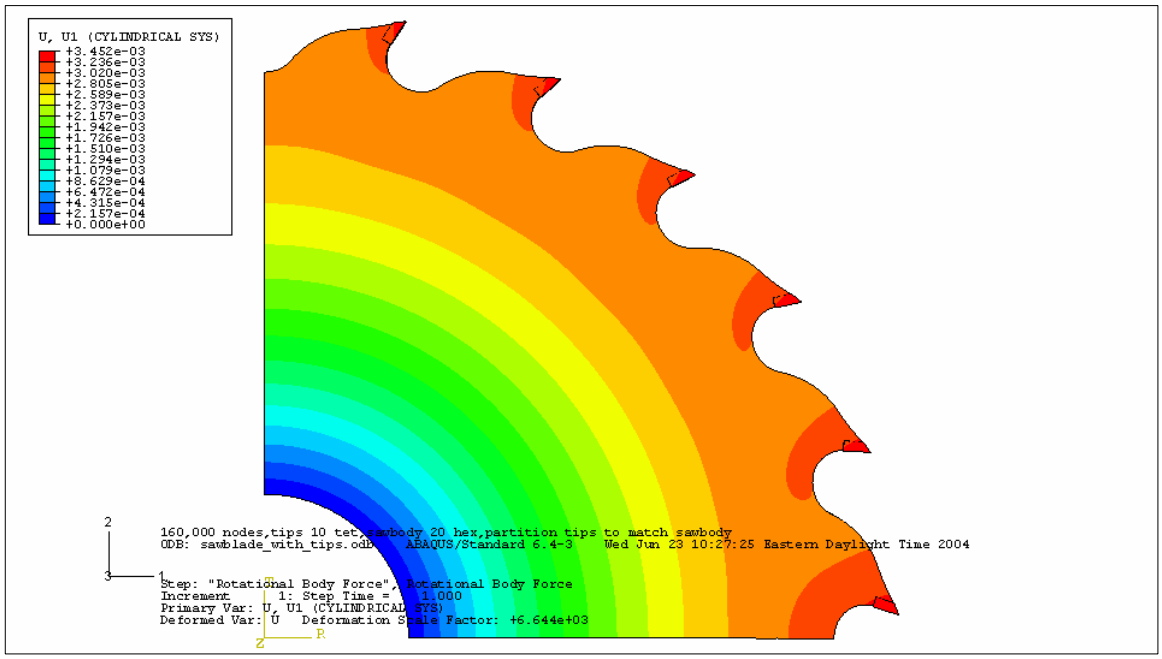

Figure 6.12 Radial displacement for rotating 18-in standard cut-off sawblade with carbide saw tips.

The axial displacement from the rotating sawblade is extremely small and is seen in Figure 6.13. For example, the maximum axial displacement found is 3.537 E-5 mm. This displacement is from the Poisson's effect causing the sawbody to contract due to stresses and displacements in the radial and tangential directions. The largest contraction in the axial-direction is at the inner radius because the sawbody is stressed the highest here. The largest expansion in the axial-direction is seen at the top of the shoulder. This expansion is due to the tangential displacement of the tooth and shoulder area. This area is actually contracting more in the tangential direction than the contracting of the saw tooth area in the radial direction. Therefore, the expansion in the axial direction is due to the resulting Poisson's effect.

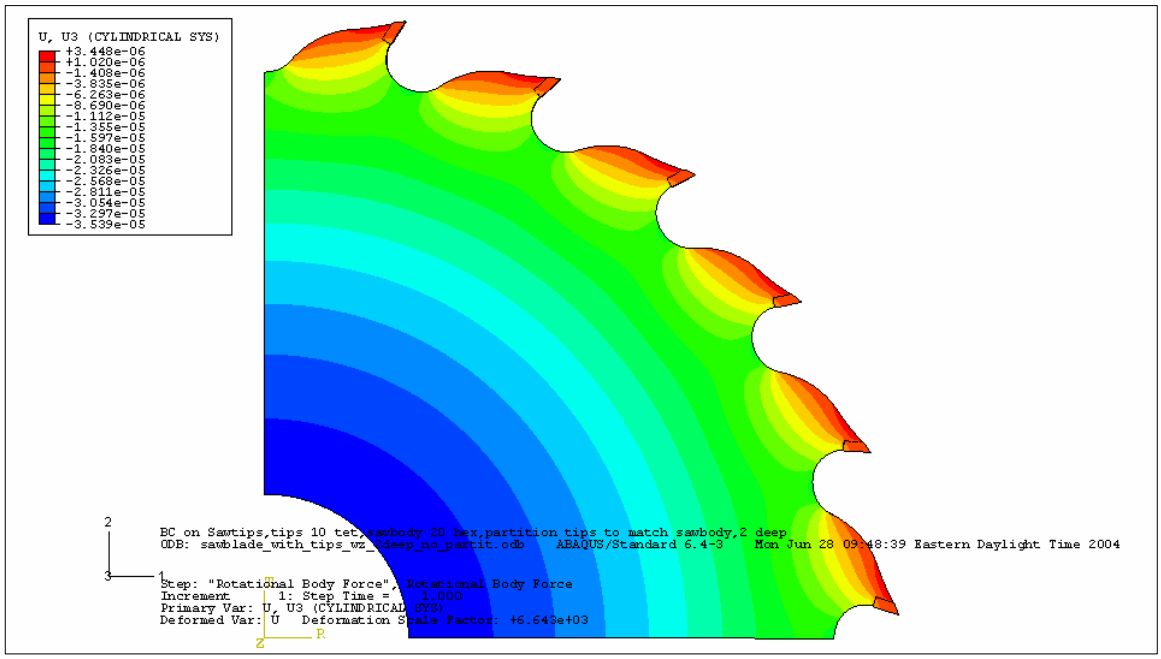

Figure 6.13 Axial displacement for rotating 18-in standard cut-off sawblade with carbide saw tips due to the Poisson's effect.

The radial stress distribution in a rotating sawblade can be seen in Figure 6.14. Again, the distribution is much the same as the case without carbide saw tips.

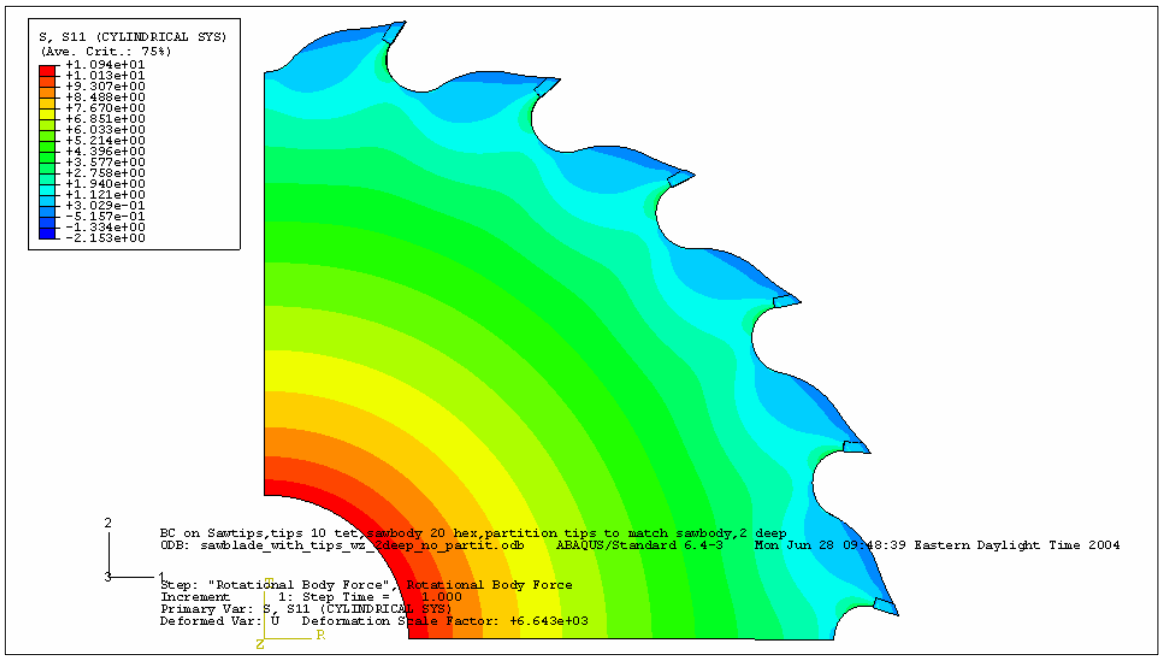

Figure 6.14 Radial stress for rotating 18-in standard cut-off sawblade with carbide saw tips due to the Poisson's effect.

The tangential stress distribution of the rotating standard sawblade with carbide saw tips is nearly the same as that of the same sawblade without carbide tips. The tangential stress is seen in Figure 6.15. The maximum tangential stress is again at the bottom of the gullets. The minimum tangential displacement is slightly higher in value because the carbide causes more radial stress at the saw pocket and tooth area due to its higher mass. The added mass induces a moment at the shoulder behind the saw tip, which causes the saw tip to displace towards the shoulder. Therefore, the top of the shoulder is in slight compression in the tangential-direction. However, this compressive tangential stress amount and area is small compared to the other tangential stresses in the rest of the sawblade. The displacement of the carbide tip also causes the bottom of the gullet under the face of the tooth to spread apart.

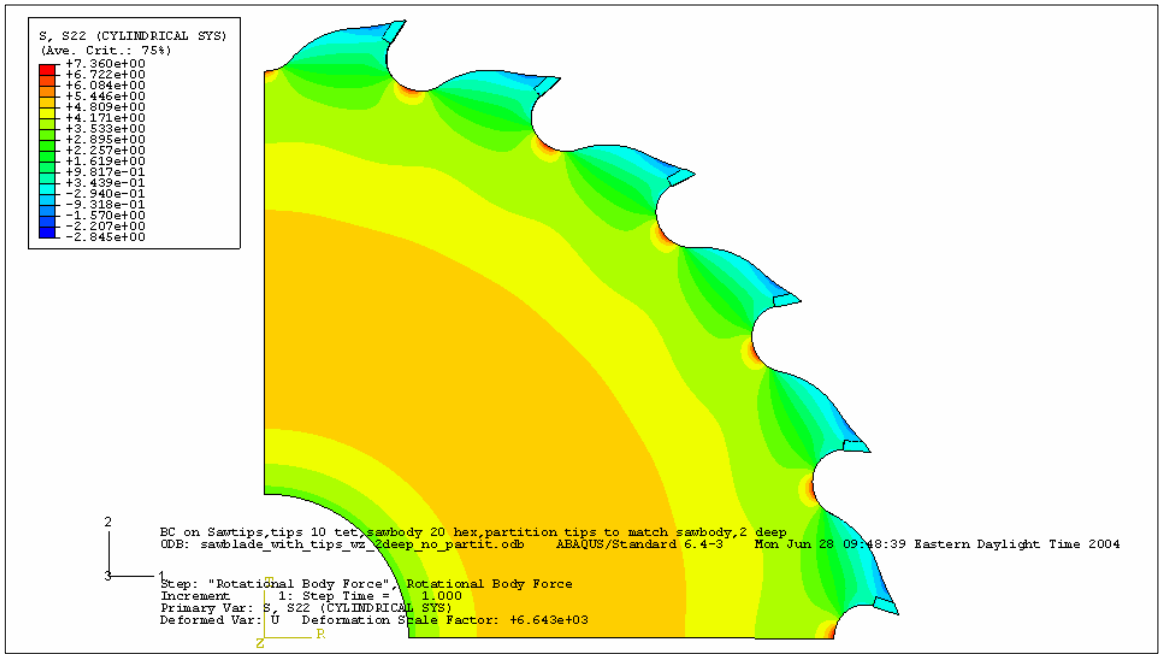

Figure 6.15 Tangential stress for rotating 18-in standard cut-off sawblade with carbide saw tips. Maximum is located at bottom of the gullets.

Next, the von Mises stress for the rotating standard sawblade is seen in Figure 6.16. This distribution is once more nearly the same as the case without carbide saw tips. The von Mises is an excellent stress to use to see how much stress is in the sawbody compared to the yield stress of the material. The stresses due to the rotational forces created at the 2122 rpm of the nominal rotational speed of this sawblade alone are quite low – the yield stress is around 690 MPa in the steel material. The rotational forces alone

do not destroy a sawblade, but rather vibrations, cutting forces, heat, and friction from cutting the material help to destroy a sawblade. In earlier pictures of the destroyed sawblades shown in this thesis, the sawblade separated at the expansion slots. This is an area that is in need of further study, hence, the reason for the next chapter.

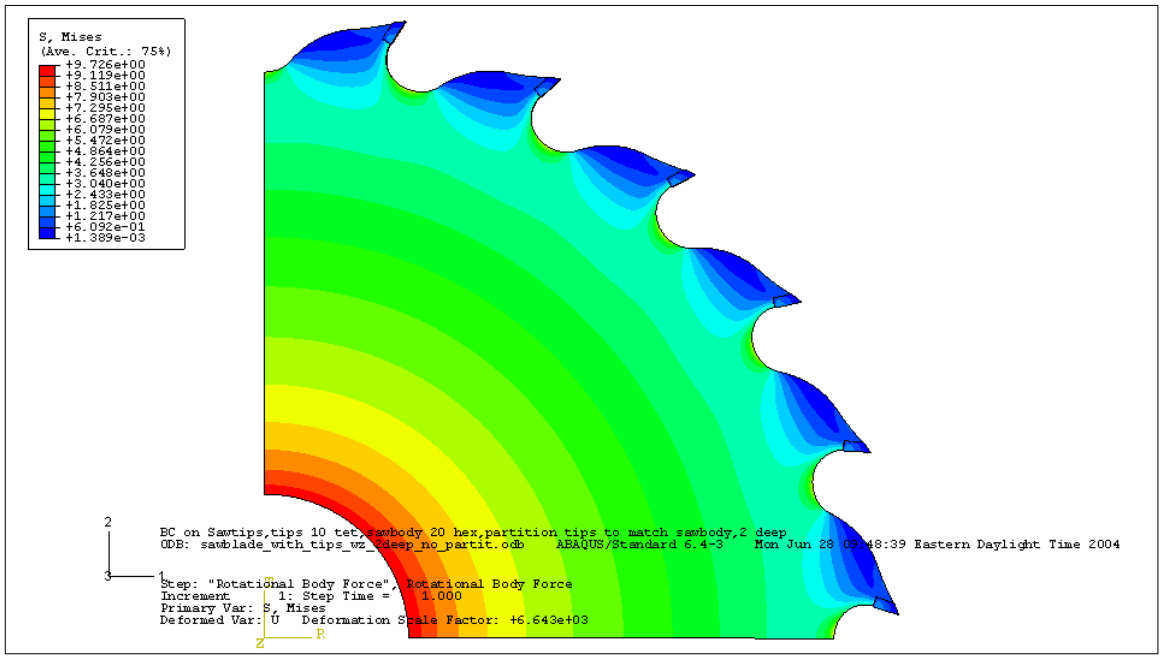

Figure 6.16 The von Mises stress for rotating 18-in standard cut-off sawblade with carbide saw tips.

Chapter 7

Stress at Expansion Slots due to Rotation in Various Sawblade Models

The next step in building the sawblade in our analysis is to create a model that has the exact geometry of the sawblade we intend to analyze. So, adding the expansion slots and examining the stresses seen by the sawblade from the rotation forces only was the next logical step. In addition, the lengths of the expansion slot were changed to see if having expansion slots and varying their lengths had a significant affect on the stresses seen in the sawbody from rotational forces. The lengths were varied from one inch to 2.5 inches in increments of a quarter inch. Again, the saw collar boundary condition was used at the inner radius.

Partitioning and Elements. The partitioning used for a sawblade with carbide teeth and expansion slots are seen in Figure 7.1. Here the use of partitioning is used to make the geometry four-sided in all areas. This helps the mesh because the 20-node quadratic brick elements used (or the eight-node linear brick elements used in some models) need four-sided geometry for mapped meshing. Furthermore, this meshing scheme results in well shaped elements which result in the nonlinear load increments executing to completion and faster convergence. For the sawblade tips, it was not conducive to use brick shaped elements because of the triangular geometry at the cutting edge of the tip. Therefore, to mesh the carbide saw tips, ten-node modified quadratic tetrahedron elements were used to match with the 20 node brick quadratic brick elements (or four-node linear tetrahedron were used to match with the eight-node linear brick element). These tetrahedron shapes are useful to mesh shapes that are round or have a triangular shape to them. As in Chapter 6, saw tips and the saw tip's pocket of the sawbody are meshed exactly the same to control the software's mesher to make nodes at the interface be at the same geometric location. This method allows for the computational model to most accurately transfer the loads, mass, stiffness, and boundary condition between the saw tips and the sawblade.

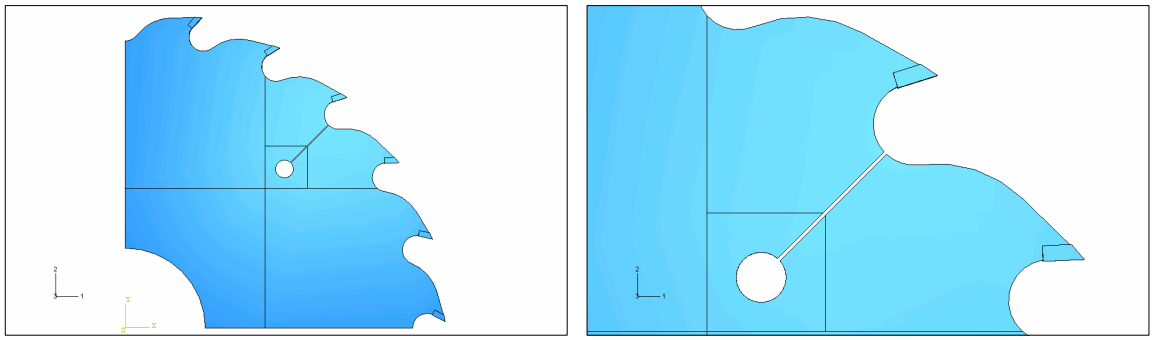

a **b**

Figure 7.1 Partitioning used for the standard sawblade. All partitioned areas are conducive to four-sided geometry.

The partitioning scheme for the sawblade was learned from analyzing a rotating 18-in disc with four, 2-in expansion slots. This partitioning scheme for the rotating disc is seen in Figure 7.2. This disc has the same thickness and radius as the standard sawblade and the 1824-233 sawblade used in our analysis.

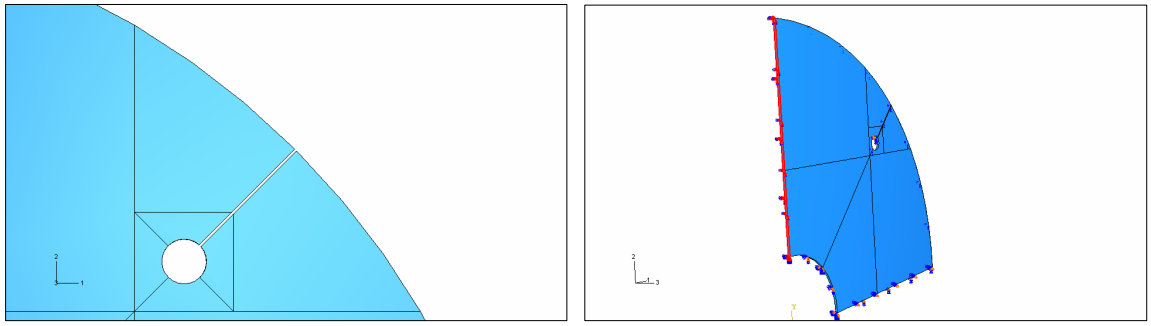

Figure 7.2 Partitioning scheme used in study of rotating 18-in disc with four, 2-in expansion slots.

Comparing various models with four, two-inch expansion slots. All the following had 2-in expansion slots for this analyses and comparison: standard sawblade, 1824-233 sawblade and the rotating disc. The three von Mises results of these three models are compared in Table 7-1. In this table, the three von Mises stresses are located at the highest stress point in the disc (and/or sawblade), which is located at the bottom of the expansion slot as seen in Figure 7.3. Also, noted is the stresses are all similar in quantity. The similarity is due to the fact that while the rotating disc does not have the added mass of the carbide, it does have more steel where the gullets and shoulder on the sawblade would be. In the end, the differences between the models nearly even out the maximum stresses of each.

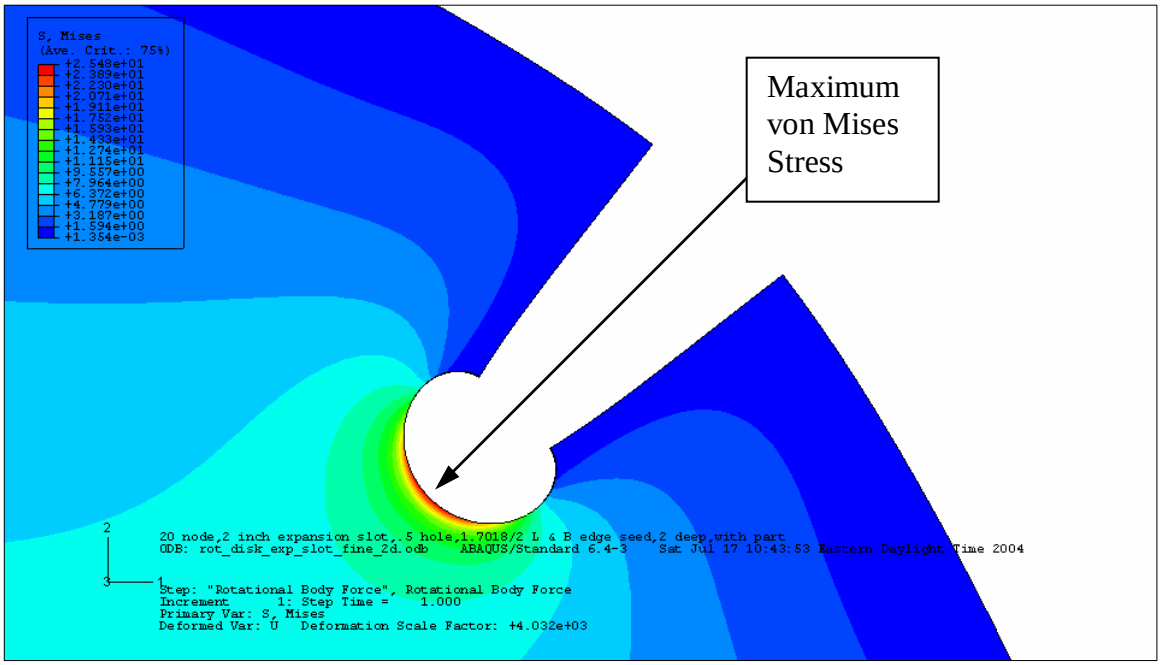

Figure 7.3 The von Mises stress in an 18-in rotating disc with four, 2-in expansion slots.

Table 7-1 Maximum von Mises stress seen at bottom of various models with four, 2-in expansion slots.

	Maximum von Mises Stress, S', (MPa)
18-in rotating disc	25.48
18-in Standard sawblade	23.51
1824-233 sawblade	25.53

The von Mises results of the models shown in Table 7-1 were converged, as shown in Figure 7.4. The von Mises stress is chosen to represent the stresses seen in the sawblade because it is a culmination of all stresses seen in the sawblade. However, the majority of the von Mises stress comes from the tangential stress and second from the radial stress at the bottom of the expansion slot. For example, the tangential stress at the bottom of the expansion slot in the rotating disc is 25.8 MPa and the radial stress is 12.3 MPa. The convergence for these results is seen in Figure 7.4. For each converged model's analysis, two elements were used to represent the thickness of the sawblade (or disc).

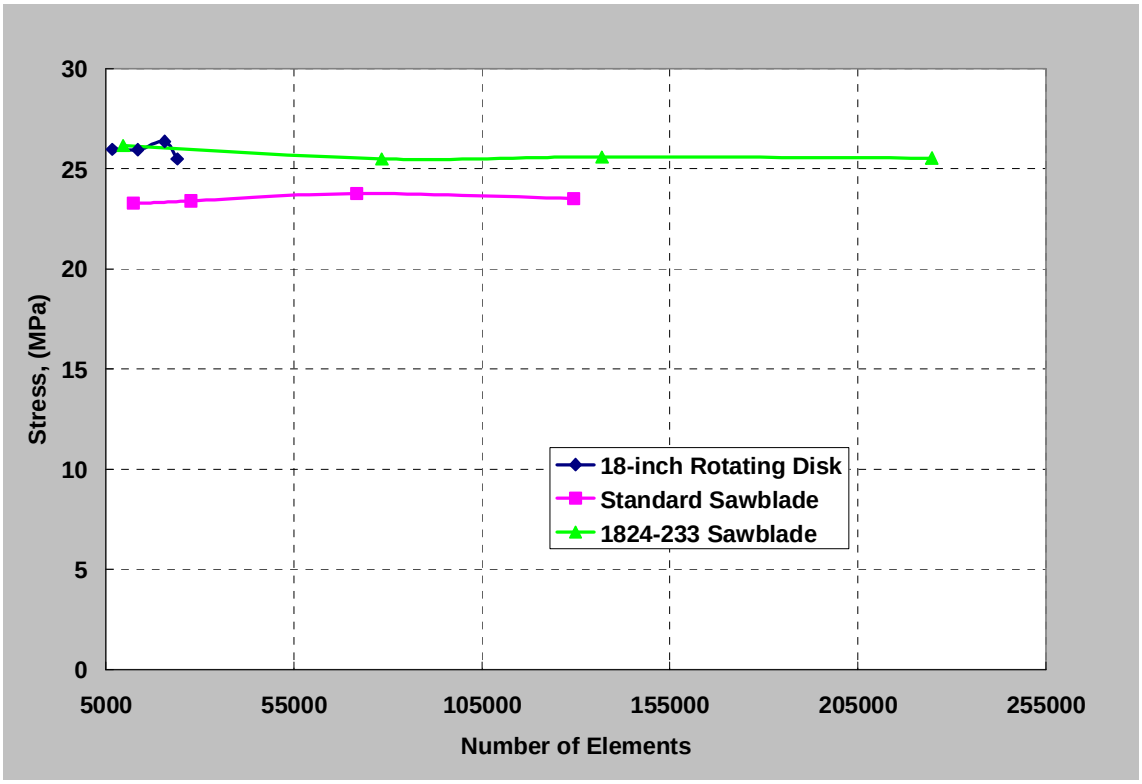

Figure 7.4 Convergence of maximum von Mises Stress at bottom of expansion slots in various rotating bodies.

The expansion slot introduces another interesting phenomenon in the body of the sawblade – the distribution of the stress at the expansion slot. At the bottom of the expansion slot, the tangential stress is at a maximum, as seen in Figure 7.5. Near the upper part of the expansion slot, the tangential stress is near zero. However, the radial stress at the bottom of the expansion slot is near zero, and the maximum radial stress is on both sides of the expansion slot, as seen in Figure 7.6. These two dominating stresses in the rotating sawblade bring about the von Mises stress at the expansion slot seen in Figure 7.7.

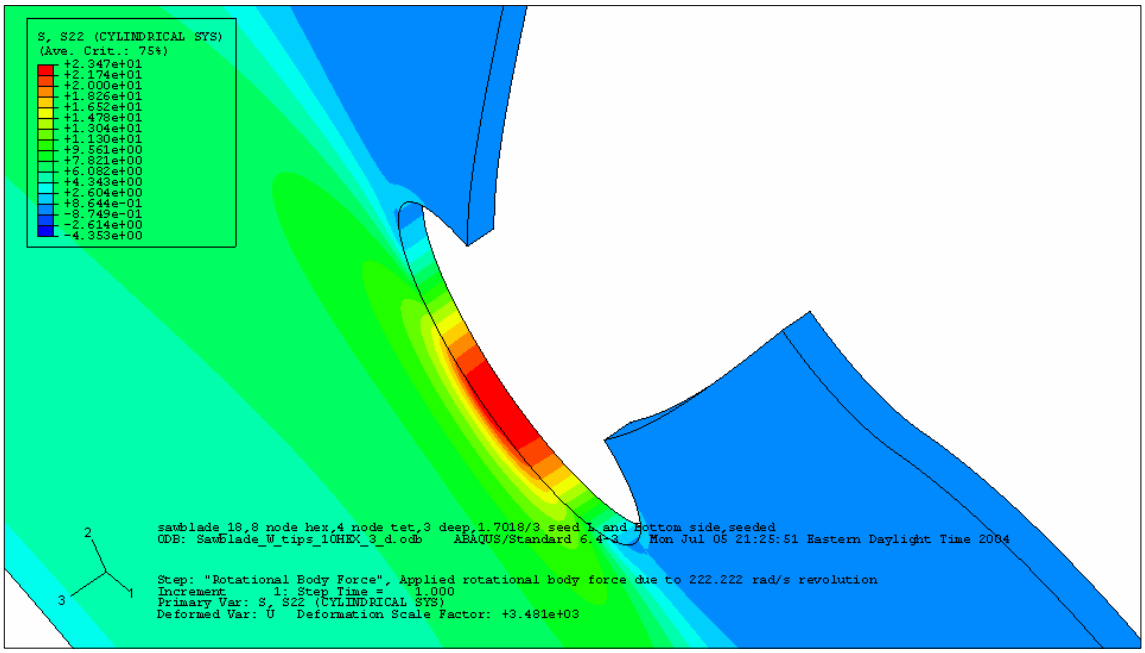

Figure 7.5 Tangential stress at expansion slot of standard sawblade with tips. Maximum of 23.5 MPa is located at bottom of stop-hole.

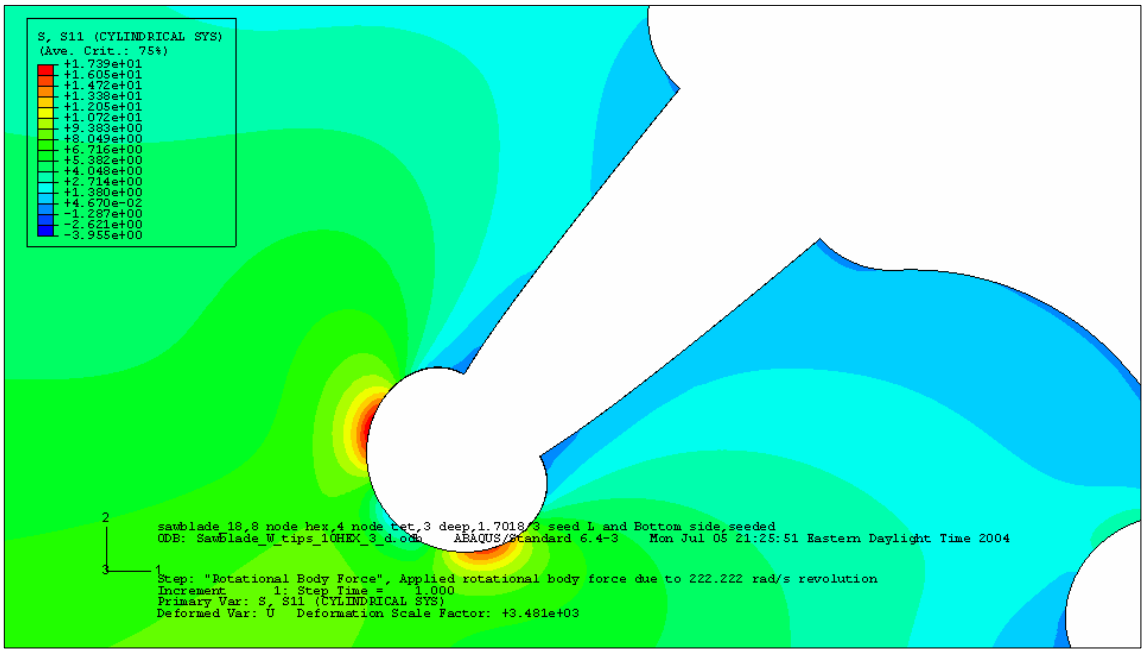

Figure 7.6 Radial stress of standard sawblade with tips. Maximum of 17.4 MPa is located at sides of stop-hole.

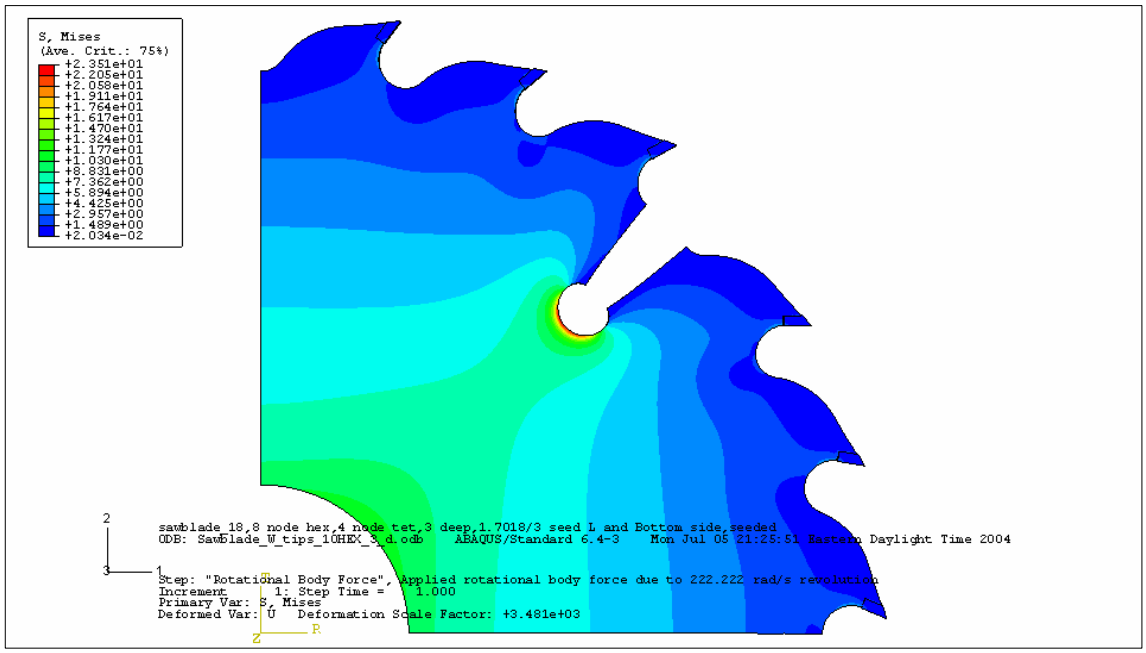

Figure 7.7 The von Mises stress of standard sawblade with tips. Maximum is at bottom of stop-hole at 23.5 MPa.

Expansion Slots with -10^{o} Hook Angle. Another sawblade model used for this thesis study is an ***ICE***^{TM} 105-1824-233 sawblade with four, 1.25-in long, negative 10^{o} expansion slots. This model was analyzed to understand the difference in stress state in the sawblade (and later in section 9.3.3 how the natural frequencies were changed) from a change in the angle of the expansion slot. For this study, a two inch expansion slot was used. Figure 7.8 shows the converged stress at 20.3 MPa at the bottom of the angled expansion slot. The stresses did not change significantly as compared to a sawblade with the same expansion slots with 0^{o} slot angle. For direct comparison between the two, the stress in a 0^{o} slot angle had nearly the same stress at 21.1 MPa.

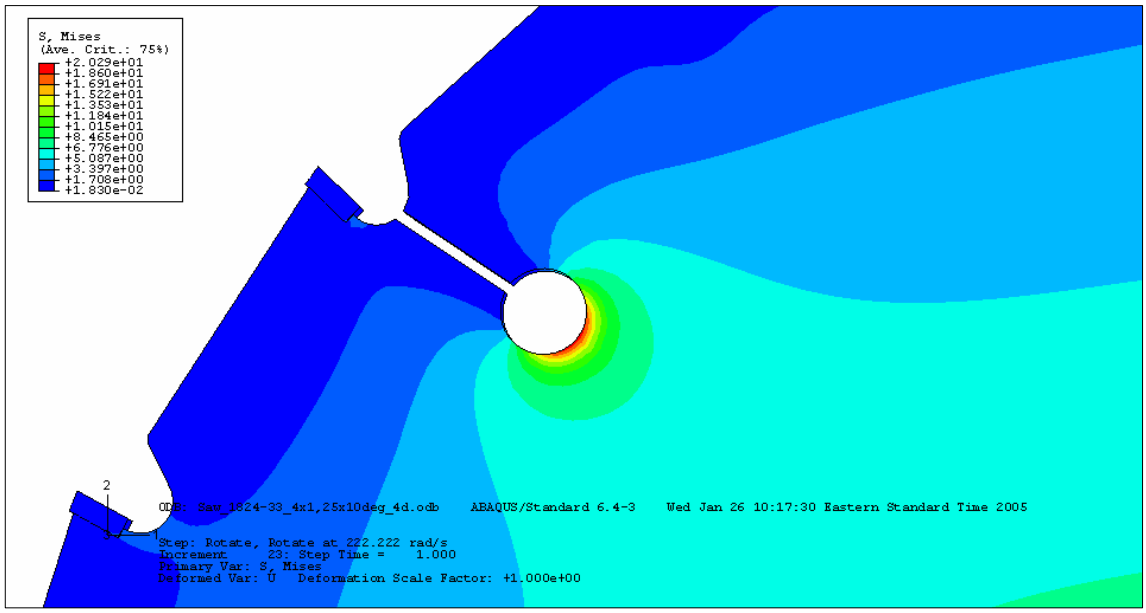

Figure 7.8 The von Mises stress of a rotating ***ICE***™ 105-1824-233 sawblade with four, 1.25-in long, negative 10° expansion slots.

Comparing the Effects of Various Expansion Slot Lengths. When comparing the state of stress in the sawblade as a function of length of the expansion slot, the longer the slot, the higher the stresses seen in the sawblade. This is expected because the longer slot length has less material available to carry the load, allowing the expansion slot to open wider and causing more stress to act on the bottom of the expansion slot. The higher stresses could also be viewed as a result of having a longer lever arm which to enact the tangential forces upon, thereby causing higher stress at the bottom of the stop hole. The stresses seen in a rotating ***ICE***™ 105-1824-233 sawblade and its corresponding slot lengths of four expansion slots are seen in Table 7-2. This same increase in stress was seen in studies of a rotating annulus with expansion slots with nearly the same results.

Table 7-2 The von Mises stress in a rotating ***ICE***™ 105-1824-233 sawblade with four expansion slots.

Expansion Slot Length	von Mises, S', (MPa)
None	10.9
25.4 mm (1-in)	18.64
31.8 mm (1.25-in)	21.12
38.1 mm (1.5-in)	22.73
44.5 mm (1.75-in)	24.25
50.8 mm (2-in)	25.53
57.15 mm (2.25-in)	26.99
63.5 mm (2.5-in)	28.45

Expansion slots will be addressed in future sections of this thesis. Specifically, the stress from cutting, and the effects on the natural frequency of the sawblade will be discussed.

Chapter 8

Stresses Due to Rotation and Cutting Action

8.1 *Calculations of Pressure on One Saw Tip in Cut*

Additional explanation is necessary regarding the purpose of the "trim saw" blades studied in this section. Trim saws are used to clean up the ends of boards and to cut specific length lumber out of boards. Trim saws are run at certain speeds and cut at certain speeds. The ends of the boards are made perpendicular and defects are removed. Removing the defects is either done by hand or by an optimizer that detects imperfections in the lumber near the ends of the board. The board can then be pulled in a way that the saw will remove this defect, thus, yielding a higher quality board. The object is to remove defects while minimizing amount of material being wasted. Speeds of 30 to 60 boards per minute are common cutting speeds for the trim saws. This yields board feet of 40 ft/min if each board is 8 inches wide and the speed set to the maximum speed of 60 boards per minute. The calculations are based on nominal parameters of 30 board ft/min. The saws used in this study will typically be used for cutting hardwoods.

These types of trim saws generally see only one board at a time and the boards are quite thin (approximately one and ½ inches). These cutting conditions allow to simplify the number of teeth in the cut at any given time. Therefore, we have chosen to use only one tooth for the cutting action of the saw.

To determine the pressure the cutting carbide tip receives, the following calculations and equations were used. The bite per tooth was found from using nominal parameters for an 18-in sawblade cutting a thin board. A thin board was used to keep the computer analysis simple and a thin board is typical cutting application for an 18-in nail cutting blade. Only one carbide tooth in the cut at a time is illustrated in Figure 8.1, which shows that only one tooth can be doing the cutting at any given time.

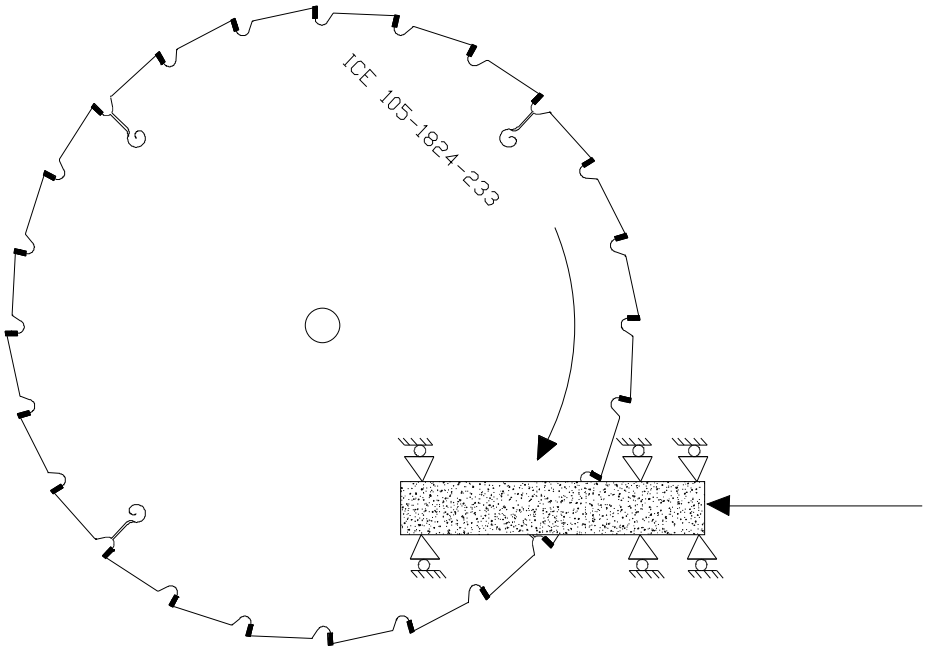

Figure 8.1 An 18-in sawblade with only one tip in the cut of a 1.5 inch thick board. This is to show how the pressure was resolved on only one tip. As the board is pushed into the saw for the cutting process, only one tip of the sawblade cuts the wood at a time.

Calculations. To find the bite per tooth, Equation 8.1-1 was used. The bite per tooth is the amount of the top tip of the carbide tip that actually does the cutting of the wood or stated another way, the bite per tooth is the distance the log or board advances into the saw between successive teeth, as seen in Figure 8.2. This is generally a small number compared to the face length of the carbide tip. The bite per tooth is found by

$$bpt = \frac{F_r \bullet 12}{RPM * \#teeth} \qquad [8.1\text{-}1]$$

where F_r is the feed rate of the board in feet per minute, *RPM* is the revolutions per minute of the sawblade, and *#teeth* is the number of teeth of the sawblade. The cutting parameters used in this thesis are as follows: F_r is 30 ft/min, *RPM* is 2122.066 rpm, and the number of teeth is 24. This gives us a bite per tooth of 0.0071 inches or 0.17954 mm.

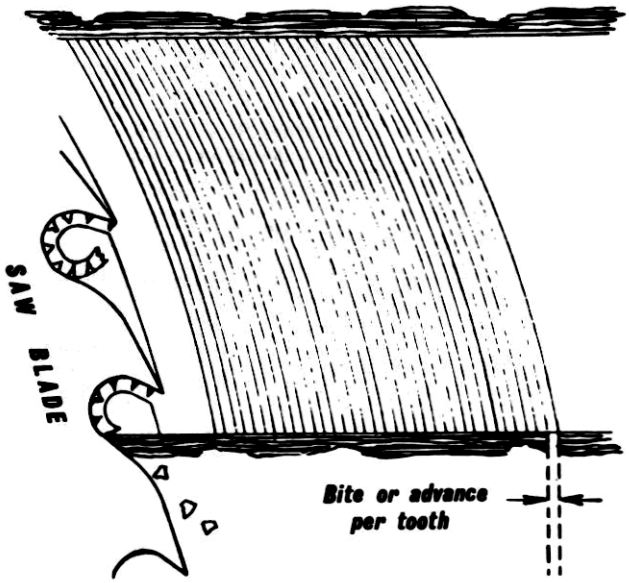

Figure 8.2 Sawblade cutting a log showing the bite per tooth, Lunstrum [3].

Now, using our nominal horsepower rating for an 18-in nail cutting sawblade, we can back calculate the amount of pressure that is exerted on each tip, *PPT*, to hold back this amount of horsepower. In other words we will be finding the amount of torque required to cut the wood. Knowing the value of the shear property of American White Oak is 13.6 MPa, gives us a good value to check our calculations. We use the center of this bite per tooth as the lever arm point from the center of the sawblade. For an 18-in sawblade, this lever arm was found to be 8.996-in or 228.395 mm. First, we must convert the horsepower to N-mm/s for the calculations to be in metric units. Seven-and-a-half horsepower converts to a power, *W*, of 5.593 x 10^6 N-mm/s. Using this value, we divide by the lever arm to find the force per second, *F'*, with

$$F' = \frac{W}{L_{arm}} \qquad [8.1\text{-}2]$$

where W is the power, and L_{arm} is the lever arm. This gives us a force per second of 2.449 x 10^4 N/s.

To get to the final PPT, we must continue through a series of steps. The area must now be found that the force per second acts upon. This will allow us to find the pressure per second, *P'*, on each the sawblade. The area is found using the bite per tooth multiplied by the width of the carbide tip. The width of the carbide tip is 4.05 mm or

0.1595 inches. This gives us an area, *A*, of 0.727 mm^2 or 0.001128 in^2. To calculate the pressure per second, *P'*, we use

$$P' = \frac{F'}{A} \qquad [8.1\text{-}3]$$

Calculating for *P'* we obtain 3.367 $x10^4$ MPa/s.

To determine the number of teeth per minute, T', is obtained using

$$T' = \#teeth \bullet rpm \qquad [8.1\text{-}4]$$

giving a T' of 50900 teeth/min or 849 teeth/s. Now, taking the inverse of the time each tooth has the pressure applied for gives the inverse of T', (inv)T', to be 1.178 $x10^{-3}$ s/tooth. The pressure on each tooth, *PPT*, is determined by Equation 8.1-5 as

$$PPT = P' \bullet inv(T') \qquad [8.1\text{-}5]$$

giving a pressure per tooth, *PPT*, of 39.66 MPa, which is within the range of the shear property of American White Oak of 13.6 MPa. We will use this 40 MPa pressure per tooth and the bite per tooth of 0.1796 mm found in our analysis of the sawblades in the next section.

8.2 *Stresses on Sawbody Due to Pressure on Various Tips of Sawblade*

The calculated pressure exerted on each tip during the cutting process, can be applied over the given area of a single tip to determine the stress in the sawblade. The saw tooth chosen for application of the pressure load in this analysis are the ones before and after the expansion slot. Cutting with these tips results in the highest stresses in the sawblade. The cutting forces applied to these tips will be in the form of pressure exerted over the entire width of the tip and the length of the bite per tooth, bpt = 0.1796 mm from Equation 8.1-1. Furthermore, the pressure used in the models is in the perpendicular

direction to the face of the saw tip as seen in Figure 8.3 and Figure 8.4. This pressure applied on the saw tip is also known as a surface traction normal to the surface. The linear speed in the tangential direction of the sawblade is far greater than the component of velocity of the wood being fed into the sawblade. For example, the linear speed at the tip of the sawblade is 10,000 ft/min verses the board speed of 30 ft/min.

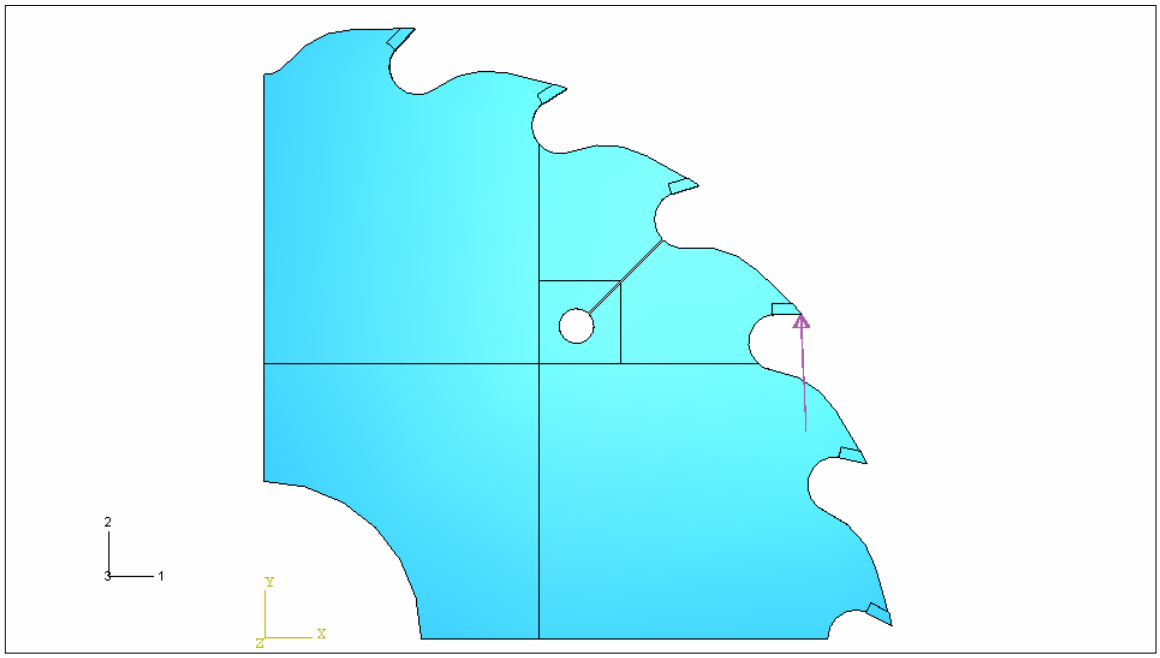

Figure 8.3 Pressure of 36.9 MPa on top of tip and down 0.007 mm. This pressure is representative of the cutting forces seen by the sawblade.

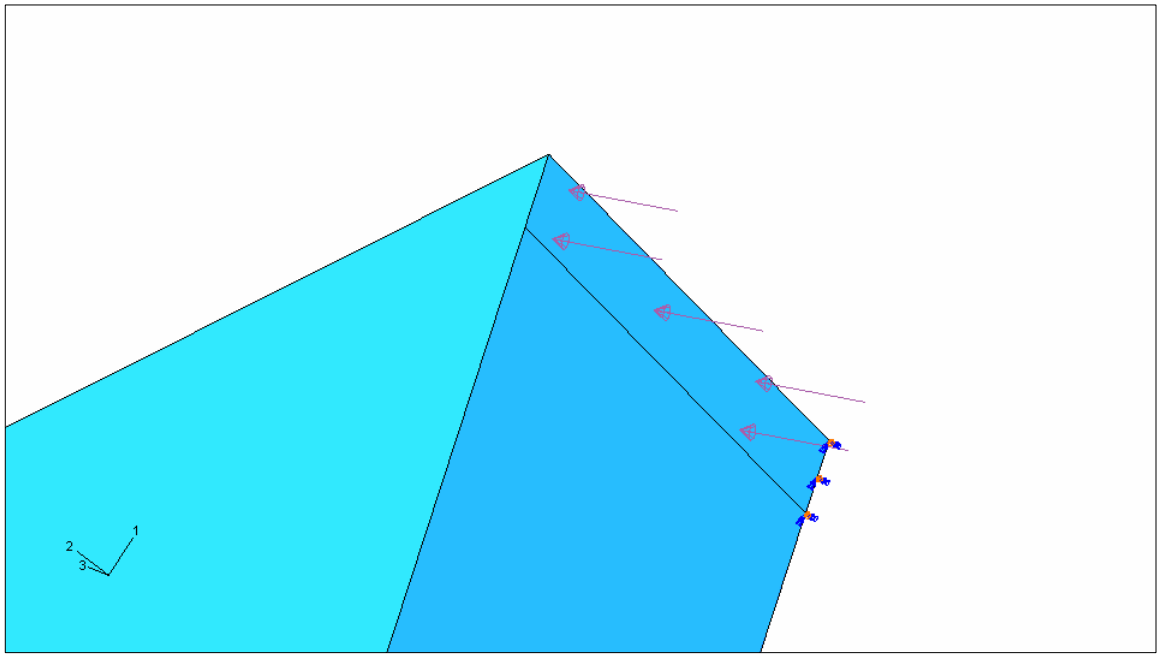

Figure 8.4 Zoomed in view showing the area of tip where pressure is applied. Area is entire width of model by 0.007 mm down from top of tip.

Pressure Applied on Carbide Tip Before Expansion Slot. Referring to the pressure applied on the carbide tip before the expansion slot, will be referred to as the pressure before the expansion slot. The results of the applied pressure of 36.9 MPa on the carbide saw tip before the expansion slot gives a maximum von Mises stress in the sawbody of 26.08 MPa at the bottom of the two inch expansion slot, as seen in Figure 8.5. This value is converged to within two percent of the previous mesh. The stress gradient still shows a high stress at the inner radius and the stress gets lower as the radius is increased away from the center. However, a sharp increase in stress is seen as the stress gradient approaches the bottom of the expansion slot due to the addition of the tip load due to the cutting load superimposed on the stresses due to the rotating sawblade. The highest stress as one would expect is seen in the carbide teeth. This value is shown in grey in Figure 8.5 at the point of the tip where the pressure is applied. The maximum von Mises seen in the carbide tip before the expansion slot is 61.2 MPa.

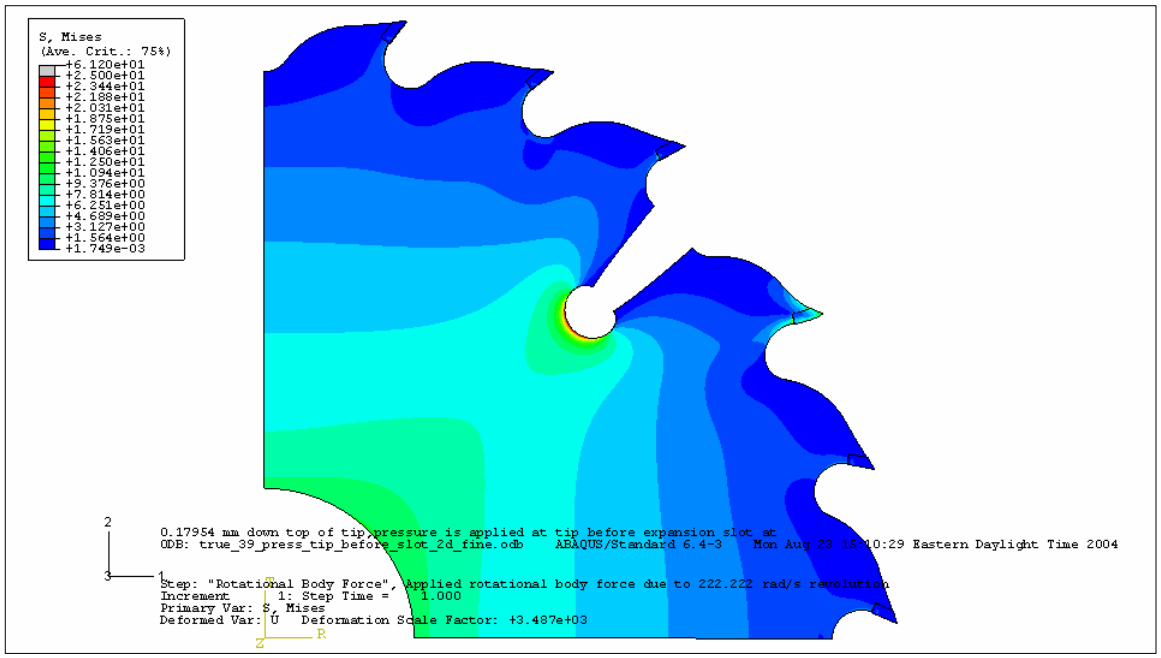

Figure 8.5 The von Mises stress in sawblade with pressure on tip before expansion slot. Maximum stress in steel sawbody is at bottom of stop hole at 26.08 MPa. (Absolute maximum is seen in the carbide tip at 61.2 MPa.)

The stresses seen in the carbide tooth are found to be greater if the applied pressure is on a tooth of the sawbody where the steel shoulder has more support behind it, such as the tooth behind the expansion slot. This is compared to the above case where the expansion slot could carry some of the tip cutting load allowing the steel shoulder to flex toward the open slot. So, if the pressure is applied to the tooth behind the expansion slot as seen in Figure 8.6.

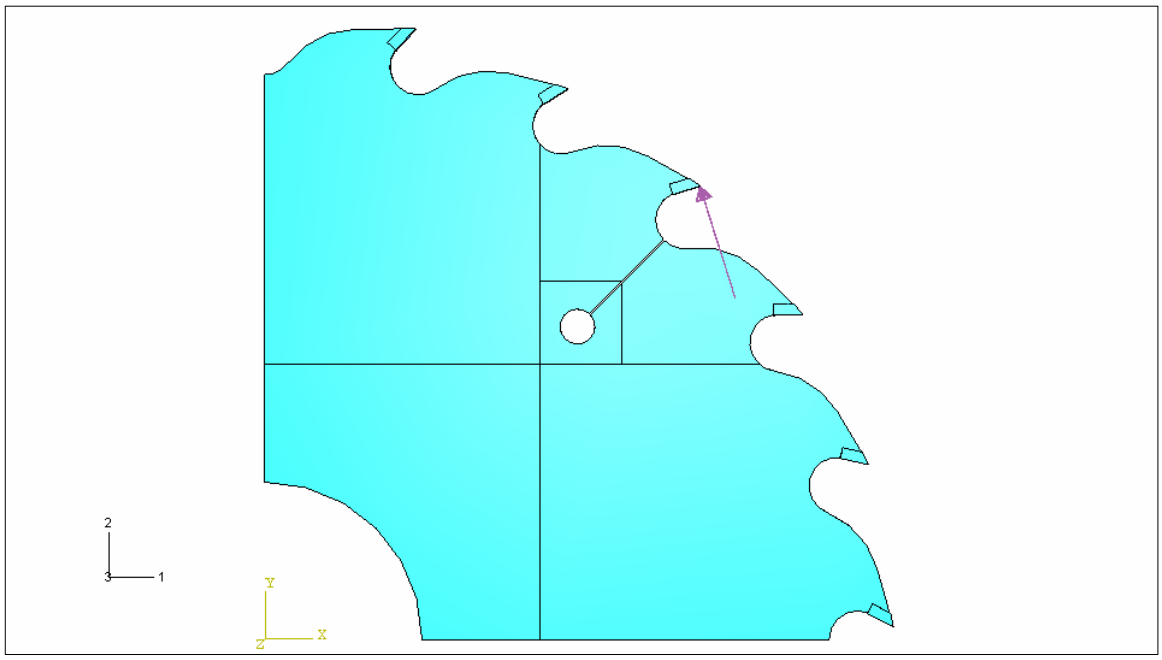

Figure 8.6 Pressure on tip after expansion slot. Pressure is applied perpendicular on face of tip located over area at top of tip to 0.007 mm down.

Pressure Applied on Carbide Tip After the Expansion Slot. Moving forward, referring to the pressure applied on the carbide tip after the expansion slot, will be known as the pressure after the expansion slot. The von Mises stresses in the carbide tooth behind the 2-in expansion slot are approximately 162.5 MPa (von Mises). It is believed that the higher stress in the tooth comes about because the sawbody has much more material behind the saw tooth making for a stiffer section versus the pressure before the expansion slot. With this low stress seen by the saw tip compared to the yield stress of carbide of 2683 MPa, it is not believed that this stress causes the wearing of the saw tip,

but the friction between the saw tip and the wood and any dirt, sand or grit embedded in the wood.

Because of the higher stresses the analysis of the pressure behind the expansion slot will be explored in more detail. The maximum von Mises stress seen at the bottom of the expansion slot is now 26.85 MPa. This is seen in grey in Figure 8.7 and the zoomed in view of the dashed box is Figure 8.8. Also, the high stress from the expansion slot results in higher stresses radially inward from the expansion slot in the sawbody. These higher stresses are seen in a color pattern of green that is flowing from the expansion slot to the inner radius.

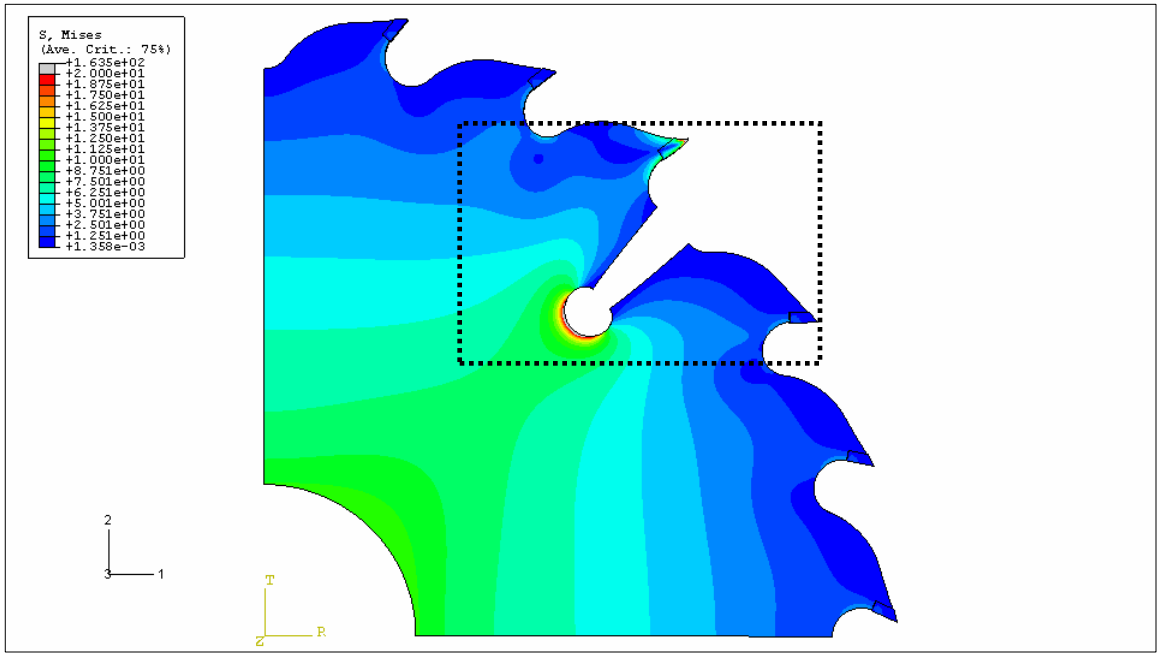

Figure 8.7 Pressure on tip after expansion slot. von Mises stress is maximum of 26.6 MPa, located at bottom of stop hole of the expansion slot.

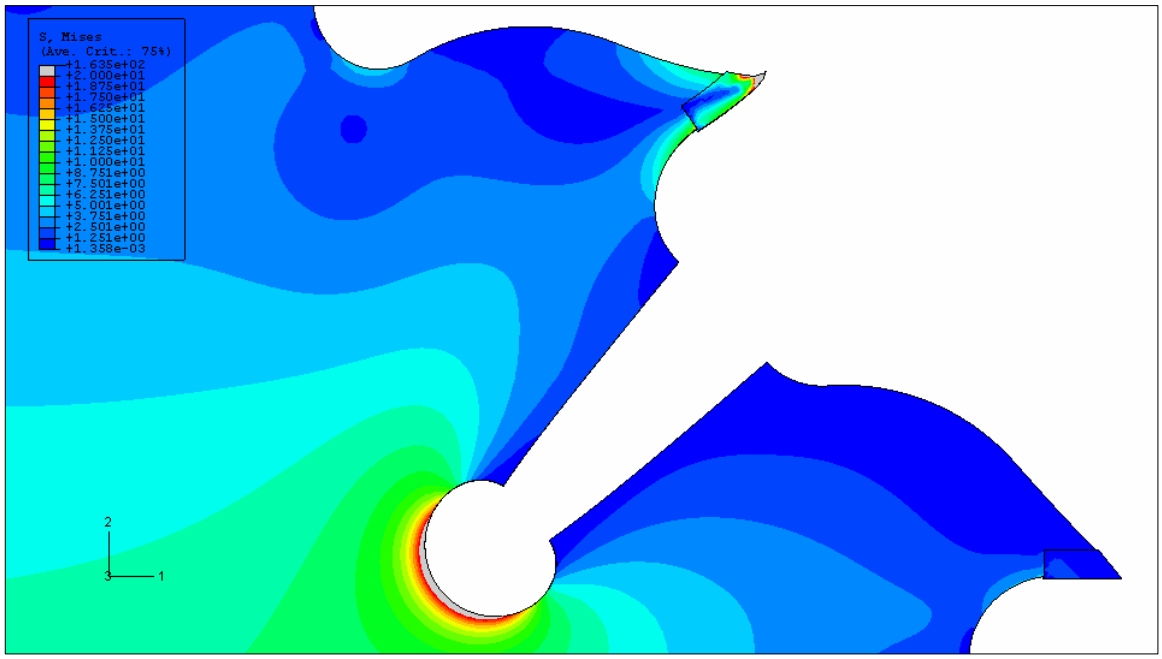

Figure 8.8 Zoomed in view of von Mises stress at expansion slot and tip after expansion slot. Maximum stress in the sawbody is in grey at 26.6 MPa (the maximum in the carbide is 163.5 MPa).

Due to the cutting forces applied as pressure on the carbide saw tip behind the expansion slot and the rotational stress, the maximum stress in the radial direction is 20.3 MPa in tension. This maximum is located at the same side of the stop hole as the tip with the applied pressure, as seen in Figure 8.9. The minimum radial stress is due to the outer surface approaching zero due to the natural boundary condition as explained earlier in the rotating disc sections.

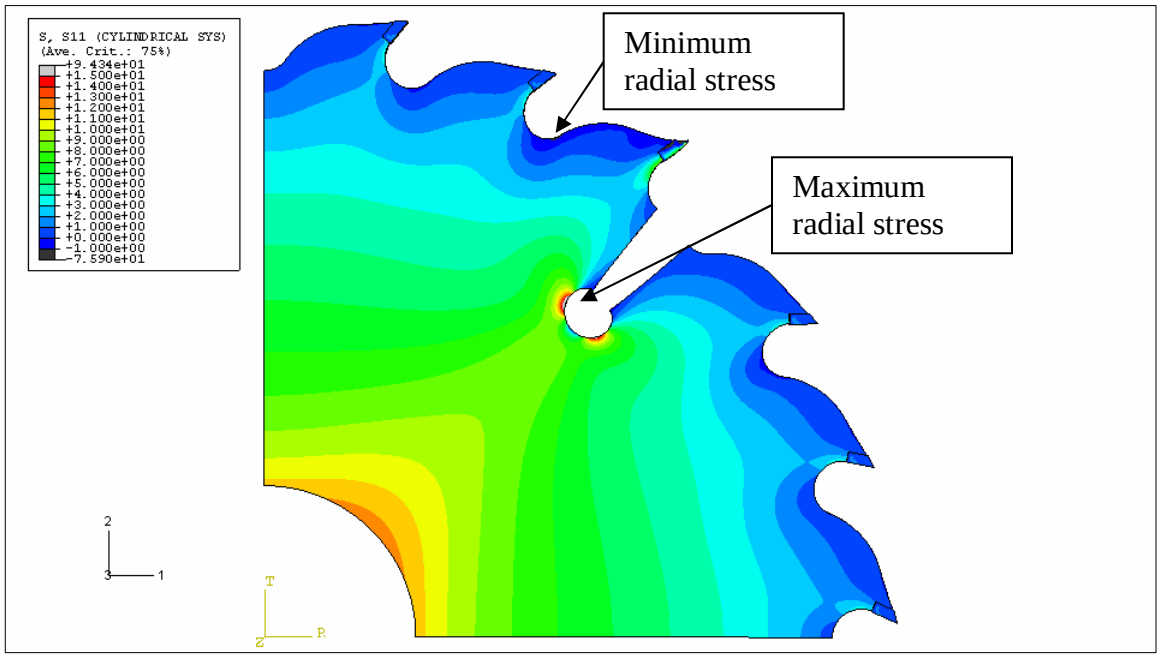

Figure 8.9 Stress in the radial direction due to pressure on tip after the expansion slot. Maximum stress in the sawbody is 20.3 MPa in tension and the minimum is approximately 1.6 MPa in compression.

From the cutting of the saw tip after the expansion slot along with the rotational stresses, the maximum tangential stress seen in the analysis is 26.4 MPa in tension located at the bottom of the stop hole. The tangential stress is seen in grey in Figure 8.10. These tangential stresses are again due to the stretching of the sawbody as the sawblade rotates and the opening of the expansion slot. The tangential stress seen by the carbide saw tip is found to be 93.8 MPa in compression.

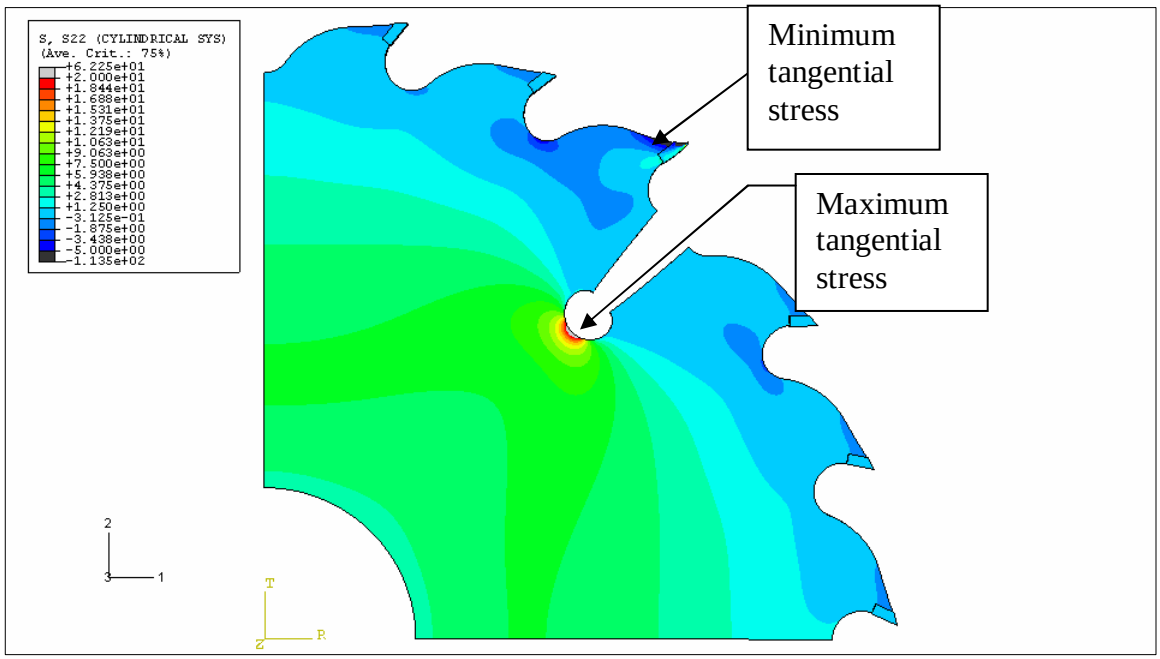

Figure 8.10 Stress in the tangential direction due to pressure on tip after the expansion slot. Maximum stress in the sawbody is 26.4 MPa in tension and the minimum is approximately 7.9 MPa in compression.

Chapter 9

Overview - Natural Frequencies of Sawblade, Non-rotating and Rotational

The stresses seen by the sawblade from the rotation and cutting forces are small compared to the yield strength of either the steel in the sawbody or the carbide in the saw tips. Therefore, a different mode is responsible for sawblade failure in the real world. However, the knowledge gained during these studies of stresses due to rotation and cutting effects enable us to more accurately view the phenomenon that causes the failure of the sawblades – vibration. For accurate analysis of the vibration of the spinning sawblade, an approach must be taken, which includes the stiffening of the rotating blade and its effect on the natural frequencies.

A modal analysis of the natural frequencies which includes the spinning sawblade is closer to representing the real world. For example, a spinning sawblade is slightly stiffer than a stationary sawblade because of the centrifugal force effects experienced by the sawbody. “Stiffer” refers to being able to better resist any transverse bending. These centrifugal force effects will work to keep the sawblade in a straight geometry when any cutting forces or vibrations attempt to displace the sawbody in the transverse direction. The true natural frequency of the rotating sawblade is extremely difficult to measure with conventional modal analysis techniques using an accelerometer. Therefore, the analysis from computer models is invaluable.

9.1 *Empirical Study of Natural Frequencies of Sawblade with Expansion Slots*

During our research investigation of the natural frequencies of a sawblade, we tested three actual sawblades of the same dimensions as that modeled in the computer analyses. These empirical tests were performed to validate the computer models’ results with the real world’s results. For the test, we used a data acquisition system called SIG LAB, a modal hammer, an accelerometer, support frame and a bungee cord. The data acquisition and modal hammer are seen in Figure 9.1, and the accelerometer, support frame and bungee cord and 18-in 24 teeth sawblade (***ICE***^{TM} 105-1824-233) is seen in

Figure 9.2. This sawblade has four expansion slots that are 1.5-in long. Shown on the computer screen is the free-vibration frequency response plot of actual results found during the test.

Boundary Conditions, Test Setup. The boundary conditions represented by our test simulate the free-free boundary condition because the sawblade is supported only by the bungee cord going through its bore. Furthermore, the bungee cord is an acceptable way to represent a free-free condition of a heavy object like a sawblade. The accelerometer is mounted to the sawblade using an accelerometer wax specifically developed for vibration testing. Several places were tested on the sawblade during the test to find the best location of the accelerometer for measuring the vibration response indicating the natural frequencies of the sawblade. Measurement of the vibration response at some accelerometer locations would not show all natural frequencies of interest. The best accelerometer location was found by trial-and-error methods. For example, to capture the second mode it was required to move the accelerometer to a different location. Tapping the sawblade with the modal hammer was also done by a best trial-and-error method. Moreover, the correct tip of the modal hammer was also experimented with to find the correct tip that would gently excite the sawblade. Due to the overloading of the sensitive accelerometer, the correct modal hammer tip along with the correct tapping force applied to the sawblade was found by trial-and-error. In the end, it was found that a soft erasure material tip along with an extremely gentle and finessed hammer stroke was the best practice technique to get correct excitation and response measurement of the sawblade. Also notable is that the sawblade gave a barely audible ring when tapped correctly.

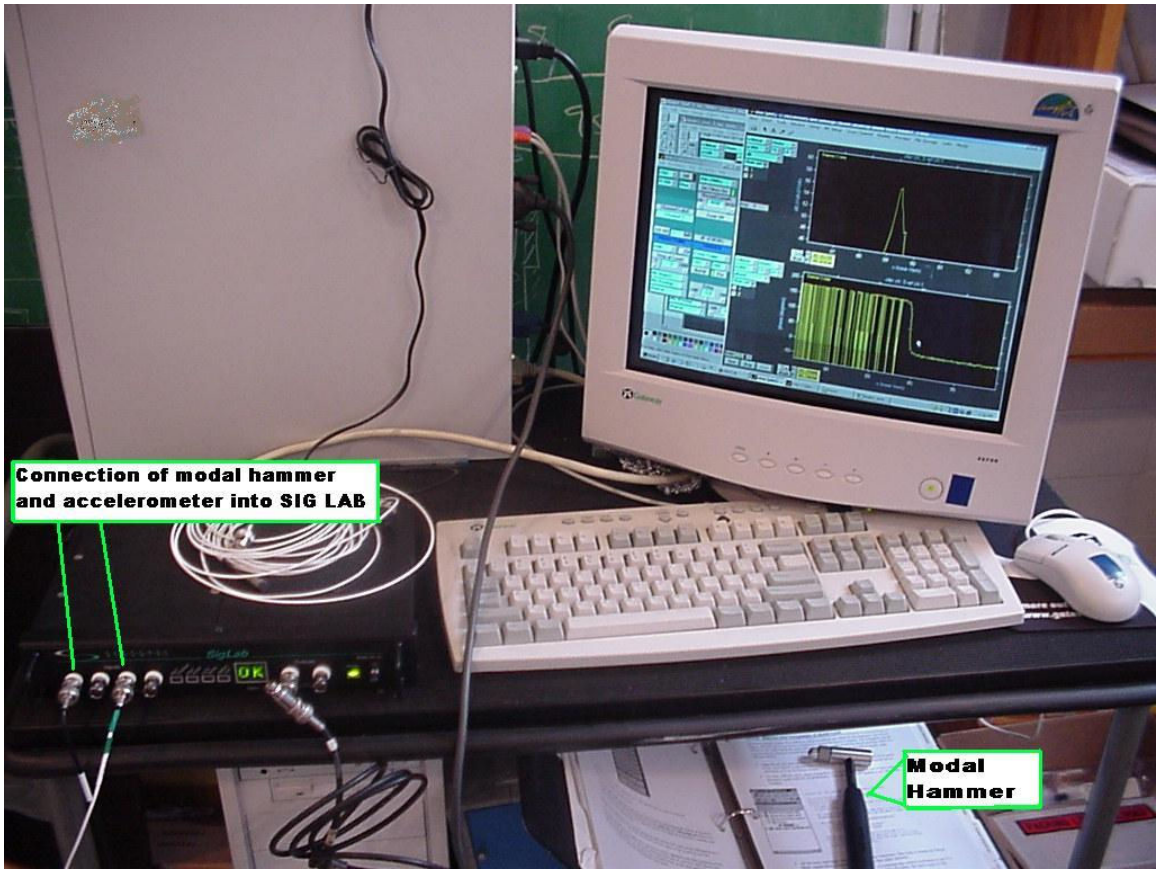

Figure 9.1 Data acquisition computer. The program used is called SIG-LAB. Also shown under the table is the modal hammer used to strike the sawblade (modal hammer wire not shown).

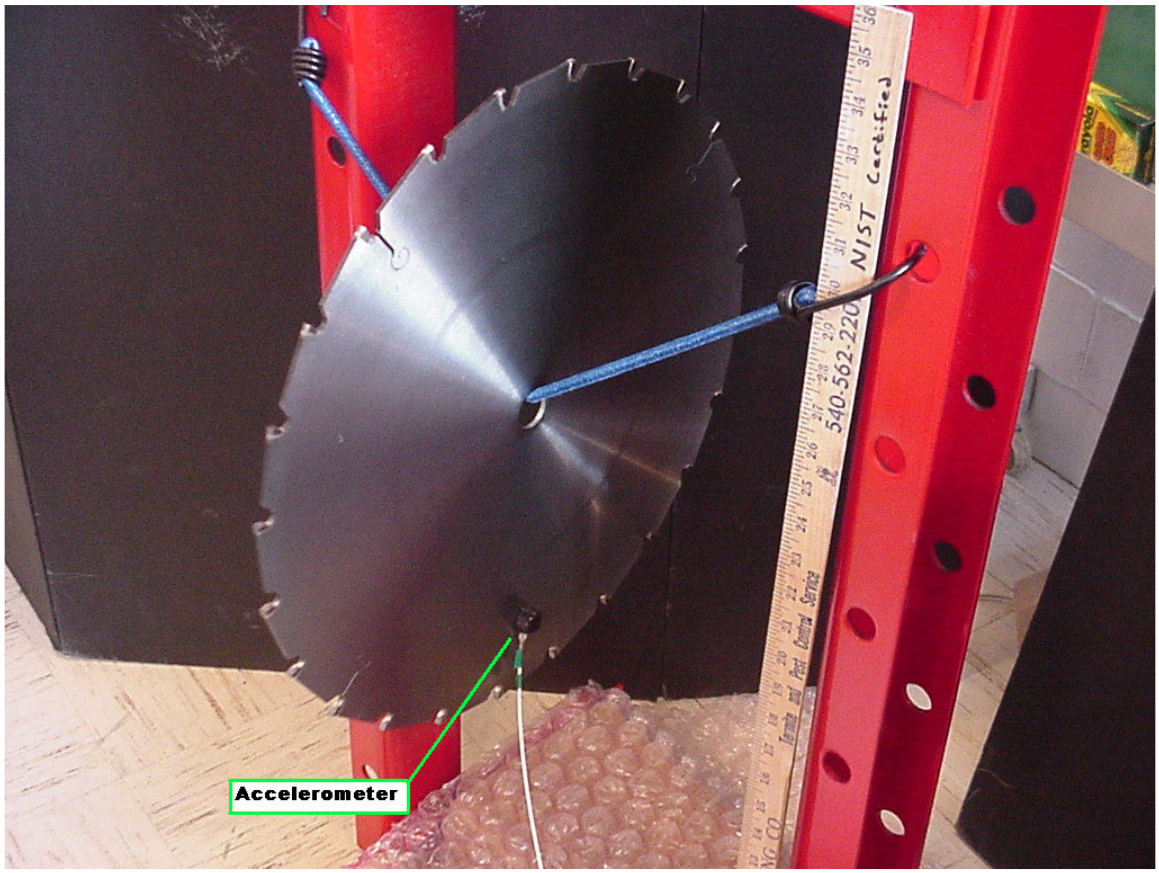

Figure 9.2 Actual test setup showing the 18-in (***ICE***^{TM} 105-1824-233) sawblade suspended in air using a bungee cord. The accelerometer is shown attached to the sawblade.

Results. The results for the first sawblade are shown in the accelerance forced-frequency-response, FRF, of Figure 9.3. An accelerance forced-frequency-response a response of the accelerations with a known force input. The frequencies at which the peaks of the FRF occur in the accelerance FRF versus frequency plot are good estimates of the natural frequencies of the sawblade. In addition, a phase shift of 180 degrees is found at the frequency of a resonance. These peaks show that modes one through four are 89.25, 89.6, 139.5, and 198.3 Hz, respectively.

An interesting phenomenon occurs in a circular disc-shaped object in the many mode shapes is periodic response shapes around the circumferential direction of the sawblade. For example, a blade may displace to either side of the sawblade in the same mode. At this mode, the sawblade has two roots at the same frequency or repeated roots. In other words, the sawblade has two eigenvalues with the same value at the same frequency. This was seen in nearly all tests when zooming into the forced-frequency

response plot around the 89 Hz natural frequency as seen in Figure 9.4**.** Here two distinct peaks can be seen representing the two symmetric mode shapes, which can be considered the same natural frequency, but mirrored images of each other. Without the experience of the FEA modal analysis, and the knowledge of how a circular disk behaves, the graphs of the accelerance FRF do not give enough information to interpret these repeated roots. There are many other modes with repeated roots as will be shown in the finite element modal analysis.

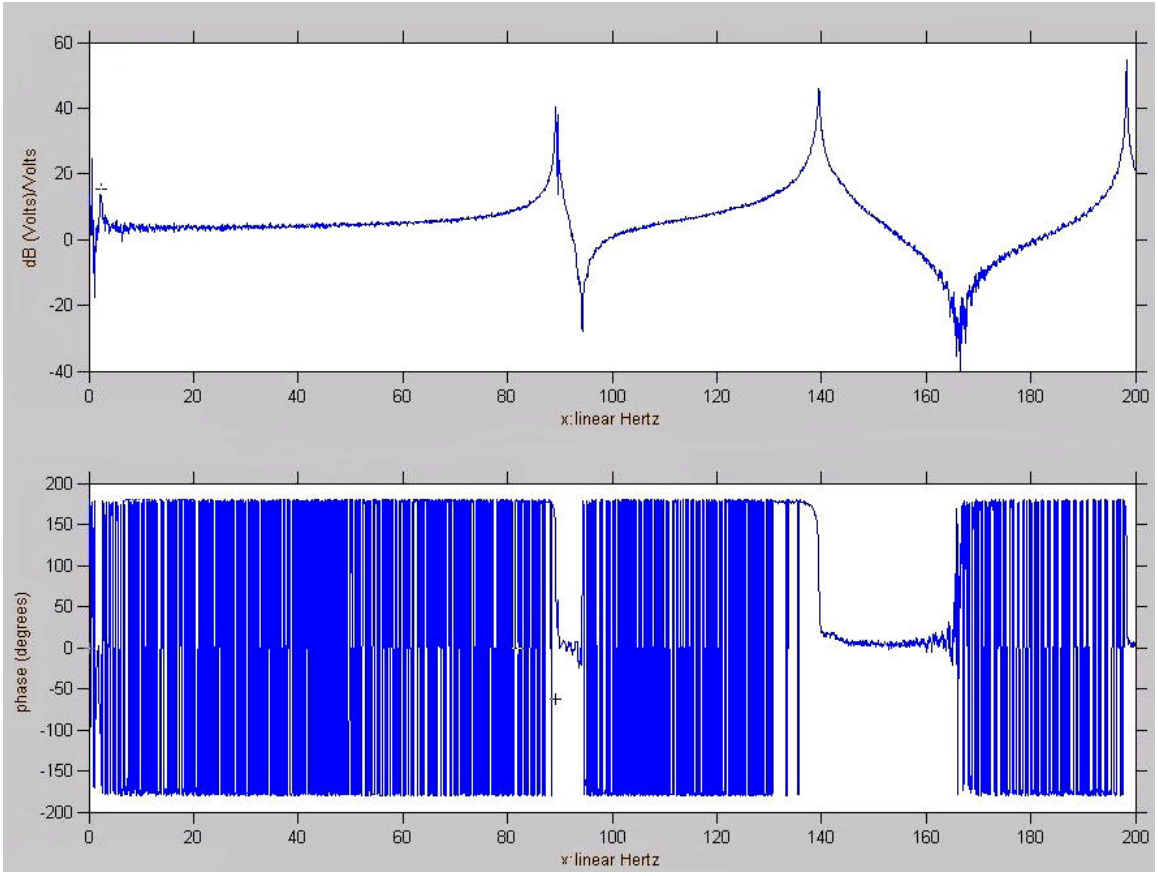

Figure 9.3 Free-vibration frequency response (FRF) of sawblade 1 test 3 showing first four mode shapes, and the corresponding phase shift. Modes one through four are 89.25, 89.6, 139.5, and 198.3 Hz, respectively.

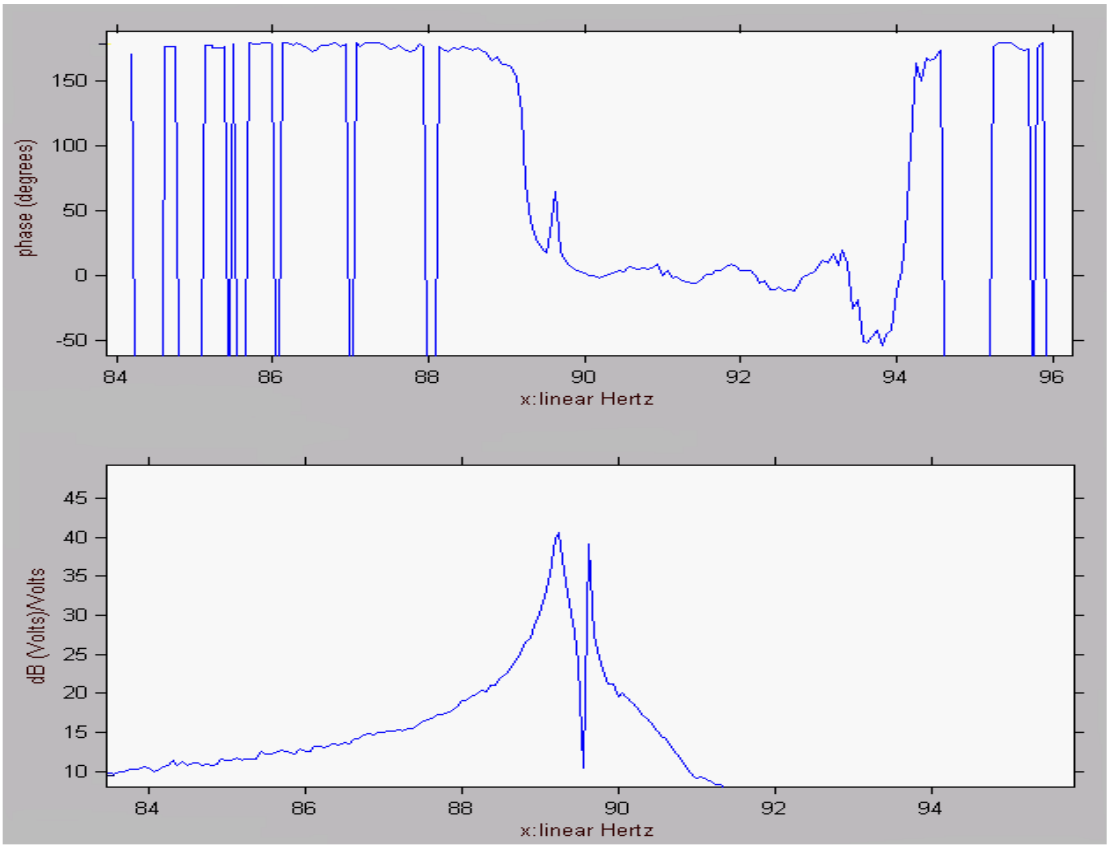

Figure 9.4 Zoomed-in picture of the repeated roots of the first natural frequency occurring at 89.25 and 89.625. This same phenomenon occurred in numerous tests of the three sawblades.

Coherence plots were also reviewed to test the validity of the results of the accelerance FRFs. The coherence plots indicate the experimental data for the acceleration response correlates well with the force input. For example the response is a result of the input. During our analysis, it was common to have coherence of greater than 0.98, as seen in Figure 9.5. A coherence of one is interpreted to mean the output of the system is perfectly correlated with the input, which implies there is no “noise” on the output signal. A coherence of 1.0 is unobtainable in practice.

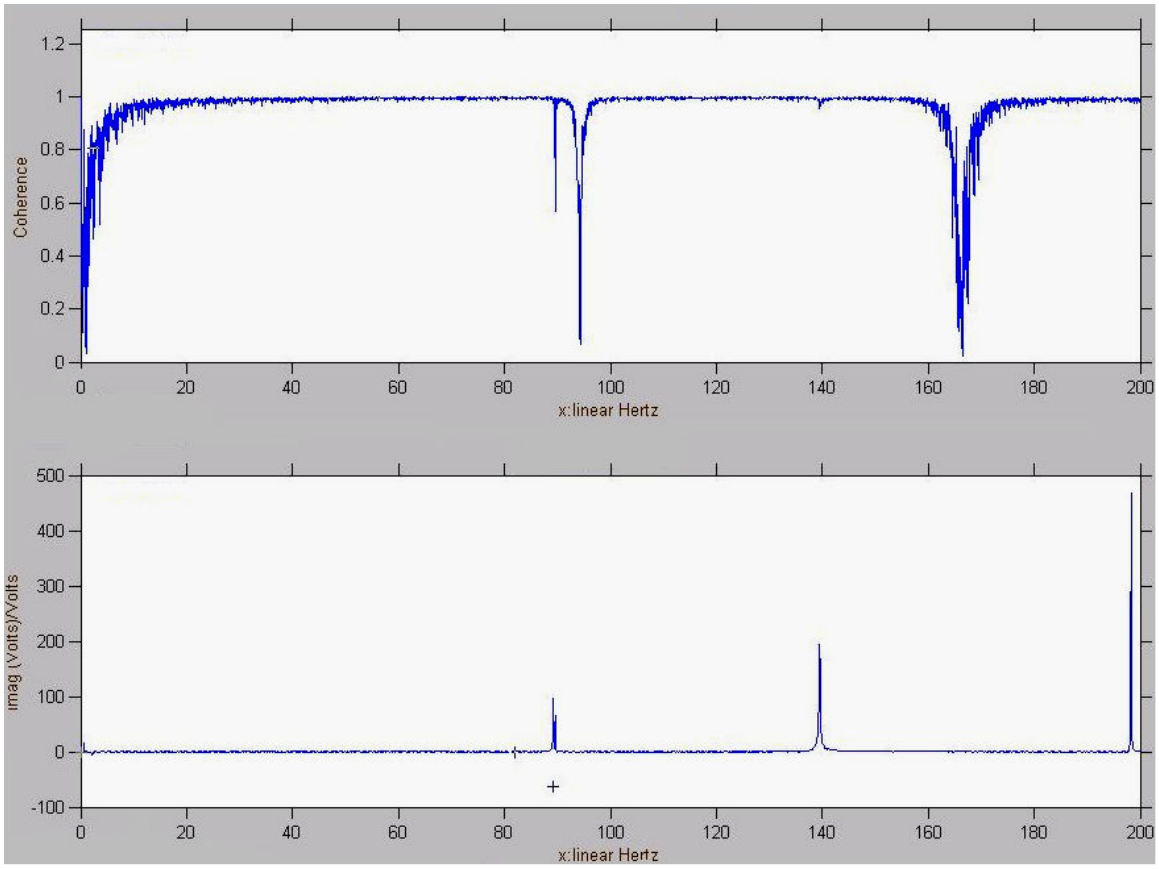

Figure 9.5 Experimental results showing coherence of sawblade 1, test 3 and imaginary parts at the natural frequencies.

The results of the empirical study were consistent between the three sawblades tested, as seen in Table 9-1. For example, the largest difference between the three sawblades was seen at mode three and mode four between sawblade 2 and 3. These results show the highly consistent process applied to the manufacturing of these sawblades.

Table 9-1 Experimental, Free-vibration response of three 18-in (***ICE***™ 105-1824-233) sawblades showing first four natural frequencies and the average of these results.

Sawblade #	Mode 1, frequency, w_o, (Hz)	Mode 2, frequency, w_o, (Hz)	Mode 3, frequency, w_o, (Hz)	Mode 4, frequency, w_o, (Hz)
1	89.25	89.6	139.5	198.3
2	89	89	139	200
3	87.5	91	141.5	198.5
AVG	89	90	140	199

The experimental modal analysis compares very well with the modal analysis from FEA for the free-free sawblade. The results for this computational analysis are compared in Table 9-2. This table shows the high correlation between the analytical results and the empirical results, helping to further validate the research results.

Table 9-2 Free-vibration response (3-D modal analysis) of exact geometry of 18-in (***ICE***^{TM} 105-1824-233) sawblades versus the experimental study results – free-free boundary condition.

Analysis Type	Mode 1, frequency, w_o, (Hz)	Mode 2, frequency, w_o, (Hz)	Mode 3, frequency, w_o, (Hz)	Mode 4, frequency, w_o, (Hz)
Analytical	**89**	**90**	**140**	**199**
Experimental	86.7	91.161	150.02	199.83

9.2 *Natural Frequencies of Annulus With and Without Expansion slots*

To get accurate believable results of the free-vibration modal analysis, models of an annulus were analyzed in both non-rotating and rotating states. As expected, the rotating state had slightly higher natural frequencies. Moreover, models with no-expansion slot were also slightly stiffer and exhibited slightly higher natural frequencies than models with expansion slots. The annulus modeled in this section all had a saw collar boundary condition. The annulus analyzed had the same nominal geometry (blade thickness, inside and outside radius) as the saw blades studied in this thesis. Furthermore, the same material properties of steel were used, as well as the same rotational speeds.

The same boundary conditions were used with the inner radius being a fixed boundary condition. One change from the previous models is the fact that no symmetry about any axis could be used to obtain vibration mode shape results. The reason no symmetry can be used is because the nodes and elements in a free-vibration modal analysis are not all symmetric modes. The modes of vibration include both symmetric and asymmetric mode shapes. Therefore, the thickness represented by the model is exactly the same thickness (instead of half-thickness) as the actual sawblade. In more detail - the modal analysis is the solution (set of eigenvalues and eigenfunctions) that solves the characteristic matrix equation.

Due to the symmetric shape of the sawblade, many modes are repeated and are actually the same mode; this was seen in the experimental modal analysis. However, when solving the eigenvalue matrix equation, each repeated root (eigenvalue) will be unique mathematically. For example, Figure 9.6 shows the repeated mode shapes of mode one and mode two. In the physical world these models are considered the same mode, but they are a unique solution to the eigenvalue problem. Other examples of the 20 modes reported in the analysis of the annulus that can be considered the same mode are modes four and five, six and seven, eight and nine, 10 and 11, 13 and 14, 15 and 16, 17 and 18, and 19 and 20.

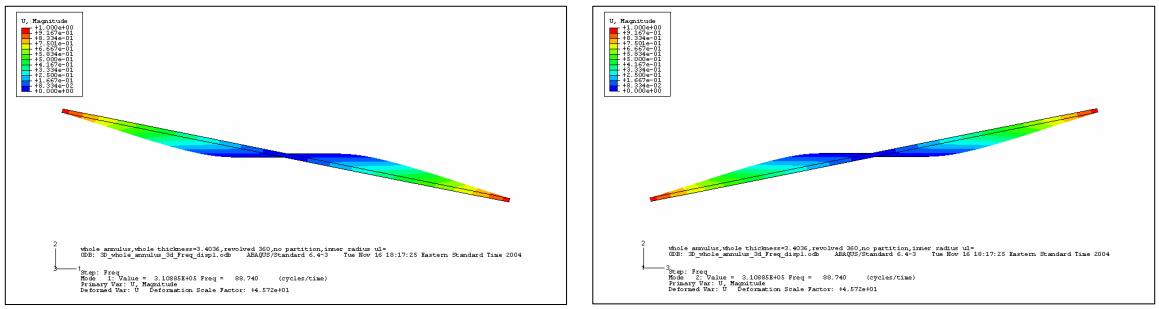

a **b**

Figure 9.6 Symmetric mode shapes of non-rotating annulus. Non-rotating results after convergence for (a) Mode 1 at 97.735 Hz and (b) Mode 2 at 97.735 Hz with sawcollar boundary condition.

Mode three is a unique mode shape and due to its axisymmetric shape can easily be modeled (computationally) as an axisymmetric model. In fact, the bowl-shape mode modal analysis of the 3-D non-rotating sawblade model using linear reduced hexahedral elements agreed quite well with the axisymmetric first mode having converged results of 93.047 Hz and 93.382, respectively. Figure 9.7 and Figure 9.8 show a graphical representation of the solved first axisymmetric mode shape.

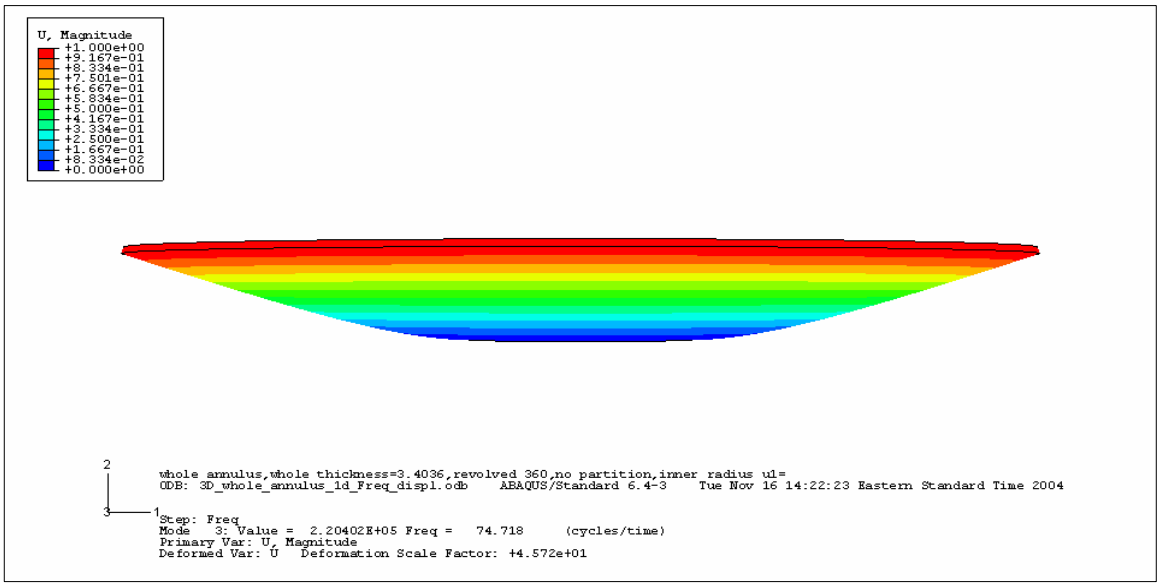

Figure 9.7 Mode three of 3-D model - bowl shape mode.

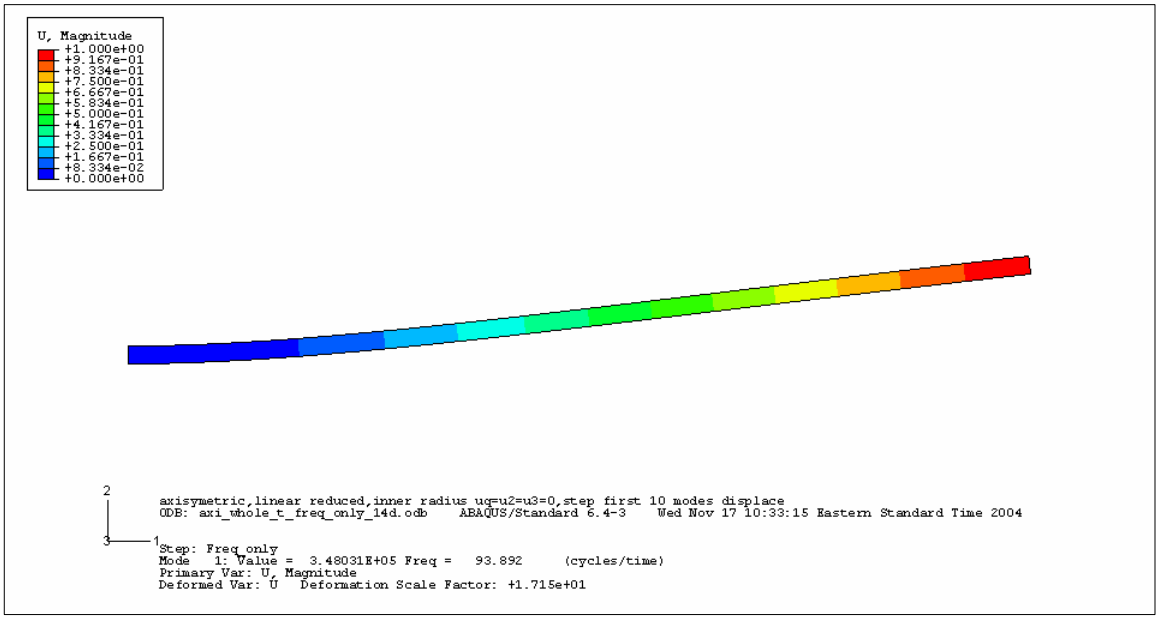

Figure 9.8 Mode one of axisymmetric model - bowl shape mode.

For the results of the converged 3-D annulus modal analysis of natural frequencies one through 15 using full integration hexahedral elements see Table 9-3. In this table, the annulus natural frequencies are analyzed for both the non-rotating and rotating model states. In both cases, the boundary condition of the annulus is to have the inner radius fixed representing the clamping forces of the saw collar. To get these results the analysis was done in three steps. The first was to perform a modal analysis to obtain the natural frequencies in a non-rotating state. Second, rotate the annulus at 2166 rpm

allowing the stresses from the centrifugal forces to come into effect. Third, perform another modal analysis with these newfound stresses found throughout the annulus. The increase in the natural frequency from the increased stiffness of the annulus due to the stresses from centrifugal forces is generally approximately 10 Hz for all modes compared to the non-rotating state.

Table 9-3 Converged 3-D annulus without expansion slots modal analysis of natural frequencies one through 15 using full integration hexahedral elements (saw collar boundary condition).

NON-ROTATING FREQUENCY			ROTATING FREQUENCY		
two-peak mode =	98	Hz	two-peak mode =	106	Hz
two-peak mode (symmetric) =	98	Hz	two-peak mode (symmetric) =	106	Hz
bowl-shape mode =	106	Hz	bowl-shape mode =	112	Hz
four-peak mode =	124	Hz	four-peak mode =	135	Hz
four-peak mode (symmetric) =	125	Hz	four-peak mode (symmetric) =	136	Hz
six-peak mode =	242	Hz	six-peak mode =	251	Hz
six-peak mode (symmetric) =	242	Hz	six-peak mode (symmetric) =	251	Hz
eight-peak mode =	420	Hz	eight-peak mode =	428	Hz
eight-peak mode (symmetric) =	432	Hz	eight-peak mode (symmetric) =	440	Hz
ten-peak mode =	662	Hz	ten-peak mode =	669	Hz
ten-peak mode (symmetric) =	662	Hz	ten-peak mode (symmetric) =	669	Hz
upside-down cake pan mode =	674	Hz	upside-down cake pan mode =	681	Hz
first center body mode =	703	Hz	first center body mode =	710	Hz
first center body mode (symm) =	703	Hz	first center body mode (symm) =	710	Hz

Annulus with Expansion Slots Modal Analysis. For the next analysis, four expansion slots were added to the annulus beginning with 1.5-in, the popular length used in the sawblades represented by the annulus. Varying the annulus length from 1.5 to three inches in increments of ½-in allowed for a good comparison to base the results of the actual sawblade models analyzed later. The stop hole at the end of each of these expansion slot lengths was ½-in in diameter. Each analysis used the most common number of expansion slots for the sawblade model with four expansion slots. The same mode shapes and phenomenon of the repeating symmetric modes was also seen in the expansion slot analyses. Results for the first 15 modes of these varying slot lengths were found along with the non-rotating and rotating results. Again, mode one and mode two

were symmetric modes and mode three was the bowl-shape mode. Mode shape one, two and three are the most important in our analyses because these modes have the most energy and are the most likely the ones to do the most damage to the actual sawblades. The first and third modes can bee seen in Figure 9.9.

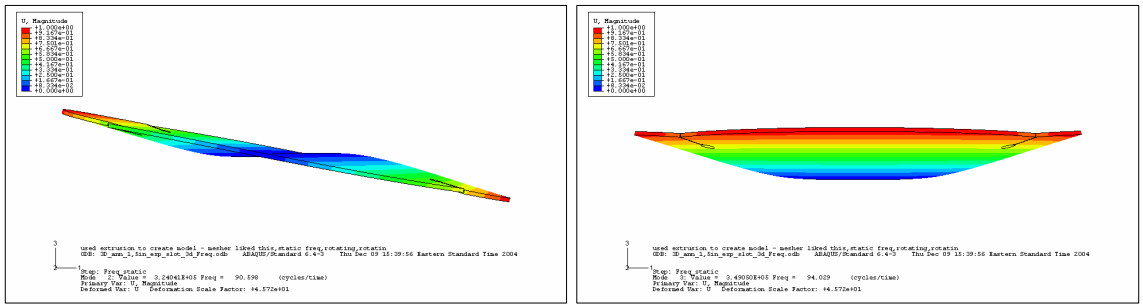

a **b**

Figure 9.9 Annulus with four expansion slots 1.5-in long. (a) first mode shape and (b) third mode is bowl-shape.

The difference in the mode shapes of the annulus with and without expansion slots is shown in Figure 9.10. Here it can be seen that the approximate mode shape of the annulus with expansion slots has a displacement peak at the outer tip one side of the expansion slot. However, because a modal analysis does not take into account any input force, the displacement magnitude results cannot be directly compared between the models or different mode shapes of the same model. Further study using a transient response analysis with varied frequency and consistent amplitude inputs would need to be performed to quantify the differences in the dynamic displacement between models.

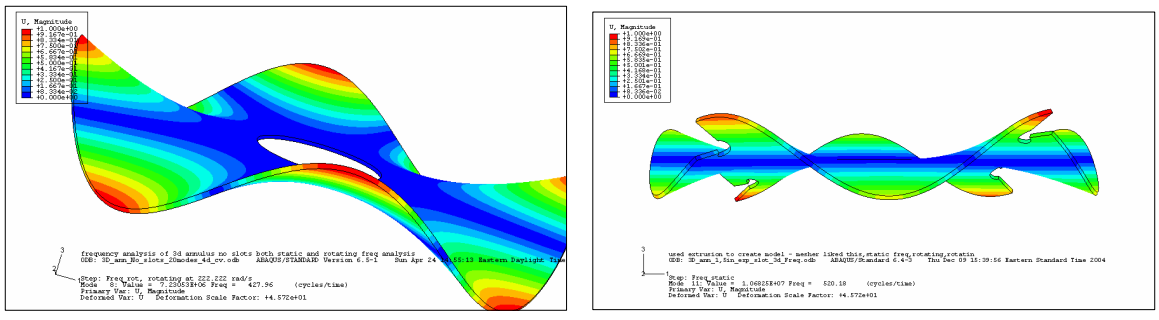

a **b**

Figure 9.10 Eight-peak mode shape of annulus. (a) without expansion slot and (b) with four, 1.5-in expansion slots.

An interesting phenomenon happens with the mode shapes associated with higher natural frequencies. The displacement peaks are no longer only at the outer rim, but are now within the center area of the body. Hence the naming of this type of mode shape – first center body mode shape. This mode shape is seen in Figure 9.11.

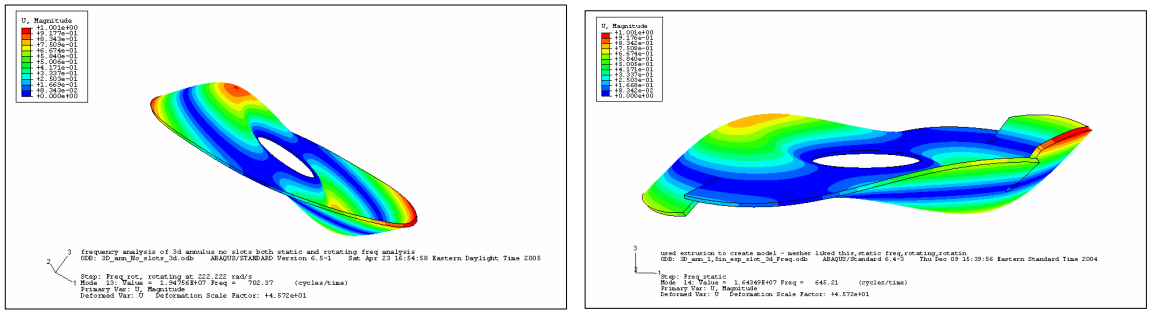

a b

Figure 9.11 First center body mode shape of annulus. (a) without expansion slot and (b) with four, 1.5-in expansion slots.

Results. The results of the annulus with four, 1.5-in expansion slots showing the natural frequency values of non-rotating and rotating analysis is seen in Table 9-4. The natural frequencies drop slightly compared to the annulus without expansion slots seen in Table 9-3. For example, a six percent difference is found when the two-peak mode with the no-expansion slot case and the 4, 1.5-in expansion slot case (using the same mesh size and approximately the same number of elements and converged solutions). Likewise, when comparing the bowl-shape modes between the no-expansion slot and the four, 1.5-in expansion slot cases it is found there is only a nine percent difference. The break in the geometry at the expansion slots allows for a less stiff circular plate, this causes the natural frequencies to be lower for the expansion slot cases.

Table 9-4 Converged 3-D annulus with four, 1.5-in expansion slots modal analysis of natural frequencies one through 15 using full integration hexahedral elements (saw collar boundary condition).

NON-ROTATING FREQUENCY			ROTATING FREQUENCY		
two-peak mode =	92	Hz	**two-peak mode =**	101	Hz
two-peak mode (symmetric) =	92	Hz	**two-peak mode (symmetric) =**	101	Hz
bowl-shape mode =	96	Hz	**bowl-shape mode =**	103	Hz
four-peak mode =	115	Hz	**four-peak mode =**	127	Hz
four-peak mode (symmetric) =	116	Hz	**four-peak mode (symmetric) =**	127	Hz
six-peak mode =	206	Hz	**six-peak mode =**	216	Hz
six-peak mode (symmetric) =	209	Hz	**six-peak mode (symmetric) =**	219	Hz
eight-peak mode =	348	Hz	**eight-peak mode =**	356	Hz
eight-peak mode (symmetric) =	351	Hz	**eight-peak mode (symmetric) =**	359	Hz
ten-peak mode =	521	Hz	**ten-peak mode =**	528	Hz
ten-peak mode (symmetric) =	527	Hz	**ten-peak mode (symmetric) =**	534	Hz
upside-down cake pan mode =	618	Hz	**upside-down cake pan mode =**	626	Hz
first center-body mode =	648	Hz	**first center-body mode =**	657	Hz
first center body mode (symm) =	649	Hz	**first center body mode (symm) =**	657	Hz
twelve-peak mode =	688	Hz	**twelve-peak mode =**	694	Hz

Beyond changing the 1.5-in expansion slot length to 2.5-in length, the slot length does not have much effect on changing the natural frequency. For another comparison example from the non-rotating analysis results, the first mode (two-peak mode) and second mode (bowl-shaped mode) have only one and zero percent differences between 1.5-in and 2-in (using the same mesh size and approximately the same number of elements), respectively. Also, the change between having four, 2-in and four, 2.5-in expansion slots has only a two percent difference for both the two-peak mode and the bowl-shape mode. More examples of the differences between the first 15 non-rotating natural frequencies for varying expansion slot lengths are seen in Table 9-5 for the non-rotating cases and Table 9-6 for the rotating cases. More on varying expansion slot lengths for a sawblade model will be discussed in the next sections.

Table 9-5 Converged results of 3-D non-rotating annulus with varying expansion slot lengths (saw collar boundary condition).

Number of Expansion Slots, Length	**0, 0**-in	**4, 1.5**-in	**4, 2**-in	**4, 2.5**-in
NON-ROTATING FREQUENCY				
two-peak mode =	98 Hz	92 Hz	93 Hz	91 Hz
two-peak mode (symmetric) =	98 Hz	92 Hz	93 Hz	91 Hz
bowl-shape mode =	106 Hz	96 Hz	96 Hz	94 Hz
four-peak mode =	124 Hz	115 Hz	113 Hz	109 Hz
four-peak mode (symmetric) =	125 Hz	116 Hz	116 Hz	113 Hz
six-peak mode =	242 Hz	206 Hz	197 Hz	188 Hz
six-peak mode (symmetric) =	242 Hz	209 Hz	198 Hz	188 Hz
eight-peak mode =	420 Hz	348 Hz	315 Hz	285 Hz
eight-peak mode (symmetric) =	432 Hz	351 Hz	332 Hz	322 Hz
ten-peak mode =	662 Hz	521 Hz	471 Hz	428 Hz
ten-peak mode (symmetric) =	662 Hz	527 Hz	472 Hz	429 Hz
upside-down cake pan mode =	674 Hz	618 Hz	583 Hz	499 Hz
first center body mode =	703 Hz	648 Hz	621 Hz	602 Hz
first center body mode (symm) =	703 Hz	649 Hz	646 Hz	623 Hz
second center body mode =	802 Hz	688 Hz	647 Hz	624 Hz

Table 9-6 Converged results of 3-D rotating annulus with varying expansion slot lengths (saw collar boundary condition).

Number of Expansion Slots, Length	**0**	**4, 1.5**-in	**4, 2**-in	**4, 2.5**-in
ROTATING FREQUENCY				
two-peak mode =	106 Hz	101 Hz	102 Hz	100 Hz
two-peak mode (symmetric) =	106 Hz	101 Hz	102 Hz	100 Hz
bowl-shape mode =	112 Hz	103 Hz	104 Hz	102 Hz
four-peak mode =	135 Hz	127 Hz	124 Hz	120 Hz
four-peak mode (symmetric) =	136 Hz	127 Hz	127 Hz	124 Hz
six-peak mode =	251 Hz	216 Hz	206 Hz	197 Hz
six-peak mode (symmetric) =	251 Hz	219 Hz	207 Hz	197 Hz
eight-peak mode =	428 Hz	356 Hz	323 Hz	292 Hz
eight-peak mode (symmetric) =	440 Hz	359 Hz	340 Hz	329 Hz
ten-peak mode =	669 Hz	528 Hz	478 Hz	434 Hz
ten-peak mode (symmetric) =	669 Hz	534 Hz	479 Hz	435 Hz
upside-down cake pan mode =	681 Hz	626 Hz	589 Hz	505 Hz
first center-body mode =	710 Hz	657 Hz	630 Hz	612 Hz
first center body mode (symm) =	710 Hz	657 Hz	655 Hz	632 Hz
second center body mode =	810 Hz	694 Hz	656 Hz	633 Hz

9.3 *Natural Frequencies of Sawblade without Expansion Slots*

As expected, the natural frequencies of the sawblade are slightly lower than the natural frequencies of the annulus. This is due to the added mass of the carbide, and the loss of steel at the gullets. This loss of steel gives way to some loss of stiffness at the

outer rim of the sawblade versus the annulus' solid outer rim. Moreover, due to the steel of the shoulder and tip pocket hanging away from the majority of the sawblade's more solid geometry of its sawbody gives way to less stiffness versus the annulus. The natural frequency results for the nail cutting sawblade (***ICE***™ 105-1824-233) are seen in Table 9-7 where the sawblade has a saw collar boundary condition. All sawblades analyzed from here to the end of this chapter have a saw collar boundary condition.

Table 9-7 Sawblade (***ICE***™ 105-1824-233) sawblades converged modal analysis results.

NON-ROTATING FREQUENCY			ROTATING FREQUENCY		
two-peak mode =	98	Hz	**two-peak mode =**	107	Hz
two-peak mode (symmetric) =	99	Hz	**two-peak mode (symmetric) =**	108	Hz
bowl-shape mode =	103	Hz	**bowl-shape mode =**	109	Hz
four-peak mode =	124	Hz	**four-peak mode =**	135	Hz
four-peak mode (symmetric) =	124	Hz	**four-peak mode (symmetric) =**	135	Hz
six-peak mode =	220	Hz	**six-peak mode =**	230	Hz
six-peak mode (symmetric) =	221	Hz	**six-peak mode (symmetric) =**	231	Hz
eight-peak mode =	363	Hz	**eight-peak mode =**	372	Hz
eight-peak mode (symmetric) =	381	Hz	**eight-peak mode (symmetric) =**	389	Hz
ten-peak mode =	561	Hz	**ten-peak mode =**	569	Hz
ten-peak mode (symmetric) =	563	Hz	**ten-peak mode (symmetric) =**	571	Hz
upside-down cake pan mode =	644	Hz	**upside-down cake pan mode =**	652	Hz
first center-body mode =	678	Hz	**first center-body mode =**	686	Hz
first center body mode (symm) =	679	Hz	**first center body mode (symm) =**	687	Hz
twelve-peak mode =	776	Hz	**twelve-peak mode =**	784	Hz

Again, the same phenomenon as seen in the case of the modal analysis of the spinning annulus, there are repeated modes due to symmetry of the geometry, boundary conditions, material properties, and loading. This phenomenon is seen throughout these analyses and for this reason when analyzing the models, mode one and two can easily be considered to be the same mode of the structure. Other examples of the modes reported for the annulus that can be considered the same mode are defined in the tables of results for the model. Though the symmetric mode shapes are nearly the same in all analyses, there are some deviations as the modes get higher in frequency.

Many of the mode shapes of the nail cutting sawblade (***ICE***™ 105-1824-233) seen in Table 9-7 are seen in Figure 9.12. Figure 9.12 shows the approximate mode shapes the sawblade will undergo when excited upon impact with a nail. The first few mode shapes contain the highest energy and, therefore will cause the most damage to the structure of the sawbody, and attempt to shorten the life of the sawblade. The higher

mode shapes are a combination of displacement peaks located at the outer tips and displacements of the inner sawbody. These higher mode shapes vary widely and are shown in Figure 9.12 (a) through (i).

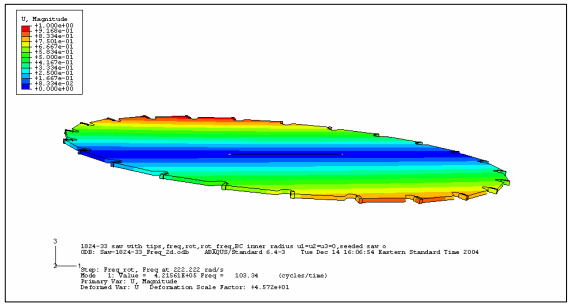

a

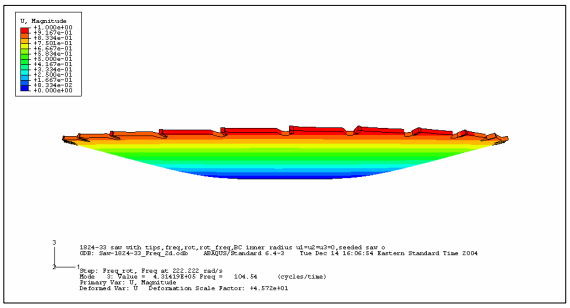

b

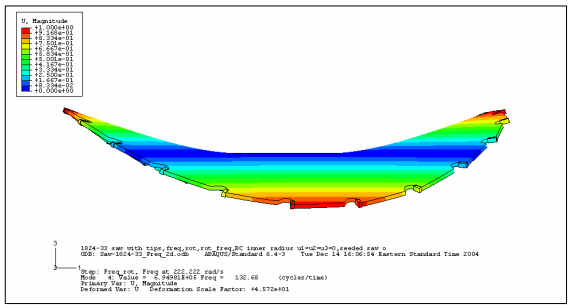

c

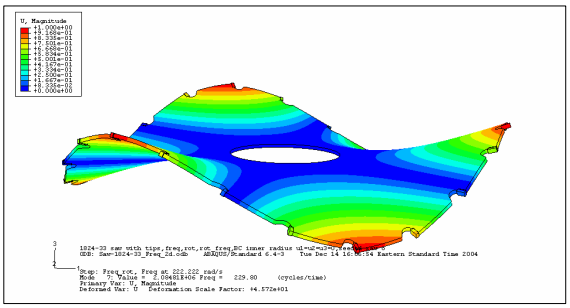

d

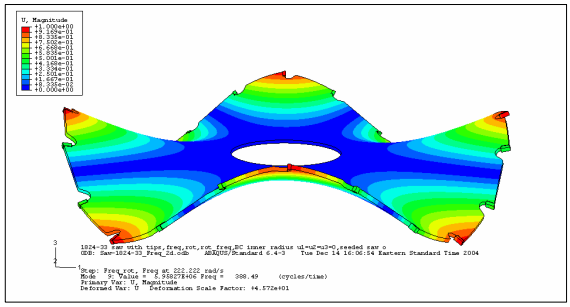

e

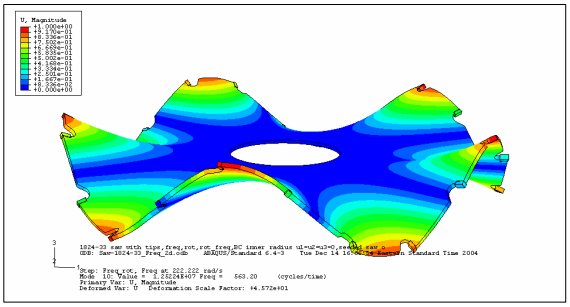

f

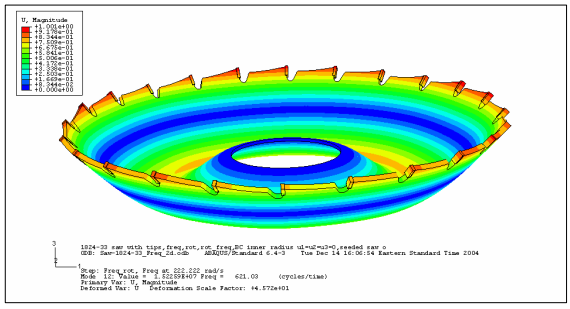

g

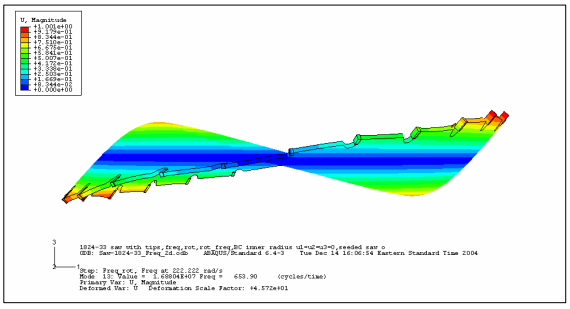

h

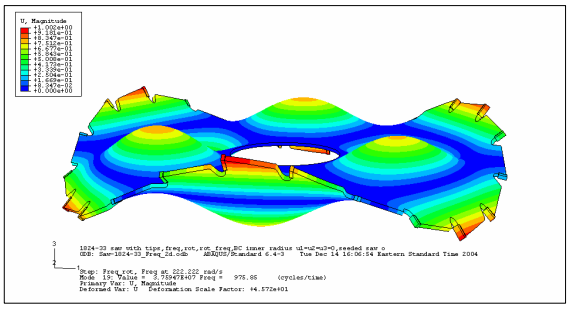

i

Figure 9.12 Mode shapes of nail cutting sawblade **(*ICE*™ 105-1824-233)**. (a) two-peak mode, (b) bowl-shape mode, (c) four-peak mode, (d) six-peak mode, (e) eight-peak mode, (f) ten-peak mode, (g) upside-down cake pan mode, (h) first center-body mode, (i) higher mode shape.

During the modal analysis of the sawblade, an analysis of the standard sawblade was also performed to get a general behavior of an 18 inch sawblade at its natural frequencies. The data for the modal analysis of the standard sawblade with no-expansion slots is found in Table 9-8. The rotating and non-rotating sawblades were relatively close in natural frequencies. The largest deviation between the standard sawblade and the nail cutting sawblade for the first ten modes was only 2.7 percent difference. Also, the mode shapes are very nearly the same. The mode shapes for the standard sawblade are seen in Figure 9.13.

Table 9-8 Standard sawblade converged modal analysis results.

NON-ROTATING FREQUENCY			ROTATING FREQUENCY		
two-peak mode =	100	Hz	**two-peak mode =**	108	Hz
two-peak mode (symmetric) =	100	Hz	**two-peak mode (symmetric) =**	108	Hz
bowl-shape mode =	102	Hz	**bowl-shape mode =**	109	Hz
four-peak mode =	127	Hz	**four-peak mode =**	138	Hz
four-peak mode (symmetric) =	127	Hz	**four-peak mode (symmetric) =**	138	Hz
six-peak mode =	223	Hz	**six-peak mode =**	232	Hz
six-peak mode (symmetric) =	223	Hz	**six-peak mode (symmetric) =**	232	Hz
eight-peak mode =	360	Hz	**eight-peak mode =**	368	Hz
eight-peak mode (symmetric) =	378	Hz	**eight-peak mode (symmetric) =**	387	Hz
ten-peak mode =	550	Hz	**ten-peak mode =**	557	Hz

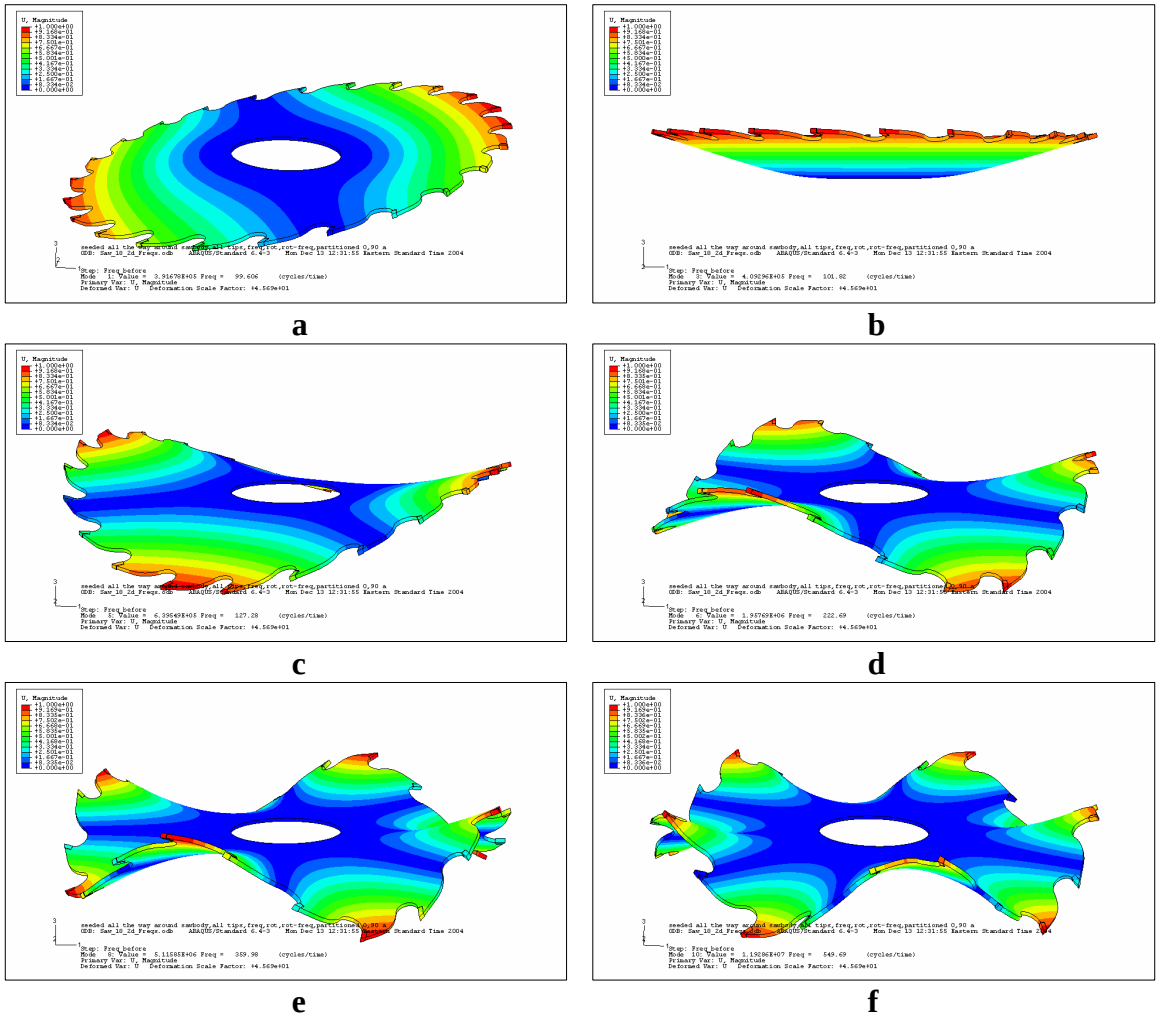

Figure 9.13 Mode shapes of standard 18-in 24 tooth sawblade. (a) two-peak mode, (b) bowl-shape mode, (c) four-peak mode, (d) six-peak mode, (e) eight-peak mode, (f) ten-peak mode.

9.3.1 Varying Expansion Slot Lengths of Sawblade with Four Expansion Slots

Varying the expansion slot lengths of the nail cutting sawblade (***ICE***™ 105-1824-233) does not raise the natural frequency as one may assume. For example, having expansion slot lengths of one inch and performing a rotating sawblade modal analysis yields first, second and third natural frequencies of 106, 106 and 107 Hertz, respectively. Likewise, the same analysis having a length of expansion slots two and one half inches, has first, second and third natural frequencies of 105, 105 and 106 Hertz. These values of

the natural frequencies are converged to within two percent difference. As in the analysis of the sawblades with out expansion slots, there are several mode shapes obtained from the modal analysis solution (including the first and second mode) that can be considered the same mode.

The analysis results of varying expansion slots of the nail cutting sawblade (***ICE***^{TM} 105-1824-233) are seen in Table 9-9 and Table 9-10. After analyzing this sawblade with seven various lengths from one to 2.5 inches, in increments of a quarter inch, the data reveals that the natural frequency does not significantly change with varying expansion slot lengths. Changing the expansion slot lengths does affect the order of some of the higher mode shapes.

Table 9-9 Converged natural frequencies of the nail cutting sawblade (***ICE***^{TM} 105-1824-233) with varying expansion slot lengths.

Rotating Analysis						
Number of Expansion Slots	**0**	**4 Exp. Slots**				
Expansion slot length, (inches)	**N/A**	**1**	**1.25**	**1.5**	**1.75**	**2**
two-peak mode =	107 Hz	106	105	104	105	105
two-peak mode (symmetric) =	108	106	105	104	105	105
bowl-shape mode =	109	107	107	106	107	106
four-peak mode =	135	131	130	129	128	126
four-peak mode (symmetric) =	135	134	132	129	129	128
six-peak mode =	230	222	217	211	208	202
six-peak mode (symmetric) =	231	222	218	212	208	203
eight-peak mode =	372	358	345	330	317	302
eight-peak mode (symmetric) =	389	363	355	346	342	334
ten-peak mode =	569	531	512	489	469	446
ten-peak mode (symmetric) =	571	533	513	490	471	446
upside-down cake pan mode =	652	641	637	631	634	633
first center body mode =	686	674	668	660	660	655
first center body mode (symm) =	687	676	669	661	661	656
12-peak mode =	784	709	662	613	569	525
12-peak mode (symmetric) =	787	739	720	701	690	676
second center body mode =	809	790	786	781	786	781
second center body mode (symm) =	810	798	791	783	789	789
14-peak mode =	1010	938	887	839	801	765
14-peak mode (symmetric) =	1014	941	888	839	803	767

Table 9-10 Converged natural frequencies of the nail cutting sawblade (***ICE***™ 105-1824-233) with varying expansion slots.

Rotating Analysis		
Number of Expansion Slots	**4 Exp. Slots**	
Expansion slot length, (inches)	**2.25**	**2.5**
two-peak mode =	104 Hz	105
two-peak mode (symmetric) =	104	105
bowl-shape mode =	105	106
four-peak mode =	123	121
four-peak mode (symmetric) =	127	128
six-peak mode =	196	190
six-peak mode (symmetric) =	196	191
eight-peak mode =	283	266
eight-peak mode (symmetric) =	327	322
ten-peak mode =	423	402
ten-peak mode (symmetric) =	423	403
upside-down cake pan mode =	629	455
first center body mode =	646	632
first center body mode (symm) =	647	642
12-peak mode =	488	643
12-peak mode (symmetric) =	660	651
second center body mode =	782	730
second center body mode (symm) =	747	730
14-peak mode =	767	737
14-peak mode (symmetric) =	767	784

One phenomenon resulting from a sawblade with expansion slots versus one without is the fact that the mode shapes tend to align themselves with the expansion slots. This ensures that the same flexure point at the expansion slot will be the point of fatigue failure in the sawblade at the expansion slot and will again be a cause of failure in the sawblade. The expansion slot is critical section in the design of the sawblade due to the way the stresses from rotating, cutting and vibration modes all concentrate at the bottom of the expansion slot. This flexure about the expansion slots is illustrated well in Figure 9.14 where the expansion slot is two inches in length and the four-peal mode shape is shown. The sawblade will open in both directions about the expansion slot at a frequency

of 126 times per second. It is assumed, even at low energy levels, that it does not take long to fatigue a sawblade at these rotational speeds.

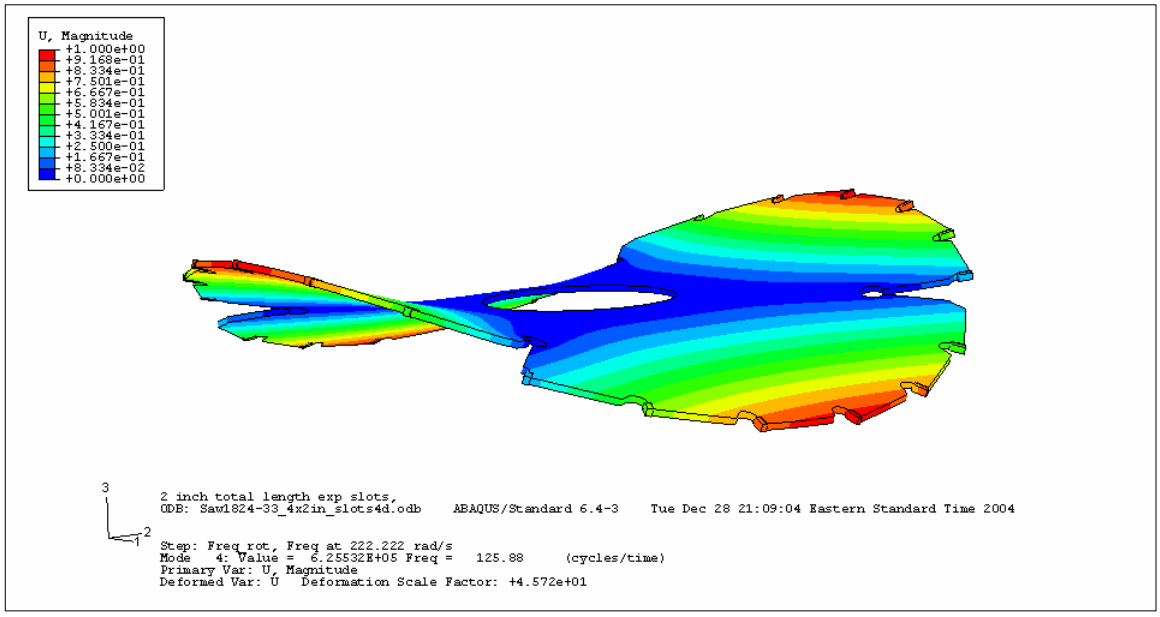

Figure 9.14 Four peak mode of ***ICE***™ 105-1824-233 sawblade with four, two inch expansion slots. Figure illustrates the expansion slots acting like flexure points of this mode shape.

Examples of other mode shapes where the expansion slots act as a point of flexure for the vibrating sawblade are seen in Figure 9.15. Having a sawblade with expansion slots does not guarantee that all vibration modes will flex at the point of the expansion slot, but it is a highly likely occurrence for various mode shapes. This phenomenon is seen for the various expansion slot lengths analyzed. However, the longer the expansion slot length, the more pronounced this displacement becomes for a lower frequency mode shape. Therefore, the longer expansion slots would be more susceptible to larger displacements at the expansion slots, and would likely fail in fatigue earlier than a sawblade with shorter expansion slots.

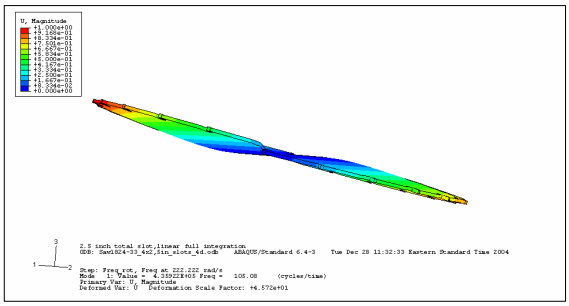

a

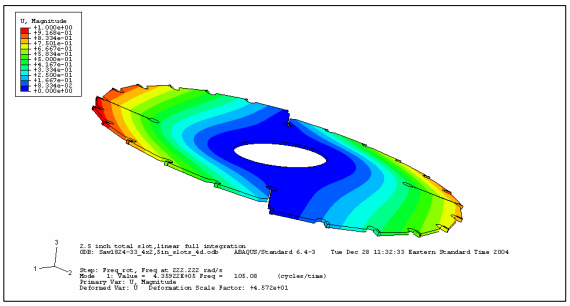

b

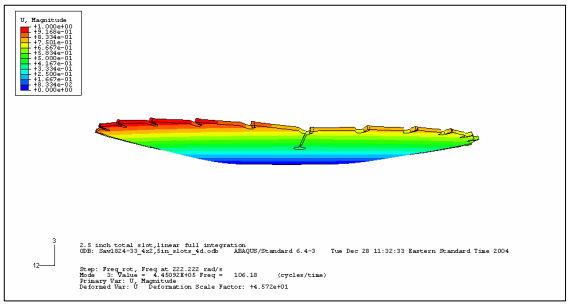

c

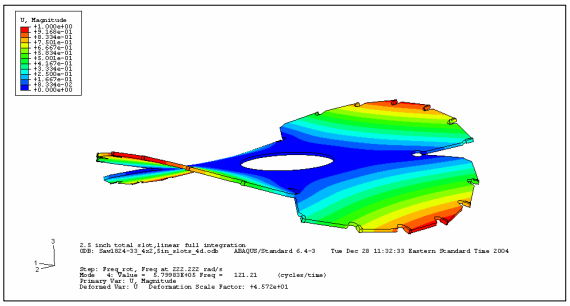

d

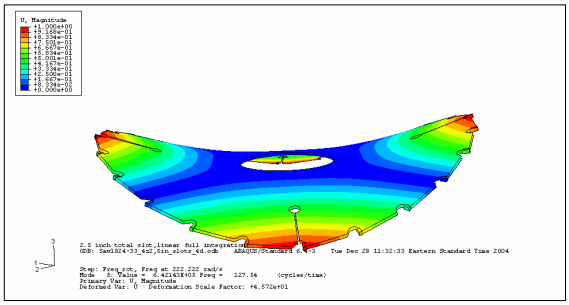

e

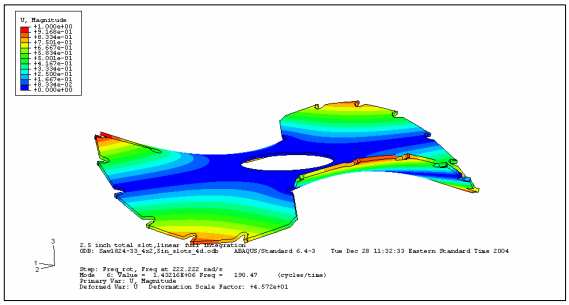

f

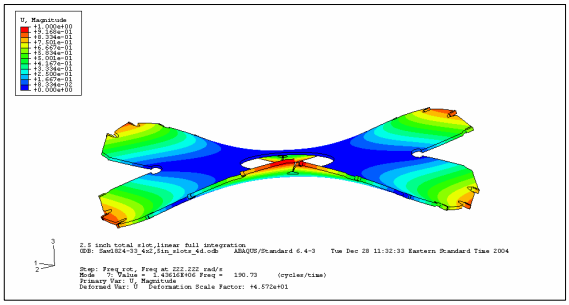

g

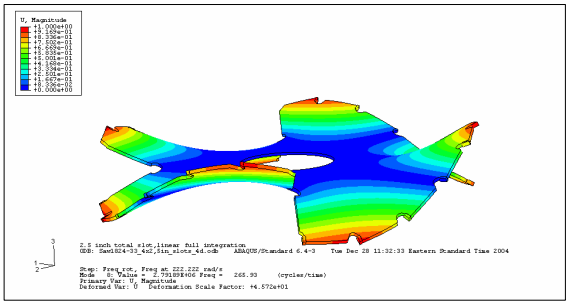

h

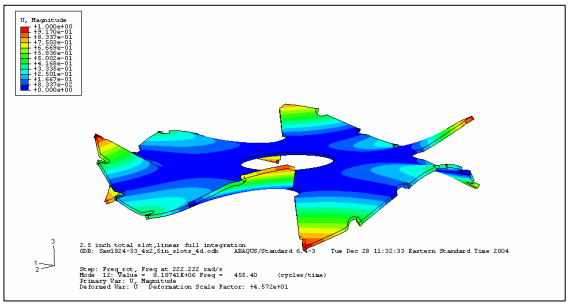

i

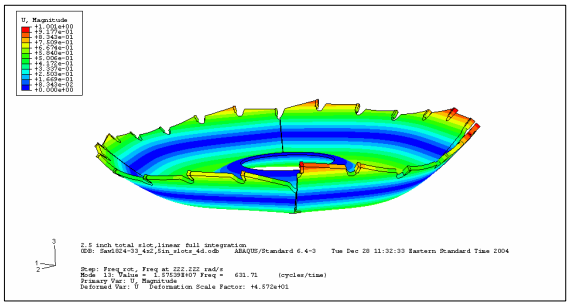

j

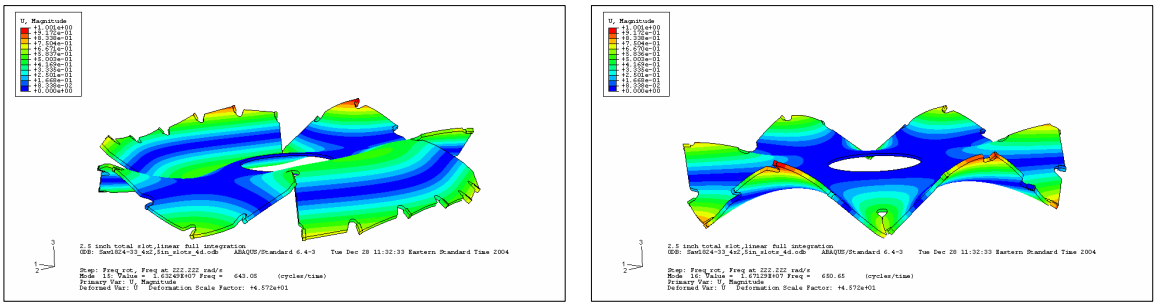

k **l**

Figure 9.15 Various mode shapes of ***ICE***™ 105-1824-233 sawblade with four, 2.5 inch expansion slots. (a) two-peak mode, (b) two-peak mode (symmetric), (c) bowl-shape mode, (d) four-peak mode, (e) four-peak mode symmetric, (f) six-peak mode, (g) six-peak mode symmetric, (h) eight-peak mode, (i) ten-peak mode, (j) upside-down cake pan mode, (k) first center body mode, and (l) twelve-peak mode.

The desire is to find the expansion slot lengths and numbers for a given sawblade that results in the highest first, second, third and successive natural frequencies. This will help ensure the sawblade operates farther away from the natural frequencies and does not excite the first several natural frequencies with the highest energy levels. Having these higher frequencies results in a sawblade that will have a greater longevity and be able to run longer and cut truer throughout its lifetime versus a sawblade with lower natural frequencies.

9.3.2 Varying Number of Expansion Slots of Sawblade with Best Expansion Slot Length

This research also includes a study to determine if varying the number of expansion slots would have an effect on raising the natural frequency of the sawblade. Again, the nail cutting ***ICE***™ 105-1824-233 sawblade was used with the saw collar boundary condition. The results from changing the number of expansion slots gave better results than varying the length of the slots. For this analysis, slot lengths of 1.25 inches (31.75 mm) were used. Due to the number of teeth, gullets, and shoulders being 24, the few ways to evenly divide 24 used three, eight, and the standard four expansion slots. The results for these varying expansion slots analysis is seen in Table 9-11.

Table 9-11 Varying expansion slot numbers of ***ICE***™ 105-1824-233 sawblade and results on natural frequencies.

Rotating Analysis			
Number of Expansion Slots	**3 Exp. Slots**	**8 Exp. Slots**	**4 Exp. Slots**
Expansion slot length, (inches)	**1.25**	**1.25**	**1.25**
one-peak mode =	112 Hz	115	105
two-peak mode =	118	116	105
partial bowl-shape mode =	127	120	107
four-peak mode =	138	135	130
four-peak mode (part-symmetric) =	153	141	132
six-peak mode =	226	221	217
six-peak mode (part-symmetric) =	223	223	218
eight-peak mode =	280	326	345
eight-peak mode (part-symmetric) =	382	369	355
ten-peak mode =	542	486	512
ten-peak mode (part-symmetric) =	561	488	513
12-peak mode =	687	611	662
first center body mode =	711	637	668
first center body mode (part-symmetric) =	771	703	n/a
first center body mode (repeated-part-symmetric) =	780	716	n/a
12-peak mode (part-symmetric) =	818	724	n/a
second center body mode =	869	817	786
second center body mode (part-symmetric) =	902	821	n/a
14-peak mode =	950	855	887
14-peak mode (part-symmetric) =	960	863	n/a

The results for the sawblade with eight expansion slots raised the natural frequencies an average of 11.3 Hz for the first three mode shapes, and an average of only 2 Hz for the first 20 mode shapes. Whereas, the results for three expansion slots raised the natural frequency an average of 13.3 Hz for the first three mode shapes and an average of 43.2 Hz for the first 20 mode shapes.

Another interesting phenomenon of having expansion slots other than the standard four slots is the introduction of mode shapes that are unique to a sawblade having three and eight expansion slots. It is the asymmetric geometric features, like # of expansion slots, which make it hard for the structural mode shapes to naturally couple and lock in with the geometry. For example, the first center body mode has a third mode shape that is only partially symmetric to the original first center body mode. Also, the second center body mode and the 14 peak mode have new partial symmetric mode shapes for results. The reason for this introduction to partially symmetric mode shapes is because the sawblade's geometry with three expansion slots is no longer symmetric. Vibration modes

are standing waves that set up at particular frequencies because geometry scales, and boundary conditions reinforce the energy in the waves which are setup. The waves naturally fit into and couple with the geometry. Views of these mode shapes are seen in Figure 9.16. Here the normally symmetric bowl-shape mode has a near perfect symmetric displacement around its outer rim, the three expansion slot configuration breaks up the sawblade geometry so energy can not be easily reinforced resulting in a resonance. Likewise, the first center-body mode only has two modes from the mathematical solution; here results have three solutions with varying shapes that are not nicely symmetric as in the case of four expansion slots.

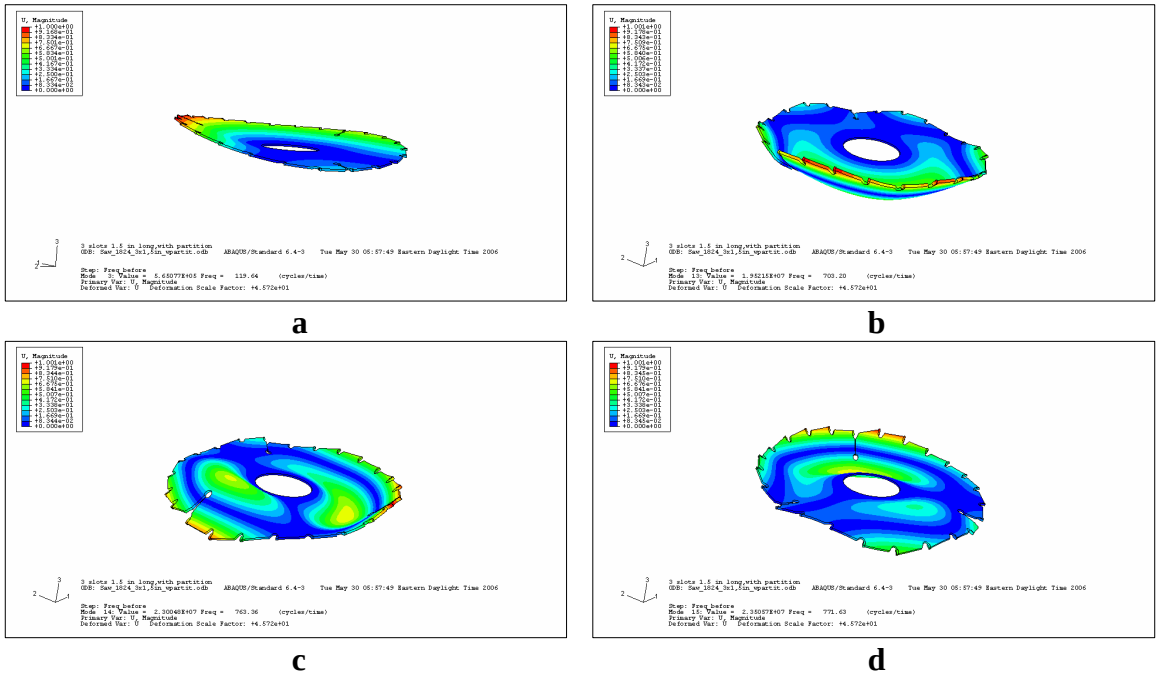

Figure 9.16 Partial mode shapes of ***ICE***™ 105-1824-233 sawblade with three expansion slots 1.25-in long.

Examples of mode shapes for the ***ICE***™ 105-1824-233 sawblade with eight, 1.25-inch expansion slots are see Figure 9.17. The same mode shapes as in the four expansion slot are found in the eight expansion slot analysis results.

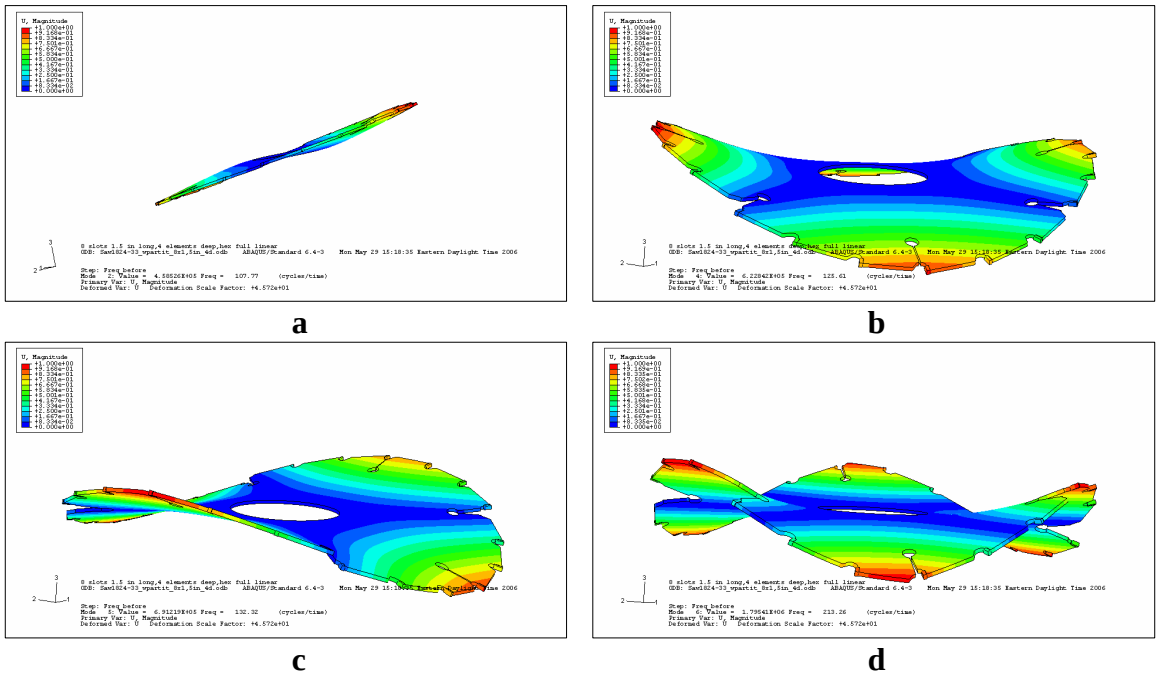

Figure 9.17 Examples of mode shapes of ***ICE***™ 105-1824-233 sawblade with eight expansion slots 1.25 inches long.

9.3.3 Varying Expansion Slot Angle (-10°) on Sawblade with Best Expansion Slot Length

Another analysis of the ***ICE***™ 105-1824-233 sawblade has been performed on a model with -10° expansion slots to see what, if any, impact the slot angle will have on the natural frequencies and the von Mises stress in the sawbody from rotational forces. As seen in Table 9-12, the difference in the natural frequencies for a rotating sawblade with -10° expansion slots versus one with 0° expansion slots is negligible for the first four modes. The highest difference seen in the first 20 modes is only about six Hz.

Table 9-12 Free vibration study **c**omparison of changing expansion slot angle on ***ICE***™ 105-1824-233 sawblade.

Rotating Analysis		
Number of Expansion Slots, Angle	**4, 0° Exp. Slots**	**4, -10° Exp. Slots**
Expansion slot length, (inches)	**1.25**	**1.25**
von Mises, S', (Mpa)	**21.12**	**20.29**
Frequency, (Hz)		
two-peak mode =	105 Hz	105 Hz
two-peak mode (symmetric) =	105	105
bowl-shape mode =	107	107
four-peak mode =	130	130
four-peak mode (symmetric) =	132	131
six-peak mode =	217	217
six-peak mode (symmetric) =	218	217
eight-peak mode =	345	346
eight-peak mode (symmetric) =	355	354
ten-peak mode =	512	512
ten-peak mode (symmetric) =	513	513
upside-down cake pan mode =	637	635
first center body mode =	668	662
first center body mode (symm) =	669	667
12-peak mode =	662	667
12-peak mode (symmetric) =	720	722
second center body mode =	786	784
second center body mode (symm) =	791	788
14-peak mode =	887	888
14-peak mode (symmetric) =	888	891

Figure 9.18 shows examples of the natural frequency mode shapes of the ***ICE***™ 105-1824-233 sawblade with -10° expansion slots. These results for the mode shapes are virtually the same as the identical sawblade with 0° expansion slots. This is because the -10° expansion slot is probably not enough to break up the symmetry of the sawblade. The vibration waves can likely still fit between the expansion slots.

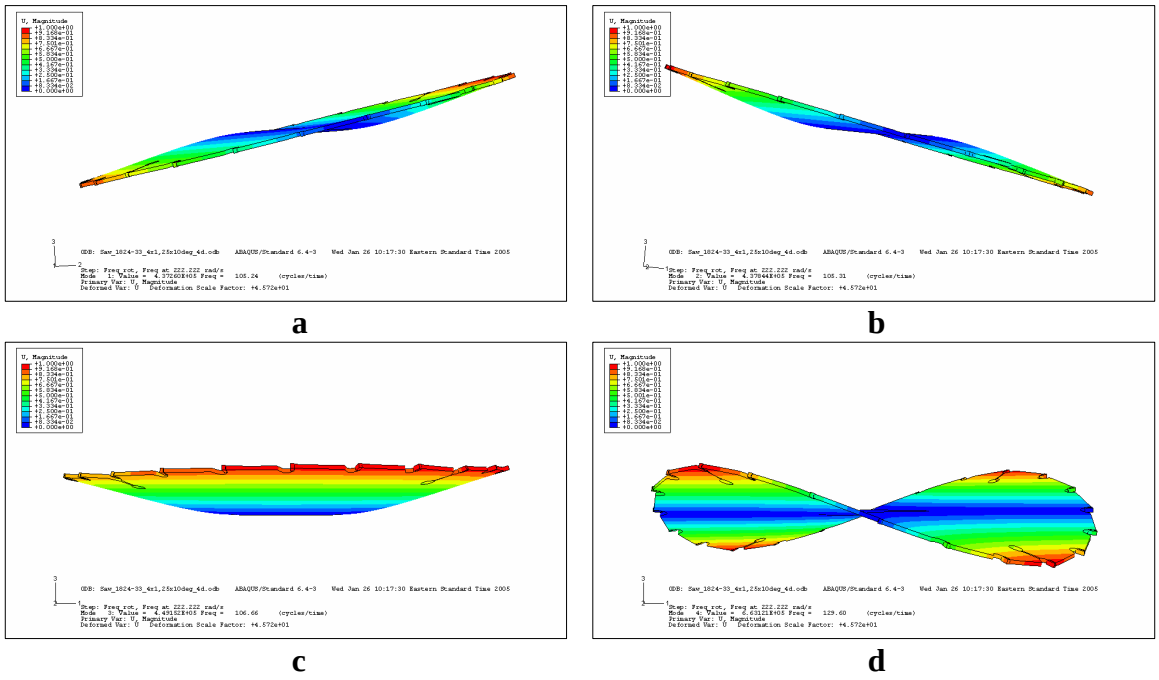

Figure 9.18 Rotating natural frequency of ***ICE***™ 105-1824-233 sawblade with -10° expansion slots.

Chapter 10

Natural Frequency of Sawblade with Residual Stress Rings

There are several mode shapes from the modal analysis (including the first and second mode) with repeated roots that can be considered the same mode. Therefore, the third mode (bowl-shape mode) can be considered to be the second natural frequency for the sawblades and annuli analyzed.

It is because of this phenomenon that we consider the bowl-shape mode as one mode of particular interest for the sawblade. Analyzing this mode will also keep the model an axisymmetric model. Because of the large jobs needed to run the non-linear three dimensional models when taking steel into the plastic zone and the large number of steps needed to run, the models were unable to be run with jobs of this magnitude on today's modern computers. The file sizes were greater than 40 GB and were unable to be run on even powerful computer clusters.

The axisymmetric model is capable of illustrating the second mode, the bowl-shape mode, and a powerful tool to reveal what happens within the sawblade when residual stress rings are placed in the sawbody. This model also provides a better understanding of the stresses found within the sawbody from the residual stress placed in the material. The bowl-shaped mode is invaluable when attempting to find the placement, depth, and number of the stress rings within the sawbody needed for optimum performance of the sawblade. Optimum performance here is measured as a state of residual stress within the sawblade that results in the largest shift in natural frequencies. Having less excitation of those natural frequencies the sawblade is operating at a given speed, any excitation associated with running speed will be less likely to excite the higher natural frequencies.

The natural frequencies of various bodies analyzed using finite element analysis are seen in Table 10-1. These results have been compared to the axisymmetric model of a free-vibration analysis with saw collar boundary condition. There will be three steps to the axisymmetric analysis: 1) residual stress, 2) rotate the sawblade, and 3) modal analysis. These results are expected to represent the *ICE*™ 105-1824-233 sawblade model because the bowl-shape modes' frequencies of the sawblade and annulus are close

(within 4.6 percent difference without expansion slots and within 1.2 percent difference with four, 1.25-in expansion slots) prior to the residual stresses. We will assume the approximation is in the results for this case will be representative of the *ICE*™ 105-1824-233 sawblade's natural frequencies.

Table 10-1 Bowl-shape mode shapes of various analyzed bodies compared to the axisymmetric results.

	Bowl-shape mode frequency, f, (Hz)	Percent difference from axysimmetric model, (%)	Upside-down cake pan mode frequency, f, (Hz)	Percent difference from axysimmetric model, (%)
Axisymmetric	106		623	
Annulus	112	-5.9	681	-9.2
Annulus with 4, 1.5-in expansion slots	103	2.7	626	-0.4
Standard 1824 Sawblade w/o exp. slots	109	-3.0		
***ICE* 105-1824-233 sawblade w/o exp. slots**	109	-3.0	652	-4.6
***ICE* 105-1824-233 sawblade with 4, 1.5-in expansion slots**	106	-0.2	631	-1.2

10.1 *Contact of Rollers with Sawblade*

Hertzian Stresses. To get an understanding of the answers the computer is simulating, we used equations for the Hertz contact problem. The rollers contacting the sawbody resemble the contact stress and equations between two cylinders commonly called Hertzian stresses. An illustration of this contact type is found in Figure 10.1. The Hertzian contact stresses are given according to the following equations by Shigley [16]. First, the half-width, *b*, used in the Hertzian equations is found using:

$$b = \sqrt{\frac{2F}{\pi l} \bullet \frac{\left(1-\upsilon_1^{\,2}\right)/E_1 + \left(1-\upsilon_2^{\,2}\right)/E_2}{1/d_1 + 1/d_2}} \qquad [10.1\text{-}1]$$

where l is the length, d_1 and d_2 are diameters. The contact area is a narrow rectangle of width $2b$ and length l, with an elliptical pressure distribution is elliptical. Equation 10.1-1 is used for two cylinders in contact along their curved surfaces with both axes of rotation aligned. For our study, the sawblade represents a wide, flat plate with infinite diameter. Therefore, d_2 is equal to infinity in Equation 10.1-1. This approximation can provide an estimate of the maximum pressure and stress of the results we wish to obtain.

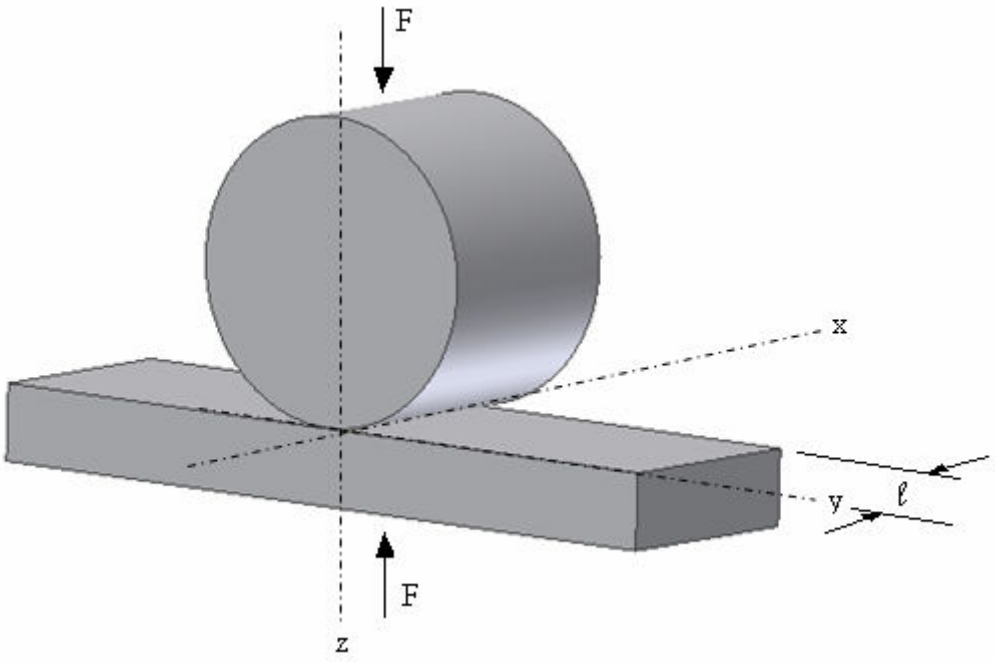

Figure 10.1 Cylinder contacting flat plate.

Next, using b from Equation 10.1-1 the maximum pressure, p_{max} within the contact area of the cylinder and flat plane is found according to:

$$p_{\max} = \frac{2F}{\pi b l} \qquad [10.1\text{-}2]$$

where F is the uniformly distributed force applied through each cylinders center.

The state of stress on the axis going through both cylinders' centers is obtained using the normalized stress equations:

$$\sigma_x = -2\upsilon p_{\max}\left(\sqrt{1+\frac{z^2}{b^2}}-\frac{z}{b}\right) \qquad [10.1\text{-}3]$$

$$\sigma_y = -p_{\max}\left[\left(2-\frac{1}{1+\frac{z^2}{b^2}}\right)\sqrt{1+\frac{z^2}{b^2}}-2\frac{z}{b}\right] \qquad [10.1\text{-}4]$$

where z is the depth away from the surface of each cylinder at the initial point of contact. σ_x is the stress along the length (axial-direction) of the cylinders and σ_y is the stress in the circumferential direction to the cylinders.

The stress along the z-axis is found using:

$$\sigma_z = \frac{-p_{\max}}{\sqrt{1+\frac{z^2}{b^2}}} \qquad [10.1\text{-}5]$$

And, the shear stress in the zy plane is found according to

$$\tau_{zy} = \frac{\sigma_z - \sigma_y}{2} \qquad [10.1\text{-}6]$$

For each of the normal stresses, the maximum is found at the surface of the cylinder or the surface of the flat plane. However, the maximum shear stress is found below the surfaces of both the cylinder and the flat plate. The maximum equivalent stress is found just below the surface and is 60 percent of p_{max}.

Hertzian stresses of this type work well for simple geometries such as cylinders and flat planes. However, when the more complex shape of the rollers is used to induce the residual stresses in sawbodies is analyzed; Equations 10.1-1 through 10.1-6 cannot

accurately represent surfaces of two radii as in the rollers. The rollers used in this research have a radius of 101.6 mm (4-in) and a crown radius of 101.6 mm (4-in).

Rollers on a Sawblade. Figure 10.2 illustrates the rollers and the way they interact with the sawblade. The force is acted upon the rollers towards the sawblade; this can also be viewed as a displacement, which is the way it is done in the saw shop at Reeds Carbide Saw and Tool in Lynchburg, VA [14], where a mark on the saw stretcher roller machine that lets them know the displacement for the rollers for tensioning a particular sawblade. Once the rollers are loaded with enough force (or displacement) to place the material in the sawbody in the plastic zone, the roller and sawblade are rotated together without slipping until a continuous residual stress ring is left in the sawblade.

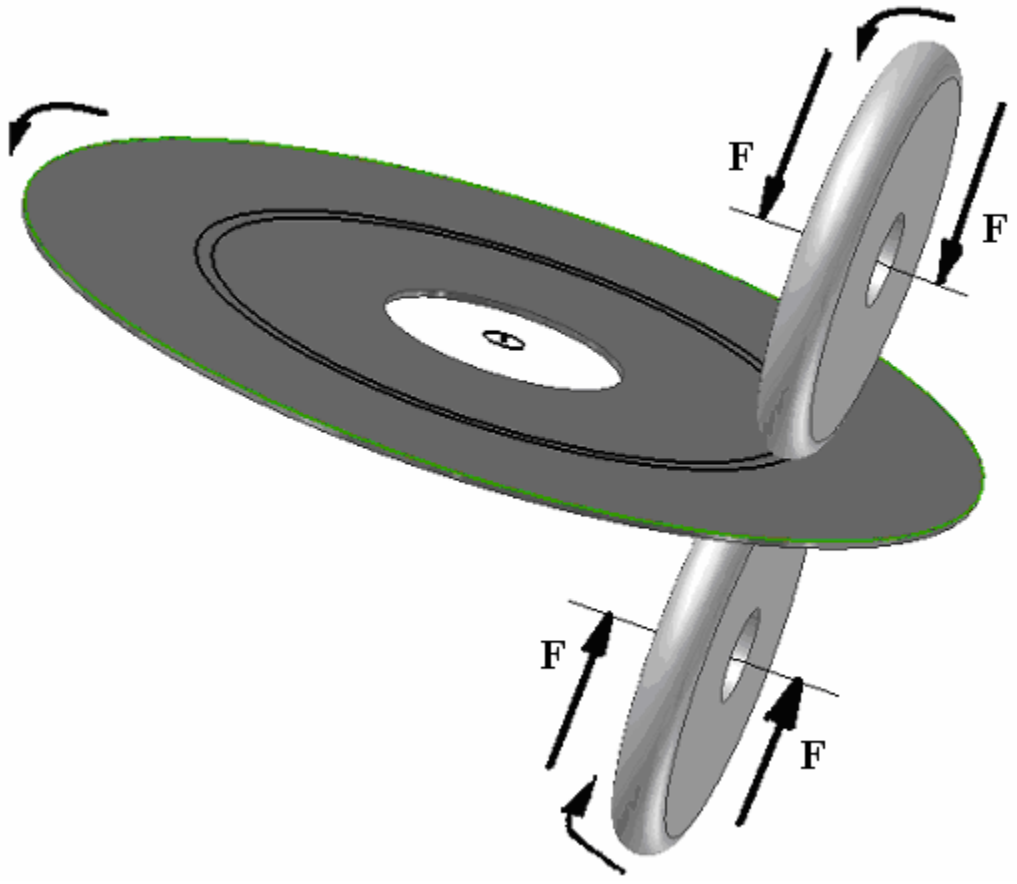

Figure 10.2 Rollers on annulus with force towards annulus leaving a residual stress ring in the annulus.

Because the shape defining the rollers is neither a cylinder nor a sphere, equations by Young [17] are needed to estimate the stresses in the sawbody. To solve these equations, the equivalent curvature radius, r^*, and the parameter λ defined by:

$$1/r^* = 1/r_1 + 1/R_1 + 1/r_2 + 1/R_2 \qquad [10.1\text{-}7]$$

and

$$\lambda^2 = (2/\pi)\arccos\bullet \left\{ r^* \sqrt{\left[\begin{array}{l} \left(1/r_1 - 1/R_1\right)^2 + \left(1/r_2 - 1/R_2\right)^2 + \\ 2\left(1/r_1 - 1/R_1\right)\left(1/r_2 - 1/R_2\right) * \cos 2\phi \end{array} \right]} \right\} \qquad [10.1\text{-}8]$$

where r_1 is the radius of the crown of the roller and R_1 is the radius of the roller. Likewise, r_2 is the radius of the flat plate along the crown's direction and R_2 is the radius of the flat plate along the face of the roller direction. Both r_2 and R_2 are infinite for the flat plate. And, ϕ the angle between the crown radius of the roller, r_1 and the flat plate's infinite radius, r_2, is 0^o because we can consider that the plane of r_1 and r_2 are parallel. Next, for $\lambda > 0$, the elliptical contact area, A_c, and the maximum contact pressure p_{max} are found using:

$$A_c \cong \pi(3Fr^*/2\lambda E^*)^{2/3} \qquad [10.1\text{-}9]$$

$$P_{\max} = \frac{3F}{2A_c} \qquad [10.1\text{-}10]$$

where E^* is the equivalent Modulus of Elasticity. This new Modulus of Elasticity is found using the modulus of elasticity and Poisson's ratio for each contacting body according to

$$1/E^* = (1-\upsilon_1^2)/E_1 + (1-\upsilon_2^2)/E_2 \qquad [10.1\text{-}11]$$

When using Equation 10.1-9, an overestimation of seven to eight percent of the actual area of contact is obtained. This results in a P_{max} and maximum equivalent stress underestimation by this same amount.

The results obtained from Equations 10.1-1 through 10.1-11 enable us to get an idea of the stress gradients we are expecting from our model's results. For example, we should see the largest shear stress just below the surface. Also, we should see the largest stresses in the x, y, and z directions at the interface surfaces between the rollers and the sawblade. The curve in Figure 10.3 is of a cylinder compressing a flat plate. This figure is a typical representation of the stress gradient from contact. Here the graph depicts what happens at the surface to 1.6 mm below the surface for a cylinder acting on a flat plate with F = 25000 N, b = 1.07167, $E_1 = E_2$ = 205000 MPa, d_1 = 203.2 mm, $v_1 = v_2$ = 0.3, and l = 25 mm. This results in a P_{max} = 594 MPa. The equivalent maximum stress is 0.6*P_{max} is 356 MPa.

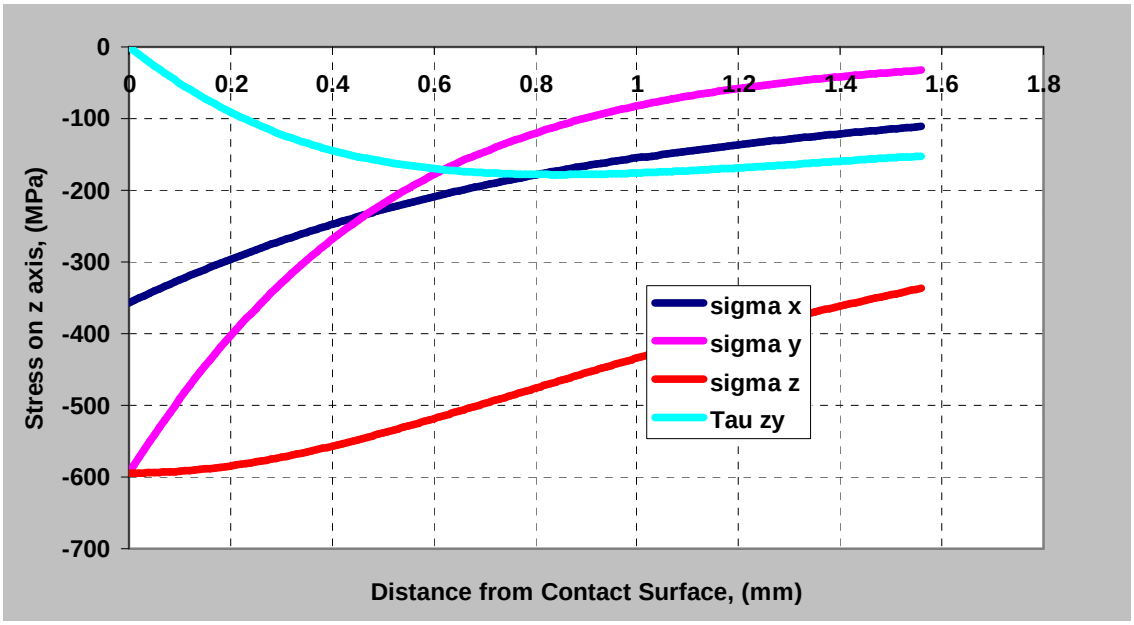

Figure 10.3 Hertzian stresses of cylinder on flat plate.

Likewise, the equivalent stress of the flat plate in contact with a roller of radius and crown is increased because the area of contact is smaller than a flat plate in contact with a cylinder. For example, the area of contact of the flat plate in contact with a cylinder of L = 25 mm and radius = 101.6 mm used to make the curves in Figure 10.3 is

53.6 mm^2 versus an area of 20.7 mm^2 for a roller radius of 101.6 mm and crown of 101.6 mm in contact with the same flat plate. Therefore, the maximum pressure of the roller in contact is 1812 MPa versus 594 MPa. This maximum pressure gives an equivalent stress of 1087 MPa, enough to push the steel in the sawbody into the plastic zone. The stresses seen in Figure 10.3 should also be about three times higher for the contact of the steel roller on the steel sawbody; however, the same general curve shapes are expected.

10.2 *Finding Depth of Rollers Displacement and Results*

While there is not a viable way in finite element analysis to exactly represent a roller on a sawblade, one way to closely approximate what happens is to have a curved shape contact the sawblade in the path that the roller would make rolling around the sawbody when making the residual stress ring. This is seen in Figure 10.4, where the annulus is half the thickness of the sawblade to represent the top half of the sawblade. The annulus has the same inner and outer radius of the sawblade we are studying. The stress in this annulus is not enough to place the steel into the plastic portion of the stress-strain curve. The roller has geometry such that the crown of an actual roller is represented. This crown has the same radius of a real roller at 101.6 mm (four inches).

Applying the load at one time using a ring with the same crown as the roller is a Figure 10.4 first approximation to the roller applying the load by rolling across the sawblade in the same circular pattern. Applying the roller force this way is not exactly the way the tension is placed into the sawblade in the real world. For example, tensioning in the real world only applies pressure at the area of contact between the bottom of the rollers and the sawbody at any given time. However, the rollers in this thesis apply the load at the whole circular pattern on the sawbody at once. Meaning, the sawbody carries much more force at one time.

In addition, the roller places a perfect concentric circle with the exact same displacement of the rollers, applying equal force at all relative points of contact. This equal force would be difficult to achieve in the real world due to the roller not being perfectly round and the sawblade thickness not being perfectly flat. However, the assumption of the real world applying nearly equal displacement of the roller is a good approximation because of the high consistency of today's manufacturing processes.

Therefore, these models best represent the realistic behavior of the sawblades under the condition that the tension is placed into the sawblade at one pressure loading over the entire circular pattern at once.

Other ways the analysis in this thesis differs from the real world are the mathematical models represent a “perfect” sawblade. “Perfect” meaning the sawblades have no defects in the material, no residual stresses from the manufacturing processes used to make the sawblade (prior to the tensioning process) and no thermal residual stresses from brazing the saw tips.

The type of loading used in the analysis yields the same general movement of the steel as hammering and rolling. Relative to the point of contact, the material on the outer portion of the sawbody is displaced radially outwards and the material on the inner portion is displaced radially inwards. The maximum displacement also occurs just outside the point of contact as in cases of hammering or roll tensioning. As in hammering or roll tensioning, the outer rim is in a state of tension. This analysis also proves that a state of too much tensioning can be achieved using this loading type, just as is the case from too much hammering or roll tensioning.

Boundary Conditions and Meshing Scheme of the 3-D Model. The boundary conditions are such that a quarter-model and half the thickness of a sawblade will allow for the nodes to stay on the planes of symmetry. The other boundary conditions are on the flat faces of the roller and annulus that make this annulus a quarter of a circle. These faces have constrained symmetric boundary conditions about the x-axis or z-axis depending on the face. This is due to the assumption that these nodes are only free to move along the radial and axial directions of the annulus.

A detailed partitioning and biasing of the meshing scheme is used to keep the nodes of the roller in exact contact with the nodes of the annulus. This meshing scheme also allows for a coarser mesh at areas of non-contact and the local mesh refinement near the points of contact.

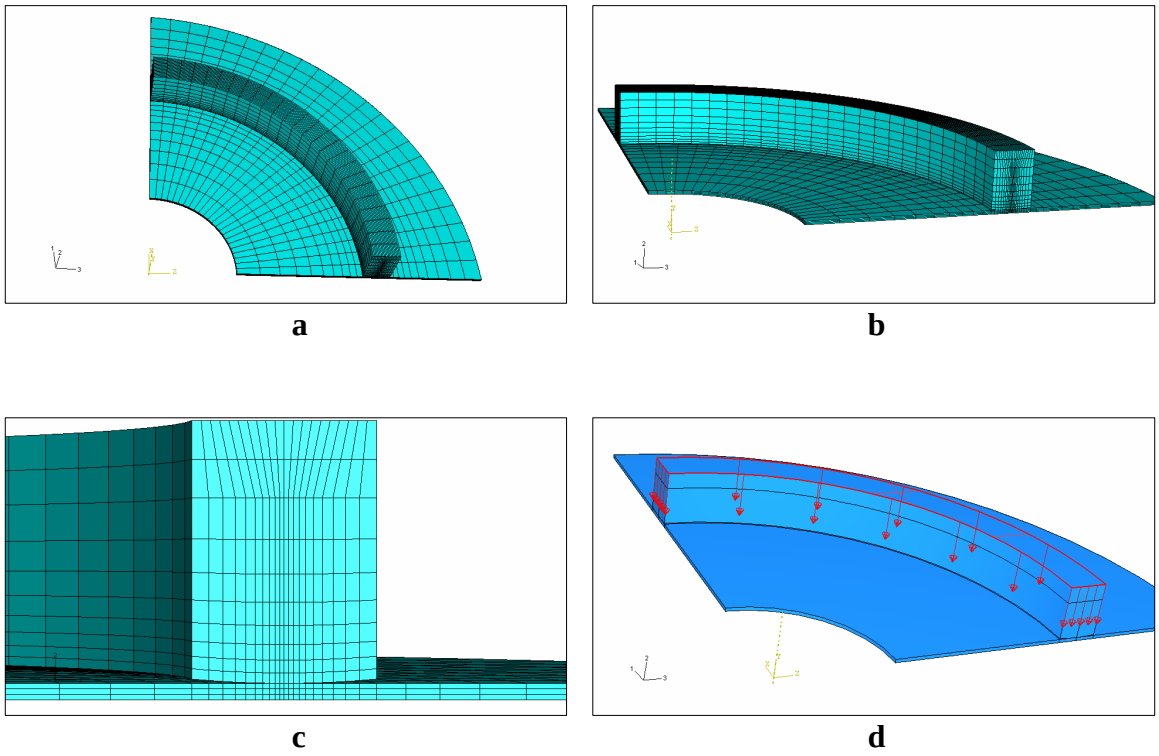

Figure 10.4 Simulated roller on sawblade. (a) and (b) show the simulated roller on a quarter model. (c) shows the mesh is partitioned and biased in such a way as to have the nodes of the simulated roller and the annulus meet at exactly the same points. (d) shows the displacement applied to the roller.

Elements for Elasto-plasticity models. The incompressible makeup of metals undergoing plastic deformation gives rise to careful consideration of which element to use. Some elements will suffer from volumetric locking and will be too stiff to accurately represent the deformations in the model when used with kinematic constraints designed to represent incompressibility of the plastic material.

Elements that may suffer volumetric locking are the quadratic (second order) reduced and quadratic full integration elements. The second order quadratic elements can be used, but should be used with great care if the strains surpass 20 to 40 percent. Because first order elements truly use a constant volume strain, they are excellent when representing plastic deformation in ductile metals. The best elements to select for elasto-plastic analysis are linear (first order) full integration elements to accurately represent incompressibility, Hibbit, Karlsson, and Sorensen [7].

Results of 3-D Elastic Model. The results of the model portrayed in Figure 10.4 are seen in Figure 10.5. Downward displacement of the roller is used to describe the contact between the roller and the sawblade. The flat, top-side of the roller is displaced 0.0055 mm towards the eighth-model annulus. This induces a stress in both the sawblade and the roller. All points in the sawblade and roller are in the elastic region of the materials stress-strain curve in this figure. The roller location is 2/3 the outer radius located at a radius of 152.4 mm.

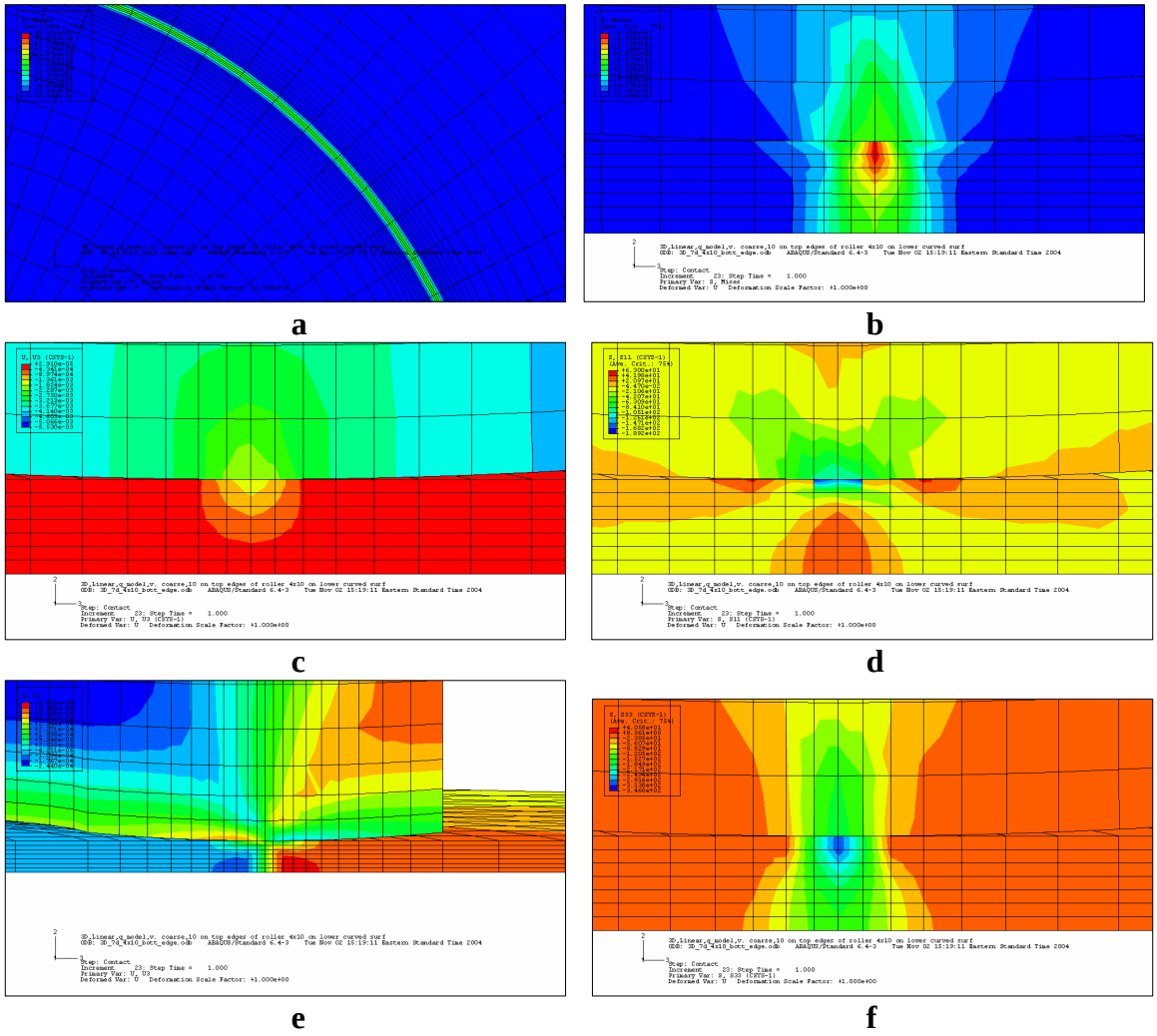

Figure 10.5 Three-dimensional analysis results of pressing quarter-circle shape with crown of 101.6 mm (four inches) into an eighth-model of a sawblade. The displacement of the roller is -0.0055 mm on the top line of roller. (a) The von Mises stress at contact area of ring top view, (b) von Mises stress at cross section area of sawblade and roller, (c) displacement in z-direction, (d) radial stress, (e) radial displacement, (f) stress in z-direction.

The stress distribution shown in Figure 10.5 (a) is the expected semicircular shape. The stress gradients of Figure 10.5 agree with the results from the hand calculations. As in Figure 10.5 (b), the maximum von Mises stress is just below the surface of the annulus at 280.6 MPa at the center of contact between the roller and annulus. The displacement in the annulus in the z-direction (axial-direction, seen in Figure 10.5 (c)) resulting from the roller contact is a small indentation of -1.824 E-3 mm.

The radial stress is seen in Figure 10.5 (d), where the annulus develops an initial compressive state of stress. However, away from the point of contact, the stress state becomes tensile. It is believed that this comes about from the curved indentation in the sawblade pulling material inwards to the bottom of the point of contact indentation. However, most of the stress induced in the annulus is pushing the material away from the point of contact of the roller, as seen in Figure 10.5 (e). In Figure 10.5 (f), the material in the annulus is pushed radially away from the point of contact. The displacement happens even far away from the point of contact, and moves material on the outer area of the sawblade about twice as much as the material on the inner area is displaced. For the stress in the axial direction of the annulus, the maximum occurs at the surface at 346 MPa in compression. This stress decreases throughout the thickness away from the point of contact.

Axisymmetric Model. Next, the analysis of the axisymmetric model is used to represent the annulus in elastic deformation. Therefore, it is it is necessary to show that in the elastic zone the axisymmetric models and the three dimensional models agree. For example, the stress gradients for the axisymmetric model seen in Figure 10.6 look quite similar to the stress gradients found in the stress gradients for the three-dimensional model seen in Figure 10.5. The same displacement of the top of the roller is used in both these axisymmetric and three-dimensional models.

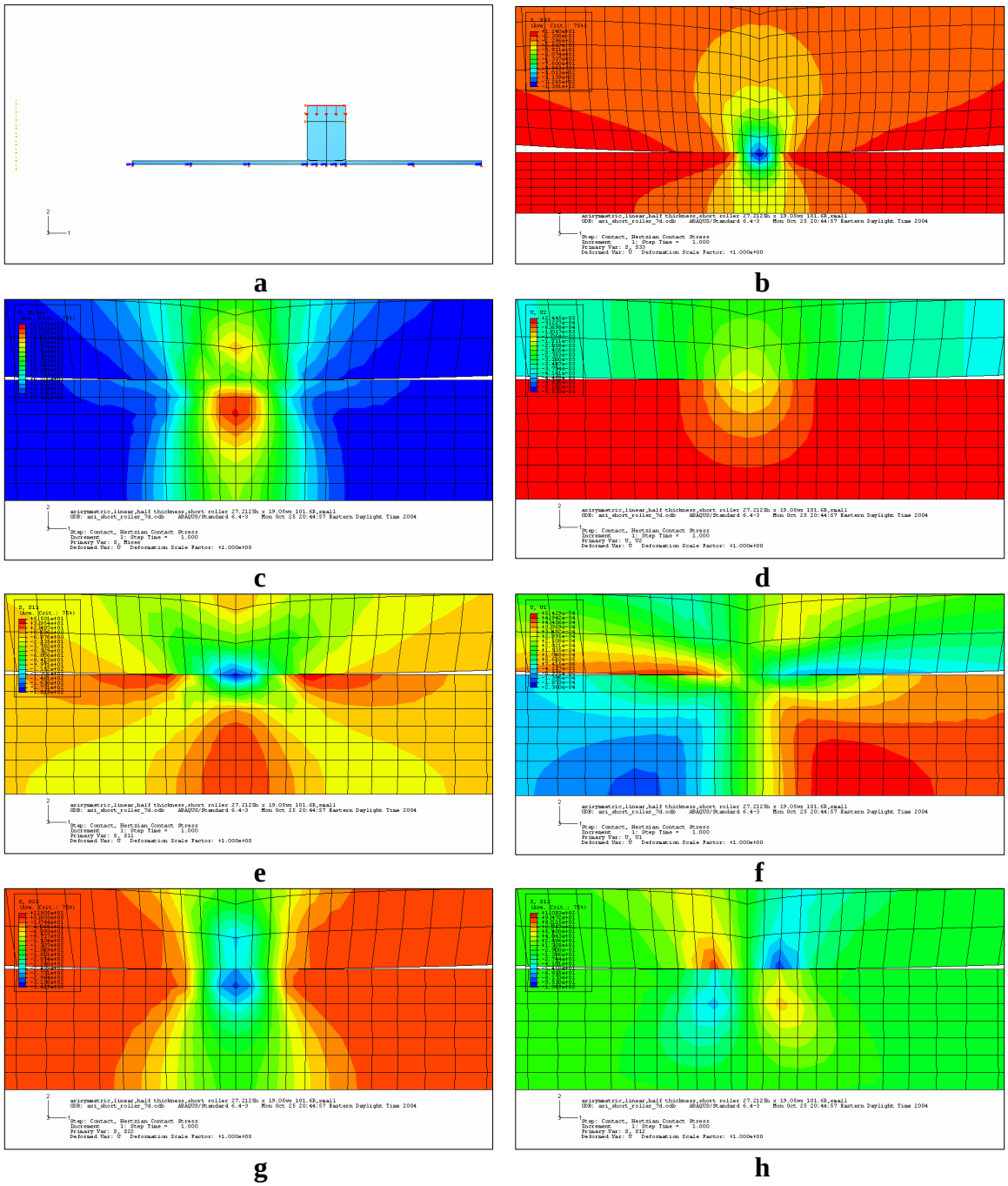

Figure 10.6 Elastic analysis of an axisymmetric results of pressing a roller onto an annulus. (a) axisymmetric model setup showing the top-side of the roller displacement of 0.015 mm, (b) circumferential stress, (c) von Mises stress at area of contact, (d) displacement in axial-direction (z-direction), (e) radial stress, (f) displacement in radial-direction, (g) stress in axial-direction, (h) shear stress in radial and axial directions.

As seen in Table 10-2, the difference between the axisymmetric model and the three-dimensional model with the same displacement of the top of the roller causing

contact with the annulus is quite similar. In fact, the largest difference in the maximum von Mises stress is only 17 percent at the point of maximum just below the contact surface. This difference of the maximum values is considered negligible because the stress distributions from comparing Figure 10.5 and Figure 10.6 are near the same. Therefore, the models in the rest of this research will find the results of various stresses in the annulus using an axisymmetric model because of the savings in computational effort.

Table 10-2 Axisymmetric elastic model versus three-dimensional eighth-model annulus with roller contact.

Stress Direction	Model		
	Axisymmetric, half thickness	Three-Dimensional, 1/8 model	Percent difference
Radial, (MPa)	-188	-182	4
Axial, (MPa)	-305	-309	-1
von Mises, (MPa)	237	277	-17
Displacement			
Radial, (mm)	0.00054	0.00056	-4
Tangential, (mm)	n/a		
Axial, (mm)	-0.0016	-0.0018	-14

Displacement for Correct Plastic Deformation of Sawblade. Following the comparison of the axisymmetric and the three-dimensional models, it is necessary to find out how much displacement of the roller is needed to place the sawbody (annulus) in the plastic zone while keeping the rollers in the elastic zone. This is necessary because a single set of rollers may last several years and plastically deform many sawblades throughout its lifetime.

So, a method was used to establish a limit of displacement of the roller where the sawblade is in the plastic zone and another limit where the sawblade is not in the plastic zone. Then, between these limits lies a point picked for yielding the steel in the sawblade, thereby leaving the residual stresses in the sawblade without yielding the steel in the rollers. After trial and error methods, it was found that a displacement of 0.15 mm on the top side of the roller towards the annulus would place the annulus into the plastic zone without yielding the roller. With this displacement on the top side of the roller, the annulus von Mises stress of 837 MPa, exceeding its yield point of 690 MPa and causing the material in the annulus to flow. At this same point in time, the roller saw stress of

only 774 MPa or 66 percent of its yield point. The steel used for the analysis of the sawbody is A514 heat-treated medium carbon steel. The steel used for the analysis of the rollers is AISI 4140H is a low alloy steel with medium carbon. (More detail of materials properties used is given in section 3.3.)

For the elasto-plastic analysis, while the annulus is in contact with the roller, the displacement of 0.015 mm results in an indentation depth of 0.0851 mm on the top side of the annulus and 0.0833 mm on the bottom side of the annulus. These values should be the exact same, and are in fact only two percent different. When the roller is released, the surface of the annulus springs outward slightly from the release of the rollers and the elasticity of the steel annulus. The final indentation depth left in the top side of the annulus is 0.076 mm and the bottom side is 0.078 mm. The final indentation left in the annulus is approximately 7.5 mm (0.295 inches) in width.

These displacement results of the roller and sawblade are seen in Figure 10.7. In Figure 10.7 (a), the annulus and roller are in maximum contact and the displacement of the roller is seen. At the right (outer rim side) of the roller, the displacement is to the left from the reactant forces from the annulus. In other words, the roller displaces opposite the annulus' displacement in the radial direction on each side of the contact point. Figure 10.7 (b) shows no residual stress left in the rollers when released from the annulus. Figure 10.7 (c) and Figure 10.7 (d) show the indentation (residual displacements) left in the annulus from the contact.

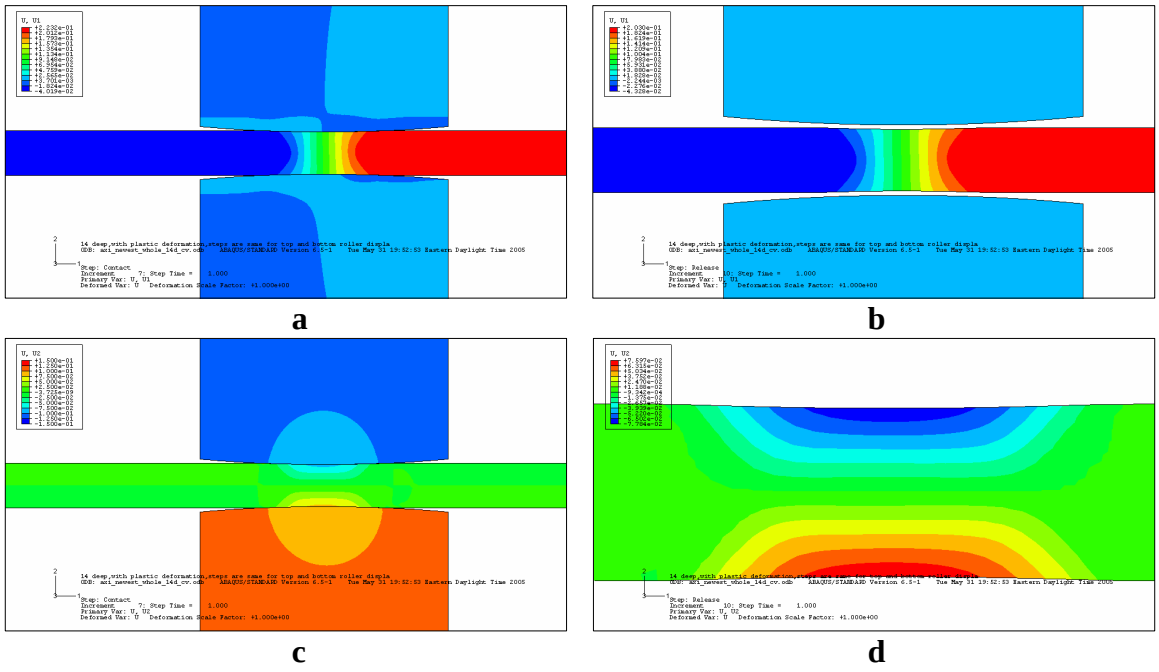

Figure 10.7 Elasto-plastic analysis of annulus from roller contact at 152.4 mm from center of annulus. (a) radial displacement of roller and annulus in maximum contact, (b) radial displacement of annulus, (c) axial displacement of roller and annulus in maximum contact, (d) axial displacement of annulus.

The material in the annulus flows or moves quite a bit more toward the outer rim. These different material flow-directions both begin at the point of contact of the roller. In fact, the amount the material moves towards the outer rim is about ten times the distance the material moves towards the inner radius. A computer model is seen in Figure 10.8, where the red and orange colors represent positive displacement or to the right (outer rim) and blue and light blue colors represent negative displacement or to the left (inner rim). Figure 10.9 shows the amount the material, located at the top of the annulus, displaces in the annulus from one roller at 152.4 mm. The curve begins at 19.05 mm (1.5 inches) at the inner radius of the annulus and ends at 228.6 mm (9 inches) at the outer radius. This curve shows the larger amount of displacement towards the outer rim of the sawblade in comparison to the inner radius. The displacement peaks are at just to the outside of the contact area of the roller and the annulus at 149.7 mm and 157.5 mm in the model.

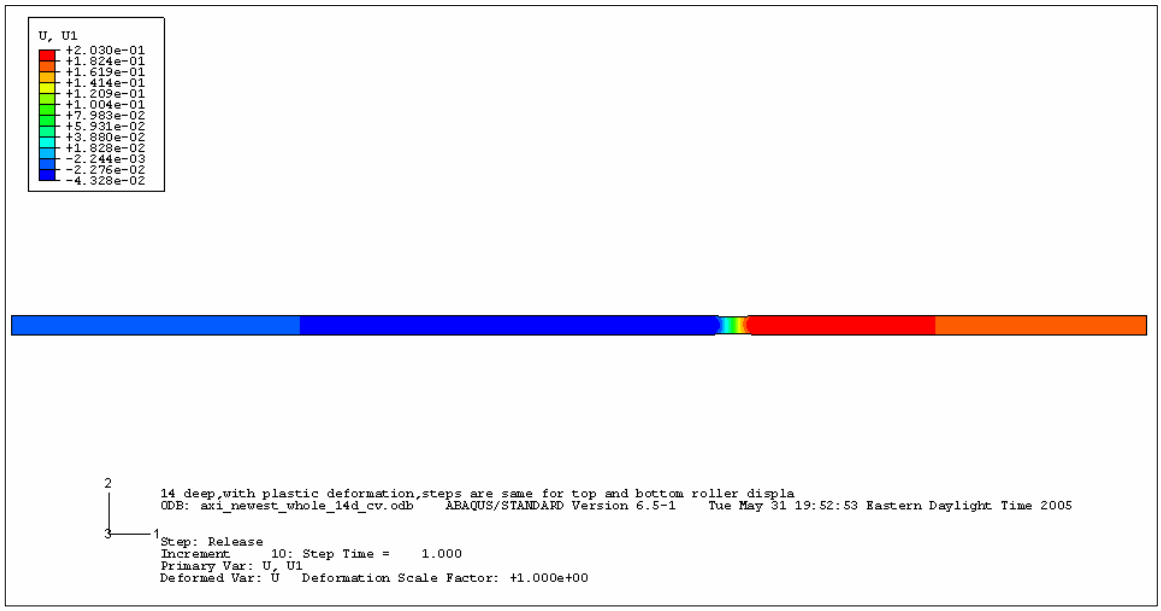

Figure 10.8 Elasto-plastic analysis of residual radial displacement in annulus after roller contact at 152.4 mm from center of annulus.

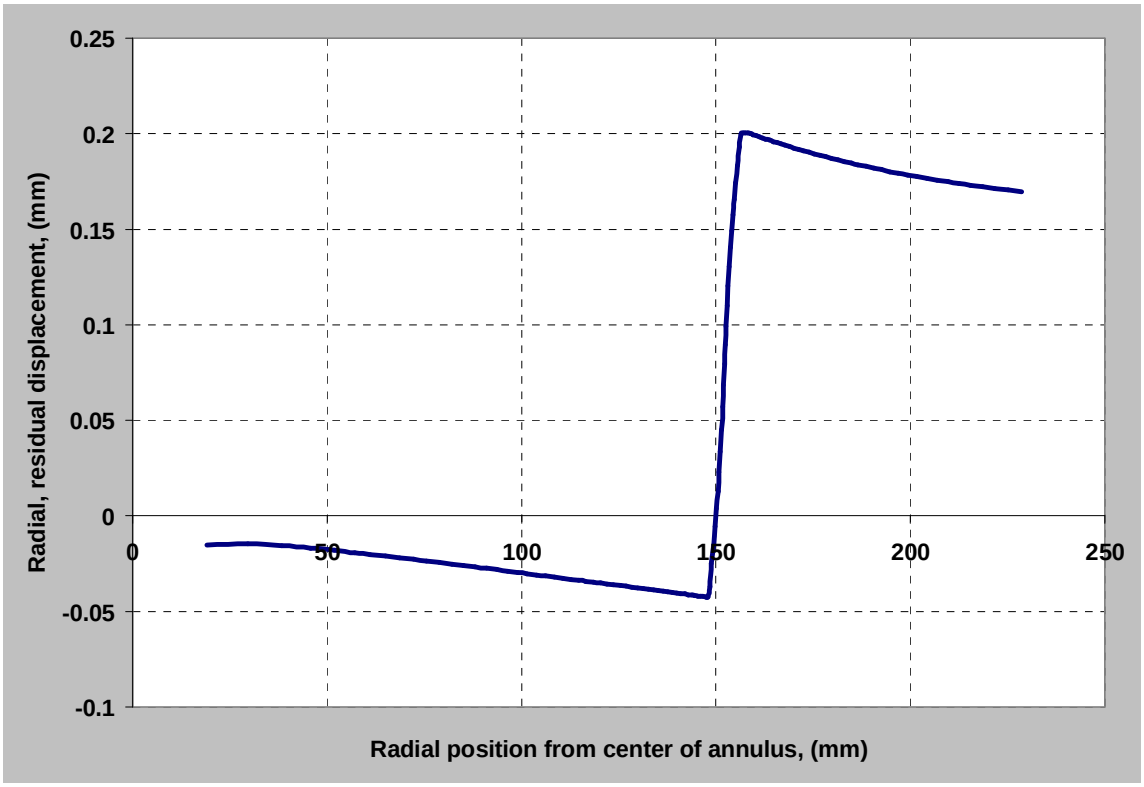

Figure 10.9 Amount annulus displaces radially from contact rollers at 152.4 mm from the center of the annulus (path is along top of annulus).

The radial displacement comes from the stress induced by the rollers which pushes the material away from the rollers and yields the material in the annulus. After the

contact with the roller, the annulus is left with residual stress in it. The radial stress during the maximum contact with the rollers and annulus along with the residual stress in the annulus from contact can be seen in Figure 10.10. The vast majority of the radial stress induced in the annulus is compressive.

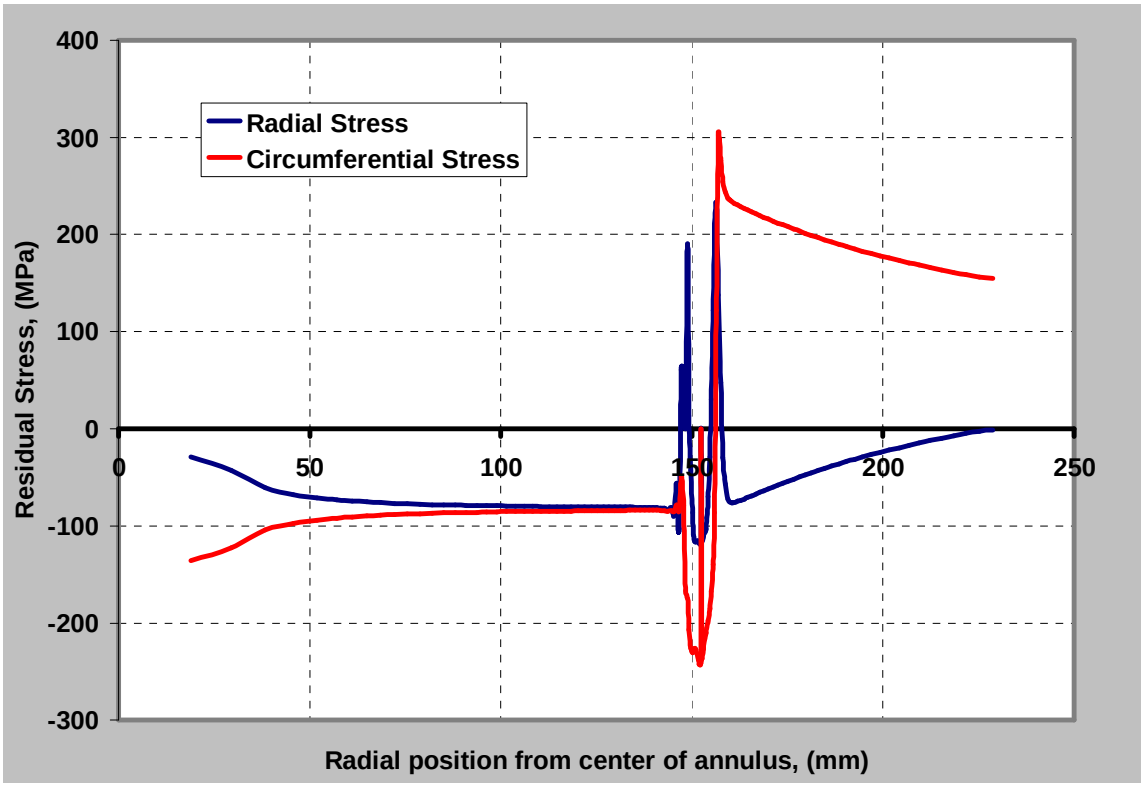

Figure 10.10 Residual **r**adial and circumferential stresses left in annulus from contact rollers at 152.4 mm from the center of the annulus (path is along top of annulus).

Because any increase in the radius of the annulus causes a direct increase in the circumference, *C*, according to

$$C = 2\pi r \qquad [10.2\text{-}1]$$

there are also residual circumferential displacements. Theses residual circumferential displacements are accompanied with residual circumferential stresses seen in Figure 10.11, where part d shows the overall residual stresses in the annulus from the contact of the roller. When the roller makes contact with the annulus and begins to push material out radially, the circumference has to grow in proportion, imparting tension in the

circumferential direction. When the roller releases from the annulus, radial displacements are left, thereby leaving circumferential displacements. Therefore, the annulus is left with tensile circumferential stresses from the contact location to the outer rim portion.

Compressive circumferential stresses are induced in the annulus because of the geometry and the material attempting to resist the contraction of the inner circumference. As the inner radius is forced to be made smaller, the material resist this contraction, thereby compressive stresses are induced towards the inner rim from the point of contact with the roller.

It is believed the circumferential stresses are the leading stress desired from tensioning a sawblade and they are the type of stress that does the work of adding stiffness to the sawblade. This added stiffness is the number one contributor to raising the natural frequency of the sawblade. Also, the “adding tension to a sawblade” comes about from this residual tensile stress left in the sawblade (annulus) at the cutting portion of the sawblade.

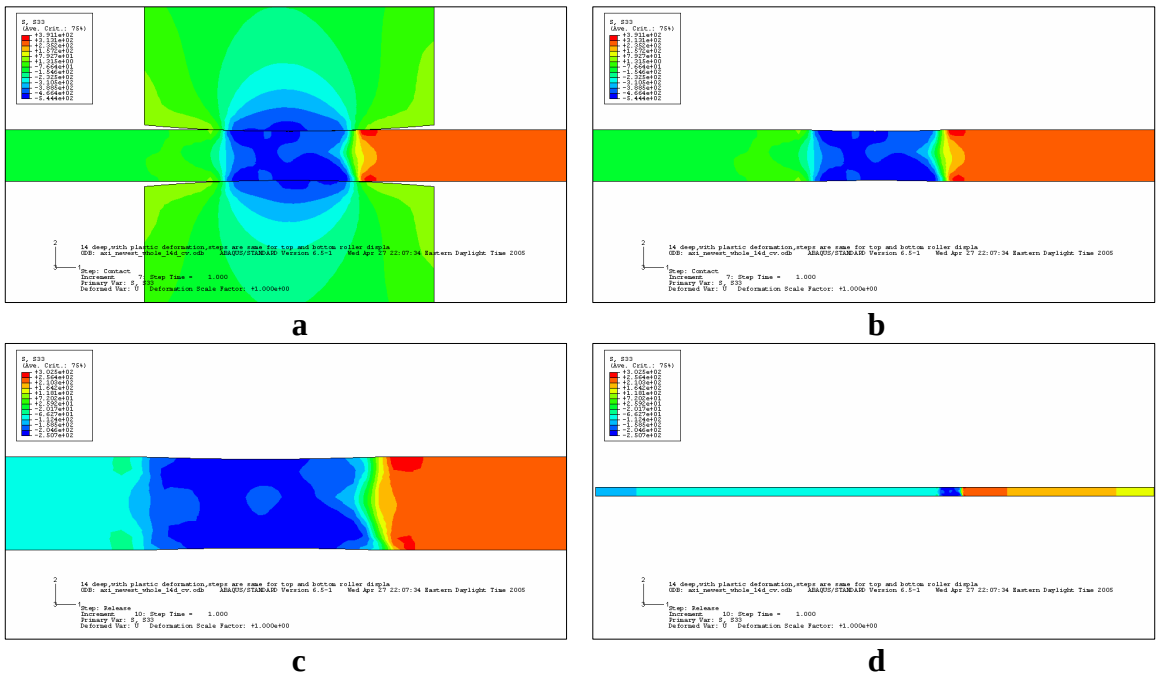

Figure 10.11 Circumferential stress in annulus from contact with rollers at 152.4 mm from center. (a) rollers in maximum contact with annulus, (b) also maximum contact with rollers (rollers not shown), (c) residual circumferential stress, (d) overall view of residual circumferential stress in annulus.

The axial and shear stresses seen in Figure 10.12 and Figure 10.13 have only local effects on the annulus. Except near the point of contact, these two stresses do not have any significant effect on the annulus. In fact, away from the point of contact the axial and shear residual stresses in the annulus are zero. At the location of the contact of the roller, there residuals are quite high at 346 MPa compression and 301 MPa, for axial and shear stress, respectively.

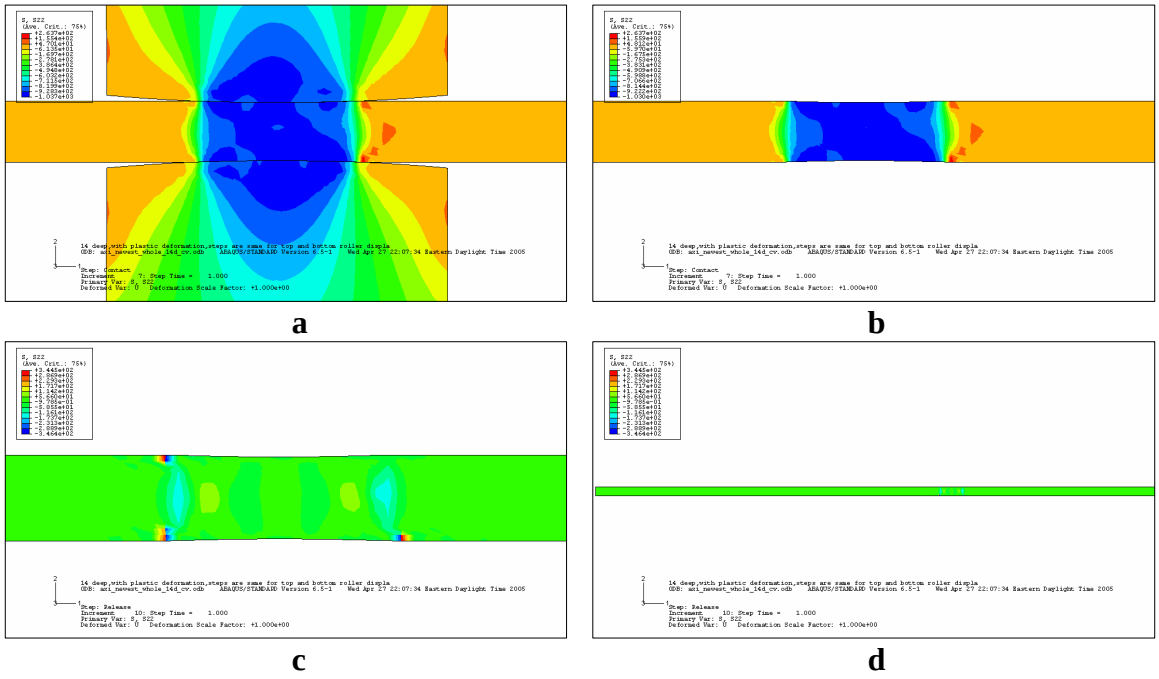

Figure 10.12 Axial stress in annulus from contact with rollers at 152.4 mm from center. (a) rollers in maximum contact with annulus, (b) also maximum contact with rollers (rollers not shown), (c) residual axial stress, (d) overall view of residual axial stress in annulus.

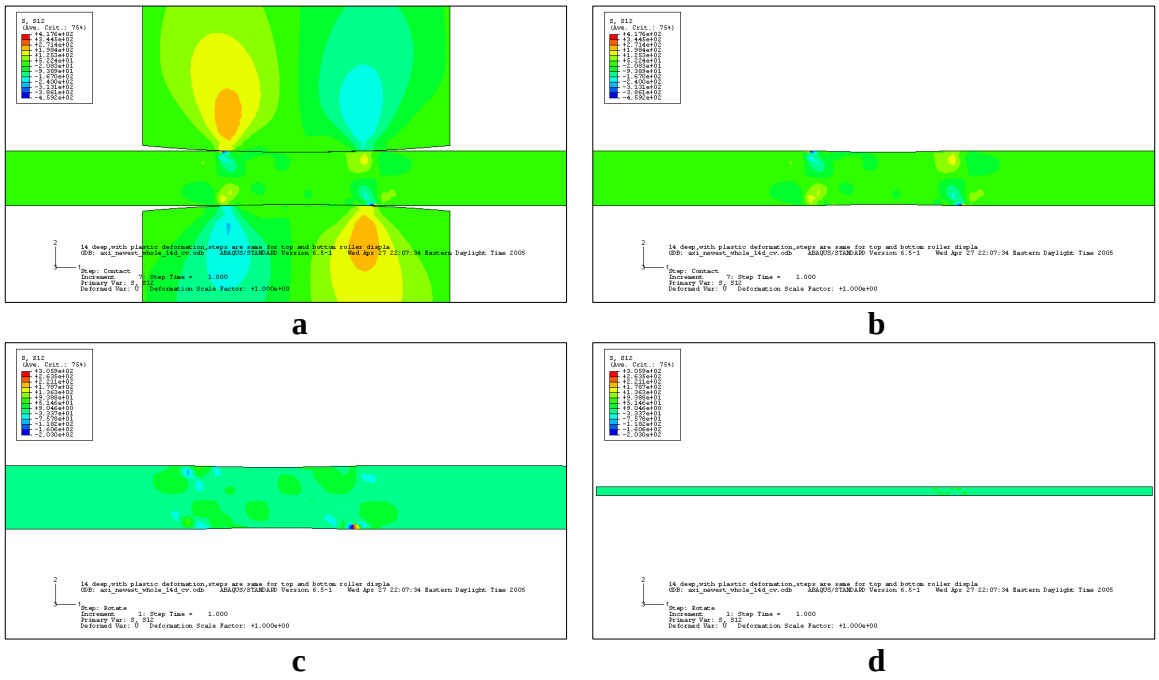

Figure 10.13 Shear stress in annulus from contact with rollers at 152.4 mm from center. (a) rollers in maximum contact with annulus, (b) also maximum contact with rollers (rollers not shown), (c) residual shear stress, (d) overall view of residual shear stress in annulus.

The von Mises is shown in Figure 10.14, where the von Mises from contact is shown in Figure 10.14 (a) and (b), and the residual von Mises stress is shown in Figure 10.14 (c) and (d). On a line drawn from top to bottom of the annulus through the point of contact, the stresses are highest from the compressing forces of the rollers. The high shear stresses and radial stresses just outside of the contact area dominate the von Mises stress, thereby causing it to be high at this localized area. The axial stress also causes localized residual von Mises stresses at the point of the compression of the rollers. As seen in Figure 10.14 (d), the stress are highest radially outward from the point of contact from the high circumferential stress dominating the von Mises stress all the way to the outer rim of the annulus.

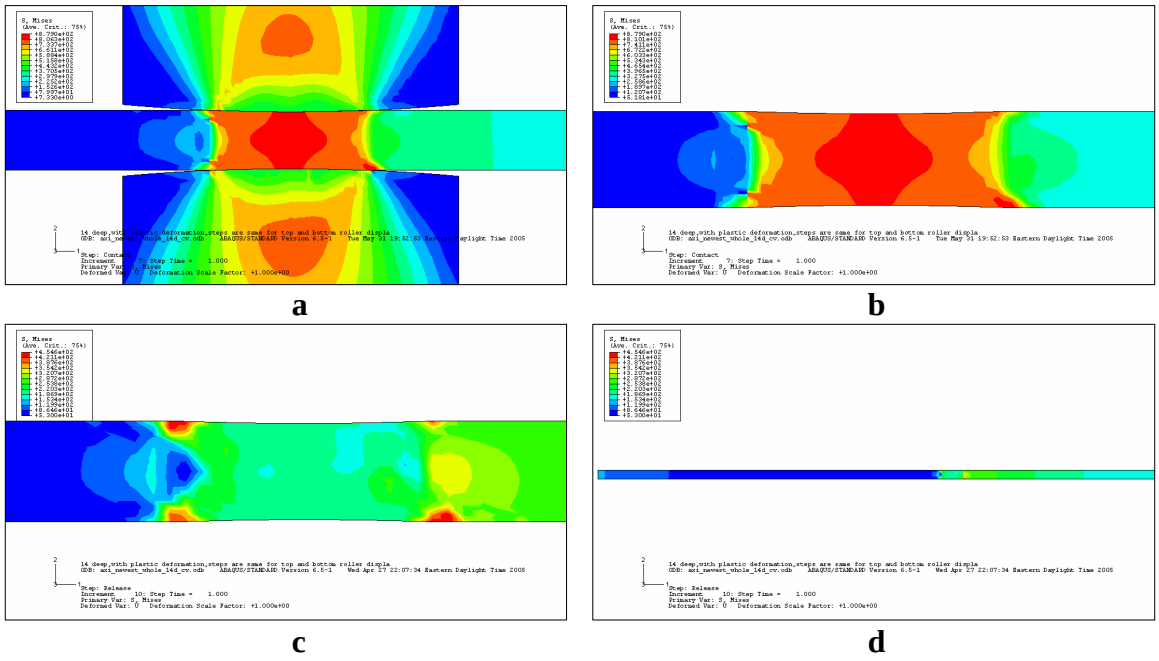

Figure 10.14 The von Mises stress in annulus from contact with rollers at 152.4 mm from center. (a) rollers in maximum contact with annulus, (b) also maximum contact with rollers (rollers not shown), (c) residual von Mises stress, (d) overall view of residual von Mises stress in annulus.

10.3 *Results from Varying Number of Rings and Placement of Rings*

To find the best placement of the residual stress rings in the sawblade, an annulus was used and the residual stress rings were placed at various concentric-circle radial locations and various numbers of rings were used. Each set of residual stress rings (one set includes the top and bottom sides of the annulus) was placed in the annulus one at a time. The saw stretcher roller machine also places one set (a top and bottom residual stress ring) in the sawblades at a time. For example, numerous models were analyzed having the residual stress rings placed in one of five positions. The positions seen in were all based on two-thirds the outer radius (152.4 mm). The rings were placed at either one inch, or 1.5 inches radially inward or radially outward from this two-thirds radius base-position making a total of five possible ring locations as seen in Table 10-3. Furthermore, the rings were analyzed from using one ring at each of the five locations to using combinations of up to five residual stress rings placed in the same annulus. All possible combinations analyzed using these five rings totaled 31 different models.

Table 10-3 Roller locations.

No. of Rollers	Roller Locations, R, (mm) (radial distance from center of annulus)	Roller Locations, R, (inch)
1 Roller	114.3	4.5
	127	5
	152.4	6
	177.8	7
	190.5	7.5
2 Rollers	114.3, 127	4.5, 5
	114.3, 152.4	4.5, 6
	114.3, 177.8	4.5, 7
	114.3, 190.5	4.5, 7.5
	127, 152.4	5, 6
	127, 177.8	5, 7
	127, 190.5	5, 7.5
	152.4, 177.8	6, 7
	152.4, 190.5	6, 7.5
	177.8, 190.5	7, 7.5
Three Rollers	114.3, 127, 152.4	4.5, 5, 6
	114.3, 127, 177.8	4.5, 5, 7
	114.3, 127, 190.5	4.5, 5, 7.5
	114.3, 152.4, 177.8	4.5, 6, 7
	114.3, 177.8, 190.5	4.5, 7, 7.5
	114.3, 152.4, 190.5	4.5, 6, 7.5
	127, 152.4, 177.8	5, 6, 7
	127, 152.4, 190.5	5, 6, 7.5
	127, 177.8, 190.5	5, 7, 7.5
	152.4, 177.8, 190.5	6, 7, 7.5
Four Rollers	114.3, 127, 152.4, 177.8	4.5, 5, 6, 7
	114.3, 127, 152.4, 190.5	4.5, 5, 6, 7.5
	114.3, 127, 177.8, 190.5	4.5, 5, 7, 7.5
	127, 152.4, 177.8, 190.5	5, 6, 7, 7.5
	114.3, 152.4, 177.8, 190.5	4.5, 6, 7, 7.5
Five Rollers	114.3, 127, 152.4, 177.8, 190.5	4.5, 5, 6, 7, 7.5

In the literature research of the saw tensioning, it was not found that a particular order for the placement of the residual stresses was recommended. Likewise, during this study, the order of placement was not found to have significant impact on the results. However, for consistency, the rings were placed in this order of precedence:

1) 152.4 mm (2/3 radius or 6 inches)
2) 127 mm (5 inches)
3) 114.3 (4.5 inches)
4) 177.8 (7 inches)
5) 190.5 (7.5 inches)

The number of calculation steps to analyze a typical axisymmetric model with residual stresses was 97 time steps; the number of steps needed to solve the three-dimensional model would be considerably greater.

Partitioning. As in the cases of section 10.2, detailed partitioning and biasing of the meshing scheme is used to keep the nodes of the rollers in exact contact with the nodes of the annulus. Therefore, each of the five-roller sets along with the annulus at the contact points needed their mesh partitioning and biasing to match. This matching is seen in Figure 10.15, where a three roller model is shown for ease of viewing the partition matching.

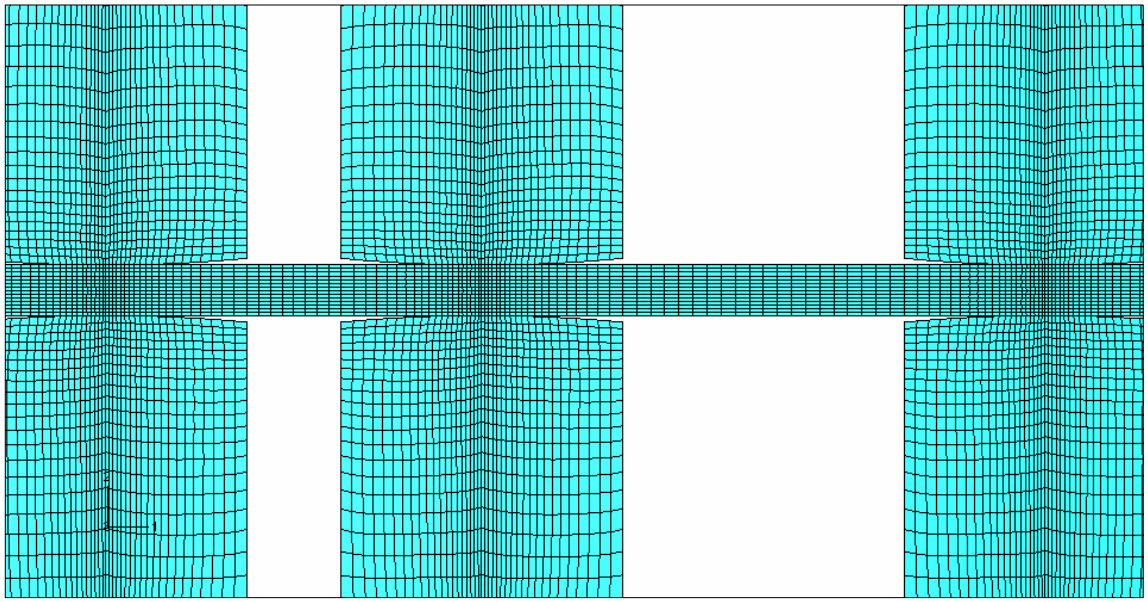

Figure 10.15 Matching biased and partitioned meshing of annulus and rollers.

Boundary, Loading and Contact Conditions. The largest model consisted of 13 unique boundary conditions, loading conditions, and contact conditions to analyze five top and five bottom rollers used to compress the annulus. To accurately represent the sawblade using an axisymmetric annulus, an annulus with the same inner bore of 19.05 mm (1.5 inches) was used during the roller contacting and releasing steps. This ensured all effects of the inner geometry were represented in the computer model, in addition to the saw collar not holding the sawblade during the tensioning process. An example of the typical

unique boundary conditions and loading conditions are seen in Figure 10.16, where the rollers used are at 152.4 mm and 127 mm. The steps are described as follows:

- Step 1 is the initial boundary condition, which has the top and bottom roller sides constrained in the radial directions.
- Step 2 the addition of the constraint at the centerline of the annulus on the plane of symmetry, and the contact displacement of the first top and bottom rollers towards the annulus is 0.15 mm.
- Step 3 includes the release of the first contacting set of rollers, which are displaced 0.15 mm away from the annulus.
- Step 4 constrains the first set of rollers at zero displacement, and adds the radial displacement constraints to the second set of rollers, while displacing them 0.15 mm towards the annulus.
- Step 5 includes the release of the second contacting set of rollers, which are displaced 0.15 mm away from the annulus.
- Step 6 Constrains both sets of rollers from displacing, while the annulus is given the same saw collar constraint as other axisymmetric models, the centerline boundary condition of the annulus is removed, and the rotational body forces are applied to the annulus.
- Step 7 is the modal analysis, which has the same constraints as step 6.

In addition to the unique boundary and loading conditions, unique contact conditions for the leading face of each roller are turned on and off depending on which step and which roller is contacting or releasing from the annulus. During the rotation and modal analysis, all contact conditions are off.

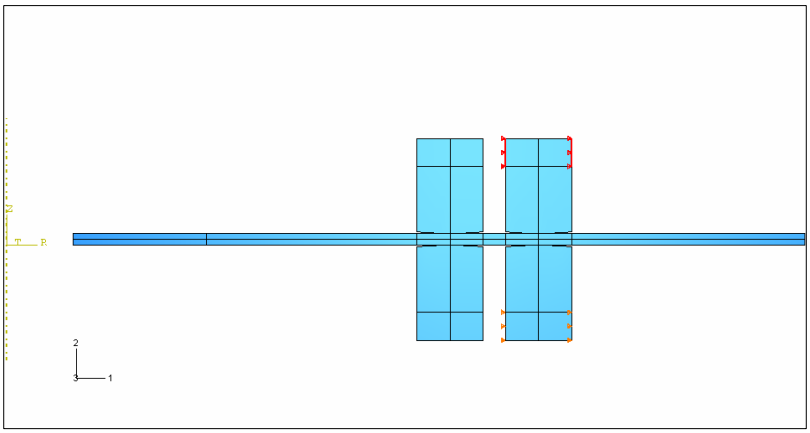

Step 1

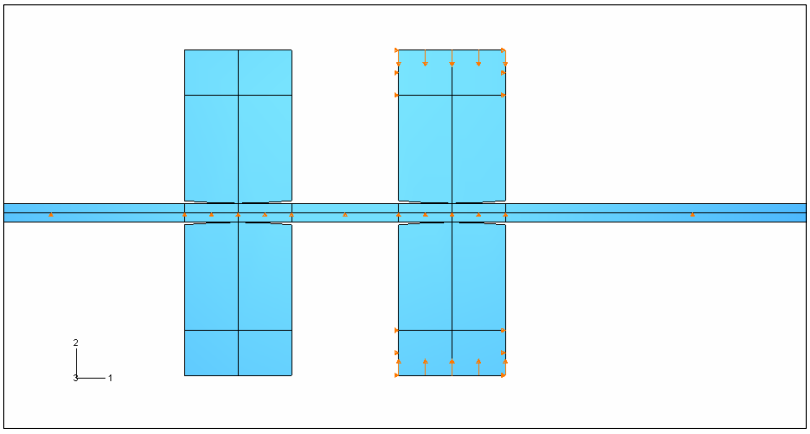

Step 2

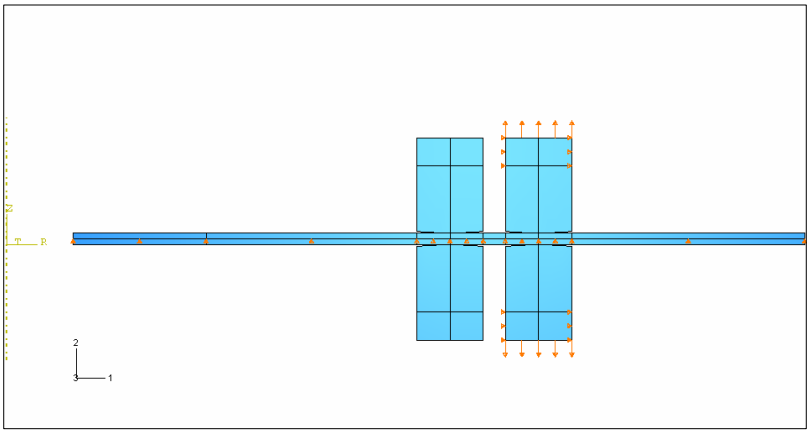

Step 3

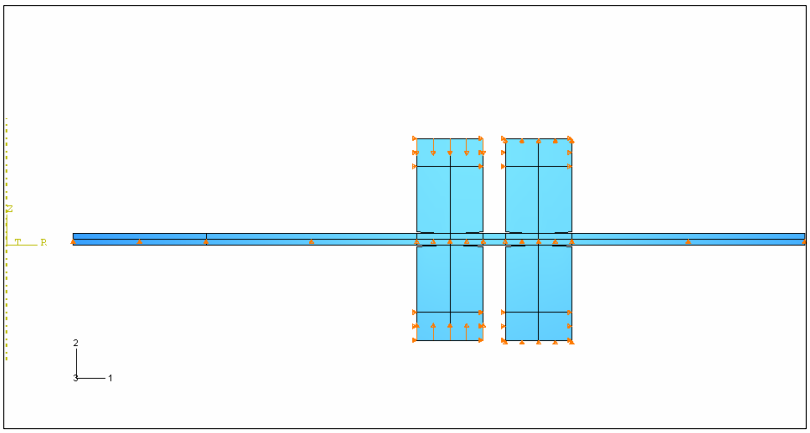

Step 4

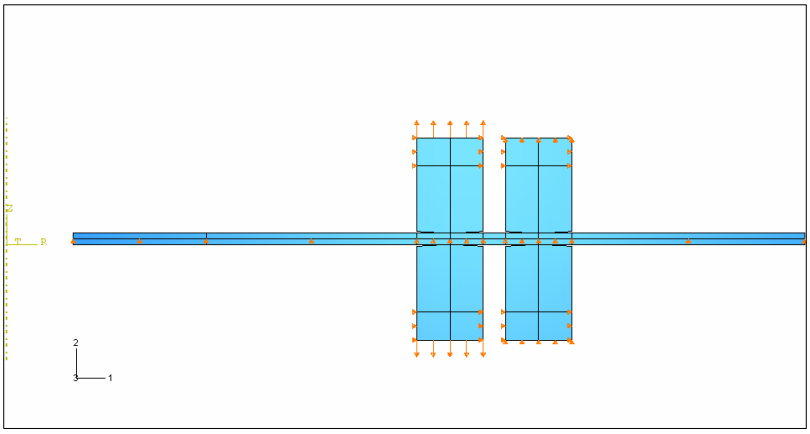

Step 5

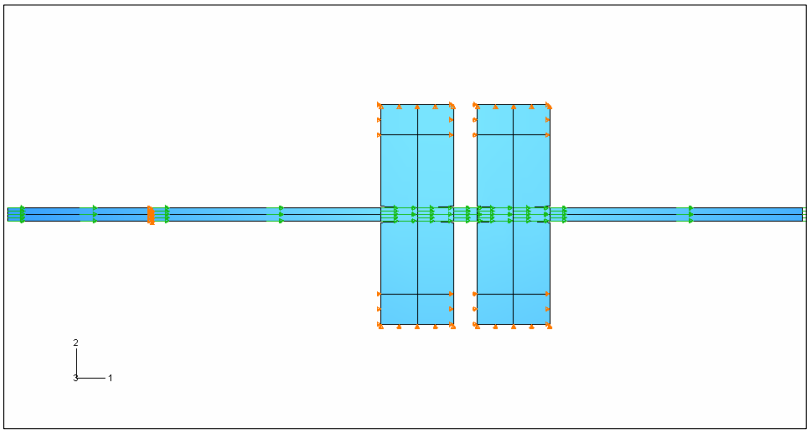

Step 6

Figure 10.16 Boundary conditions, displacements, and loading conditions for the case of two sets of rollers. One roller set is located radially 152.4 mm and the other is 127 mm.

Modal Analysis. For the last step, the vibration modal-analysis is performed with new stresses from rotating the annulus. The higher the natural frequency of a rotating annulus

with a particular placement and set of residual stress rings the better it is believed to perform for cutting purposes.

To accurately represent a sawblade, a whole thickness model must be used. All natural frequencies can only be found using the 3-D models without the use of symmetric boundary conditions.

The results of the vibration modal-analysis of an annulus at 152.4 mm (2/3 the radius) with a top side of the roller displacement of .015 mm leaving residual stresses in the annulus can be seen in Figure 10.17. This is a typical example of the bowl-shape mode and upside-down cake pan mode of the annulus with any tested placement(s) of the residual stress rings.

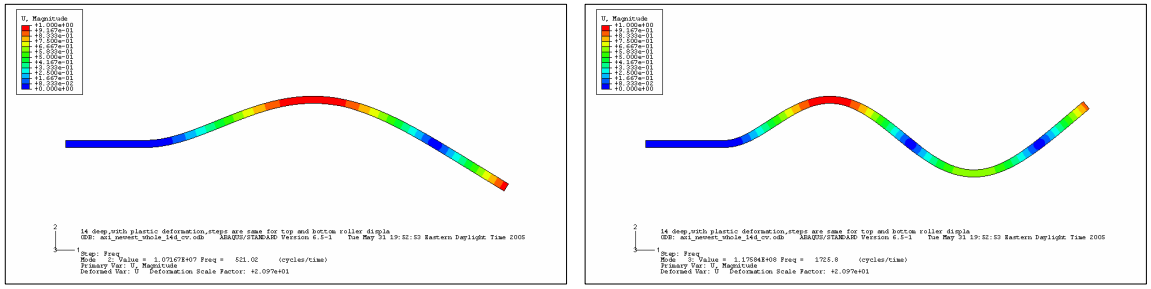

a **b**

Figure 10.17 Vibration modal-analysis of annulus with residual stress at 152.4 mm from center radius. (a) bowl-shape, (b) upside-down cake pan mode.

The results of inducing residual stress in an annulus using five rollers (top and bottom) is seen in Figure 10.18 of an over tensioned annulus. According to John Hodges [15] and R. S. Ponton [2] it is possible to over-tension a sawblade. This is verified in our research model where five rollers (top and bottom) have been used to place five residual stress rings in the annulus before the rotating and natural frequency analysis. The natural frequency drops back to the original natural frequency (105 Hz. for the original versus 108 Hz. for the over-tensioned). However, unlike the original annulus without residual stress, the over-tensioned annulus can not be re-tensioned because of all the internal permanent residual stresses now in the annulus. This over-tensioned annulus has been stretched and cannot, with any reasonable manufacturing process, be brought back to a state of no-tensioning and is now scrap. This analysis was a good check for the analysis to show that in the computer model the annulus can be over-tensioned to prove the models agree with the real world sawblades in tension.

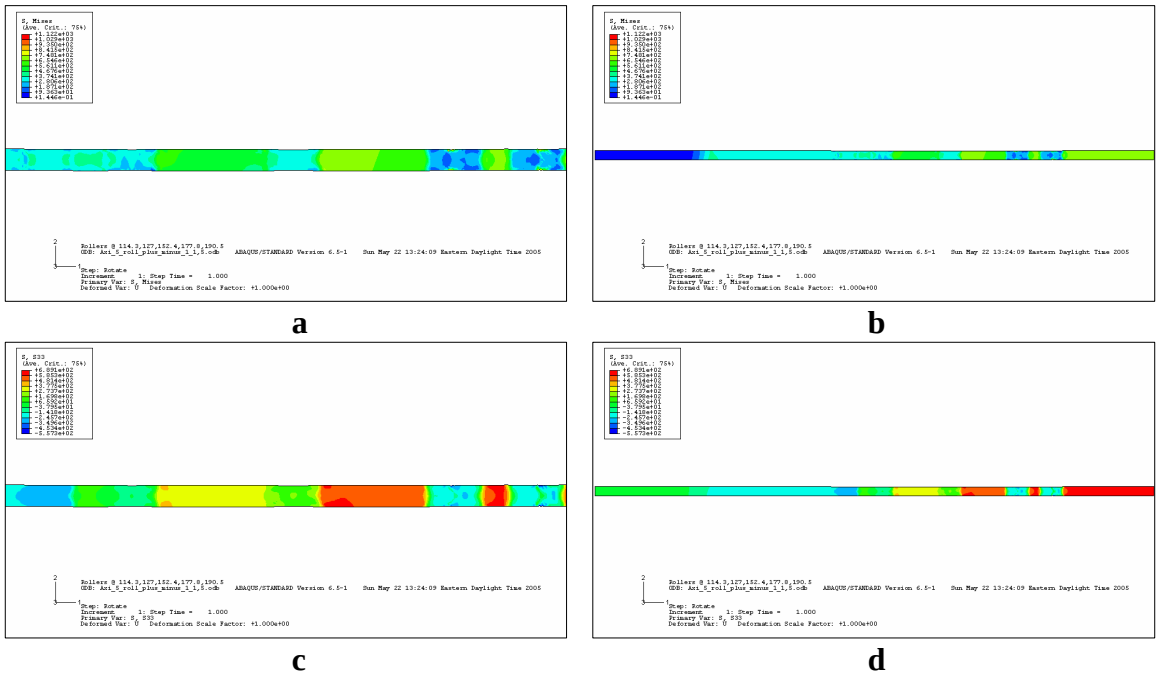

Figure 10.18 Axisymmetric model with five rollers (top and bottom) inducing residual stress in 18-in annulus. (a) shows the von Mises stress at the five residual stress locations, (b) overall von Mises in annulus, (c) circumferential residual stress showing the effects of the five rollers, (d) overall circumferential stress.

The results of analyzing the 31 cases of various residual ring placements and combinations are summarized in Table 10-4. The drastic increase in the bowl-shape natural frequency can be seen in nearly any combination versus the annulus without residual stress. However, the best case is when the residual stress ring is placed at 2/3 radius (152.4 mm) for the 18-in annulus analyzed. These results agree with the interview with R. S. Ponton where he said that the best location to add the residual stress ring was about 2/3 of the outer radius of the sawblade [2]. There also is a good place to place the single residual stress ring at 5/6 the radius (190.5 mm) for the 18-in annulus analyzed.

Table 10-4 Results of various numbers and placement combinations of residual stress on annulus.

No. of Rollers	Roller Locations, R, (mm) (radial distance from center of annulus)	Bowl-shape mode Frequency, (Hz)	Upside-down cake pan mode Frequency, (Hz)
No Residual Stress	N/A	105.81	623.49
1 Roller	114.3	466.75	1557.7
	127	476.15	1577.4
	152.4	521.02	1725.8
	177.8	501.54	1638
	190.5	521.09	1654.5
2 Rollers	114.3, 127	379.34	1585
	114.3, 152.4	396.31	1592.5
	114.3, 177.8	354.86	1486.3
	114.3, 190.5	436.94	1598.2
	127, 152.4	379.34	1585
	127, 177.8	363.14	1493
	127, 190.5	391.76	1512
	152.4, 177.8	403.83	1593.7
	152.4, 190.5	445.23	1648.2
	177.8, 190.5	429.46	1578.3
Three Rollers	114.3, 127, 152.4	210.87	1454.1
	114.3, 127, 177.8	185.45	1358.6
	114.3, 127, 190.5	230.21	1377.2
	114.3, 152.4, 177.8	222.57	1426
	114.3, 177.8, 190.5	272.25	1435.1
	114.3, 152.4, 190.5	321.15	1522.7
	127, 152.4, 177.8	267.13	1503.3
	127, 152.4, 190.5	273.32	1461.6
	127, 177.8, 190.5	287.2	1443.4
	152.4, 177.8, 190.5	356.26	1579.4
Four Rollers	114.3, 127, 152.4, 177.8	91.548	1383.7
	114.3, 127, 152.4, 190.5	103.44	1387.2
	114.3, 127, 177.8, 190.5	53.552	1314.8
	127, 152.4, 177.8, 190.5	196.78	1409.2
	114.3, 152.4, 177.8, 190.5	237.06	1471.1
Five Rollers	114.3, 127, 152.4, 177.8, 190.5	108.04	1388.2

Gains from the Study. The gains from this study reveal that the 18-in sawblade studied in this thesis can be tensioned with only one residual stress ring. The residual stress ring location is best at the 2/3 or 5/6 the radius. Spending the extra effort of putting in more

residual stress rings does not raise the natural frequency as much as one, properly placed ring. Using a roller ring depth of 0.15 mm allows us to yield the sawblade and not over-stress the roller. Having no residual stress ring to raise the natural frequencies of the 18-in sawblade increases the chance that the operating frequencies will excite the natural frequencies.

The study also reveals knowledge for the best number and length of expansion slots. The results have shown that having three expansion slots to disrupt the symmetry of the sawblade is best to raise the natural frequencies. However, the expansion slots alone are not enough – residual stress rings must be used for optimum performance of the 18-in sawblades studied. Keeping the expansion slot as short as possible lowers the stress concentration allowing for less chance of cracking at the bottom of the expansion slot.

The study has revealed more insight of how residual stresses affect the sawblade below the surface. The study has revealed that the circumferential stresses are the dominating results from placing the residual stress ring. Furthermore, the study has quantified the radial displacement, radial stress and circumferential stresses within the body of the sawblade both below and at the surface.

For the residual stress ring at 2/3 radius, the radial displacement at the area radially outward from the contact area is approximately four times the radial displacement of areas inwards the contact area. The study has quantified the circumferential stress placed in the sawbody and shows it is also higher by approximately two times area outwards of the contact area versus areas closer to the center of the sawblade from the contact area. In addition, the roles of the shear stresses and axial stresses from placing the residual stress ring are essentially only localized stresses at the area of the roller contact.

In the sawblade design performance, the residual stress rings allow the sawblade to run truer, free from wobble and vibrations. This will allow the sawblade to cut the material leaving a cleaner cut. In turn, this will save horsepower due to the thinner cross sectional area of a sawblade that does not wobbles side to side at its saw tips. In addition, this will allow for fewer broken saw tips from the chatter of a sawblade with no tensioning. The beneficial factors will all result in a cooler running sawblade, which will make it last longer. The amount of fatigue from the vibrations will be drastically reduced by using properly placed residual stress rings as found in this thesis.

Issues that remain to be studied, which are outside the scope of this thesis are the thermal stresses induced from the cutting and rubbing of the sawblade. This study would need to explore the thermal gradient induced and compare the compressive stresses induced into the sawbody that may offset the residual stress rings induced into the sawbody. Questions would need to be investigated to see how much the thermal stresses lower the natural frequencies of the sawblade. The study could explore at what point the saw tips should be replaced due to the increase in heat within the sawbody from cutting with dull saw tips. At what point does the added heat from the dull saw tips begin to reduce the tensioning in the sawblade back towards equilibrium is a good topic to study.

Chapter 11

Conclusions

The work developed in this thesis was to provide a better understanding of a rotating sawblade. Specifically, the paper gives insight into the stresses resulting from the processes of rotating, cutting and the tensioning of a circular sawblade, and the impact of design decisions and parameters on sawblade performance.

The problem of analyzing a sawblade with regard to rotational and simple cutting loads, natural frequencies, length, number, and angle of expansion slots, and location of residual stress from saw tensioning has been explored in this thesis. The conclusions derived from this study are listed:

1. Placing a single residual stress ring has the best effect on raising the natural frequency of an 18-in sawblade.
2. This single residual stress ring is best if located at either 2/3 radius or 5/6 the radius of the sawblade.
3. The shorter an expansion slot is made the less stress will be found in the sawblade at the bottom of the stop hole of the expansion slot. Thereby decreasing the amount of stress the sawbody sees from the cutting and rotating actions.
4. The cutting forces of the sawblade are not high enough to be the number one contributing factor to the longevity of the sawbody.
5. The vibrations seen by the sawblade appear to be the most significant contributor to cause the sawbody to wear out.
6. The vibration mode shapes tend to align themselves with the expansion slots, thereby increasing the chances of fatigue at the expansion slots due to the vibration of the sawblade.
7. The finite element analysis is proved valid for the reporting of the stresses from rotating a sawblade, free-vibration analysis, and over-tensioning by means of very high correlation with analytical studies, experimental modal analysis and many year of practical experience by qualified individuals in the field.

11.1 *Summary of Contributions*

The general contributions this research has made are the demonstrated use and validation for the finite element analysis as a way to find the stresses under the surface of a sawblade when it is rotating and cutting. Also,

1. The stresses of a sawblade with various numbers, lengths, and angles of the expansion slots have been determined for a sawblade is undergoing rotation.
2. The natural frequencies and mode shapes of a sawblade with various numbers, lengths, and angles of the expansion slots have been determined for a sawblade undergoing rotation.
3. The research has shown the effects of placing residual stresses in a sawblade and has shown what happens within the material under the surface of the sawblade – these stresses were not previously quantified before.
4. The research has found the effects of placement location, number, and combination of residual stress rings on the natural frequencies of a rotating annulus.
5. The research has quantified the displacement of the rollers toward the sawblade to induce the sawbody material in the plastic zone while simultaneously keeping the roller material in the elastic zone.
6. The research has verified the best placement of the residual stress ring in an 18-in sawblade.
7. The stress within the annulus with residual stress ring has been quantified at an area below the surface and throughout the geometry.

11.2 *Future Recommended Studies*

Future recommended studies include a periodic time-domain dynamic analysis, where a sinusoidal calculated force representing the contact of the sawblade and the wood. This force should be pulsated at several trial designated points on the sawblade.

Furthermore, the frequency range of this study would begin at the spin speeds or perhaps near some of the lower natural frequencies which would couple easily with the loads associated with cutting wood. This could be done in small incremental steps of about 1 Hz to get a best representation of how the sawblade responds. The response could then be found in terms of displacement in all directions, and the magnitude of all directions combined. Further, the amount of stress at certain frequencies could be found. Also, as part of the analysis, the higher energy modes could be found in terms of modal participation factors to see how the natural modes of vibration couple in with the loading and boundary conditions. These studies could further the design of the sawblades in an effort to keep the excitation frequencies away from the higher-energy destructive modes found. Also, this study could help in the design of the sawblades by helping to find ways to keep the displacements from the vibrations low.

Along with theses studies, a matrix of sawblades that have undergone residual stresses at various radii of the sawblade versus no residual stress could be analyzed with the same transient analysis showing stresses and displacements in the sawbody. This matrix could utilize several points of placing the sinusoidal force allowing us to find the target residual stresses to use in the sawblades due to the lowering of stress and displacements of the sawbody.

In addition to these studies, the amount of displacement of sawblades with lateral forces applied to the sawblade in an effort to quantify and compare the stiffness of sawblades with various residual stresses and without any residual stresses. This could be done as a simple spring curve giving force versus lateral displacement of the sawblade.

Finite Element Analysis and Sawblades. Finite element analysis has proven to be very effective at exploring the performance and design of sawblades. Good approximations can be achieved for the amount and types of stress seen by the sawblades during the rotating and cutting of material. The simulations represented by the mathematical models are great at providing insight into the case studies represented. Finite element analysis is a power tool when coupled with experience and engineering knowledge. This could be a vital tool in the design and optimization of expansion slots and residual stress rings. Finite element analysis can quantify and qualify why residual stress rings, expansion slots and other features are put into a sawblade and with enough

exploration one can find the best shape, placement and quantity of features of the sawblade. New concepts for the geometry or materials of a sawblade can be verified and improved upon with the use of finite element analysis. Much insight can be obtained from the finite element models, which show the stresses and displacements in the sawbody during and after the tensioning process and the cutting loading conditions. In addition, the analysis can also show the points of yielding in the sawbody.

The applicability and utility of using finite element analysis in sawblade design is its ability to simulate nearly any kind of geometry, material properties, loading, and boundary conditions. However, some drawbacks are evident with FEA, such as: the residual stresses in 3-D models and the amount of time required simulating the real world conditions of sawblades. FEA requires an engineer to formulate the analysis and interpret the results; FEA needs to be backed up with calculations, experiments, or experience to validate the answers. The answers obtained by FEA are only approximations of what will take place within a sawblade; it cannot predict flaws in the material or manufacturing processes or the material being cut. To completely verify the answers sought after, only experiments using the actual sawblade in the actual conditions will confirm results. However, finite element analysis has a future in the sawblade industry due to its immense ability to simulate and approximate the physics involved in cutting materials with a sawblade.

References

[1] PLANK, D., STEPHENSON, E. Circular Saws. (1972).
[2] PONTON, R. S. Conducted numerous interviews, President/owner of International Carbide and Engineering, Inc. in Drakes Branch, VA.
[3] LUNSTRUM, S. Circular Sawmills and Their Efficient Operation, U.S. Department of Agriculture, USDA Forest Service State and Private Forestry. (1993).
[4] STAKHIEV, Y. "Research on circular saw disc problems: several of results," Springer-Verlag Heidelberg 62(1) (February 2002).
[5] QUELCH, P. Armstrong Filer's Handbook. Armstrong Manufacturing Co. 2nd Revised Ed. (1996).
[6] WILLISTON, E. SAWS Design Selection Operation Maintenance. Miller Freedman Publications. (1978).
[7] HIBBIT, KARLSSON & SORENSEN. Getting Started with ABAQUS/Standard. Hibbit, Karlsson & Sorensen, Inc. (1996).
[8] BORESI, A., SCHMIDT, R. Advanced Mechanics of Materials. John Wiley & Sons, Inc. 6th ed. (2003).
[9] DENIG, J. Small Sawmill Handbook. Miller Freeman, (1993).
[10] BROCKENBROUGH, R., MERRITT, F. Structural Steel Designer's Handbook. McGraw-Hill, Inc 3rd edition (1999).
[11] BEER, F., JOHNSTON, JR, E. Mechanics of Materials. McGraw-Hill, Inc. 2nd ed. (1992).
[12] RAO, S. Mechanical Virations. Addison-Wesley Publishing Co., Inc. 2nd ed. (1990).
[13] THOMSON, W. Theory of Vibration With Applications. Pentice Hall (1988).
[14] http://www.matweb.com
[15] HODGES, J. Conducted interview, Customer Service Manager at Reeds Carbide Saw and Tool, in Lynchburg, VA.
[16] SHIGLEY, J. Mechanical Engineering Design. McGraw-Hill, Sixth Ed. (2001).
[17] YOUNG, W.C., Roark's Formulas for Stress and Strain, McGraw-Hill, (1989).
[18] "Residual Stress," <<http://www.scudc.scu.edu/cmdoc/dg_doc/develop/process/physics/b3400001.htm>>.
[19] "Effects of Residual Stress on the Operating Performance," Physique and Industrie, <<http://www.physiqueindustrie.com/residual_stress.htm#Production>>.
[20] Q. YAO, J. QU, "Effect of Thermal Residual Stresses on the Apparent Interfacial Toughness of Epoxy/Aluminum Interface," Packaging Research Center, Georgia Institute of Technology.
[21] The Hanchett Saw and Knife Fitting Manual. 8th Edition, Hanchett Manufacturing Co., (1956).
[22] QUELCH, P. Sawmill Feeds and Speeds. Revised Edition, Armstrong Manufacturing Co. (1994).
[23] A. SURYANARAYANA, R. RADTKE, "Novel Methods of Brazing Dissimilar Materials, Advanced Materials & Processes," (March 2001).
[24] M. SCHWARTZ, Brazing for the Engineering Technologist, (1995).
[25] Brazing Handbook, American Welding Society, (1991).
[26] T. WALZ, Intro: Brazing Tungsten Carbide and Ceramics For Saws, Tools & Wear Parts, Book Northwest Research Institute, Inc. <http://www.carbideprocessors.com/Brazing/indes.htm>.
[27] E. FENTON, Brazing Manual, Reinhold Publishing Corp. (1963).
[28] O.D. VELEV, N.D. DENKOV, V.N. PAUNOV, P.A. KRALCHEVSKY AND K. NAGAYAMA, *Langmuir*, 9, 3702 (1993).
[29] L. MARTENS, W. TILLMANN, E. LUGSCHEIDER, G. ZIEGLER, "Strength of microstructure of brazed cemented carbide and silicon and nitride joints," *Journal of Materials Processing Technology* 58 (1996).
[30] JACK L K, Lecture in Class Notes, November 14 and 17 (2003).
[31] HANDY AND HARMON, The Brazing Book, NY, (1985).
[32] S. DARWISH, R. DAVIES, "Investigation of the heat flow through bonded and brazed metal cutting tools," *Int. J. of Mach. Tools and Man.* 29(2) (1989).

[33] F. MASON, "Better Carbide Tools FEA Way," *Manufacturing Engineering* 115 (July 1995).
[34] B. RICCARDI, C. NANNETTI, J. WOLTERSDORF, E. PIPPEL, T. PETRISOR, "Brazing of SiC and SiC_f/SiC composites performed with 84Si-16Ti eutectic alloy: microstructure and strength," *Journal of Materials Science* 37 (2002).
[35] "Tungsten," <http://chemserv.bc.edu/web_elements/W.html>.
[36] L. YAJIANG, Z. ZENGDA, H. XIAO, W. JUAN, "Microstructure and XRD analysis in the brazing zone of new WC-TiC-Co hard alloy," *Materials Research Bulletin* 37 (2002).
[37] K. BROOKES, World Directory and Handbook of Hardmetals, (1982) Engineer's Digest Limited and International Carbide Data.
[38] "Residual Stress," <<http://www.scudc.scu.edu/cmdoc/dg_doc/develop/process/physics/b3400001.htm>>.
[39] "Effects of Residual Stress on the Operating Performance," Physique and Industrie, <<http://www.physiqueindustrie.com/residual_stress.htm#Production>>.
[40] C. BAUER, R. FARRIS, M. VRATSANOS, "Determination of the Stresses and Properties of Polymer Coatings," Plenum Publishing Corp. New York, NY, Polymer Science and Engineering Dept. (May 1988).
[41] KIASAT, "Curing Shrinkage and Residual Stresses in Viscoelastic Thermosetting Resins and Composites," Delft University of Technology (May 2000).
[42] G. HUMFELD, JR., D. DILLARD, "Residual Stress Development in Adhesive Joints Subjected to Thermal Cycling," *J. Adhesion* 00 (1997).
[43] Q. YAO, J. QU, "Effect of Thermal Residual Stresses on the Apparent Interfacial Toughness of Epoxy/Aluminum Interface," Packaging Research Center, Georgia Institute of Technology.
[44] R. HAMACHA, B. DIONNET, A. GRIMAUD, F. NARDOU, "Residual stress evolution during the thermal cycling of plasma-sprayed zirconia coatings," *Surf. and Coatings Technology* 80 (1996).
[45] D. JOH, K. BYUN, J. HA, "Thermal Residual Stresses in Thick Graphite/Epoxy Composite Laminates – Uniaxial Approach," University of Missouri Rolla (October 3, 1992).
[46] M. HUANG, Z. SUO, Q. MA, "Plastic ratcheting induced cracks in thin film structures," *J. Mech. and Phys. of Sol.* 50 (2002).
[47] J. FELBA, K. FRIEDEL, P. KRULL, I POBOL, H. WOHLFAHRT, "Electron beam activated brazing of cubic boron nitride to tungsten carbide cutting tools," *Vacuum* 62 (2001).
[48] Lucas-Milhaupt, Inc., Tech data sheet, <<http://www.topfloorserver.com/lucasmilha/upt/pdf/br505.pdf>>.

Vita

Charles B. Ponton worked in the industrial sawblade industry for several years in the manufacturing and repairing of the sawblades found in this thesis. He received a B.S. degree in mechanical engineering in 2003 from Virginia Tech. Chuck taught as a Graduate Teaching Assistant for the senior mechanical engineering lab courses at Virginia Tech under Dr. Robershaw. He worked with Dr. West for guidance through the research and writing process of this thesis. He graduated with an M.S.M.E. degree in 2007 from Virginia Tech while working in the naval and marine industry as a mechanical engineer.